Improving the Functional Control of Ferroelectrics Using Insights from Atomistic Modelling

Jacob Bernard John Chapman

2018

A dissertation submitted in partial fulfilment of the
requirements for the degree of

Doctor of Engineering

*THE CENTRE FOR DOCTORAL TRAINING IN MOLECULAR
MODELLING AND MATERIALS SCIENCE*

Department of Physics and Astronomy
University College London

Supervised by
Prof D. M. Duffy
Dr A. V. Kimmel

Declaration

I, Jacob Bernard John Chapman, confirm that the work presented in this Thesis is my own, except where indicated. Where information has been derived from other sources, I confirm that this has been indicated in this Thesis.

Acknowledgements

I would like to start by expressing my sincere gratitude to my project advisors Prof Dorothy Duffy and Dr Anna Kimmel who have guided me throughout my time at UCL. Your support, knowledge, ideas and insights have been greatly appreciated and have helped develop my research practices and methodologies. I am specifically thankful for the freedom you granted, allowing me to start collaborations and investigate new ideas beyond the scope of our original project which were exceptionally rewarding and fruitful, whilst keeping me on track to complete this achievement. I would also like to profoundly thank Dr Oliver Gindele with whom I shared an office and worked closely throughout my project. You all helped me understand more problems and ideas than I can count.

My gratitude goes out to my my father John, my mother Caralyn, my grandparents, my brothers Bertie and Cory, my step-father Pete, my mother-in-law to-be Susan and everyone in my extended family who have supported me in my academic pursuits.

I am also especially grateful to all those in the ferroelectrics community who have given time to discuss my research, its direction and have helped shape my academic career. In particular, I would like to thank Prof Ron Cohen who introduced me to the problem of ageing in ferroelectrics and with whom I subsequently worked closely on the topic, Prof Marty Gregg who shared many discussions regarding ferroelectric films and contributed Figures and knowledge to several conference presentations, Prof Pavlo Zubko who dedicated a lot of time to review my manuscripts before submission and to discuss ultrathin films, heterostructures and superlattices. I am further thankful to Dr Martin Hÿtch who was gracious to share Figure 6.6a-c and talk about TEM and domain wall motion in Pt-PZT-STO capacitors, and to Prof Markys Cain who helped formulate my project.

I extend the warmest gratitude to everyone at the M3S CDT and fellow postgraduate students at NPL who I shared the past four years working beside. Thank you for all your support and the laughs we shared.

And finally, I would like to thank Helen my wonderful fiancée, to whom I dedicate this thesis. Thank you for all your support, encouragement and perseverance through all the highs and lows of this stage of my life. Without you, this accomplishment would not have been possible.

The work presented in this thesis and contributed towards the publications given in Appendix B were carried out within the Centre for Doctoral Training in Molecular Modelling and Materials Science (M3S CDT) based within the Condensed Matter Materials Physics (CMMP) group at University College London (UCL) completed between 2014 and 2017, in a project co-funded by the UK Engineering and Physical Sciences Research Council (EPSRC, Grant no. EP/G036675/1) and the Mathematics, Modelling and Simulation Department at the National Physical Laboratory (NPL) for the National Measurement Office of the UK Department of Business Innovation and Skills. Computational facilities (Grace and Legion) were provided by University College London, (Puppis and Salviati) by the London Centre for Nanotechnology and access to the National Supercomputing Facility ARCHER were provided by our membership of the UK's HPC Materials Chemistry Consortium, funded by the EPSRC (EP/L000202).

Abstract

Lead zirconate titanate is a ferroelectric material of considerable interest with a wide range of technological applications. It has been the subject of many experimental and theoretical studies yet there are a number of unsolved questions preventing further miniaturisation and optimisation of this and other ferroelectric materials. Exotic ultra-dense domain morphologies, as an example, offer an exciting avenue for the development of novel nanoelectronics. In this work, large scale molecular dynamics is used to construct a strain-temperature phase diagram of the domain morphology of $PbTiO_3$ ultrathin films. By sampling a wide range of strain values over a temperature range up to the Curie temperature T_c, it is found that epitaxial strain induces the formation of a variety of closure- and in-plane domain morphologies. The local strain and ferroelectric-antiferrodistortive coupling at the film surface vary for the strain mediated transition sequence and this could offer a route for experimental observation of the morphologies. Remarkably, a new nanobubble domain morphology is identified that is stable in the high-temperature regime for compressively strained $PbTiO_3$. It is demonstrated that the formation mechanism of the nanobubble domains morphology is related to the wandering of flux closure domain walls, which is characterised using the hypertoroidal moment.

Molecular dynamics calculations, supplemented with electrical measurements from collaborators, are used to provide insight into the microscopic switching properties of near-morphotropic PZT. The simulations and experiments exhibit qualitatively similar hysteretic behaviour of the polarisation at different temperatures, showing widening of the Polarisation - Electric field hysteresis loops, and the decrease of the coercive field towards high temperatures. Remarkably, polarisation switching at low temperatures is shown to occur via a polarisation rotation and growth mechanism that is fundamentally different from the high temperature switching, where nucleation is rate limiting. Analysis of B-cation contributions show that nucleation and switching are facilitated by Zr centred unit cells and, by extension, Ti centred unit cells in Zr-rich environments. Ti-rich clusters in morphotropic PZT, at low temperature, are observed to have suppressed ferroelectric displacements which may incorrectly be perceived as ferroelectrically inactive '*dead-layers*'.

Finally, fundamental insight into the microscopic mechanisms of the ageing processes are provided. From simulations of the prototypical ferroelectric material $PbTiO_3$, it is demonstrated that experimentally observed ageing phenomena can be reproduced from intrinsic interactions of defect-dipoles related to dopant-vacancy associates, even in the absence of extrinsic effects. Variation of the dopant concentration is shown to modify the material's hysteretic response, identifying a universal method to reduce loss and tune the electromechanical properties of inexpensive ceramics for efficient technologies.

Contents

List of Figures

List of Tables

1

Introduction

The study of ferroelectric (FE) behaviour has grown rapidly over the past three decades with FE devices gaining an increasing market share in all corners of the electronics industry [1]. Increasing demand is warranted to understand the fundamental nature of equilibrium domain structures and their dynamic properties motivated for continued integration into increasingly miniaturised electronics. Down-scaling the volume of individual capacitors has enabled a systematic gain in the available storage density such that as of 2012 the total amount of electronically stored data is estimated to exceed 5x10^{21} bits [2]. However, fundamental scaling limits are being reached for many device architectures. Any further improvements to the storage densities, operational lifetimes, read and write speeds within both random access and solid state memories requires a detailed investigation into novel nanoscale ferroelectric properties [3, 4]. Central to this development is the need to understand intrinsic finite size effects on the ferroelectric order which remains contested in the literature [5]. However, with recent predictions of phenomena including vortex polarisation states [5–7], it is speculated that nanoscale ferroelectronic capacitors may have the ideal intrinsic properties to exceed the industry-wide target of 1 Tbit/inch^2 storage [1, 2].

The ferroelectric phenomenon, defined as having multiple stable and switchable polar states, was first observed in Rochelle salt in 1920 [8]. Owing to the fragility and water solubility of the salt few practical applications were initially predicted [9]. Opinion unanimously reversed after several perovskite oxides (ABO_3) were discovered to be ferroelectric in the 1940's spawning immediate identification of electromechanical applications in thermal imaging, ultrasound and SONAR [10]. Bloembergen was awarded the 1981 Nobel prize for the discovery that periodic arrangements of antiparallel ferroelectric domains maximised the efficiency of wavelength conversion in laser spectroscopy [11, 12]. More recently, the archetypal ferroelectrics barium titanate ($BaTiO_3$) and lead titanate ($PbTiO_3$) have sparked interest due to the switchability between degenerate and oppositely polarised tetragonal states of each formula unit at room temperature offering a natural atomic scale method for storing Boolean logic [8].

Many device architectures have been realised based upon the ferroelectric instability. Arguably, one of the most important uses of ferroelectrics has been to replace conventional DRAM capacitors producing non-volatile alternatives (FeRAM and PET) [13]. To remain competitive against competing technologies, including MRAM, the operational lifetime will require consistent switching for more than 10^{12} cycles without operationally impinging fatigue [14]. However, the current level of understanding and lack of full-scale device models relating to the processes of fatigue have prevented accurate predictions of the functional lifetimes [15]. Atomistic modelling using a semi-empirical shell-model could provide the necessary large scale simulations required. More accurate and physically representative *ab initio* approaches such as density functional theory and the effective Hamiltonian method have provided key insights into ferroelectric behaviour, however, the limitations in system size make the simulation of realistic domain dynamics in nanostructures intractable [16]. Alternatively, atomistic modelling has already proven capable; accurately reproducing many fundamental features of ferroelectricity including the non-trivial phase transitions [17, 18], spontaneous domain formation [19], surface relaxations [20, 21] and the ferroelectric stability limit observed on ultrathin films [19]. Atomistic scale simulations using interatomic shell-model potentials have proven to be a particularly efficient approach to study ferroelectric behaviour; capable of capturing the subtle balance between Coulomb, short-range and long-range interactions [17, 22, 23] whilst remaining scalable to millions of atoms [24].

The past two decades in the field have been especially active, stimulated by improvements in material characterisation and synthesis techniques which in turn have provided an unprecedented ability to control and manipulate local atomic structures to fine-tune ferroelectric properties. Simultaneously, improvements in theoretical models, advances in available computational power and the efficiency and scalability of algorithms, have resulted in accurate simulation techniques incorporating atom numbers comparable to experimental methods. This has directly enabled reactive feedback between atomistic models and experiments that have vastly accelerated our understanding of ferroelectric and piezoelectric behaviour. Nonetheless, development of ferroelectric components has been bottlenecked in recent years due to several critical gaps in knowledge. For example, one of the most industrially successful ferroelectric materials, owing its large dielectric constants, is lead zirconate titanate $Pb(Zr_{1-x}Ti_x)O_3$ yet the origins of its superior dielectric properties remain contested. Further for this material and its parent compound $PbTiO_3$, it has been highlighted that it has become necessary to identifying how microstructure affects domain wall motion as a step to improve polarisation switching rates in order to improve device read and write speeds. And further, the mechanisms resulting in the fatigue of macroscopic hysteresis properties with time, known as ageing, are yet to be characterised.

In this thesis shell-model forcefields are used to investigate lead zirconate titanate $Pb(Zr_{1-x}Ti_x)O_3$ (PZT) and its parent compound lead titanate $PbTiO_3$ (PTO), the most widely used and industrially significant ferroelectric materials. I address three questions vital for the future development of ferroelectric based devices:

1. What are the ferroelectric and dielectric properties of $PbTiO_3$ ultrathin films and $PbZr_{1-x}Ti_xO_3/SrTiO_3$ heterostructures?
2. How does the temperature and local composition initiate and affect switching dynamics in lead zirconate titanate?
3. What causes perovskite ferroelectrics to 'age'?

The thesis is organised as followed. In Chapter 2 a basic overview of ABO_3 perovskite ferroelectric materials is presented. Their characteristic properties are introduced and the key motivations for the thesis project are discussed. Chapter 3 details the computational methodologies and frameworks upon which the subsequent research is obtained. Further insight is given regarding the fundamental properties of ferroelectric materials, building upon the computational methods described. Chapter 4 is dedicated to detailing the formalisms of properties of interest calculated from simulations, benchmarking their implementation in codes written for this work and now used by several research groups around the World. In Chapter 5, ferroelectric and piezoelectric properties of $PbTiO_3$ ultrathin films are systematically investigated as a function of strain and temperature, identifying a previously unknown domain structure and the mechanism of its formation. Novel characteristics at the domain walls and surfaces such as Bloch-Néel rotations and ferroelectric-antiferrodistortive coupling are observed. The results in this Chapter identify exotic features that can be exploited in nanotechnologies. Chapter 6 develops the methodology of Chapter 5 to investigate $PbTiO_3/SrTiO_3$ superlattices and PZT epitaxially grown on a strontium titanate $SrTiO_3$ (STO) substrate deposited with a Pt electrode, through the fitting of an STO forcefield and tethering parameters for an existing Pt potential. Chapter 7 analyses the dynamics of domain wall motion and switching in morphotropic and rhombohedral PZT. The effects of local composition are discussed and related to different mechanisms for switching observed at different temperatures. The results in this chapter will help to inform the best compositional configurations to achieve ultra-fast switching in ferroelectric electronic devices. The work in Chapter 8 culminates with a detailed study into the microscopic mechanisms responsible for the experimentally observed ‘ageing’ of ferroelectric materials. Each known phenomenon is married to a specific dipole arrangement from dopant-vacancy associates identified from molecular dynamics simulations. This work reveals a systematic approach to reduce losses and tune electromechanical properties of these materials. Finally, the results presented in this thesis are summarised in the conclusions of Chapter 9.

2

Ferroelectricity: Background

A conventional ferroelectric material is an insulator with at least two stable or metastable polar states which can be switched between with an electric field. They are critical components in many current applications, as well as in the next generation of emergent technologies. Ferroelectrics have been of fundamental physical interest since the 1960's and earlier, yet basic questions about the origins of their behaviour remain. In this Chapter we introduce typical ferroelectric materials and explore the principles of ferroelectricity through phenomenological models. This Chapter begins with an introduction into the concept of a ferroelectric phase transitions using Landau-Devonshire theory.

2.1 Ferroelectric Phase Transitions

Phase transitions are qualitative changes to the equilibrium state of a system due to external stimuli and are ubiquitous to ferroelectric materials. A quantitative description can be understood from extrema in the systems thermodynamic potential [25]. For bulk ferroelectrics in equilibrium, the thermodynamic state can be fully specified by two order parameters: polarisation P_i and strain η_{ij}; and three applied variables of stress σ_{ij}, temperature T and electric field $\mathcal{E}_i$ [26]. Landau-Devonshire theory [27–31] is a phenomenological thermodynamic model which attempts to relate these parameters by assuming that near the phase transition the thermodynamic potential, here the Gibbs free energy density $\mathcal{G}$, can be Taylor expanded from the prototype state with respect to the order parameters:

$$\mathcal{G}_0 = U - TS - \sigma_{ij}\eta_{ij} - \mathcal{E}_i P_i = \mathcal{F}_0(T) - \mathcal{E}P \tag{2.1}$$

$$\mathcal{G} = \mathcal{F}_0 + \sum_n \frac{1}{n}\mathcal{F}_n P^n - \mathcal{E}P \tag{2.2}$$

where U is the internal energy density, S is entropy, $\mathcal{F}_0$ is the free energy density of the prototype state, $\mathcal{F}_n$ is the nth expansion coefficient of the free energy and $-\mathcal{E}P$ is the interaction energy density. Here we only consider an expansion with respect to the polarisation with a condition of no stress for simplicity and subjected to the restraint that $P(T) = -P(T)$ such that only positive expansion terms remain finite. The equilibrium state is then determined by the minima in $\mathcal{G}$:

$$\frac{\partial \mathcal{G}}{\partial P} = 0, \qquad \frac{\partial^2 \mathcal{G}}{\partial P^2} > 0 \tag{2.3}$$

Since the dielectric equation of state can be calculated from the free energy density as [32]:

$$\mathcal{E} = \left.\frac{\partial \mathcal{G}}{\partial P}\right|_T = \mathcal{F}_2 P + \mathcal{F}_4 P^3 + \mathcal{O}(P^5) \tag{2.4}$$

the global minima in $\mathcal{G}$ corresponds to the equilibrium condition of P under zero-field displacement, defined as the spontaneous polarisation P_s. The dielectric susceptibility is defined as the rate of change of the polarisation with respect to the displacement field $\mathcal{E}$ in the limit $P \to 0$, such that:

$$\left.\frac{\partial^2 \mathcal{G}}{\partial P^2}\right|_{P=0} = \left.\frac{\partial \mathcal{E}}{\partial P}\right|_{P=0} = \frac{1}{\chi} \tag{2.5}$$

Landau-Devonshire theory assumes that near the transition temperature ($T \approx T_0$) the dielectric stiffness $\kappa = 1/\chi$ is linear to reproduce the Curie-Weiss behaviour[1] of κ most often observed in ferroelectrics for $T > T_0$ [26,32]:

$$\kappa = \frac{1}{\chi} = \frac{1}{C\epsilon_0}(T - T_0) = \mathcal{F}_2, \qquad (C > 0, T > T_0) \tag{2.6}$$

Substituting the dielectric stiffness into the Gibbs free energy density gives the general expression:

$$\mathcal{G}(P) = \frac{1}{2C\epsilon_0}(T - T_c)P^2 + \frac{1}{4}\mathcal{F}_4 P^4 + \mathcal{O}(P^6) - \mathcal{E}P \tag{2.7}$$

The behaviour of a ferroelectric phase transition between the paraelectric phase ($T >> T_0$) and ferroelectric phase ($T << T_0$) is then determined by the free energy profile during the transition. Two solutions to equation 2.7 are possible dependent upon the sign of $\mathcal{F}_4$, causing either a continuous or discontinuous transition in the polarisation during the phase transition discussed in the following subsections.

2^{nd} Order Transitions ($\mathcal{F}_4 > 0$)

If $\mathcal{F}_4 > 0$, then below the transition temperature ($T < T_0$), the quadratic term in the free energy is negative and the quartic term positive causing the formation of a characteristic $\mathcal{W}$-potential with two degenerate minima (Figure 2.1a(blue)). Consequently, below T_0 an equilibrium state occurs with a spontaneous polarisation. Applying the minimisation conditions to Eqn. 2.7 when $\mathcal{E} = 0$ gives a solution of the spontaneous polarisation as [32]:

---

[1] Equation 2.6 is the electrical equivalent of the magnetic Curie-Weiss law

$$P_s = \pm\left(\frac{\mathcal{F}_2}{\mathcal{F}_4}\right)^{1/2} = \pm\left(\frac{1}{C\epsilon_0\mathcal{F}_4}(T_0 - T)\right)^{1/2}, \qquad T < T_0, \mathcal{F}_4 > 0, \mathcal{F}_6 = 0 \tag{2.8}$$

When $T > T_0$ the terms in the Gibbs energy density are both positive creating a flat well with a single minimum centred at the origin (Figure 2.1a(purple)). This equilibrium state therefore corresponds to a non-polar *paraelectric* phase. Evolution of the polarisation during this transition is continuous (Figure 2.1b) occuring in ferroelectrics such as triglycine sulfate [33].

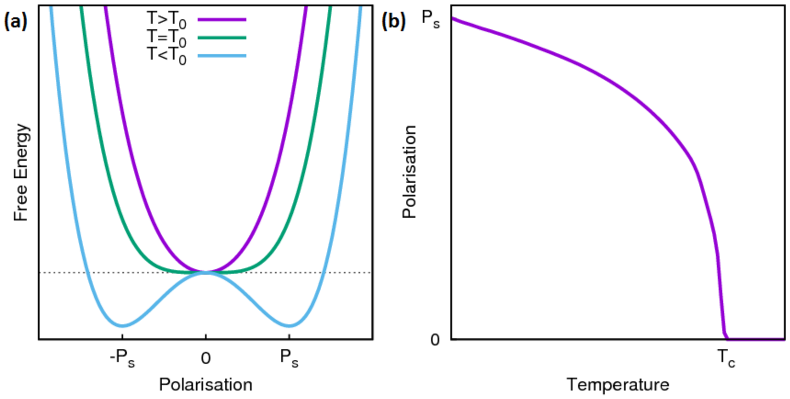

Figure 2.1: 2nd order phase transitions from Landau-Devonshire theory. (a) Temperature dependence of the free energy surface with respect to the polarisation order parameter. (b) Temperature dependence of polarisation.

1^{st} Order Transitions ($\mathcal{F}_4 < 0$)

Perovskite ferroelectrics, such as those considered throughout this thesis, most commonly undergo discontinuous first order phase transitions related to the change in symmetry from a group to subgroup of the two phases. For example, whilst the tetragonal (T), orthorhombic (O) and rhombohedral (R) phases of $BaTiO_3$ all have spacegroups which are a subgroup of the cubic $Pm\bar{3}m$ phase, there is no group-subgroup relation for the T-O or O-R transitions [26] resulting in a discontinuous jump in the enthalpy [33]. Such a phenomenon can be explained in the Landau-Devonshire formalism when $\mathcal{F}_4 < 0$. In this case, for finite stable solutions, the Gibbs free energy density (2.7) must be truncated to a 6^{th} order polynomial. It is defined that the $\mathcal{F}_2$ coefficient still obeys the Curie-Weiss relation (2.6).

Due to the negative quartic term, even for cases where $T > T_0$ (i.e. the quadratic term is positive), there may exist minima in the free energy density when the polarisation is non-zero. The free energy is shown in Figure 2.2a as a function of temperature showing minima for $T > T_0$ (purple). As the temperature is reduced towards T_0 these minima at non-zero polarisations become lower in energy. The temperature at which the polar and non-polar minima are degenerate (green) is defined as the Curie temperature T_c. Further reductions in temperature for $T_0 < T < T_c$ cause the polar states to become the thermodynamically stable state, resulting in a discontinuous change in the polarisation as the polar state becomes favourable (Figure 2.2b).

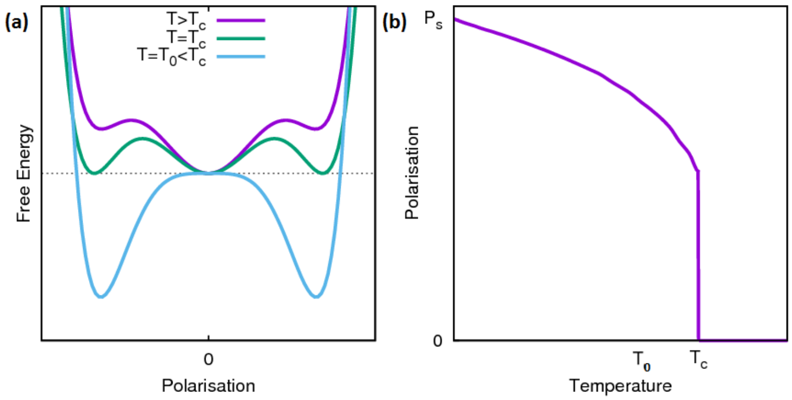

Figure 2.2: 1st order ferroelectric phase transitions from Landau-Devonshire theory. (a) Temperature dependence of the free energy surface with respect to the polarisation order parameter. (b) Temperature dependence of polarisation.

2.2 Strain-Coupling

In the previous section the Gibbs free energy density was only expanded relative to the polarisation. However, perovskite ferroelectrics also have a dominant feature of being extremely sensitive to elastic stress σ_{ij} [26, 32, 34]. It is, therefore, necessary to understand how applied stress will affect the properties of these materials. Landau-Devonshire theory can be extended to incorporate these effects by including terms from the Cauchy strain tensor η_{ij}:

$$\eta_{ij} = \frac{1}{2}\left(\frac{\partial u_i}{\partial r_j} + \frac{\partial u_j}{\partial r_i}\right) \tag{2.9}$$

where u_i is the displacement along i of a point in the material relative to position r_i.

Common industrial applications such as FeRAM or high sensitivity actuators take advantage of homogeneous biaxial strain though epitaxial growth of tetragonal (001) ferroelectrics onto a (001) substrate with different lattice parameters [35]. In such cases, the in-plane strains (η_{11} & η_{22}) are fixed and defined by the lattice mismatch between the ferroelectric and substrate bulk lattice parameters (a & a_s, respectively):

$$\eta_{11} = \eta_{22} = \frac{a - a_s}{a_s} \tag{2.10}$$

Pertsev *et al* identified that, in addition to the fixed in-plane strain, the correct mechanical boundary conditions occur in the limit of vanishing shear strains with the out-of-plane normal and shear stresses free to fully relax [36, 37]. Consequently, they were able to show the functional form of the free energy density to be minimised to be [35–38]:

$$\begin{aligned}\mathcal{G}(P,\eta)+\mathcal{E}P &= \frac{1}{2C\epsilon_0}(T-T_0)P_3^2+\mathcal{F}_4P_3^4+\mathcal{O}(P_3^6)\\ &\quad+\frac{1}{2}C_{11}(2\eta_{11}^2+\eta_{33}^2)+\frac{1}{2}C_{12}(2\eta_{11}^2+4\eta_{11}\eta_{33})\\ &\quad+2g_0\eta_{11}P_3^2+(g_0+g_1)\eta_{33}P_3^2\end{aligned} \tag{2.11}$$

where the first line is the original expansion with the classic $\mathcal{W}$-potential (Eqn. 2.7). The terms in the second line relate the elastic constants C_{ij} to the strain deformations, giving the elastic energy contributions to the free energy density. The third line contains the terms corresponding to the '*polarisation-strain coupling*' which acts to renormalise the quadratic term of the free energy [39]:

$$\left[\frac{1}{2C\epsilon_0}(T-T_0)+2g_0\eta_{11}+(g_0+g_1)\eta_{33}\right]P_3^2 \tag{2.12}$$

This polarisation-strain coupling causes giant piezoelectric responses typically 100-fold greater than non-ferroelectric piezoelectrics such as quartz [40]. Moreover, these additional coupling terms can be used to tune the coefficient of the quadratic term via the epitaxial strain conditions enabling so-called '*strain-engineering*' of the ferroelectric instability. By modifying the strain, the coefficient can be made more negative, lowering the energy of the double well in the $\mathcal{W}$-potential and increasing the stability of the ferroelectric phase as was shown experimentally by Choi *et al* for $BaTiO_3$ grown on single crystal substrates of $DyScO_3$ and $GaScO_3$ [41]. These epitaxial films were found to increase the transition temperature by 500 K and the spontaneous polarisation by 250% relative to bulk $BaTiO_3$. For non-ferroelectric materials, reductions in the quadratic coefficient can even induce a ferroelectric phase as has been predicted for rocksalt BaO and EuO [42]. $SrTiO_3$, an incipient ferroelectric below 37 K, has been experimentally shown to support in-plane polarisation at room temperature when epitaxially grown onto $DyScO_3$ [43]. Alternatively, if strain conditions cause the quadratic term coefficient (2.12) to become less negative, the ferroelectric character of the material will be reduced or even suppressed entirely if it becomes positive.

If higher order strain terms are considered in the free energy expansion (2.11), then additional cofactors will enter into the coefficient for the quartic term [26]. As the sign of this coefficient leads to the order of the phase transition, external stresses from lattice mismatch, chemical substitutions or hydrostatic pressures can change the order of the transition. Notably, the phase transition of $PbTiO_3$ has been shown to become second-order under pressures exceeding 12.1 GPa [44].

2.3 Phonons

Landau theory provides an excellent phenomenological introduction to ferroelectric phase transitions but makes no effort to describe the underlying physical origin. One of the most convincing microscopic models was derived by Cochran [45] who framed the problem in term of lattice dynamics. In this Section, the concept of lattice dynamics and *soft modes* are briefly introduced to aid the concluding sections of this Chapter. Greater detail on the fundamental physics of the ferroelectric phenomena including lattice dynamics are presented in Section 3.2.

Phonons are quasiparticles describing lattice vibrations, the collective excitations of the ions from their equilibrium Bravais sites. The adiabatic (Born-Oppenheimer) approximation (see §3.1) is applied wherein electrons are assumed to remain in their groundstate. If atomic displacements are small, the potential energy can be considered harmonic such that the restoring force acting upon an ion κ is linear. In this case, the total energy $E_{\mathrm{i+e}}$ of small lattice vibrations can be expanded as:

$$E_{i+e}(\{\tau\}) = E_{i+e}^{(0)} + \frac{1}{2} \sum_{\kappa\alpha} \sum_{\kappa'\alpha'} \tau_{\kappa\alpha}^{(a)} C_{\kappa\alpha\kappa'\alpha'} \tau_{\kappa'\tau'}^{(b)} + \mathcal{O}(\tau^4) \tag{2.13}$$

where $C_{\kappa\alpha\kappa'\alpha'}$ are the interatomic force constants for displacements of atom κ in cell a along direction α:

$$C_{\kappa\alpha\kappa'\alpha'} = \frac{\partial^2 E_{i+e}}{\partial \tau_{\kappa\alpha}^{(a)} \partial \tau_{\kappa'\alpha'}^{(b)}} \tag{2.14}$$

Assuming a periodic crystal, the classical equation of motion derives from Newton's second law using the derivative of equation 2.13. One expects planewave solutions of the form:

$$\tau_{\kappa\alpha}^{(a)}(t) = \epsilon_{m\mathbf{q}\kappa\alpha} \exp(i\mathbf{q} \cdot \mathbf{R}_{\kappa\alpha} - \omega t) \tag{2.15}$$

generating the eigenequations:

$$\sum_{\kappa'\alpha'} \tilde{C}_{\kappa\alpha\kappa'\alpha'}(\mathbf{q}) \epsilon_{m\mathbf{q}\kappa'\alpha'} = M_\kappa \omega_{m\mathbf{q}}^2 \epsilon_{m\mathbf{q}\kappa\alpha} \tag{2.16}$$

$$= \sum_{\kappa'\alpha'} \sqrt{M_\kappa M_{\kappa'}} \tilde{D}_{\kappa\alpha\kappa'\alpha'}(\mathbf{q}) \epsilon_{m\mathbf{q}\kappa'\alpha'} \tag{2.17}$$

where $\tilde{C}_{\kappa\alpha\kappa'\alpha'}$ is the Fourier transform of the force constants matrix (eqn. 2.14), M_κ is the mass of ion κ and $\tilde{D}_{\kappa\alpha\kappa'\alpha'}$ is the Fourier transform of the Dynamic matrix. The eigenvectors of equation 2.16 describe the lattice vibrations (phonons) of the system.

The simple case of a 1-dimensional diatomic chain of atoms has two solutions to the eigenequation (2.16). The eigenvalues for the two branches $w(q)$ are shown in Figure 2.3 and referred to as a dispersion curve. The subfigure shows the patterns of ionic displacements for *optical* and *acoustic* phonons of the same frequency. In three dimensions, solutions of eqn. 2.16

permit transverse and shear waves as well as the compressive waves considered in 1D.

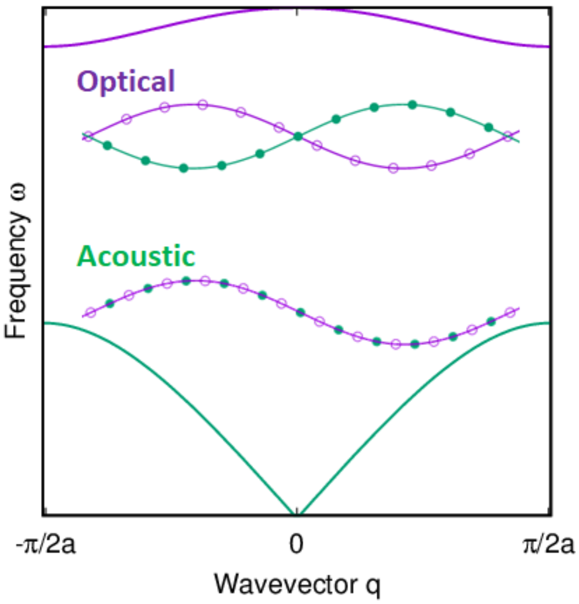

Figure 2.3: Phonon dispersion of the optical (purple) and acoustic (green) modes of a 1D diatomic chain. The sub-figure shows the pattern of ionic displacements for transverse optical and acoustic waves of the same frequency.

The seminal paper by Cochran related the zone centre (q=0) optical phonon frequency to the $\mathcal{F}_2$ Landau coefficient [45]:

$$\omega^2_{m,q=0} \propto \frac{1}{\chi} \tag{2.18}$$

This relation holds remarkably well for many ferroelectric materials. Example prototypical perovskite ferroelectrics are introduced in the following Section.

2.4 Ferroelectric Perovskites

An important and extensively utilised group of ferroelectric materials are perovskite oxides. A perovskite is a ternary compound with a general formula of ABX_3, where A is commonly a mono- or divalent metal and B is a tetra- or pentavalent metal in an equal ratio. X is often oxygen but can also be a halogen if A and B are mono- and divalent metals such as neighborite ($NaMgF_3$). As only oxygen is considered in this thesis X shall be defined as O henceforth. The oxygen anions create a corner linked network of octahedra with the B-cation populated within the octahedral cage (BO_6) and the A-cations occupying the sites between 8 octrahedra (Figure 2.4) [32].

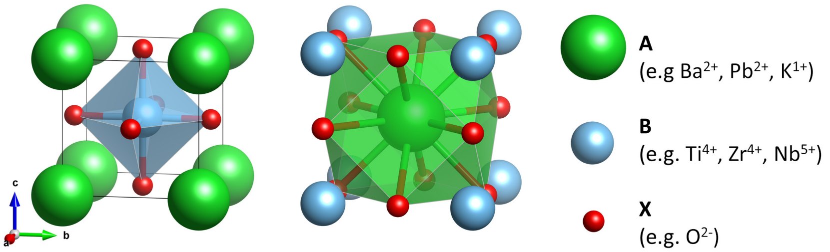

Figure 2.4: The ideal cubic $Pm\bar{3}m$ perovskite structure ABX_3 depicted in the conventional B-cation centred unit cell with a BX_6 octahedron (left) and an A-cation centred unit cell with an AX_{12} cuboctahedron (right). Polyhedra show the coordination of the centre cation.

The ideal perovskite structure is cubic in the $Pm\bar{3}m$ space group. This centrosymmetric reference structure is the high-temperature paraelectric phase of most ferroelectric perovskites. The physical properties of these perovskites are extremely diverse such that they may be metallic, insulating, magnetic, ferroelectric, piezoelectric or multiferroic depending on the cationic ordering [26]. Perovskites that do not manifest ferroelectric behaviour in bulk fail to do so due to suppression of the ferroelectric instability (see § 3.2) by a competitive type of order. The eponymous perovskite $CaTiO_3$ is such an example, wherein quantum fluctuations suppress the ferroelectric order by enabling tunnelling between the minima in the potential energy landscape (Fig. 2.1) making it an incipient ferroelectric [46].

Barium Titanate: $BaTiO_3$

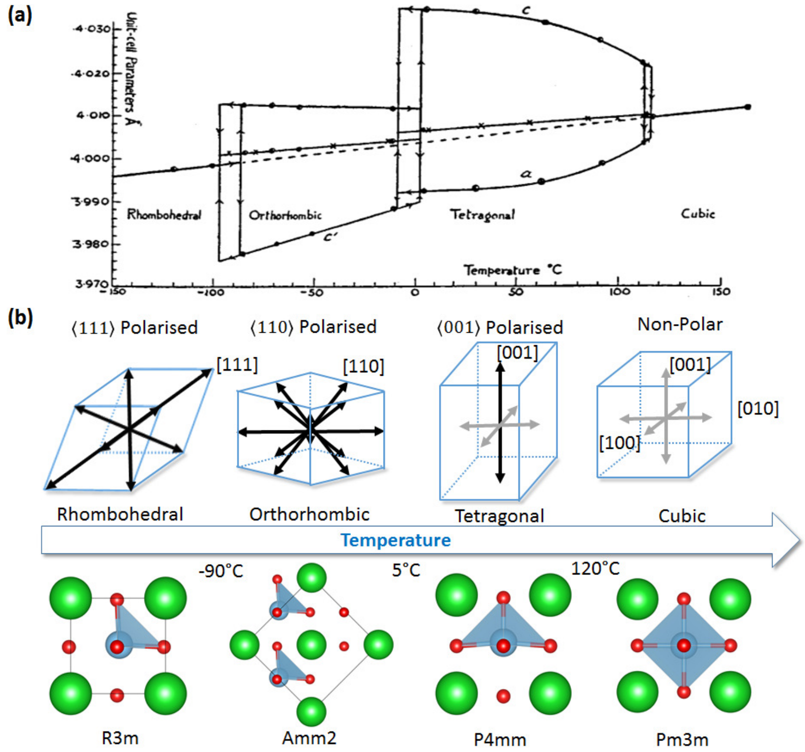

Figure 2.5: Polymorphic phase transition sequence of $BaTiO_3$. (a) Temperature dependence of the lattice parameters. Reprinted with permission from ref. [47]. Copyright 2001 American Chemical Society. (b) Structure and polarisation axis of the respective phases.

$BaTiO_3$ was the first perovskite identified as being ferroelectric and it has been extensively studied to investigate the onset of ferroelectricity and subsequent ferroelectric phase transitions ($A=Ba^{2+}$, $B=Ti^{4+}$, $X=O^{2-}$). At high temperatures $BaTiO_3$ adopts the prototype cubic perovskite structure ($Pm\bar{3}m$ space group) which is paraelectric due to the centrosymmetry. When cooled, $BaTiO_3$ undergoes a series of first order phase transitions (see § 2.1) into successively lower symmetry ferroelectric phases going to tetragonal (*P4mm*) at 393 K, orthorhombic (*Amm2*) at 278 K and rhombohedral (*R3m1*) for temperatures below 183 K (Figure 2.5a) [32] . Each transition condenses displacements of the B-cation (Ti) and octahedral cage relative to the A-cations (Ba), reorientating the spontaneous polarisation from $\langle 001 \rangle$ in the tetragonal phase, to $\langle 011 \rangle$ in the orthorhombic and subsequently $\langle 111 \rangle$ in the rhombohedral phase (Figure 2.5b). It is noteworthy that the ferroelectric $KNbO_3$ is isostructural with $BaTiO_3$ with respect to the temperature driven phase transition sequence even though K is monovalent and Nb is tetravalent [26].

Lead Titanate: $PbTiO_3$

Lead titanate ($PbTiO_3$), which shares the same cation valencies as $BaTiO_3$, similarly adopts a $Pm\bar{3}m$ cubic phase at high temperatures with an experimentally measured lattice parameter of 3.96 Å at its transition temperature of 763 K [48]. Below this temperature, $PbTiO_3$ undergoes a displacive first order transition into a tetragonal ferroelectric phase (*P4mm*) polarised along [001]. At room temperature, the polarisation is measured as 75 $\mu C/cm^2$ with lattice constants a=3.899 Å and c=4.153 Å [49]. Unlike $BaTiO_3$ or $KNbO_3$, no additional phase transitions are observed at lower temperatures.

The diverse range of ferroelectric phase transitions observed is non-trivial with its physical origin still contested. Using an analytic shell-model, Cochran identified the delicate balance between competing short and long range forces that caused a softening and eventual *freezing-in* of specific transverse optical phonon modes into the lattice structure [45]. Strong experimental evidence for the existence of these soft modes has been shown through inelastic neutron scattering [50] and for related LO-TO splitting (where the degeneracy of the longitudinal and transverse optic modes at the Brillouin zone centre are lifted [51]), verifying the displacive instability at the microscopic level. It was well established that the polarisability of oxygen in simple oxides was intrinsically linearly dependent on the disposable volume [50, 52]. Further insight into the phase transition mechanism was made when Migoni *et al* [53], using an empirical shell-model, predicted the polarisability to be highly non-linear and anisotropic in ferroelectric perovskites, causing speculation that the lattice instability arose due to hybridised bonding between the oxygen and transition metals. This characteristic mixed covalent-ionic signature was later proven through density functional theory (DFT) finding hybridisation between the filled O *2p* and empty Ti *3d* orbitals in both $BaTiO_3$ and $PbTiO_3$ [34]. This work was further able to identify the degree of covalency offered by the A-cation which plays a dominant role in the ferroelectric phase transition sequences between different perovskites. Pb has a higher degree of covalency relative to Ba which restricts the symmetry breaking and the bulk phase transition sequence to just cubic and tetragonal. In particular, the Pb-*6s* states hybridise with the O-*2p* whereas Ba states have no significant hybridisations with the valance band [26]. The covalency of the hybridised bonds are additionally shown to lead to extreme sensitivity to changes in bond lengths so atomic displacements result in dynamic charge transfer of electrons and an anomalous contribution to the Born effective charges Z^* [54]. This is explored further in § 3.2.

Lead Zirconate Titanate: $\mathbf{PbZr_{1-x}Ti_xO_3}$

Perovskite oxides readily form solid solutions from isoelectronic substitutions such as lead zirconate titanate $Pb(Zr_{1-x}Ti_x)O_3$ (PZT, see phase diagram in Figure 2.6), formed from the parent compounds $PbTiO_3$ (PTO) and $PbZrO_3$ (PZO) [26]. PZT is a popular ferroelectric solid solution due to its high piezoelectric response and large polarisation such that it accounted for 98% of the actuator market in 2014 [55]. Unlike the ferroelectric $PbTiO_3$ discussed in the previous section, PZO is antiferroelectric with an orthorhombic (*Pbam*) phase below 503 K and $Pm\bar{3}m$ cubic above. It has a 40-atom unit cell with lattice parameters of a=5.886 Å, b=11.749 Å and c=8.248 Å [56].

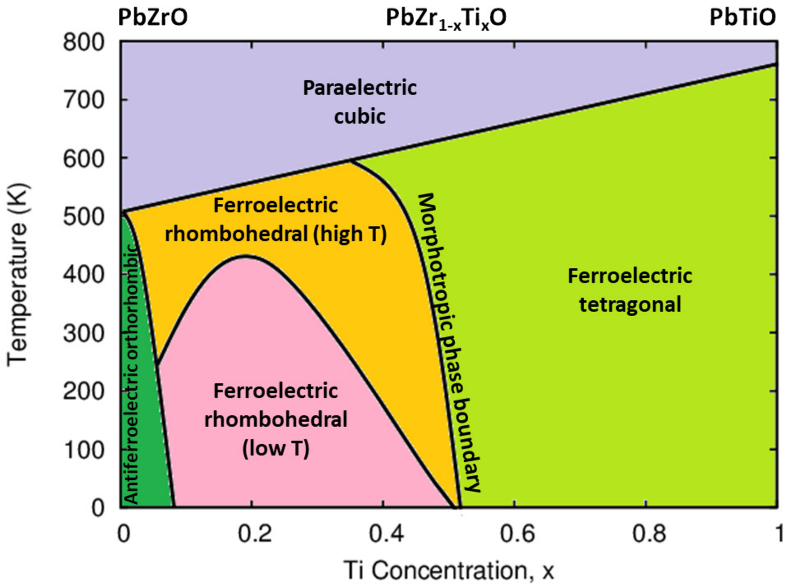

Figure 2.6: Polymorphic phase diagram of $Pb(Zr_{1-x}Ti_x)O_3$.

Adding PZO to pure PTO initially results in a decrease in the tetragonality[2] of the tetragonal phase until a roughly equal composition of each parent compound is reached (x≈0.5). Starting from pure PZO and replacing Zr cations with Ti quickly destabilises the antiferroelectric phase at x=0.06 producing two structurally similar rhombohedral phases polarised along ⟨111⟩ of space groups *R3c* and *R3m* [57]. Of particular significance for technological purposes is the narrow composition near x=48%, where the crystal structure abruptly changes between the rhombohedral and tetragonal phases, known the morphotropic phase boundary (MPB). Applying an

---

[2] c/a distortion

electric field in the MPB generates anomalously large changes in strain and relevant piezoelectric coefficients [58]. The large electromechanical response observed in the MPB has been suggested to occur due to an electric field driven rotation of the polarisation between $\langle 111 \rangle$ and $\langle 001 \rangle$ via continuous pathways through common monoclinic subgroups (Cm) [59, 60].

Despite recent advances relating to the MPB in PZT it remains poorly characterised. In particular, little is known about the dynamic properties during polarisation switching events. Since Ti and Zr are isoelectronic it could be expected that the B-cation distribution is random or only weakly ordered. Indeed, recent multiphase calculations at x=0.4 show a relatively flat energy landscape [60]. The local chemistry due to permutational freedom will undoubtedly change the dynamics dependent on whether a local region is Ti or Zr rich since the static local structure is similarly complex. Indeed the Ti and Zr cations have been observed to have different displacements dependent upon their octahedral environment [61] and this results in local monoclinic, rhombohedal and triclinic phases not identified in the bulk symmetry [55, 60, 62]. A detailed understanding of how local ordering affects both piezoelectric and ferroelectric properties is of fundamental scientific and industrial interest, as it will identify methods to tune and control the electromechanical response.

2.5 Domains and Domain Walls

In Sections 2.1 and 2.2, behaviour of the intrinsic polarisation of ferroelectric materials due to temperature changes and applied stresses were shown from simple thermodynamic arguments. However, no comment was made about the physical origin of this order parameter which microscopically arises due to the atomic arrangement of the ions (and further enhanced from electronic contributions as will be discussed in §3.2). As has been shown, above T_0 these systems have a minima in the free energy when there is no spontaneous polarisation. Structurally it is found that in this non-polar phase, these materials have centrosymmetric symmetry [32][3].

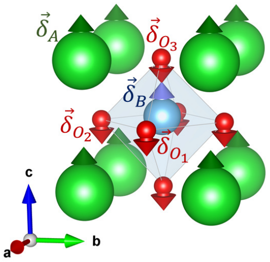

Figure 2.7: Ferroelectric displacement $\boldsymbol{\delta_i}$ of each ion from the prototype state after a structural phase transition to a ferroelectric state.

As the temperature is reduced below the Curie temperature, the system becomes ferroelectric due to a structural phase transition which breaks and lowers the symmetry by shifting ions from their centrosymmetric Wyckoff positions. From the modern theory of polarisation [63–65], polarisation should not be considered as an equilibrium property of a state, but should be defined relative to the difference between two states. As such, the '*ferroelectric displacement*' $\boldsymbol{\delta}_i$ is defined as the displacement of each ion i from its centrosymmetric coordinate (Figure 2.7), which creates a dipole moment $\mathbf{d}_i$ with respect to the paraelectric phase:

$$\mathbf{d}_i = q_i \boldsymbol{\delta}_i \tag{2.19}$$

In the frame of reference with this dipole at the origin, the potential V induced at position $\mathbf{r}$ by the dipole moment of ion i is:

$$V(\mathbf{r}) = -\frac{1}{4\pi\epsilon_0}\mathbf{d}\cdot\nabla\left(\frac{1}{r}\right) \tag{2.20}$$

We can consider the distributed polarisation as the sum of the dipole moments ($\mathbf{P}(\mathbf{r}') = \iiint \mathbf{d}_i d\mathbf{r}'$) which can be shown to generate a potential energy field from the charge density within a volume Ω enclosed by surface S

---

[3] There are exceptions such as KH_2PO_4 [9].

as[4] [26]:

$$V(\mathbf{r}) = \frac{1}{4\pi\epsilon_0}\left(-\iiint d\mathbf{r}'\frac{\nabla\cdot\mathbf{P}(\mathbf{r}')}{|\mathbf{r}-\mathbf{r}'|} + \oiint \frac{d\mathbf{S}\cdot\mathbf{P}(\mathbf{r}')}{|\mathbf{r}-\mathbf{r}'|}\right) \tag{2.21}$$

From the functional form of the potential energy we see that it is generated from the distributed charge density $\rho(\mathbf{r}) = -\nabla\cdot\mathbf{P}(\mathbf{r})$ and the bounding surface charge density $\sigma = \mathbf{S}\cdot\mathbf{P}(\mathbf{r})$ [26]. The accumulation of the generated bound charges on the surface (or any nonhomogenous distribution of polarisation) of a ferroelectric can have enormous consequences on the energy stored in the field which the system will attempt to minimise [25].

For the case of the prototype ferroelectrics ($PbTiO_3$ and $BaTiO_3$), cooling below the transition temperature causes a structural phase transition from non-polar $Pm\bar{3}m$ cubic to polar $P4mm$ tetragonal. As each direction along the principle axes in the cubic phase is identical, there are six degenerate states along which elongation of the cell and condensation of the polarisation will form, resulting in approximately equal volume fractions [66]. However, due to the generated potential field (2.21) and strain from lattice mismatching, adjacent cells where the lattice parameters and polarisations are unmatched will be energetically unfavourable [67]. Consequently, local regions of ferroelectric crystals become spontaneously ordered, polarising in parallel to minimise the overall energy state. These regions of uniform polarisation are called domains. The transitional region between neighbouring domains over which the polar axis reorientates is called the domain wall and defined by the relative angle between the polarisation of the adjacent domains. For tetragonal ferroelectrics the me-

---

[4] According to the modern theory of polarisation such a definition is erroneous and only precisely corresponds to the correct change in polarisation if the formal polarisation $\mathbf{P} = \frac{e}{(2\pi)^3}\Im\sum_n\int d\mathbf{k}\langle u_{n\mathbf{k}}|\nabla_{\mathbf{k}}|u_{n\mathbf{k}}\rangle + \frac{e}{\Omega}\sum_s Z_s^{ion}\mathbf{r}_s$ vanishes for the centrosymmetric reference state which is not always true. However, for illustrative purposes here such a definition is sufficient. Detailed discussions on the modern theory of polarisation can be found in ref [26].

chanically compatible orientations[5] allow for 180° domain walls separating oppositely oriented polar domains (Figure 2.8a) and 90° walls separating mutually perpendicular domains (Figure 2.8b).

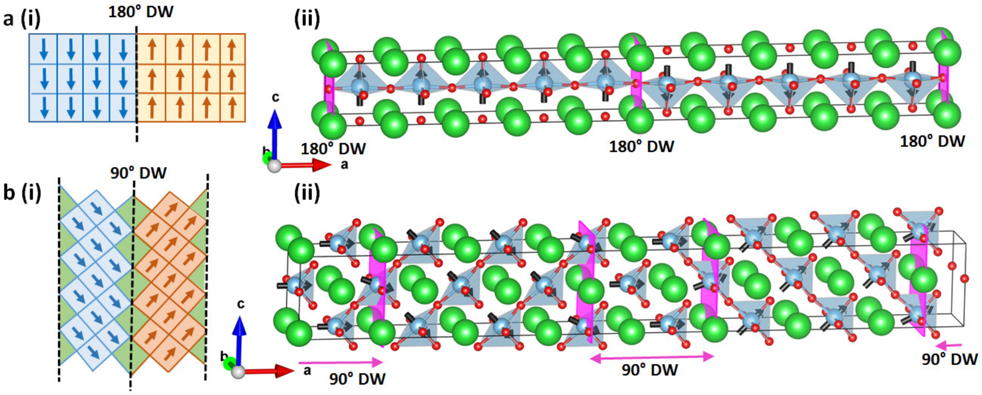

Figure 2.8: Cartoon schematic (i) and atomistic representation (ii) of 180° (a) and 90° (b) domain walls in tetragonal phase ferroelectrics. Arrows represent the local polarisation within each conventional unit cell. Pink planes designate approximate domain wall boundaries.

Since the strain tensor changes across a 90° domain wall it is also ferroelastic and responsive to strain fields [25]. Ferroelectrics with other structural phases, such as the rhombohedral phases of $BaTiO_3$ and PZT which have 8-degenerate polarisable orientations, can permit other species of domain walls (71° & 109°) [68].

The precise formation, size and shape of domains are a result of the minimisation of the total crystal energy and specific boundary conditions. If we consider the geometry of a uniaxial ferroelectric lamina *in vacuo* with the polarisation oriented out-of-plane P_z, which shall be called a (001) '*thin film*', then the resulting surface charges from the discontinuity in the distributed charge at the surface termination will generate an electric field called the '*depolarising field*' $\mathcal{E}_d$. Under open-circuit boundary conditions,

---

[5] Mechanical (elastic) compatibility restraints requires that two adjacent domains with strains $\eta_{ij}(A)$ and $\eta_{ij}(B)$, must satisfy the condition $(\eta_{ij}(A) - \eta_{ij}(B))ds_i ds_j = 0$ for any domain wall vector $d\mathbf{s}$ [66].

whereby there is no external mechanism to compensate the surface charges, the out-of-plane displacement field in the vacuum D_z^{vacuum} and the film D_z^{film} must be continuous and therefore self-consistently satisfy [38]:

$$D_z^{film} = \epsilon_0 \mathcal{E}_d + P_z = D_z^{vacuum} = 0 \tag{2.22}$$

Consequently, the depolarising self-field within the film generated from the bound charges is:

$$\mathcal{E}_d = -\frac{P_z}{\epsilon_0} \tag{2.23}$$

which is negative with respect to the direction of the polarisation such that the interaction energy density acts to reduce the out-of-plane polarisation of the film (ie acts to depolarise). From equation 2.23 it is clear that the depolarising field can be extremely strong. For a high polarisation ferroelectric such as $\mathrm{PbTiO_3}$ which has a spontaneous polarisation of 80 μC/cm^2, eqn. 2.23 returns a field of approximately 90 GV/m. Even weakly polarised ferroelectrics such as $\mathrm{NaNbO_3}$ or $\mathrm{PbTa_2O_6}$ with $P \approx 10$ μC/cm^2 [32] yield depolarising fields 10 GV/m, an order of magnitude greater than typical coercive fields that will destabilise and destroy any out-of-plane polarisation [12]. Alternatively, the large electrostatic energy cost of the potential at the surface can be minimised and out-of-plane polarisations stabilised by:

1. Breaking into domains with opposite polarity such that the net surface charge neutralises. It should be noted that each domain interface will attempt to allow div$\mathbf{P} \rightarrow 0$, but will still have a small stray fields perpendicular to the surface whose interactions contribute to the energy and determine the domain pattern. Nonetheless, this intrinsic mechanism is effective enough to allow ferroelectricity to persist to films 1.2 nm thick [69]. For further details see Chapter 5 and references therein.

2. Compensating the surface charge using electrodes or surface absorbates [66]. Charge supplied from electrodes is able to screen the depolarising field. Whilst experimentally the screening is never perfect, it was shown by Ghosez and Junquera using DFT that mobile charge carriers in idealised metallic $SrRuO_3$ electrodes can maintain ferroelectricity in (001) $BaTiO_3$ thin films down to thickness of 2.4 nm [70]. It has further been shown both theoretically and experimentally, that the chemical potential between absorbates and open surfaces can act analogous to an applied voltage by varying the oxygen partial pressure on $PbTiO_3$ films to facilitate domain growth [71, 72]. Similarly, passive OH absorption has also been shown to stabilise a the out-of-plane polarisation in epitaxial $PbTiO_3$ films three unit cells thick [73].

These suggest mechanisms for sustaining ferroelectricity in finite crystals and provide explanations for experimental observations of switchable ferroelectricity in thin films with open surfaces [38]. For ferroelectrics that have incomplete screening and form periodic domain patterns, the stray fields near the domain walls influence the domain size and are dependent upon the depolarising fields of the original unscreened system. This situation was first considered by Kittel in 1946 for ferromagnetic systems [74] but the analysis has been shown valid for 180° domains in all types of ferroic materials (ferroelectrics [75], magnetoelectric multiferroics [12, 76]). It was realised that small domains will generate smaller stray depolarising fields so the energy density E^{dom} of the domain must be proportional to the domain width w:

$$E^{dom} \propto Uw \tag{2.24}$$

where U is the volume energy density [12]. However, as the domain width is reduced there will be a linear increase in the relative number of domain walls per unit volume such that domain wall energy will scale inversely with domain width ($\propto w^{-1}$). The effective domain wall energy E^{wall} will be dependent upon the domain wall energy density σ and will be proportional the surface area of the interface between domains and will therefore be proportional to the film thickness d:

$$E^{wall} \propto \frac{\sigma d}{w} \tag{2.25}$$

By summing the contributions from expressions 2.24 and 2.25 and minimising with respect to the domain width, Kittel's relation is found:

$$w \propto \sqrt{\frac{\sigma d}{U}} \tag{2.26}$$

showing a square root dependence between the domain width and the film thickness. Whilst derived with respect to 180° domains in ferromagnetic materials it has been observed to hold true over 6-orders of magnitude from nanoscopic scales to the correlated behaviour of domain bundles [12, 77]. The same square-root dependence has further been identified in ferroelectric nanodots with periodic twinned 90° domains suggesting the universal nature of this relation [78].

In Kittel's study three possible magnetic domain morphologies where considered:

1. '*Landau-Lifshitz*' stripe domains with flux-closure domain caps (Figure 2.9a(I));
2. Purely 180° stripe domains as considered in the derivation of the Kittel relation (2.26) above (Figure 2.9a(II));
3. A monodomain orientated in-plane (polarised perpendicular to the surface normal, Figure 2.9a(III)).

Calculations of the energy, accounting for domain wall energy, magnetostatic energy and magnetic anisotropy, as a function of thickness found

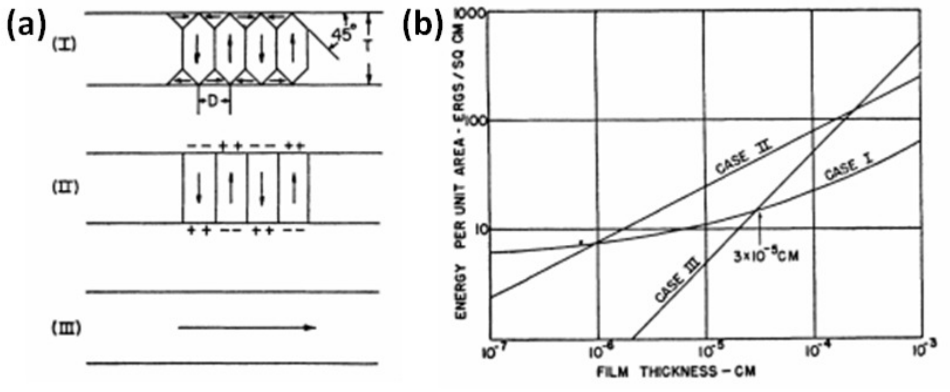

Figure 2.9: (a) Domain structures in ferromagnetic thin films. (I) Landau-Lifshitz domains. (II) Open flux 180° stripe domains. (III) Uniformly magnetised in-plane. (b) Domain energy with film thickness for each configuration. Figures reproduced with permission from Ref. [74]. Copyright 1946 American Physical Society.

that case 3 is most favourable for extremely thin films [74]. The Landau-Lifshitz morphology (case 2) is most generally favourable at thin and intermediate thicknesses (Figure 2.9). A transition to 180° open flux stripe domains only occurs for very thick films or for magnetic materials with a significantly pronounced anisotropy such as in cobalt [74].

Whilst formally the theory for ferroelectrics is the same [75], it was originally thought Landau-Lifshitz domains wouldn't exist in ferroelectric materials. In particular, because ferroelectrics are highly anisotropic with high polarisation-strain coupling (§2.2) such that the elastic energy contribution would create a large penalty due to the electrostrictive[6] cost of ferroelectric displacements perpendicular to the easy axis. It was therefore commonly believed that ferroelectrics would have atomistically sharp domain walls and domain structures analogous to case 2 (Figure 2.9a(II)), as is found in the highly anisotropic ferromagnetic cobalt. Conversely, for ferromagnetic materials the exchange energy which aligns spins is the key contribution, favouring Bloch domain walls spanning many nanometres.

---

[6] $\eta_{ij} = Q_{ijkl} P_k P_l$

However, recent theoretical and experimental observations have provided strong evidence that despite the electrostriction, Landau-Lifshitz domain architectures do exist in ferroelectric ultrathin films (see Chapter 5).

2.6 Poling

A defining characteristic of ferroelectrics from other high dielectric materials such as pyroelectrics is the capability of reversing the polarisation by the application and removal of an electric field [32]. First shown in 1920 [79], the observation of a dielectric hysteresis such as shown schematically in Figure 2.10, provides an important method for the identification and characterisation of ferroelectric behaviour. The mechanism for switching is now understood to require nucleation (correlated behaviour and length scales larger than a single unit cell) and the growth/reduction of domains via domain wall motion (see Chapter 7 and references therein) [26].

In its relaxed state dependent upon the boundary conditions, history and loading, a ferroelectric material will consist of domains. If these are arranged in such a way that the net polarisation cancels (such as open-circuit thin films discussed in §2.5) then the piezoelectric effects will similarly cancel such that the crystal won't display characteristic piezoelectric properties [25]. However, a polar state may be recovered by applying a large electric field in a process called poling. In polycrystalline ferroelectrics, such as ceramics, individual grains cannot be reorientated, but the domains within the grains can be realigned with the applied field. In the polydomain state, at low field strengths the field is unable to switch the domains such that a ferroelectric acts like a linear dielectric with a large susceptabily χ_{ij} [32]:

$$P_i = \chi_{ij} E_j \tag{2.27}$$

Similar behaviour is observed at very high field strengths when the ferro-

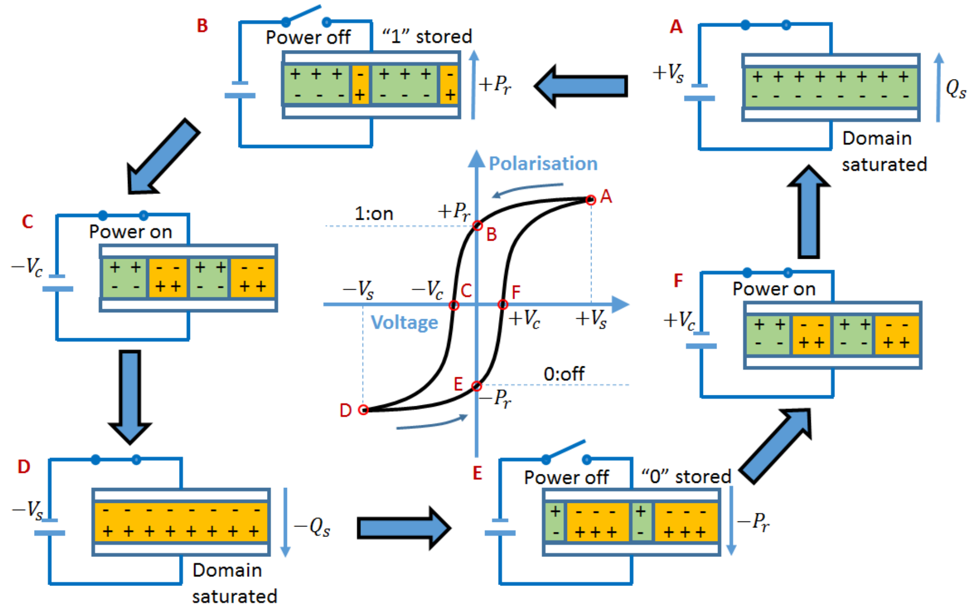

Figure 2.10: Polarisation-field hysteresis of a ferroelectric capacitor. An applied voltage V supplies an electric field $\mathcal{E}$ across a ferroelectric capacitor which can grow aligned domains until saturation with polarisation charges of $\pm Q_s$. The polarisation that remains when the field is removed is the remnant polarisation $\pm P_r$. The field that the polarisation reaches zero is the coercive field $\pm V_c$ (or $\pm \mathcal{E}_c$).

electric is fully saturated with a single domain (A,D in Figure 2.10) [32]. However, as the coercive field E_c is neared (C,F in Figure 2.10), domains aligned with the field will be energetically favourable and grow via domain wall motion until saturated ($B \rightarrow C \rightarrow D$ in Figure 2.10). This is because the field acts as a linear bias in the free energy creating asymmetry in the characteristic $\mathcal{W}$-potential and a lowering of the relative energy state of polarisations aligned with the field. In this region the dielectric response is highly non-linear and equation 2.27 becomes invalid.

The remnant polarisation (B,E in Figure 2.10) is the zero-field displacement and can have any value between $\pm P_s$ in a polydomain (single-crystal) ferroelectric[7]. A remnant polarisation less than $|P_s|$ occurs due to

---

[7] In a polycrystalline ferroelectric the remnant polarisation is limited below $|P_s|$ due

stresses or mobile charge carriers not reaching equilibrium causing a frequency dependence in measured hysteresis curves. A consequence of a non-zero remnant polarisation is the opening of the hysteresis curve, the area of which is the work required to twice switch the polarisation at a given frequency [32]. This can be seen considering the power per unit volume imparted to the ferroelectric from the applied field [80]:

$$p_a(\boldsymbol{\mathcal{E}}) = \boldsymbol{\mathcal{E}} \cdot \frac{\partial}{\partial t}\mathbf{P} \tag{2.28}$$

and the power density supplied to field:

$$p_f(\boldsymbol{\mathcal{E}}) = \boldsymbol{\mathcal{E}} \cdot \frac{\partial}{\partial t}\epsilon_0\boldsymbol{\mathcal{E}} \tag{2.29}$$

giving the total power per unit volume as:

$$p = p_a + p_f = \boldsymbol{\mathcal{E}} \cdot \frac{\partial}{\partial t}(\epsilon_{\mathbf{0}}\boldsymbol{\mathcal{E}} + \mathbf{P}) = \boldsymbol{\mathcal{E}} \cdot \frac{\partial \mathbf{D}}{\partial t} = \mathcal{E}\frac{\partial D}{\partial t} \tag{2.30}$$

Since power is the rate work W_e is done, we find the following equivalence with equation 2.30:

$$\frac{\partial W_e}{\partial t} = \mathcal{E}\frac{\partial D}{\partial t} \tag{2.31}$$

$$\implies W_e(D) = \int_{-\infty}^{t} dt\mathcal{E}\frac{\partial D}{\partial t} = \int_0^D \mathcal{E}\delta D \tag{2.32}$$

where we choose the applied and displacement fields to be zero at $t = -\infty$ and integrated over its history giving the work as a function of the displacement field $\mathbf{D}$ [80]. Given for ferroelectric materials $\epsilon_0\delta_{ij} << \chi_{ij}$ [25], the approximation $\mathbf{D} \approx \mathbf{P}$ [81] can be made such that the area enclosed in the P-E hysteresis is the work to twice switch the polarisation to recover its initial state:

---

to the grain alignments. For example, a tetragonal ceramic ferroelectric with 6 domain states can only exhibit a maximum remnant polarisation of $0.83P_s$ [25]

$$W_e(D) \approx W_e(P) = \oint_P \mathcal{E}\delta P \tag{2.33}$$

Whilst the P-E hysteresis is a classic indicator of ferroelectric behaviour, it can often be mistaken from non-linear dielectric loss [32]. Such a distinction was famously emphasised by J. Scott [82] showing true hysteresis for the ferroelectric commonly called 'bananas' ($Ba_2NaNb_5O_{15}$) and a lossy dielectric curve from a banana skin electroded with silver paste. Nonetheless, equation 2.33 provides the energy lost in these *lossy* dielectrics, which are caused from leakage currents arising from factors including grain boundaries, Fowler-Nordheim tunnelling or Schottky injection [26]. For ferroelectric materials on the other hand, the opening of the hysteresis is due to energy being stored by the creation of domains aligned with the applied field via nucleation and subsequent domain wall motion. This occurs when the energy penalty for increasing the domain wall area A and induced depolarising energy cost $U_{depolarisation}$ is balanced by the nucleation of domains of total volume V [32]:

$$\Delta\mathcal{F} = \sigma A + U_{depolarisation} - \mathbf{D} \cdot \boldsymbol{\mathcal{E}} V \tag{2.34}$$

The rate of nucleation is therefore proportional to $\exp(-\beta\Delta\mathcal{F})$, where $\beta = 1/kT$ is the thermodynamic beta [32]. In bulk ferroelectrics, domains remain stable as the energy required to nucleate a typical domain is $10^8 kT$ such that the probability of nucleation from thermal fluctuations is negligible [83]. $\Delta\mathcal{F}$ can be considerably smaller where the polarisation is inhomogeneous, such as pre-existing domain walls or surfaces, and act as nucleation sites.

This nucleation-growth mechanism has been shown to be formally equivalent to an elastic manifold in a weakly pinning fluctuating potential that is caused by defects [84, 85]. In the weak field limit, the aggregate propagation of domain walls can be characterised by a creep process obeying:

$$v(\mathcal{E},T) \propto \exp\left[-\beta U_b\left(\frac{\mathcal{E}_0}{\mathcal{E}}\right)^{\mu}\right] \tag{2.35}$$

where v is the domain wall velocity, $\mathcal{E}_0$ is the '*crossing field*' (a critical field at which depinning occurs at 0 K), U_b is the energy barrier and μ is a dynamical exponent characterised by the defects [84]. Theoretically, a value $\mu = 1$ occurs from random field defects [86] (which asymmetrises the $\mathcal{W}$-potential) and $\mu = 0.5$ is found when there is random bond disorder [87](which changes the depth and curvature of the $\mathcal{W}$-potential). The creep equation has been found to fit experimental data for domain wall velocities well for a range of ferroelectrics [26, 88]. A classic stochastic model by Miller and Weinreich [89] to explain the origins of domain wall creep (2.35), calculated the critical nuclei on 180° domain walls to be atomistically thin sharp walled triangular plates that would grow along the domain wall (Figure 2.11(i)). Successive steps would propagate the domain wall according to equation 2.35 with $\mu = 1$. However, recent calculations have shown that this topology of nucleus overestimates the activation field $\mathcal{E}_a = U_b\beta\mathcal{E}_0$ by an order of magnitude [86, 87]. Shin *et al* [90] were able to show that in the Miller-Weinreich formalism, the depolarising energy incorrectly dominated the energetics due to the assumed sharp interface of the nucleus. Instead, they were able to show that square nuclei with diffuse and bevelled boundaries corrected the activation energies and maintained the creep behaviour (Figure 2.11(ii)). Further, an inherent $\mu = 1$ is implied as the calculations were performed in defect-free $PbTiO_3$ and $BaTiO_3$ suggesting deviations in μ occur via random bond disorder.

When the applied field exceeds $\mathcal{E}_0$, ferroelectrics are found to experience a pinning-depinning transition whereby the domain wall velocity becomes linearly dependent upon the field and independent of the tempera-

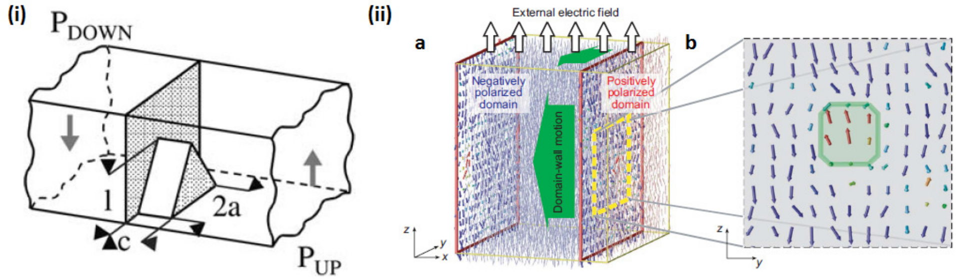

Figure 2.11: The critical nucleus on 180° domain walls (a) Triangular step nucleation described by Miller and Weinreich. Figure reprinted (adapted) with permission from Ref. [89]. Copyright 1960 American Physical Society. (b) Diffuse bevelled nucleation described by Shin *et al* [90]. Reproduced (adapted) with permission from [90]. Copyright 2007 Nature Publishing Group.

ture:

$$v \propto (\mathcal{E} - \mathcal{E}_0)^{\theta} \tag{2.36}$$

where θ is related to the dimensionality of the domain wall [84]. As such 180° domain wall motion in prototypical ferroelectrics is well understood. For low field strengths the combination of the large nucleation barrier with respect to thermal fluctuations and the size of the critical nucleus creates the Arrhenius dependence of the domain wall creep. For high fields, the domain wall velocity is rate limited by the growth as the nucleation barrier U_b tends to zero, creating a linear relation with field strength [84]. However, the switching process for ceramics, thin films and solid-solution ferroelectrics is still poorly understood (See Chapter 7 and references within).

Defects can have a profound influence on the domain structure and domain wall dynamics beyond modifying μ. Oxygen vacancies V_O for example, commonly formed in the synthesis of perovskite oxides to charge compensate impurities such as iron from precursors, have been shown to migrate towards and subsequently pin domain walls as they have lower formation energies at the interface compared to within the bulk [91, 92][8]. In

---

[8] Ionic mobilities in typical perovskite ferroelectrics are 10^{-12}cm^2/Vs [9]

90° domain walls this can create different concentrations of V_O and free electrons on either side of the domain wall resulting in asymmetric charge distributions [93]. Further, vacancies in an acentric sites will have an associated dipole moment $\bar{\Delta}\mu$ that can change the macroscopic polarisation $\Delta P = N\bar{\Delta}\mu$ [32] which can have an enormous effect on the electromechanical response of the material (see Chapter 8).

2.7 Industrial Applications of Ferroelectrics

Ferroelectric materials have been widely used in technological applications since the discovery of ferroelectricity in Rochelle salt, which was quickly adopted for use in transducers for photograph pick ups and microphones [32]. The discovery of ferroelectricity in $BaTiO_3$ and other simple perovskite oxides opened other cost-effective technological avenues creating the electronic-ceramics industry. These new materials enabled developers to match electrical and mechanical impedances for efficient power conversion such as condensers [32]- billions of which are still made yearly costing less than a penny per unit [9]. The non-linear dielectric properties make ferroelectrics ideal for optical-parametric and electro-optical devices [32]. More recently, attention has been turned to their application in lucrative memory devices such as Ferroelectric Random Access Memory (FeRAM) and the the Piezoelectronic Transitor (PET). The World Semiconductor Trade Statistics (WSTS) predicts the semiconductor market to grow to $378 billion in 2017 with its largest growth from memory chips which will increase market volume by 30.4% [94].

FeRAM is a form of random access memory using ferroelectric capacitors. Non-volatility of the memory is achieved by utilising the remnant polarisation of the ferroelectric with the sign of the polarisation representing Boolean logic states of “1” or “0” ($\pm P_r$). Tetragonal phase PZT is favoured due to its large remnant polarisation and square hysteresis [95].

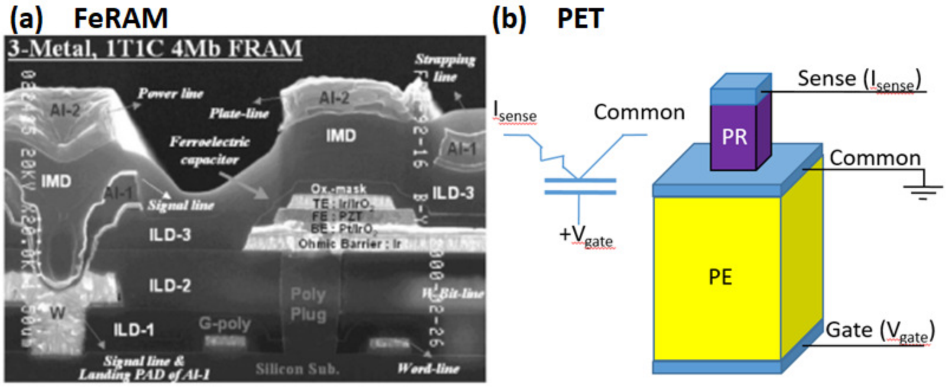

Figure 2.12: Practical applications of ferroelectric capacitors (a) Ferroelectric random access memory (FeRAM). SEM cross-section of a FeRAM capacitor. Reproduced with permission from [15]. Copyright 2005 American Physical Society. (b) Piezoelectronic transistor (PET) concept. This component would be housed within a high-yield mechanical clamping structure such that expansion of the piezoelectric (PE) compresses the piezoresistive component (PR).

High volume commercial 1Mbit FeRAM memory chips were introduced by Fujitsu and Ramtron in 2006 [96]. Figure 2.12a shows an SEM cross-section of a commerical 4 Mb Samsung FeRAM capacitor. In 2007, Flash memory represented 93% of the non-volatile memory market due to the relative low density of the available FeRAM chips [96]. However, in the next 3-5 years it is expected that the scalability and chip density of ferroelectric capacitors will greatly outpace Flash memory [97]. As an example, Flash is fundamentally slow since it operates using a floating gate which is activated applying a large voltage of 12-18 V and injecting electrons using a tunnelling current. Ferroelectric capacitors, on the other hand, can be switched much faster with a lower power consumption only requiring a 1-5 V potential [96]. Further, ferroelectric memory using optical techniques to record and read data is, in principle, only limited by the diffraction of light allowing storage densities approaching 10^8 bits/cm^2. This is 1000-fold greater than the theoretical storage density possible for magnetic based systems and can potentially be further increased using holographic methods [32].

The Piezoelectronic Transistor (PET) is a complementary technology to FeRAM, designed to circumvent speed and power limitations reached by conventional metal oxide semiconductors (CMOS) whose clock-speeds have failed to improve since 2003 due to a breakdown of Dennard scaling [98]. The PET consists of two distinct materials, a piezoelectric (PE) and a piezoresistive (PR) element, surrounded by a high yield mechanical clamping structure. To activate the transistor, an input signal is supplied as a gate voltage to the PE causing it to expand due to electrostriction. This expansion causes the adjacent PR component to become compressed which induces an insulator-to-metal transition allowing a current to pass through a sensing channel. Other technologies being developed to overcome the plateaued clock-speeds such as field-effect transistors, nano-electro-mechanical switches and quantum capacitive devices have so-far demonstrated insufficient ON/OFF ratios or uncompetitive switching speeds in comparison to the PET concept which is estimated to allow frequencies on the order of 10 GHz [98, 99].

2.8 Motivation

Several fundamental questions necessary to improve the performance of existing FeRAM devices and to develop a practical PET remain unanswered. Two problems limiting FeRAM relate to the current poor characterisation of the domain morphologies within ferroelectric ultrathin films and how switching occurs in non-prototypical ferroelectrics. The PET requires a material with an extremely high d_{33} piezoelectric coefficient such as the relaxor-ferroelectric $(1\text{-x})Pb(Mg_{1/3}Nb_{2/3})O_3\text{-x}PbTiO_3$ (PMNPT) to produce the large strain to compress the piezoresistive material. It is important to identify intrinsic methods to improve the reversible strain such that the power and size of the piezoelectric component can be optimised. This thesis aims to address these business-critical research areas to improve the functional control of ferroelectric based devices using insights from atomistic modelling. Following an introduction of the research methods in Chapter 3, this thesis identifies the domain morphology and behaviour of $PbTiO_3$ ultrathin films in Chapter 5 and $Pt/Pb(Zr_{1-x}Ti_x)O_3$ /$SrTiO_3$ films in Chapter 6. To inform on how to improve switching kinetics for faster read-write speeds, Chapter 7 investigates the dynamics of domain switching in morphotropic PZT. In Chapter 8 the microscopic mechanisms of ageing are identified to reveal a method to improve the electromechanical response of simple ferroelectric materials.

References

In addition to the references explicitly cited in the text, this chapter has drawn from the following sources:

- M. E. Lines & A. M. Glass, '*Principles and Applications of Ferroelectrics and Related Materials*', Oxford University Press, Oxford, United Kingdom, 1977. [32]

- K. Rabe, M. Dawber, C. Lichtensteiger *et al*, '*Physics of Ferroelectrics: A Modern Perspective*, Springer Berlin Heidelberg, Berlin, Germany, 2007. [26]
- G. Catalan, J. Seidel, R. Ramesh and J.F. Scott, '*Domain Wall Nanoelectronics*', Reviews of Modern Physics **84**, 119 (2012) [12]
- P. Aguando-Puente, '*First-Principles Study of Screening Mecanisms of the Depolarising Field in Nanosized Capacitors*', PhD Thesis, Universidad de Cantabria, 2011 [38]
- O. T. Gindele, '*Atomistic Simulations of Ferroelectric Lead Zirconate Titanate*', PhD Thesis, University College London, 2016 [24]

3

Theory and Computational Methodology

> *"The underlying physical laws necessary for the mathematical theory of a large part of physics and the whole of chemistry are thus completely known, and the difficulty is only that the exact application of these equations leads to equations much too complicated to be soluble. It therefore becomes desirable that approximate practical methods of applying quantum mechanics should be developed, which can lead to an explanation of the main features of complex atomic systems without too much computation"*
>
> – Paul Dirac, *Proc. R. Soc.* ***123****, 714 (1923)*

In this Chapter, the methods and theoretical concepts underlying the calculation of ferroelectric properties used in this thesis are introduced. Starting from solution of the Schrödinger equation using the density functional theory, we progress to its application on bulk BaTiO_3, serving to enhance the theory of the computational approach and provide insights into the electronic behaviour of ferroelectric perovskites to expand upon Chapter 2. Classical interatomic potentials derived from quantum mechanical principles are then introduced, which, using molecular dynamics, make the solution of large scale and dynamic physical systems tractable to uncover fundamental and exciting material properties.

3.1 Density Functional Theory

At the nanoscale, materials exhibit properties according to quantum mechanics, which states that if the wavefunction $\Phi(\mathbf{r}, \mathbf{R})$ is known the expected value of any observable can be determined. For any system of interacting particles at any instance a time-independent Hamiltonian $\widehat{H}$ can be constructed forming the Schrödinger equation:

$$\widehat{H}(\mathbf{r}, \mathbf{R})\Phi(\mathbf{r}, \mathbf{R}) = E\Phi(\mathbf{r}, \mathbf{R}) \tag{3.1}$$

Eigenfunctions satisfying equation 3.1 are the wavefunctions, having an eigenenergy E subject to the electronic $\mathbf{r}$ and nuclear $\mathbf{R}$ coordinates. For a general system, the Hamiltonian can be decomposed into physical operators:

$$\begin{aligned}\widehat{H}(\mathbf{r}, \mathbf{R}) &= \widehat{T}_i(\mathbf{R}) + \widehat{U}_{ii}(\mathbf{R}) + \widehat{T}_e(\mathbf{r}) + \widehat{U}_{ee}(\mathbf{r}) + \widehat{U}_{ie}(\mathbf{r}, \mathbf{R}) &(3.2)\\ &= -\sum_I \frac{\hbar^2}{2M_I}\nabla_I^2 + \frac{1}{2}\sum_{I\neq J}\frac{Z_I Z_J e^2}{|\mathbf{R}_I - \mathbf{R}_J|} - \sum_i \frac{\hbar^2}{2m_i}\nabla_i^2 &(3.3)\\ &+ \frac{1}{2}\sum_{i\neq j}\frac{e^2}{|\mathbf{r}_i - \mathbf{r}_j|} - \sum_{i,I}\frac{Z_I e^2}{|\mathbf{r}_i - \mathbf{R}_I|}\end{aligned}$$

where $\widehat{T}_i$ and $\widehat{T}_e$ are the nuclear and electronic kinetic energy operators, $\widehat{U}_{ii}$, $\widehat{U}_{ee}$ and $\widehat{U}_{ie}$ are the nuclear-nuclear, electron-electron and nuclear-electron interaction operators, respectively [100]. In general, solution of eqn. 3.1 is intractable for all but the simplest cases since it scales exponentially with the number of electrons N due to mutual interaction of all pairs of charges resulting in $3N$ coupled one-electron equations [101]. Necessarily several approximations are needed to make the solution tractable:

1. Born-Oppenheimer approximation
2. Density functional theory
3. Periodic boundary conditions
4. Linear combination of basis functions
5. Pseudopotentials

Born Oppenheimer Approximation

As the masses of the nuclei are much greater than the mass of electrons, it is reasonable that a perturbation to the system allows electrons to instantaneously react to movements of the nucleus enabling the electronic and nuclear positions to be decoupled: $\Phi(\mathbf{r},\mathbf{R}) \rightarrow \phi(\mathbf{r}), U_{ii}(\mathbf{R}) = constant, U_{ie}(\mathbf{r},\mathbf{R}) \rightarrow U_{ie}(\mathbf{r};\mathbf{R})$. The nuclear positions are treated as a classical parameter within the Born-Oppenheimer Hamiltonian $\widehat{H}_{i+e}$ [102], whose eigenfunctions of the Schrödinger equation are the wavefunctions of the electrons for the given set of nuclear coordinates [103] [1].

$$\widehat{H}_{i+e}(\mathbf{r};\mathbf{R}) = \widehat{H}(\mathbf{r},\mathbf{R}) - \widehat{T}_i(\mathbf{R}) \tag{3.4}$$

$$\widehat{H}_{i+e}(\mathbf{r};\mathbf{R})\phi(\mathbf{r}) = E_{i+e}\phi(\mathbf{r}) \tag{3.5}$$

Density Functional Theorems

Density functional theory (DFT) is an efficient method to solve the electronic Schrödinger equation (3.5) based upon two theorems by Hohenberg and Kohn [104]. The first states that the ground-state energy of

---

[1] As $M_i >> M_e$ therefore $\langle\Phi(\mathbf{r},\mathbf{R})|\widehat{T}_i|\Phi(\mathbf{r},\mathbf{R})\rangle << \langle\Phi(\mathbf{r},\mathbf{R})|\widehat{T}_e|\Phi(\mathbf{r},\mathbf{R})\rangle$ and can be treated as a perturbation of the electronic system. $\widehat{U}_{ie}(\mathbf{r};\mathbf{R})$ now acts as a fixed potential.

the Schrödinger equation is a unique functional of the electron density[2] $E[n] = F[n] + \int V_{ext}(\mathbf{r}) n(\mathbf{r}) d\mathbf{r}$ where $n(\mathbf{r}) = \int \psi_i^*(\mathbf{r})\psi_i(\mathbf{r}) d\mathbf{r}$. The second theorem states the electron density that minimises the energy of the universal functional $F[n]$ is the true electron density corresponding to the full solution of the Schrödinger equation.

This formalism is exact but whilst the theorems prove *at most* one universal functional $F[n]$ exists for any given $V_{ext}(\mathbf{r})$ no hint is given to what it is. The unknown component of the functional, the *exchange-correlation energy functional* E_{xc}, must be approximated. Seminal work by Kohn and Sham [108] offers an approach to practically use DFT of the Hohenberg-Kohn theorems. In their framework, the real interacting electrons are replaced by a fictitious auxiliary set of non-interacting one-electron wavefunctions in an effective potential v_s acting to incorporate the influence of many-body interactions. The problem is recast as a Schrödinger-like eigen equation [100]:

$$\sum_i \langle \psi_{j\mathbf{k}}^{\sigma}(\mathbf{r}) | \widehat{H}_{KS}^{\sigma}(\mathbf{r}) - \epsilon_i^{\sigma} | \psi_{i\mathbf{k}}^{\sigma}(\mathbf{r}) \rangle = 0 \tag{3.6}$$

with the Hamiltonian

$$H_{KS}^{\sigma}(\mathbf{r}) = -\frac{1}{2}\nabla^2 + V_{ext}(\mathbf{r}) + \int \frac{n(\mathbf{r}')}{|\mathbf{r}-\mathbf{r}'|} d\mathbf{r}' + \frac{\delta E_{xc}}{\delta n(\mathbf{r},\sigma)} = -\frac{1}{2}\nabla^2 + v_s^{\sigma}(\mathbf{r}) \tag{3.7}$$

where the terms in order of equation 3.7 are the electronic kinetic energy, the external potential including the static nuclear potential, the classic Coulomb potential $V_{Hartree}$ and the exchange-correlation potential V_{xc} containing all electron-electron interactions beyond the Hartree term [100].

---

[2] The Hohenberg-Kohn theorem is valid for non-degenerate ground-states. Generalisation to degenerate cases was later proven by W. Kohn [105] and extended for spin polarised systems in refs [106, 107]. This reformulation casting the Schrödinger equation in terms of the electronic density as the physical variable considerably reduces the number of variables involved from 3N coupled one-electron equations to a single Schrödinger-like equation dependent on a single set of coordinates [101].

Equations 3.6-3.7 are the Kohn-Sham equations. Due to the Hohenberg-Kohn theorems, the fictitious non-interacting density minimising the eigenstate is equivalent to the actual ground-state density[3]. Solution is practically obtained using a trial density $n_{in}(\mathbf{r})$ which is solved self-consistently with the output density $n_{out}(\mathbf{r})$. Throughout this report, the Broyden density mixing scheme is used to generate the next trial density.

Periodic Boundary Conditions

For solids it is natural to impose periodic boundary conditions such that the eigenstates are invariant to translation by the lattice translation operator $\widehat{T}_n$, modulo a phase factor ($u_{n\mathbf{k}}(\mathbf{r} + \widehat{T}_n) = u_{n\mathbf{k}}$) [100]. Employing *Bloch's theorem*, the wavefunction is written as a product of plane waves and a commensurate periodic function:

$$\psi_{n\mathbf{k}}(\mathbf{r}) = V^{-1/2} e^{i\mathbf{k}\cdot\mathbf{r}} u_{n\mathbf{k}}(\mathbf{r}) \tag{3.8}$$

where n is the band index and **k** a vector of the Brillouin Zone (BZ) [103]. Further, as real space is periodic so is the reciprocal (k) so one only need consider those within the irreducible BZ [109]. An infinite number of k-points must still be considered but as the eigenfunctions are periodic and smoothly varying, small volumes of k-space may be considered as homogeneous allowing finite sampling at *special* high-symmetry points [100]. Throughout this report, we use the generalised method by Monkhorst and Pack [110] to choose our special k-point grid.

---

[3] For the exact exchange and correlation V_{xc}.

Linear Combination of Basis Functions

The one-electron wavefunctions may be expanded into a linear combination of basis functions obeying *Bloch's theorem* [38]. Here we choose our basis as weighted plane waves in reciprocal space satisfying orthogonality constraints. Thus allowing the global electronic wavefunction to be written as

$$\psi_{n\mathbf{k}}(\mathbf{r}) = V^{-1/2} \sum_{\mathbf{G}} u_{n\mathbf{k}}(\mathbf{G}) e^{i(\mathbf{k}+\mathbf{G})\cdot\mathbf{r}} \tag{3.9}$$

where $\mathbf{G}$ is the reciprocal lattice vector defined to satisfy $\mathbf{G} \cdot \mathbf{R} = m2\pi$. Practically, only a finite number of $\mathbf{G}$-vectors may be considered so conventionally we limit the basis to those with a kinetic energy smaller than a chosen cut-off energy $E_{cut} \geq \frac{1}{2}|\mathbf{k} + \mathbf{G}|^2$ [100, 103].

Pseudopotentials

A planewave basis presents two main problems which can largely be overcome through the use of pseudopotentials and the frozen-core approximation. Planewaves have difficulty representing tightly bound core electrons but since these electronic states typically have no *chemical* interaction they may be considered '*frozen*' to the groundstate configuration within the isolated atom [38]. The second problem pertains to the computational cost of rapidly oscillating valence band orbitals within the core region [103]. To overcome this issue a fictitious screened and smoothed *pseudopotential* can be defined that is fitted to reproduce the valence wavefunctions and the eigenvalues of a reference all-electron calculation [100]. In this study ultrasoft pseudopotentials are used unless stated otherwise.

Limitations of DFT

It is useful to give a very brief overview of a few relevant limitations of the standard DFT method. First, in the Kohn-Sham formalism the exact exchange-correlation functional is unknown. Various approximations of the functional exist including the Local Density Approximation (LDA), Generalised Gradient Approximation (GGA) and Hybrid functionals which mixes exact Hartree exchange. For each case, the computational requirements increase. The cheapest functional is the LDA which has had remarkable success for systems with slowly varying electronic densities and even inhomogeneous electron systems. However, DFT studies of molecules or highly correlated systems have poor results unless higher order functionals are implemented. In this thesis, the Wu-Cohen GGA-level exchange correlation functional is typically used. This functional makes a correction to the tail of the exchange hole improving lattice constants, crystal structures and metal surface energies [111].

DFT is a zero-temperature method whereas experimental data is at finite temperature so care must be given making comparisons. The computational cost associated with standard DFT limits the system size that can be modelled. On high performance computing platforms DFT can model systems on the order 10^3-10^4 atoms. This places inherent restrictions on the systems with disordered structures and the accuracy of defect calculations where defects may interact with their periodic images. There have been many developments in first principles methods such as linear scaling DFT and time dependent density functional theory (TDDFT). Nonetheless, scaling to orders comparable with experiment requires techniques such as classical molecular modelling (Section 3.3).

3.1.1 Structural Optimisation and Bulk Properties

The Kohn-Sham eigenfunctions can be used to perform structural optimisation of the nuclear coordinates employing quasi-Newtonian methods [100,112,113]. According to the *Hellmann-Feynman theorem* first order derivatives of the energy E with respect to displacements of the κ^{th} atom $d\tau_{\kappa\alpha}$, including the forces $F_{\kappa\alpha}$ and stress $\sigma_{\alpha\beta}$, are available from the ground-state wavefunction [100, 103]:

$$F_{\kappa\alpha} = \frac{dE}{d\tau_{\kappa\alpha}} \qquad\qquad \sigma_{\alpha\beta} = \frac{dE}{d\eta_{\alpha\beta}} \tag{3.10}$$

In our calculations, we optimise the geometry of a system with DFT using the CASTEP code [112]. The limited-memory Broyden-Fletcher-Goldfarb-Shanno (L-BFGS) algorithm is used to minimise the forces on each atom to a tolerance of 5 meV/Å and stresses to 10 kPa. Previous authors have noted relatively flat energy surface of the ferroelectric phases in $BaTiO_3$, and that lowering of the relative energies requires a major contribution from exchange and correlation making the structure extremely sensitive to inaccuracies in the exchange-correlation (xc) functional used [103, 114]. For our calculations the GGA level Wu-Cohen (WC) exchange-correlation functional is used which implements an analytic correction to the diffuse radial cutoff of the exchange-hole, providing much greater accuracies in lattice constants, crystal structures and surface energies relative to other GGA xc-functionals [111].

Additional properties can be extracted from DFT. Constant volume calculations with symmetry satisfying cell distortions enable the energy-volume behaviour of the respective phase of $BaTiO_3$ to be shown the Appendix (Figure E.1). Due to the use of a finite cut-off energy, the basis set used for different cells vary slightly so the energies cannot strictly be compared. Fortunately, a corrective term can be applied to the correct the finite basis set error using the Francis-Payne method [115]. For each phase the bulk modulus B_0 can be found by fitting the Birch-Murnaghan equation of state (3.11) by method of least squares to the volume V - energy E relationship.

$$E(V) = E_0 + \frac{9V_0B_0}{16}\left\{\left[\left(\frac{V_0}{V}\right)^{2/3} - 1\right]^3 B_0' + \left[\left(\frac{V_0}{V}\right)^{2/3} - 1\right]^2\left[6 - 4\left(\frac{V_0}{V}\right)^{2/3}\right]\right\} \tag{3.11}$$

where V_0 and E_0 are the volume and energy in the minimum energy state. From elastic strain theory, the elastic constants C_{ij} of each phase can be calculated by applying specific strain patterns via the strain tensor η_i.

$$E(\boldsymbol{\eta}) = E_0 + \frac{V}{2}\sum_{ij}^{6} C_{ij}\eta_i\eta_j + \mathcal{O}(3) \tag{3.12}$$

Bulk properties such as the strain and bulk modulus can be included as fitting parameters when deriving forcefields and for checking the validity of the DFT calculations.

3.1.2 Density Functional Perturbation Theory

Density functional perturbation theory (DFPT) is a powerful method to extract non-equilibrium properties such as polarisabilities and phonons, based upon the density functional formalism as first proposed in ref. [116][4]. Throughout this thesis, DFPT in the framework of the variational principle derived by Gonze et al [118] is used to calculate non-linear responses to perturbations as implemented in the CASTEP package [112,119]. DFPT is used to calculated phonon dispersion curves of $SrTiO_3$ in Chapter 6, Born effective charge tensors for §3.2.1 and high frequency dielectric constant of $PbTiO_3$ in Chapter 5.

---

[4] Here, perturbation theory is applied to the Kohn-Sham equations 3.7 creating a set of *Sternheimer equations* which are solved self-consistently [100] [117].

3.2 Fundamental Physics of Ferroelectrics

In this Section fundamental concepts of ferroelectricity are explored building upon the previous Chapter and making use of DFT calculations to supplement the theory.

3.2.1 Ferroelectric Instability

The leading model for the origin of ferroelectricity was created by Cochran [45], explaining the ferroelectric instability as a competitive balance between long and short range contributions to phonon modes. Short range repulsive interactions between the atoms try to maintain the centrosymmetric configuration [38]. Conversely, hybridised bonds cause giant anomalous dynamical charges supporting long range dipole-dipole interactions favouring low symmetry ferroelectric configurations [35]. These in turn *soften* the optical modes for which the B-cation and O move in anti-phase with the lowest transverse optical (TO) mode becoming unstable ($\omega^2 < 0$) when the long-range interactions dominate [38]. The model is summarised in Fig. 3.1a and the following Sections.

Mixed Ionic-Covalent Character

The band-structure of the Kohn-Sham orbitals ψ_i^σ are shown for the cubic and tetragonal phases of $BaTiO_3$ in Figs. 3.2a&c. While the Kohn-Sham electrons are a mathematical construction not related to the actual interacting electrons other than producing the same density, it is common to interpret their energy spectrum as that from the true one-electron states[5] [114]. Each orbital predominantly forms separated bands corresponding to the intuitively expected ionic bonds. The partial density of

---

[5] Approximate functionals are known to consistently underestimate the band gap '*due to the absence of ultra-nonlocal dependence of the exchange-correlation kernal.*' [114,120, 121]

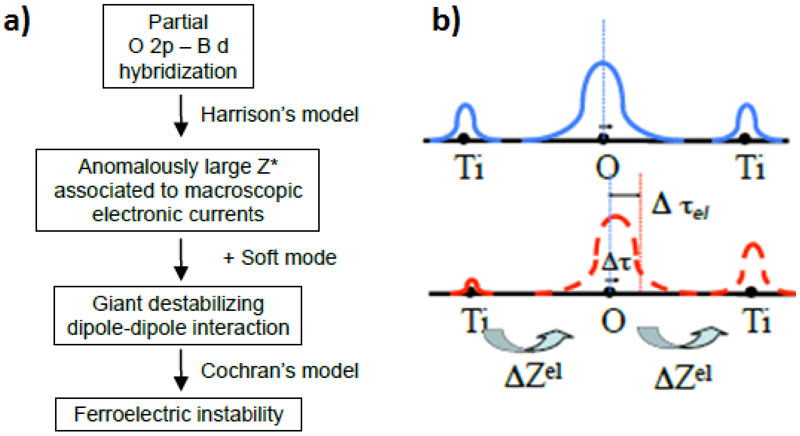

Figure 3.1: The ferroelectric instability. (a) Flowchart identifying the origin of ferroelectricity in perovskites (ABO_3) and its connection to the O *2p* - B *d* orbital hybridisations. (b) Cartoon of the concept of the Born effective charge Z^*_{Ti}, showing dynamic charge transfer along chains of Ti and apical O in perovskites which results in an anomalous charge contribution. Reproduced (adapted) with permission from Ref. [35]. Copyright 2012 John Wiley and Sons.

states for both phases show that typically, each band can be characterised by an individual orbital that contributes the majority of the energy to the state (Figs. 3.2b&d). Importantly however, there are additionally covalent features in the band-structure resulting in a '*mixed ionic-covalent*' character of the bonds from the Ti d-state electrons only partially transferring to the Oxygen 2p-states [103] as seen by overlap in the projected density of states in Figure 3.2b. This hybridisation between the O *2p* and Ti *3d* orbitals is common to the perovskite compounds and was originally predicted in LCAO calculations [122, 123] and later confirmed by DFT [34].

The bandstructure calculations performed to produce Figure 3.2 were achieved using the DFT package CASTEP [112]. 5-atom unit cells with periodic boundary conditions were geometry optimised using the BFGS routine applying symmetry operations pertinent to the cubic and tetragonal phases. An optimised $6 \times 6 \times 6$ Monkhurst-Pack k-point grid was

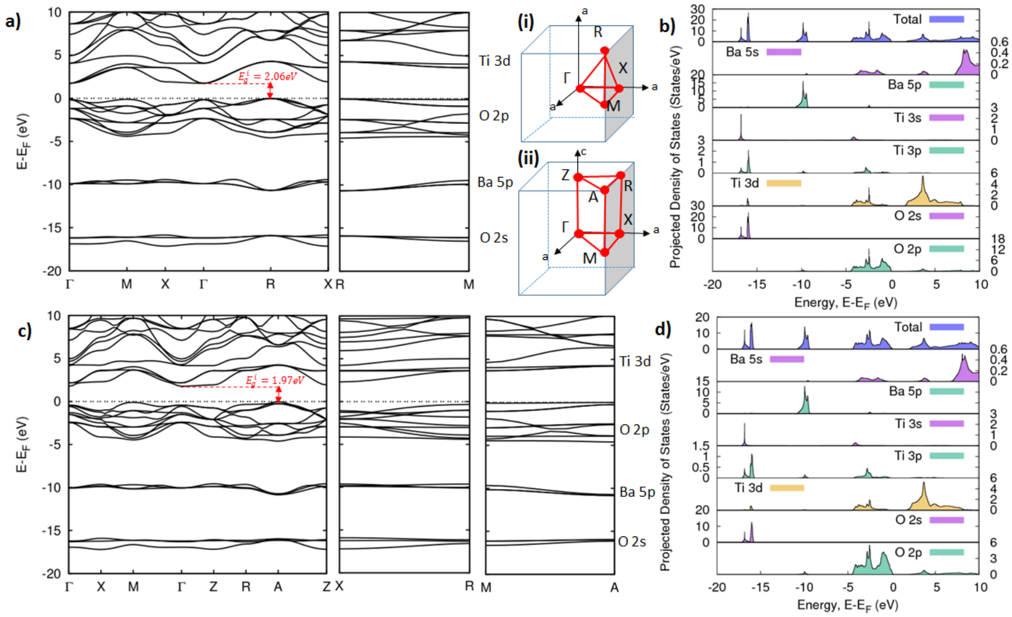

Figure 3.2: Electronic band structure of the centrosymmetric cubic (a) and polar tetragonal phase (c) of $BaTiO_3$. The k-point path represented in real-space and definition of the high symmetry coordinates for both phases are given in (i) and (ii). Partial density of states of the cubic (b) and tetragonal phase (d) showing mixed covalent-ionic character common to perovskites.

used, reducing to 10 and 18 unique k-points for the cubic and tetragonal phases, respectively. A 1000 eV cut-off energy was applied, minimising forces, energy and stress to within 5 meV/Å, 10^{-8} eV and 0.02 GPa, respectively. The Wu-Cohen exchange-correlation functional was used [111]. Partial density of states were produced using the Optados package [124], applying the optical matrix elements calculated from CASTEP, and using adptive k-smearing for BZ integrations [125]. The phase structures and other bulk properties from these calculations are given in Appendix E and compared to DFT and experimental results in the literature.

Harrison's Model: Born Effective Charges

The delocalised electrons on the B-cations in perovskites due to the B-O hybridisation have a profound effect when atoms are displaced from centrosymmetric positions. Displacement of either the B-cation or apical O anion result in a substantial polarising response since the the valence electrons are not completely bound to their ion [103]. The contributions of such distortions to the macroscopic polarisation can be quantified via the Born effective charge Z^*. For each atom κ, Z^* is defined as the change to the linear order of polarisation in direction β induced from a displacement from its sublattice in direction α under condition of no macroscopic electric field (Eqn. 3.13). Or alternatively, as the change in linear order between the force induced on atom κ in direction α from a macroscopic electric field along β.

$$Z^*_{\kappa,\alpha\beta} = -\frac{\partial^2 E_{e+i}}{\partial \mathcal{E}_\beta \partial \tau_{\kappa,\alpha}} = \frac{\partial F_{\kappa,\alpha}}{\partial \mathcal{E}_\beta} \tag{3.13}$$

$$= \Omega_0 \frac{\partial P_\beta}{\partial \tau_{\kappa,\alpha}}\Big|_{\mathcal{E}=0} \tag{3.14}$$

It was originally suggested by Harrison [126] that this covalency would be extremely sensitive to the bond length between the anion and cation, and would alter the degree of hybridisation through dynamical transfer of the electrons as the atoms are displaced. For $BaTiO_3$, if the chains of Ti and apical O bonds are considered, with the Ti coherently displaced by $\Delta\tau$ as depicted in Fig. 3.1b, then a chain of alternating lengthened and shortened bonds will exist relative to the cubic prototype. Harrison argued the covalent energy will increase in the shortened bond resulting in transfer of the electron to the oxygen ($\Delta\tau_{el}$). The converse is true of the elongated bond (Fig. 3.1b) such that even though the net charge on each atom remains constant, a current will exist due to the displacements reinforcing the polarisation and generating anomalously large effective charges [117]. Unknown to Harrison, experimental observation of the anomalous contribution was previously shown by Axe [54] corroborating the hypothesis. The relationship of Z^* to the hybridised O *2p* and B-cation *3d* states in perovskites was later proven by first principles from a band-by-band decomposition [127].

Born effective charges calculated for several perovskites in the cubic phase are provided in the Appendix (Table E.4) for the geometry optimised cell parameters using variational DFPT with norm-conserving pseudopotentials using the WC xc-functional via the CASTEP package [112, 119]. The Born effective charges were calculated using the framework of Gonze's variational DFPT method [118]. For each compound the anomalous contribution is substantially greater than the formal charge of the ion. Further, a significant anomalous contribution is attributed to Pb having more covalent character relative to Ba or Sr.

Soft Transverse Optic Modes

Lattice dynamics were later identified to be an important mechanism in the description of the ferroelectric distortion as introduced in §2.3. In the model by Cochran [45], it was identified that in the cubic phase of these ferroelectric materials, there exists an unstable transverse optic mode (having negative imaginary frequencies) at the Γ point. The phonon dispersion curve of cubic phase $BaTiO_3$ is shown in Fig. 3.3 where the soft mode is apparent at Γ. To calculate the dispersion, variational DFPT has been used as implemented in CASTEP [112, 119], applying a $4 \times 4 \times 4$ special q-point grid offset by (0.25,0.25,0.25) following a fine q-point path: Γ (0,0,0) $\rightarrow$ X $(0,0,{}^1/_2) \rightarrow$ M $(0,{}^1/_2,{}^1/_2) \rightarrow \Gamma \rightarrow$ R $({}^1/_2,{}^1/_2,{}^1/_2)$. Norm-conserving pseudopotentials were applied with the Wu-Cohen exchange-correlation functional and a $6 \times 6 \times 6$ k-point grid, keeping the geometry optimised lattice parameter 3.977 Å.

These unstable modes, referred to as '*soft*' modes, are related to antiphase motion of the B-cations and octahedral cage (Fig. 3.4a-inset), are very

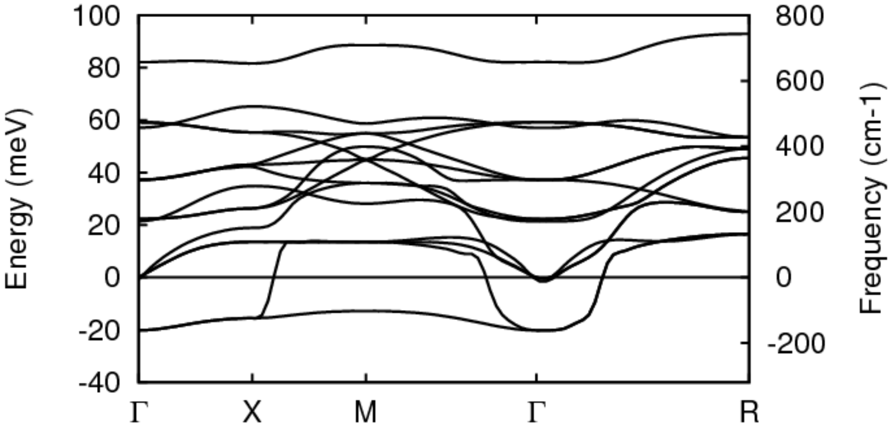

Figure 3.3: Phonon dispersion curve of the cubic phase of $BaTiO_3$ calculated using DFPT with the WC xc-functional at the equilibrium lattice parameter 3.977Å when moving between high symmetry points $\Gamma(0,0,0) \rightarrow X(0,0,^1/_2) \rightarrow M(0,^1/_2,^1/_2) \rightarrow \Gamma \rightarrow R(^1/_2,^1/_2,^1/_2)$.

polar and related to a giant LO-TO splitting [51, 128]. In the harmonic approximation of lattice dynamics, these unstable modes appear when the frequency is imaginary giving negative curvature of the energy surface producing a restoring force that promotes a lower symmetry phase [38].

Atomic displacements following the eigenmodes of the soft modes therefore lower the system energy condensing the atomic configuration into lower symmetry ferroelectric phases. This is demonstrated in Fig. 3.4a for $BaTiO_3$ using the eigendisplacement vector of the soft mode calculated at Γ with a fixed cubic cell. The eigenmode is converted into an eigendisplacement vector by the product $1/\sqrt{M_\kappa}$ [129], where M_κ is the atomic mass of the atom. From the DFPT calculation the eigendisplacement vector of each atom is determined to be $\delta(Ba) = -0.019$, $\delta(Ti) = -0.445$, $\delta(O_\parallel) = 0.349$, $\delta(O_\perp) = 0.183$.[6]

The instability is additionally linked to macroscopic strain showing further energy decreases with the cell deformations of the ferroelectric phases. Figure 3.4b shows the energy surface for soft mode distortions for the fer-

---

[6] Only z components shown. At Γ the x and y components are zero for all atoms.

roelectric phases of BaTiO$_3$, all revealing the characteristic ferroelectric $\mathcal{W}$-potential and the correct order of phase stability. These curves were produced performing single point energy calculations for coordinates created by linear interpolation between the phases: $\mathbf{r}_\kappa(\xi) = \mathbf{r}_\kappa^{\xi=0}(1-\xi) + \xi\mathbf{r}_\kappa^{\xi=1}$ where $\mathbf{r}_\kappa^{\xi=0}$ and $\mathbf{r}_\kappa^{\xi=1}$ are the corresponding coordinates to atom κ in the cubic and ferroelectric structures, respectively. Previous phonon calculations have used the LDA xc-functional which significantly underestimates lattice parameters suppressing the ferroelectric order requiring empirical use of experimental parameters. In Fig. 3.4c the effect of volume on the soft mode frequency is shown justifying our use of the WC xc-functional throughout. DFPT calculations were performed using LDA at its geometry optimised lattice parameter and using the WC exchange-correlation functional at its optimised lattice parameter and the experimentally determined lattice parameter from ref. [130]. It is important to note that the amplitude of the soft TO mode is not directly proportional to the well-depth in the $\mathcal{W}$-potential but offers an approximation to the first degree of the strength of the instability. Anharmonic effects are required to precisely define the minimum and which stabilise the soft mode.

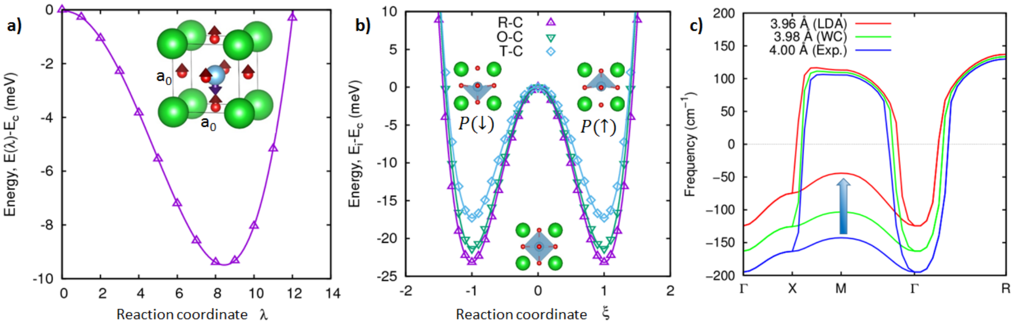

Figure 3.4: Ferroelectric instability of perovskites calculated from first-principles. (a) PES of cubic BaTiO$_3$ from the condensation of the soft-mode eigenvector at Γ ($\delta(Ba) = -0.019$, $\delta(Ti) = -0.445$, $\delta(O_{\|}) = 0.349$, $\delta(O_{\perp}) = 0.183$). (b) PES of the ferroelectric phases of BaTiO$_3$. (c) Soft modes of cubic BaTiO$_3$ calculated using lattice parameters determined from experiment and first principles applying LDA and WC xc-functionals.

3.2.2 Non-Polar Instabilities

In addition to the polar modes associated with the Γ point, many perovskites exhibit non-polar rotational instabilities from soft modes at other points in the BZ. In particular, antiferrodistortive (AFD) instabilities occur constituting rotations of the oxygen octahedra about the inversion centre (Fig. 3.5). Typically, polar and rotational modes compete so only one will present, determined by the *Goldschmidt tolerance factor*:

$$\tau = \frac{R_A + R_O}{\sqrt{2}R_B + R_O} \tag{3.15}$$

$\tau = 1$ represents the ideal case where atomic spheres of the cations just touch (R_i are the atomic radii of the perovskite atoms). If $\tau > 1$ the B cations have the available space to polarise off-centre. Alternately, if $\tau < 1$ the large size of the B-cation pushes the oxygen from the centre of the cell faces promoting the rotational modes. Even though one type of instability prevails, the suppressed instabilities make the materials susceptible to strains promoting displacements along the eigenmodes explaining the large dielectric constant and susceptibility of $SrTiO_3$ [38].

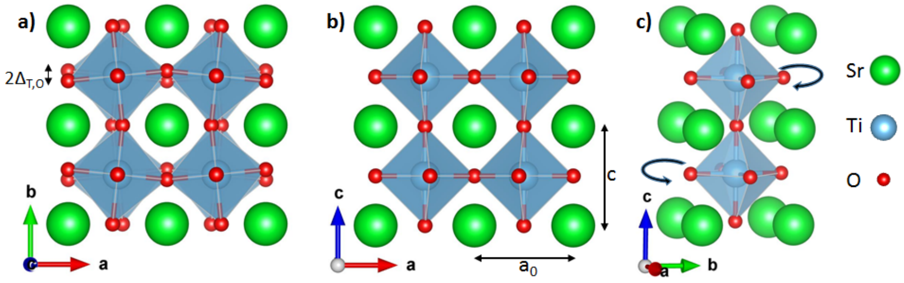

Figure 3.5: The antiferrodistortive (AFD) instability prevalent from a soft-mode at R. (a) Top view. (b) side view. (c) Perspective view showing out-of-phase rotations of octahedra. These modes with out-of-phase rotations of the TiO_4 about the $[001]_p$ axis exist in $SrTiO_3$ - denoted by $a^0a^0c^-$ in Glazer notation.

3.3 Classical Molecular Modelling

Molecular dynamics (MD) techniques require calculations of the energy but as was explored in §3.1, the internal energy is an intractable many body problem. Within the classical MD framework, the electronic influence is subsumed into an effective atom and expressed by a parametrised interatomic potential energy $U(\mathbf{r}_1, \mathbf{r}_2, ..., \mathbf{r}_N)$ as a function of the coordinates $\mathbf{r}_i$ of the N atoms (§3.3.1). This interatomic potential can be decomposed into an expansion of hierarchical many-body terms [131] with parameters fit to reproduce the potential energy surface of the quantum mechanical system (§3.3.4):

$$U = \sum_{i=1}^{N} U_i + \frac{1}{2!} \sum_{i=1}^{N} \sum_{j=1}^{N} U_{ij} + \frac{1}{3!} \sum_{i=1}^{N} \sum_{j=1}^{N} \sum_{k=1}^{N} U_{ijk} + \mathcal{O}(U_{ijkl}) \tag{3.16}$$

where U_i are self-energies, U_{ij} are pairwise interactions and U_{ijk} are three-body interactions. Three-body terms such as bond-angles, and higher order terms such as torsion, are not used in this thesis. The self energy includes contributions from intramolecular interactions such as core-shell polarisation (§3.3.2) and external fields which are expressed as a potential energy field. Pairwise additive terms include van der Waals and Coulomb intermolecular interactions (§3.3.1). Given an interatomic potential energy, the dynamical trajectory can be solved by integrating the classical equations of motion (§3.3.3).

3.3.1 Intermolecular Interactions

Coulomb Interaction: Ewald Summation Method

Coulomb interactions are long-range forces acting between charged particles and can account for up to 90% of the total energy of an ionic material [131]. Given two particles with charges q_i and q_j, Coulomb's law states the potential energy U^{LR} as:

$$U_{ij}^{LR} = \frac{q_i q_j}{4\pi\epsilon_0 r_{ij}} \tag{3.17}$$

Whilst the Coulomb interaction has a simple form it is only conditionally convergent in 3D periodic systems due to the competition between the decay of the interaction strength ($\propto 1/r_{ij}$) and the increase in the number of contributing ions to the potential ($\propto r_{ij}^2$) as $\mathbf{r}_{ij}$ is increased [132]. Ewalds method [133] provides a convergent, well-defined limit to the Coulomb potential when evaluating the Madelung potential[7] in an infinite system. This approach divides the interaction into two components incorporating spherical Gaussian clouds of width $\sqrt{2/\zeta}$ of the form [134]:

$$\rho(r) = -q_i(\zeta/\pi)^{3/2} e^{-\zeta r^2} \tag{3.18}$$

where r is the distance from the origin and ζ characterises the profile of the Gaussian.

A spherical Gaussian is centred on each point charge such that a neutralising charge of -q_i surrounds the ith ion. From long range, the Gaussian distributions appear as a delta function centred on the point charges (also a delta function) and therefore cancel, removing the long range effects. The short range assembly creates a convergent finite sum in real space using the complementary error function [134]:

$$U_{real}^{LR} = \frac{1}{2}\sum_{i\neq j}^{N} \frac{q_i q_j}{r_{ij}} \operatorname{erfc}(\zeta^{1/2} r_{ij}) \tag{3.19}$$

To recover the original charge distribution, a second set of Gaussians is superimposed on the first, with charges equal to the original ions. This cancels the first set as shown in Figure 3.6. The potential produced by the

---

[7] The potential of all crystal ions felt by the ions on each site $U_i^M = \frac{1}{4\pi\epsilon_0}\sum_{i\neq j}\frac{Z_j}{r_{ij}}$.

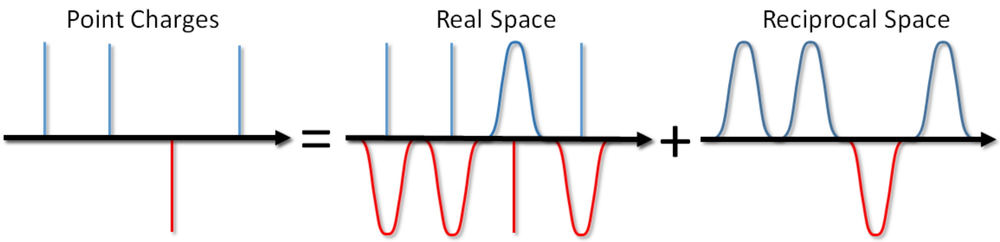

Figure 3.6: The Ewald summation method considers a set of point charges as a sum of screened charges in real space minus the sum of the screening background in reciprocal space.

second set of Gaussians is obtained from Poissons equation and is rapidly convergent when summed in reciprocal space using a Fourier Transformation [134]:

$$U^{LR}_{reciprocal} = \frac{1}{2}\sum_{i,j}^{N}\sum_{k\neq 0}\frac{4\pi q_i q_j}{Vk^2}\exp(i\mathbf{k}\cdot\mathbf{r}_{ij})\exp(-k^2/4\zeta) \tag{3.20}$$

where $\mathbf{k}$ is the reciprocal-lattice vector of magnitude k and V is the volume of the periodic system. In this formalism, a spurious self-interaction occurs between the point charge of each ion and its complementary Gaussian. This can be corrected by a self energy term:

$$U^{LR}_{self} = -\sum_{i}^{N} q_i^2\left(\frac{\zeta}{\pi}\right)\frac{1}{2} \tag{3.21}$$

The total energy is then the sum of the real and reciprocal summations with the self energy correction:

$$U^{LR}_{Total} = U^{LR}_{Fourier} + U^{LR}_{self} + U^{LR}_{real} \tag{3.22}$$

In practise the Ewald summation method is not used as it is formally an $\mathcal{O}(N^2)$ algorithm (but can reduced to $\mathcal{O}(N^{3/2})$). In this thesis the smoothed particle mesh Ewald (SPME) method is used [135]. This is a slight modification to the Ewald summation that improves the scalability to $\mathcal{O}(N \log N)$ by using exponential Euler splines to interpolate complex exponentials in the reciprocal space term [134]. The choice of ζ is chosen in consideration with the reciprocal lattice vectors and the real space cutoff radius used for short-range interactions (r_{cut}, see §3.3.1). The summation of the real space terms is truncated to r_{cut} so ζ must ensure contributions from r> r_{cut} are negligible and compensated by the reciprocal space sum [132]. The parameters used in the Ewald summation throughout are selected to ensure the relative error $(\exp(-(\zeta r_{cut})^2)/r_{cut})$ in the real space sum is below 10^{-8}. A subtlety in both the Ewald summation and SPME is a constraint of charge neutrality but this can be overcome using the Fuch correction [132]. 2D periodicity can be handled in an analogous approach devised by Parry [136, 137].

Buckingham Potential: Van der Waals and Pauli Repulsion

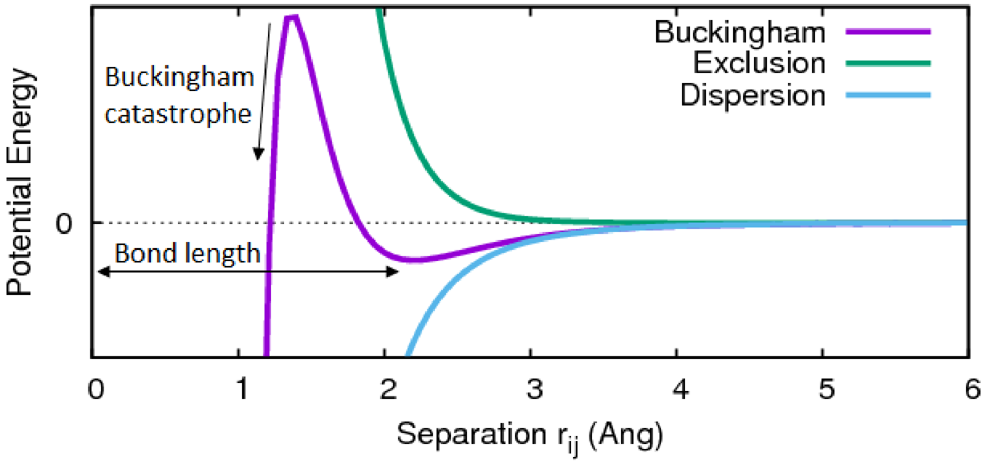

Figure 3.7: Short range interatomic behaviour is incorporated by a Buckingham pair potential which includes dispersion and Pauli exclusion related terms. The local minimum corresponds to the equilibrium bond length.

Short range interatomic interactions occur due to two principle quantum effects. Attractive van der Waals interactions and repulsion due to Pauli exclusion. The dispersive forces occur due to random multipole fluctuations creating instantaneous interactions of the form:

$$U_{ij}^{Disp}(r_{ij}) = \sum_{n=3}^{\infty} -\frac{C_{2n}}{r_{ij}^{2n}} \approx -\frac{C_6}{r_{ij}^6} \tag{3.23}$$

Typically dipole-dipole interactions are dominant allowing the series to be truncated to the $1/r_{ij}^6$ term. The Pauli exclusion principle states that no two fermions can share the same quantum state, prohibiting overlap of the electron densities, manifesting in a repulsive force that increases exponentially with reduced ionic separation r_{ij}. Both of these complex interactions can be approximated using a Buckingham potential U_{SR}^{Buck}:

$$U_{SR}^{Buck}(r_{ij}) = A_{ij} \exp\left(-\frac{r_{ij}}{\rho_{ij}} \right) - \frac{C_{ij}}{r_{ij}^6} \tag{3.24}$$

where the set of coefficients A_{ij}, ρ_{ij} and C_{ij} for each unique pair of species is fitted to *ab initio* data to attempt to reproduce the quantum mechanical potential energy surface.

When the dispersion term C_{ij} is non-zero, the Buckingham potential asymptotically approaches $-\infty$ for small separations creating an infinitely attractive force. This is known as the *Buckingham catastrophe* (Figure 3.7). For a well parametrised interatomic potential, provided a system is started off with a reasonable set of initial conditions and not perturbed too severely, the energy barrier of the Buckingham potential is usually sufficient to prevent the catastrophe occurring.

The Buckingham potential is short-range, tending to zero for large ionic separations. As such it becomes convenient to truncate the radius of the potential to reduce the computational expense by not including negligible interactions from atoms outside of a defined spherical cut-off radius r_{cut}. It is necessary to ensure this cut-off radius is sufficiently large to retain the correct properties. In this thesis a cut-off radius of 8 Å is used throughout. To avoid a discontinuous change in the energy surface at the cut-off radius, the potential is shifted to keep it smooth and continuous. An additional term is added to the interatomic potential to correct the long-range behaviour due to the shift [132]:

$$U_{ab}^{correction} = 2\pi \frac{N_a N_b}{V} \int_{r_{cut}}^{\infty} g_{ab}(r) U_{ab}^{buck}(r) r^2 dr \tag{3.25}$$

where N_a and N_b are the number of species types a and b in the system of volume V and g_{ab} is the pair correlation function where it is assumed $g(r > r_{cut}) = 1$.

3.3.2 Intramolecular Interactions

Core-Shell Model

Electronic polarisability of ions is an essential feature required to stabilise ferroelectric phases and maintain a correct directional response to the crystalline environment. The core-shell model introduces a dipolar polarisability by replacing each rigid ion with a massive core of mass M and charge Xe, and a light shell of charge Ye and mass m, tethered by a spring (Figure 3.8). The sum of the masses equals the atomic mass of the ion and the sum of the charges equal the full ionic value. The electronic polarisability is then captured by the dipole moment produced by the relative core-shell displacement [138]. Short range potentials only act between shells and there is no electrostatic self-interaction between the core and shell of the same atom. The potentials acting upon each constituent part of the core-shell atom is depicted in Figure 3.8.

Early shell models featured massless shells which would be relaxed using energy minimisation techniques with no inertial delay. Here, the adiabatic method of Fincham *et al* [139] is used whereby the assigned mass

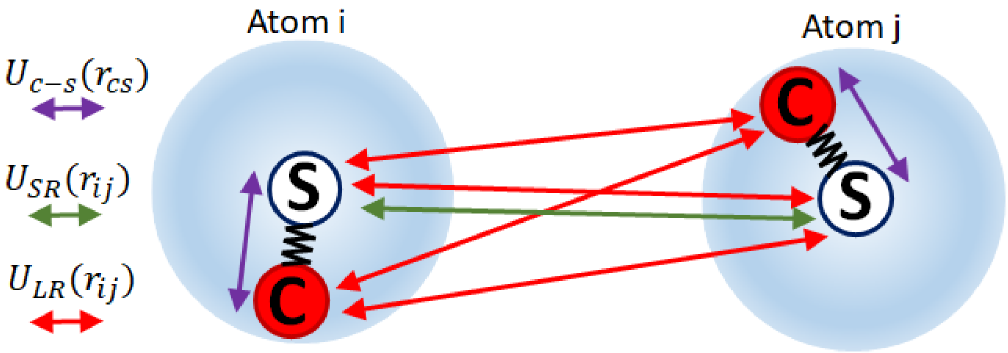

Figure 3.8: The core-shell model decomposes each atom into a massive core (C) and a light shell (S) which are tethered by a spring potential (purple). Electrostatic interactions are treated between all cores and shells of other atoms (red). Short range potentials interact between neighbouring shells (green).

allows the shells to be treated by numerical integration of the equation of motion in the same manner as a rigid ion (see §3.3.3). Provided the shell mass is sufficiently small, the vibrational frequency of the spring will be far greater than the ionic frequency, ensuring the shell moves adiabatically [132].

Due to the non-linear and anisotropic polarisability of oxygen an anharmonic, isotropic potential has been used to account for the dynamic covalency [50, 53]:

$$U_{c-s}(r_{cs}) = \frac{1}{2!}k_2 r_{cs}^2 + \frac{1}{4!}k_4 r_{cs}^4 + D(r_{cs}) \tag{3.26}$$

Early models used an anisotropic shell model but found its use limited due to the necessity of having a well defined environment [140]. The 2nd and 4th order spring constants (k_2 and k_4) are included as parameters when fitting the interatomic potential to the QM potential energy surface. The final term in equation 3.26 is a penalty function designed to create a large restoring force if the relative displacement of the core and shell of an atom becomes too large, preventing core-shell separations.

3.3.3 Molecular Dynamics

Molecular dynamics (MD) simulations are similar to real experiments. First a sample is selected. In this case an interatomic potential is defined and a system of N atoms created with some reasonable initial configuration. Next the experiment is conducted and properties of interest are measured over a sufficient period to reduce background noise. In MD the classical equations of motion are time evolved until statistical properties are constant. This is a period of equilibration. Once the system is equilibrated, a production run is performed over which the properties of interest are measured and averaged [134]. Molecular dynamics in this research has been performed using a modified version of the DL_POLY package [132]. This section aims to introduce the underlying theory of the code. Further details regarding precise implementation are available in ref [132].

It is often convenient to express the interatomic potential within the Lagrangian framework of classical mechanics using generalised coordinates q and momenta $\dot{q}$:

$$\mathcal{L}(q,\dot{q}) = \frac{1}{2}\sum_{\alpha}\sum_{\beta} G_{\alpha\beta}(q)\dot{q}_{\alpha}\dot{q}_{\beta} - U(\{q\}) \tag{3.27}$$

where the first term is the kinetic energy and the second is the interatomic potential, $G_{\alpha,\beta}$ is the mass metric tensor[8]. Then according to the principle of least action, the correct classical trajectory is given by the path that extremises the action[9]. This path is also that which solves the Euler-Lagrange equation:

$$\frac{d}{dt}\frac{\partial\mathcal{L}}{\partial\dot{q}_{\alpha}} - \frac{\partial\mathcal{L}}{\partial q_{\alpha}} = 0 \tag{3.28}$$

---

[8] $G_{\alpha,\beta} = \sum m_i \frac{\partial\mathbf{r}_i}{\partial q_\alpha}\cdot\frac{\partial\mathbf{r}_i}{\partial q_\beta}$

[9] $S[q] = \int_0^T dt\mathcal{L}(q(t),\dot{q}(t))$

The Euler-Lagrange equation then gives the equations of motion. For the case of an interatomic potential acting on N atoms with kinetic energy $\frac{1}{2}m_i\dot{r}^2$, the equations of motion are shown to be Newton's laws of motion. In Cartesian coordinates the equation of motion for the ith particle will be:

$$\frac{d}{dt}\mathbf{p}_i = \mathbf{F}_i = \sum_{j\neq i}^{N} \mathbf{f}_{ij} = -\sum_{j\neq i}^{N} \frac{1}{r_{ij}} \left(\frac{\partial}{\partial r_{ij}} U(r_{ij}) \right) \mathbf{r}_{ij} \tag{3.29}$$

where $\mathbf{p}$ and $\mathbf{F_i}$ are the momentum and force acting on atom i, and $\mathbf{f}_{ij}$ is the force contribution due to the interaction with each atom j. Given the force on each particle is given by the negative gradient of the interatomic potential, the system can be time evolved from the initial configuration using an integration method. A simplified flow diagram of the MD production phase is shown in Figure 3.9.

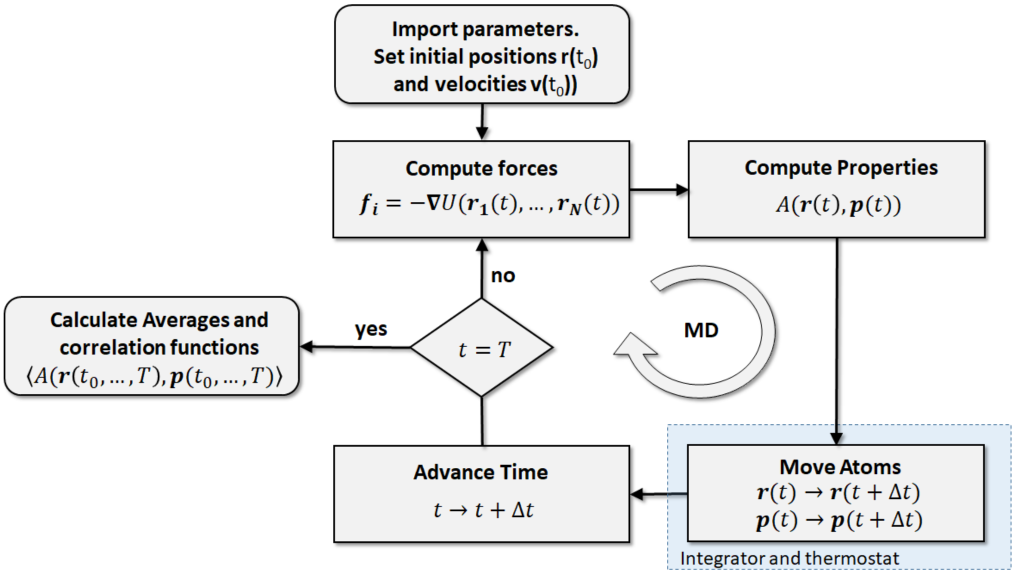

Figure 3.9: Simplified molecular dynamics process evolving the trajectory $\{\mathbf{r}, \mathbf{p}\}$ from time t_0 to T.

Integrator

The equations of motion (eqn. 3.29) can be solved numerically to evolve the trajectory of the ensemble of particles by use of an integrator. These are often derived by manipulating Taylor expansions of known initial quantities (eg $\mathbf{r}_i(t_0)$) to get stable and time reversible expressions for the same quantities at a small instant of time later ($\mathbf{r}_i(t_0+\Delta t)$). An example is the Velocity Verlet algorithm which is performed in two stages. In the first stage, knowing the positions, velocities and forces at time t, the velocity can be integrated by half a timestep. This new velocity can then move the positions by a full timestep Δt:

$$\mathbf{v}\left(t+\frac{1}{2}\Delta t\right) \Longleftarrow \mathbf{v}(t)+\frac{\Delta t}{2}\frac{\mathbf{f}(t)}{m} \tag{3.30}$$

$$\mathbf{r}(t+\Delta t) \Longleftarrow \mathbf{r}(t)+\Delta t\mathbf{v}\left(t+\frac{1}{2}\Delta t\right) \tag{3.31}$$

Since the positions are now at new coordinates they will have a different potential energy and therefore have new forces acting upon them. As such the forces need to be re-evaluated using eqn 3.29, which are used to advance the velocities by another half timestep to match the positions.

$$\mathbf{f}(t+\Delta t) \Longleftarrow \mathbf{f}(t) \tag{3.32}$$

$$\mathbf{v}(t+\Delta t) \Longleftarrow \mathbf{v}\left(t+\frac{1}{2}\Delta t\right)+\frac{\Delta t}{2}\frac{\mathbf{f}(t+\Delta t)}{m} \tag{3.33}$$

An advantage of this integrator over others is that it only requires the calculation of the force once per timestep which is computationally expensive formally scaling as $\mathcal{O}(N^2)$. Since a cut-off radius is being used for the short-range potentials and real space Ewald summation, a link cell approach can be used to reduce the force calculation to $\mathcal{O}(N)$ [132,134].

Provided a small timestep is used, then integration using the Velocity Verlet algorithm transverses a trajectory in a microcononical (NVE) ensemble of microstates [141]. Often this ensemble is inconvenient and other thermodynamical ensembles are more representative of the relevant experimental conditions. The equations of motion can be modified to generate trajectories within a different ensemble such as the canonical (NVT) or isothermal-isobaric (NPT) by use of a thermostat algorithm.

Isothermal Ensembles

Numerous thermostat algorithms exist in order to control the system temperature. As a simple method, the velocity can be rescaled to ensure that the velocity distribution of the system corresponds to a Maxwell-Boltzmann distribution with the average kinetic energy equalling the desired temperature [10] [141]. However, this approach does not allow for fluctuations that can occur in the canonical (NVT) ensemble [134].

The method that is used throughout this thesis is the Nosé-Hoover approach [142–144]. This method couples the real system to a heat bath by extending the Lagrangian with additional coordinates s and conjugate momenta $\dot{s}$ associated with the reservoir:

$$\mathcal{L}(\mathbf{r}, \dot{\mathbf{r}}, s, \dot{s}) = \sum_{i=1}^{N} \frac{m_i}{2} s^2 \dot{\mathbf{r}}_i^2 - U(\{\mathbf{r}\}) + \frac{Q}{2}\dot{s}^2 - L k_B T \ln s \tag{3.34}$$

where Q is an effective mass associated with s to control the heat transfer. L is chosen to be the number of degrees of freedom of the real system which ensures the algorithm produces a canonical ensemble of microstates [141]. From this Lagrangian new equations of motion can be derived and implemented with an appropriate integrator to allow isothermal calculations. Hoover [145] later showed that these equations of motion are unique and no other equations of the same form can create a canonical distribution [134].

Through the Melchionna modification [146], a barostat can be added

---

[10] equipartition energy: $\langle K \rangle = \frac{1}{2} k_B N_f T$, where N_f is the number of internal degrees of freedom.

to the extended system in a similar manner in order to constrain the pressure through isometric regulation of the volume, to sample an isothermal-isobaric (NPT) ensemble [132]. This can be extended to permit anisotropic variations in the volume to simultaneously manipulate the cell size and shape at constant stress ($N\sigma T$) ensemble, see ref. [132].

Ergodicity and Ensemble Observables

In an experiment, a series of measurements are performed over a range of time with the properties averaged. Molecular dynamics operates on a similar paradigm whereby the system is numerically evolved and the properties of interest (A) are averaged. The trajectory of the MD simulation explores the microcanonical phase space of the ensemble (the set of positions and momenta attainable by all N atoms at a fixed energy). Under the ergodic hypothesis, it is taken that the time average $\bar{A}$ is equal to the ensemble average $\langle A \rangle_{ens}$ [147]. That is, the average properties of a large number of short simulations sampling the phase space will be equivalent to a single long simulation. This principle is applied to other ensembles such that the observable property can be determined by [134]:

$$\bar{A} = \lim_{\tau \to \infty} \frac{1}{\tau} \int_0^{\tau} dtA = \langle A \rangle_{ens} \Longleftrightarrow A_{obs} \tag{3.35}$$

The rolling of dice gives a simple example of ergodicity. The time average of a single die thrown 10^6 times will be equal to the ensemble average, in this case the average of 10^6 dice thrown once [147]. However, not all processes are ergodic. If the dice are magnetic such that “2” and “5” are attracted but pairs of “2” or “5” are repelled, then the time and ensemble averages will differ. A relevant example are relaxor ferroelectrics such as PMNPT. Below a freezing transition temperature T_f, they become non-ergodic due to the freezing in and interaction of polar nanoregions which exhibit glass-like behaviour [147]. For the materials and conditions considered in this thesis, it is expected the ergodic principle holds.

Periodic Boundary Conditions for a MD cell

Large scale atomic simulations can now involve systems on the order of 10^9 atoms [148]. However this is still many orders of magnitude smaller than a macroscopic system. If molecular dynamics were to be performed with the atoms in a rigid container then surface effects would dominate due to the large proportion of atoms in contact with the walls of the simulation cell. For example, a simple cubic crystal containing N^3 atoms will have $N^3 - (N-2)^3$ atoms at the surface[11] which for a 1000 atom simulation would be 48.8% in direct contact with the walls.

To effectively simulate bulk properties the simulation cell can be replicated infinitely in all directions using periodic boundary conditions (PBC). This enables atoms in the principle simulation box to interact with images of atoms to reinforce the correct local environment. Any particle that leaves the principle cell will be replaced by its image entering from the opposite side. To prevent self interaction between an atom and its image the cut-off radius r_{cut} has an upper bounds of half the smallest cell dimension.

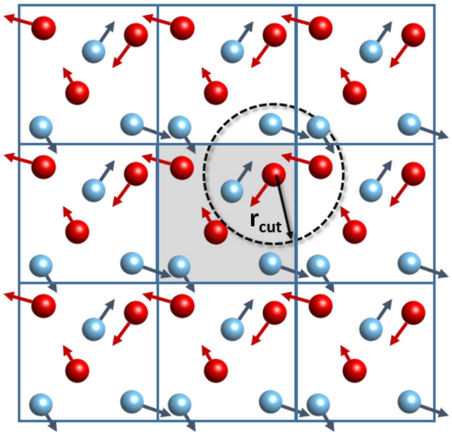

Figure 3.10: 2D representation of periodic boundary conditions applied to a cubic principle cell (grey). The velocity of each constituent atom is depicted by the vector. Atoms leaving the principle cell are replaced by their image from the opposite cell. Short range interactions occur within the sphere defined by $\mathbf{r_{cut}}$.

---

[11] $N \neq 1$

3.3.4 Forcefield Fitting

In this Section the practical principles detailing how quantum mechanical data is fitted to produce a classical forcefield is introduced. The principal forcefield to be used in this thesis is that derived by Gindele *et al* [23, 24] using similar techniques. Within this thesis, a new cubic phase $SrTiO_3$ and FCC phase Pt forcefield will be derived to be compatible with the Gindele PZT potential, such that $SrTiO_3/PbTiO_3$ superlattices and $SrTiO_3/PbZr_{1-x}Ti_xO_3/Pt$ capacitors can be accurately modelled (Chapter 6).

The fitting procedure involves a systematic adjustment of the interatomic potential parameters in equations 3.25 & 3.26 until the error between the reference f^{ref} and calculated f^{out} properties are minimised using a weighted objective function $\mathcal{F}$:

$$\mathcal{F} = \sum_{i}^{N_{ref}} w_i (f_i^{ref} - f_i^{out})^2 \tag{3.36}$$

where w_i is a weighting factor for each observable property i. Previous shell-model forcefields are known to significantly underestimate ferroelectric properties due to the strong dependence on disposable volume (Fig. 3.4c) [50, 53]. As such, the lattice parameters are given, *a priori*, the highest weighting of the fitting observables. Minimisation of Eqn. 3.36 has been performed using the *Broyden-Fletcher-Goldfarb-Shanno* (BFGS) Hessian update algorithm in conjunction with the Newton-Rhapson method, as implemented within the General Utility Lattice Program (GULP) version 4.0.3 [131]. Shells are initially set with the coordinates of their respective cores and treated using the simultaneous fitting method. All forces are converged within 10^{-5} eV/Å.

The BFGS routine is a local minimum solver so poor initial forcefield parameters or choice of weights will start in a basin of the param-

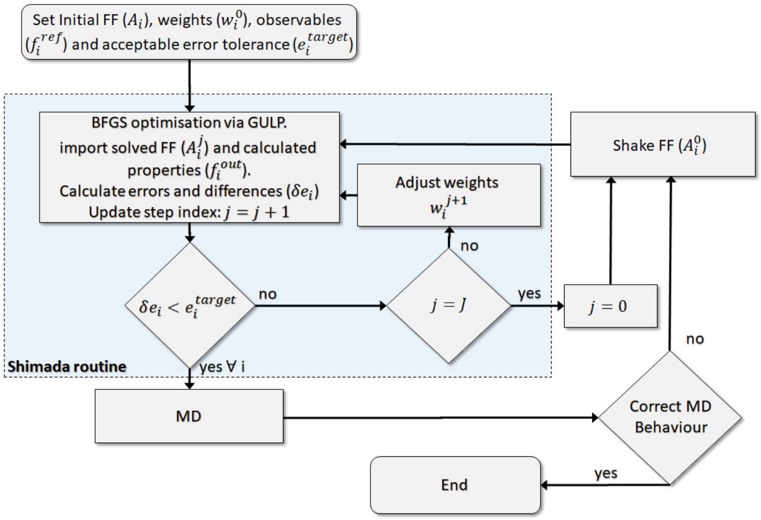

Figure 3.11: Flowchart identifying the processes used to fit the interatomic potential parameters of U_{SR} and U_{c-s} to an *ab initio* energy surface.

eter space not inclusive of the global minimum. As such, we adopt the method of Shimada *et al* [22]. In this approach, the weighting factor w_i of each parameter is simultaneously adjusted proportional to its relative error ($\delta e_i = (f_i^{out} - f_i^{ref})/f_i^{ref}$) and the target accuracy of the calculated property e_i^{target}. If $\delta e_i < e_i^{target}$ is not satisfied the weight is updated according to

$$w_i^{j+1} = \frac{|\delta e_i|^2}{e_i^{target}} w_i^j \tag{3.37}$$

where j is the fitting step index. In our implementation, we found the algorithm to often get stuck in a loop where the weights get locked in a fixed ratio preventing the routine finding a different minimum in the parametric space. To overcome this issue, a basin hopping routine is additionally included which we call the forcefield *shake*. In the shake routine, if the change in the value of a parameter $\mathcal{A}_i$ is below a set tolerance (we arbitrarily choose 10%) after J steps, then the parameter is shaken according to the Eqn. 3.38. The new parameters from the shake are accepted if after a further J steps

$\mathcal{F}^{2J} < \mathcal{F}^{j}$.

$$\mathcal{A}_i^{J+1} = \mathcal{A}_i^{J}(n+1) \tag{3.38}$$

where n is a pseudo-randomly generated number ($0 \leq n < \Delta_i$) and Δ_i is a parameter to set for each parameter to limit the maximum change in parameter $\mathcal{A}_i$. Throughout we set Δ_i to provide a maximum change of 5% for any parameter $\mathcal{A}_i$. The full procedure is outlined in the flowchart in Fig. 3.11.

3.3.5 Summary

In this Chapter, the concepts of the theoretical methods used throughout the thesis were introduced. Density functional theory serves as an accurate method to solve the Schrödinger equation and was used to demonstrate the ferroelectric instability, the mixed ionic-covalent character of the electronic structure and the anomalously large Born effective charges associated with the ferroelectric phenomenon. Interatomic potentials whose parameters are fitted to the properties determined from DFT were then discussed as implemented within the molecular dynamics framework. In the next chapter, the metrics used to quantify ferroelectric properties from classical molecular dynamics calculations are defined and their implementation validated in comparison to ab initio calculations and experiments.

References

In addition to the references explicitly cited in the text, this chapter has drawn largely from the following reviews:

- R. M. Martin, *Electronic Structure: Basic Theory and Practical Methods*, Cambridge University Press, 3rd Edition, 2013 [100]

- D. Frenkel & B. Smit, *Understanding molecular simulations: From Algorithms to Applications*, Academic Press, 2nd Edition, 2002 [134]
- P. Ghosez, *First Principles Study of the Dielectric and Dynamical Properties of Barium Titanate*, PhD Thesis, Universite Catholique de Louvain, 1997 [103]
- P. Aguando-Puente, *First-Principles Study of Screening Mechanisms of the Depolarising Field in Nanosized Capacitors*, PhD Thesis, Universidad de Cantabria, 2011 [38]

4

Metrics And Validation

The following sections outline the metrics implemented into the custom PoPP code (Polarisation and other perovskite properties), a script written to analyse perovskite ferroelectric calculations performed using trajectories calculated via the MD package DL_POLY [132]. Results of calculations are presented to test the script and validate the forcefield for its application to this research. Input files for DL_POLY have been generated using the ABbX3_CellGen module of the PoPP code. A list of custom software written to complete this thesis is provided in Appendix C.

4.1 Polarisation and Local Lattice Parameters

Arguably, one of the most insightful order parameters of ferroelectrics is the polarisation. For the asymmetric unit, the polarisation change ∂P in direction β is simply defined as that which results from the ferroelectric displacement δ of the i^{th} atom along α from its paraelectric sublattice reference site:

$$P_\beta = \frac{|e|}{V} Z^*_{i,\alpha,\beta}\delta_\alpha \tag{4.1}$$

where $Z^*_{i,\alpha\beta}$ is the (α, β) element of the Born effective charge tensor of the ith atom. Using the GULP package, the Born effective charge tensors may be extracted from the core-shell D_{c-s} and shell-shell D_{s-s} dynamic matrices ($Z^*_i = X_i\delta_{\alpha\beta} - (D_{c-s}D^{-1}_{s-s}Y)_i$) [131], where X and Y are the core and shell charges.

In most circumstances the reference paraelectric state is non-trivial and calculations of the Born effective charges through the dynamic matrices are computationally expensive. A decision to use bulk values would be erroneous due to the known deviation at surfaces and interfaces [149, 150]. Instead, we define the local polarisation at site j ($\mathbf{P}^j$) as the dipole per unit volume of a A_8BO_6 conventional unit cell centred on the B cation (at position $\mathbf{r}^j$), delimited by 8 A cations with 6 oxygen on the trigonal faces forming a complete octahedral cage about the B cation [151, 152] (Figure 4.1). The contributions from the dipoles separating all cores and shells in the cell are considered with reference to the site of the B-cation's core:

$$\mathbf{P}^j = \frac{1}{\nu^j}\sum_{i=1}^{29}\frac{1}{\omega^i}q^i(\mathbf{r}^{j,i} - \mathbf{r}^j) \tag{4.2}$$

where ν^j is the volume of the cell calculated via the local lattice parameters $\mathbf{A}^j$, $\mathbf{r}^{j,i}$ is the position vector of the ith particle in the jth unit cell with respect to the supercell origin, q^i is the charge of the ith particle species and ω^i is a weight to normalise the charge of the ith particle with respect to the number of cells it is shared amongst. The index i spans all cores of charge $q^i = X^i$ and shells of charge $q^i = Y^i$ in the cell excluding the central B core reference particle. The total charge of the i$^{\text{th}}$ particle is the sum of the core and shell charges $X + Y$. Depending on the forcefield parametrisation these are not restricted to be equivalent to the formal valence charges.

Molecular dynamics simulations were performed using two different forcefields to validate the polarisation implementation. A sample of comparisons are provided in Table 4.1 with excellent agreement observed across the full compositional range for both interatomic potential sets (See Figure D.1 in the Appendix). The first forcefield, a $\mathrm{Pb(Zr_{1-x}Ti_x)O_3}$ parametrisation by Gindele *et al* [23], will be the principal forcefield used throughout this thesis. Two structures, $\mathrm{PbTiO_3}$ and *P4mm* ordered $\mathrm{PbZr_{0.5}Ti_{0.5}O_3}$, are shown in Table 4.1 calculated at 20 K using a 12×12×12 simulation cell. The difference in the total polarisation calculated for both cases is negligible. It was shown in references [23, 24] that this polarisation only differs by 0.6% from the value calculated using equation 4.1 with the Born effective charges determined from the dynamic matrices. The second test was performed with the PMNPT forcefield by Sepliarski *et al* where a minor difference in polarisation of 1.2% was determined.

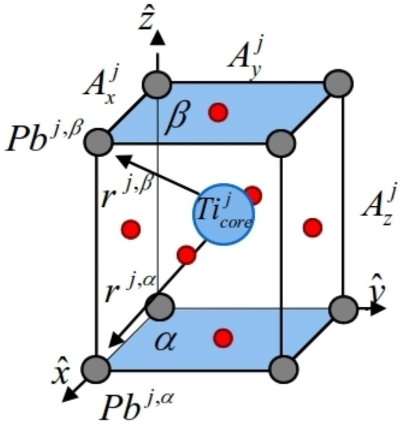

Figure 4.1: Local metrics of polarisation $\mathbf{P}^j$, lattice parameters $\mathbf{A}^j$, strain $\eta^j_{kk'}$ and other associated properties are calculated using a B-cation site centred $\mathrm{A_8BO_6}$ conventional unit cell. The A-cation sites, B-cation and oxygen are represented by grey, blue and red spheres, respectively. The assignment of A-cations to top β and bottom α faces to define the local lattice parameters has been visualised for the A_z^j case.

The total (macroscopic) polarisation $\mathbf{P}$ is the sum over the contribution from each unit cell (given by eqn. 4.2):

$$\mathbf{P} = \frac{1}{N}\sum_{j}^{N}\mathbf{p}^j \tag{4.3}$$

The polarisation components during the temperature driven phase transition of $\mathrm{PbTiO_3}$ using the forcefield from [23] is shown in Figure 4.2. The definition of polarisation on a unit cell basis enables the local polarisation to be analysed and visualised. The uniform polarisation of monodomain $PbTiO_3$ at 50 K is shown in the subfigure.

	$PbTiO_3$ (FF 1)	$PbTiO_3$ (FF 2)	$PbZr_{0.5}Ti_{0.5}O_3$ (FF 1)
PoPP code ($\mu C/cm^2$)	49.2	64.7	42.8
Reference ($\mu C/cm^2$)	49.2 [23]	65.5 [151]	42.9 [24]
Rel. Error (%)	0.0	1.2	0.2
DFT (LDA)	79.8 [153]	79.8 [153]	81.0 [154]

Table 4.1: Comparison between the calculation of polarisation using equation 4.2 and the value reported for forcefields in references [23] (FF 1) and [151] (FF 2). Core-shell forcefields consistently underestimate polarisation relative to DFT calculations. The PoPP code reproduces the polarisation of the forcefield given in the literature.

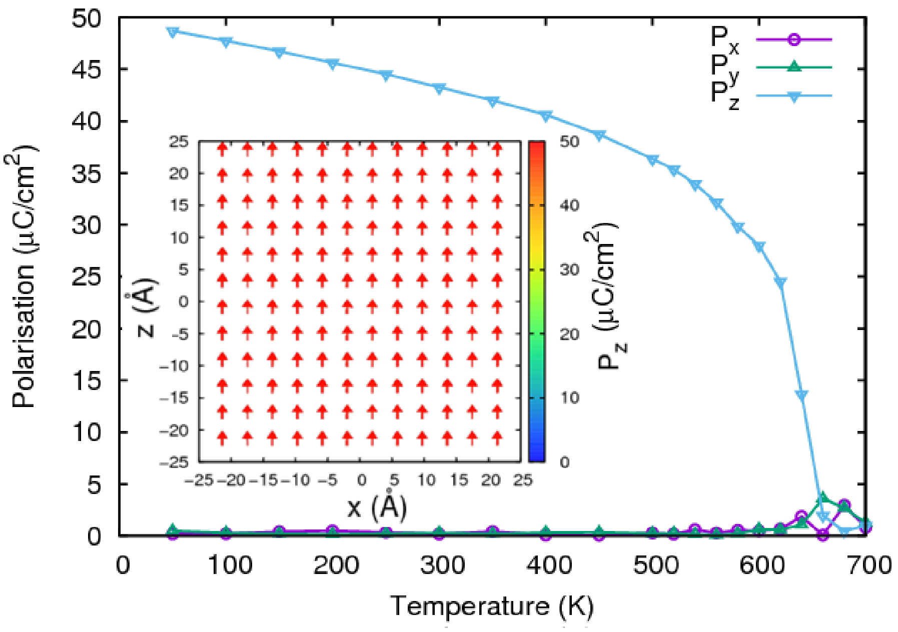

Figure 4.2: Polarisation dependence on temperature for bulk $PbTiO_3$ using the Gindele forcefield [23]. The correct physical behaviour in comparison to experiment is observed. As is common in core-shell model forcefields the transition temperature and spontaneous polarisation is undervalued. The inset shows an (010) cross-section of the dipole pattern at 50 K.

Local lattice parameters A_k^j of the j^{th} unit cell define the local strain

$\eta^{j}_{kk'}$ and volume ν^j. For each component of $\mathbf{A}^j$, the delimiting A cations are defined as belonging to a top (β) or bottom (α) face which bisects the components axis, as visualised for A^j_z in Figure 4.1. We consider only the position vectors of the delimiting A cations with respect to the reference B core ($r^{j,(i\in\{\beta,\alpha\})} := r^{j,(i\in\{\beta,\alpha\})} - r^j$):

$$\mathbf{A}^j = \frac{1}{4}\left(\sum_{\beta=1}^{4}\mathbf{r}^{j,\beta} - \sum_{\alpha=1}^{4}\mathbf{r}^{j,\alpha}\right) \tag{4.4}$$

To validate our calculations, the local lattice parameters of bulk calculations are compared to the total cell parameters normalised per unit cell using the PbTiO$_3$ forcefield derived by Gindele *et al* [23]. The error of the time averaged local lattice parameters at each site is found to differ from the total cell average by less than |0.1|% (Figure 4.3).

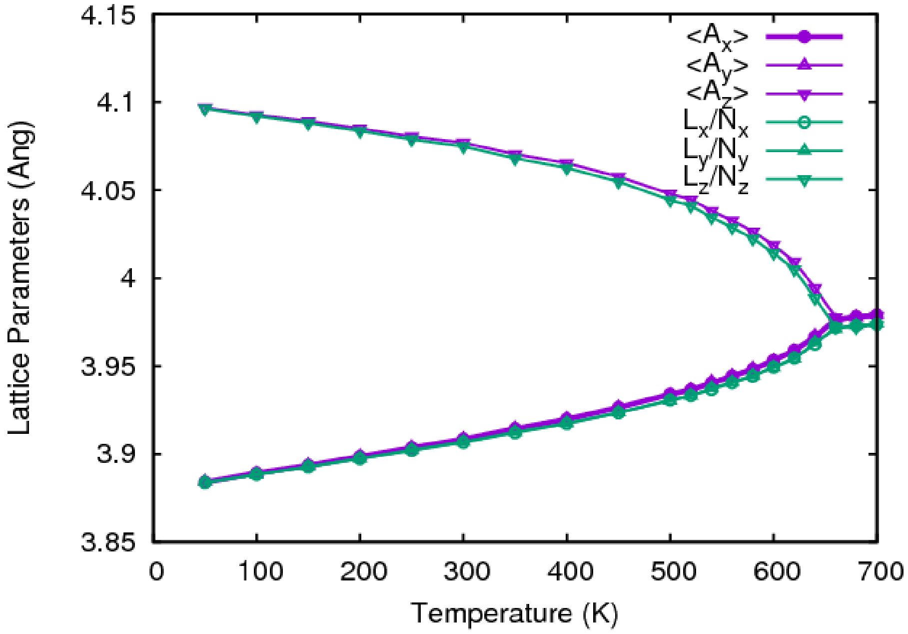

Figure 4.3: Comparison between the average unit cell lattice parameters as determined via eqn. 4.4 ($\langle A_i\rangle$) and the cell vectors calculated by DLPOLY [132] normalised by the system size (L_i/N_i).

The local lattice parameter metric then allows for macroscopic mechanical properties to be defined locally:

$$t^j = 2A_z^j/(A_x^j + A_y^j) \tag{4.5}$$

$$\upsilon^j = A_x^j\hat{\mathbf{x}} \cdot (A_y^j\hat{\mathbf{y}} \times A_z^j\hat{\mathbf{z}}) \tag{4.6}$$

$$\eta_{kk'}^j = \frac{1}{2}(\Delta A_k^j/A_{k'}^j + \Delta A_{k'}^j/A_k^j) \tag{4.7}$$

which are the tetragonality, volume and strain where $\Delta A_k^j = \bar{A}_k - A_k^j$.

4.2 Antiferrodistortive Surface Relaxations

Realistic simulations of $PbTiO_3$ based thin films are challenging due to the variety of competing lattice instabilities present from the perovskite structure. In bulk $PbTiO_3$ antiferrodistortive instabilities are suppressed by the ferroelectric (FE) distortion and do not condense in the tetragonal phase [26]. However, at surfaces the change in coordination allows a mixture of distortions to emerge simultaneously. Early *ab initio* studies of $PbTiO_3$ surface relaxations investigated a (001) PbO termination with (1×1) surface periodicity determining a ferroelectric phase orientated in-plane along $\langle 110 \rangle$ [155]. More recently, grazing incidence x-ray scattering identified an AFD c(2×2) reconstruction of the (001) surface consisting of a 10° rotation of the oxygen octahedral cages around the [001] axis through the Ti atoms [156]. This relaxation has been reproduced using DFT predicting an azimuthal cage rotation at the surface layer of 10.6° [157]. Several investigations have further identified the FE (1×1) and AFD c(2×2) distortions can coexist creating a FE-AFD relaxation [157, 158].

These characteristic PbO terminated surface relaxations are a consequence of the Pb cation's chemistry which has a propensity to shift the cation off centre, creating short and strong covalent bonds with oxygen.

The broken symmetry at the surface termination promotes the formation of shorter bonds driving the enhanced antiferrodistortive effect in $PbTiO_3$ films [157]. In contrast, Ba, which forms bonds of a more ionic nature with O in $BaTiO_3$ [34], does not experience the same AFD coupling at surface terminations. (001)PbO terminated surfaces have been shown to be more stable than TiO_2 surfaces [155].

4.2.1 Forcefield Validation for Surface Calculations

The Gindele forcefield was fitted reproduce *ab initio* bulk properties [23] and verified to correctly describe static and dynamic properties of domain walls [24]. Nonetheless, this does not guarantee the forcefield produces the correct behaviour of surfaces. In order to trust the validity of thin film calculations of $PbTiO_3$ using this forcefield it must be shown to reproduce the known FE, AFD and FE-AFD surface reconstructions.

Thin films of $PbTiO_3$ are constructed by stacking alternating (001) planes of PbO and TiO_2, starting and finishing with PbO, to create a PbO symmetrically terminated slab. 3D periodic boundary conditions are implemented requiring a vacuum region to be supplied along [001] as shown in Figure 4.4a. The thickness of the film (9 PbO & 8 TiO_2 layers) and vacuum region (16 Å) were both converged to prevent surface-surface interactions through the film and interactions between the principal film and its images. Calculations were performed with the in-plane lattice parameters fixed to the cubic phase value yielded by the forcefield at equilibrium in bulk a_0.

To study the FE surface reconstruction a (1×1) surface periodicity is defined with PbO layers consisting of two atoms and TiO_2 of 3 (see Figure 4.4b). Both the AFD and FE-AFD relaxations require c(2×2) periodicity with a=$\sqrt{2}a_0$ such that PbO layers contain 4 unique atoms and the TiO_2 layers contain 6 (see Figure 4.4b). For the non-polar AFD surface, initial atomic coordinates are placed in a *P2/m* spacegroup and relaxed

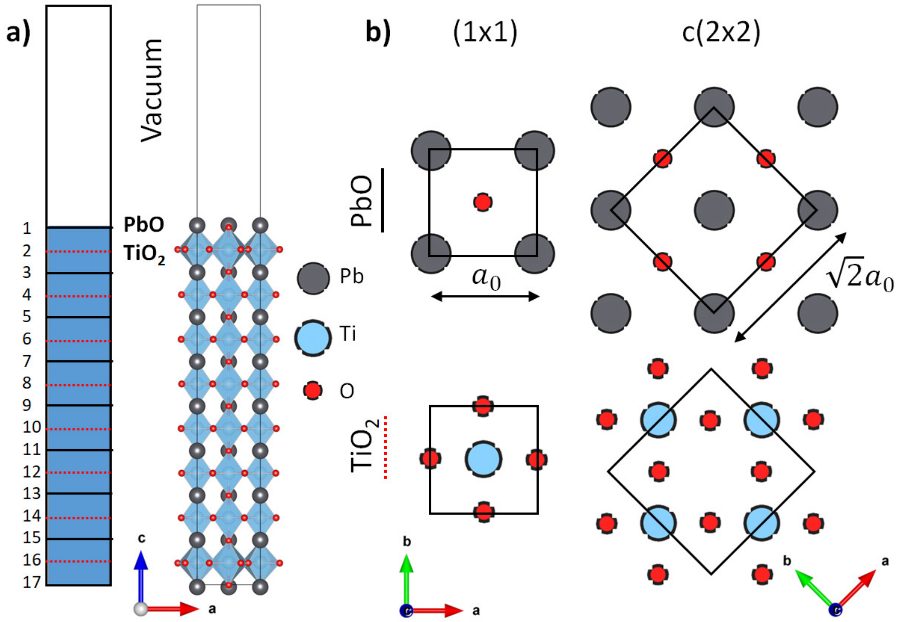

Figure 4.4: Surface calculation of $PbTiO_3$. (a) Schematic and real simulation cell of a symmetrically (001)PbO terminated film with vacuum region. (b) (001) layers of PbO and TiO_2 for the (1×1) and c(2×2) periodicities. The solid line represents the simulation cell boundaries and principle axes for the surface calculation. Pb, Ti and O are represented by grey, blue and red spheres, respectively.

according to its symmetry constraints [157]. This enables all atoms to displace along z with mirror symmetry across the central PbO plane of the film, and the equatorial oxygen atoms free to move in on the (001) plane provided inversion symmetry is maintained. The Pb, Ti and axial O are fixed to their high symmetry coordinates on the (001) planes. Symmetry constraints for the FE-AFD surface is relaxed to the *Pm* space group.

The zero temperature structures of the slabs are determined by minimising the energy using the BFGS algorithm as implemented in GULP [131]. A convergence criterion of 1 meV/Å was enforced on each ion to determine equilibrium.

The forcefield is shown to produce the surface relaxations of the FE, AFD and FE-AFD distortions in good agreement with DFT calcu-

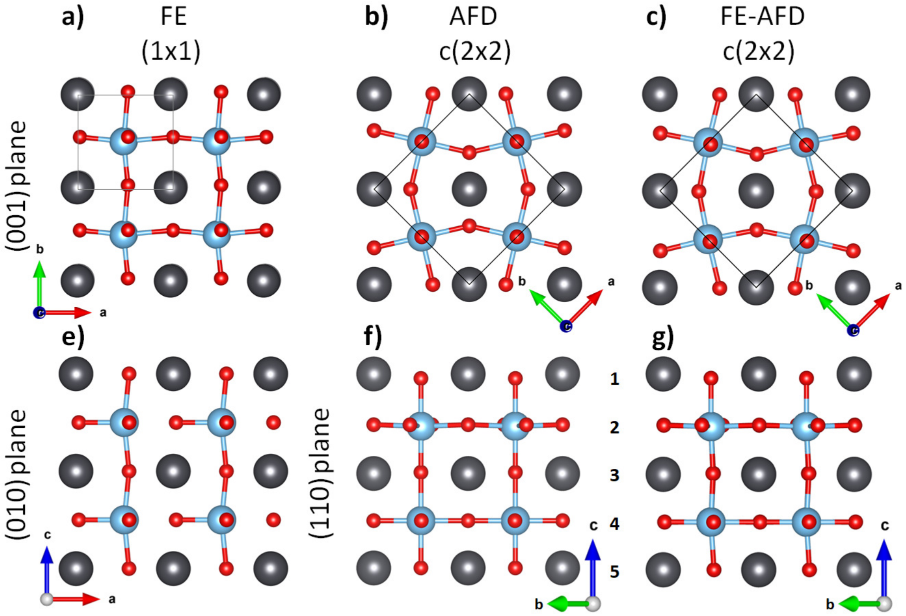

Figure 4.5: Relaxed atomic structures of the FE, AFD and FE-AFD surface reconstructions on (001)PbO terminated $PbTiO_3$ films. (a,b,c) show the (001) surface layer of the FE, AFD and FE-AFD relaxations, respectively. Only the first PbO and TiO_2 are shown. (d,e,f) show a side view of the first 5 layers of each surface reconstruction. Pb, Ti and O are depicted by grey, blue and red spheres, respectively. Miller indices of plane intersections are in relation to the principle axes of the simulation cell, shown by the solid lines in (a,b,c).

lations [157, 158]. The relaxed structures are shown in Figure 4.5. Both the FE and FE-AFD surfaces have displacements creating an in-plane polarisation orientated along ⟨110⟩. The AFD and FE-AFD both displace the equatorial oxygen atoms about the Ti on the (001) plane, resulting in octahedral cage rotations in the surface layer. As is observed from first principles, these rotations are supported in the top surface layer (both top and bottom surfaces) but are rapidly suppressed within the film. The rotations of the AFD and FE-AFD distortions reproduced from the Gindele forcefield are quantitatively compared with other forcefields and DFT in Table 4.2. The AFD rotation supported by this forcefield is 13.1° which overestimates the value determined by DFT (12.3° [158]) and experiment (10° [156]) but makes an improvement over the value supported by the forcefields from Sepliarsky *et al* [159, 160] and Shimada *et al* [22]. As is determined with DFT [158], this forcefield yields the FE-AFD distortion to be more stable relative to the AFD by 0.5 eV.

	FF (Present)	FF [160]	FF [159]	FF [22]	DFT [158]
AFD	13.1°	13.8°	–	14.4°	12.3°
AFD+FE	11.1°	–	13.5°	13.4°	10.6°

Table 4.2: Comparison between the octahedral cage rotations (Φ) between different forcefields and density functional theory for the AFD and FE-AFD surface relaxations.

Despite the AFD distortion forming due to the chemistry of the Pb atom, the shell model is able to capture the correct behaviour from the change in coordination and the resulting changes in the short and long range interactions. The quantitative agreement with DFT, experiment and other forcefields suggests the potential has a comparable accuracy and is suitable to study (001) PbO terminated surface properties.

4.2.2 Calculation of AFD modes during MD

Rotation of the octahedral cages Φ in the zero-temperature structures were manually measured using the VESTA package [161]. For large scale molecular dynamics this is infeasible so a subroutine was written to calculate Φ of each unit cell j throughout a MD simulation. The lateral rotation angle of the octahedral cage Φ^j is calculated using the opposite pairs of oxygen in the mid-plane of the unit cell. In Figure 4.1 these are the 4 oxygen atoms not on either α or β faces. A direction vector is defined for each pair of opposite oxygen orientated along the geodesic between them ($\mathbf{r}_k$ and $\mathbf{r}_{k'}$ as in Fig.4.6b). The mean angle of both vectors relative to the orthogonal axes provides the rotation angle:

$$\Phi^j = \bar{\phi}^j_k = \frac{1}{2}\left[\tan^{-1}\left(\frac{r_{k,x}}{r_{k,y}}\right) - \tan^{-1}\left(\frac{r_{k',y}}{r_{k',x}}\right)\right] \tag{4.8}$$

Direction vectors along the classical Ti-O bonds could also be chosen to calculate Φ^j. However, although ferroelectric and AFD modes usually exist at the expense of the other [38], it is known that both distortions can condense in surface layers [157]. A definition of Φ^j relying on the Ti coordinate would therefore become ill defined near surfaces and interfaces.

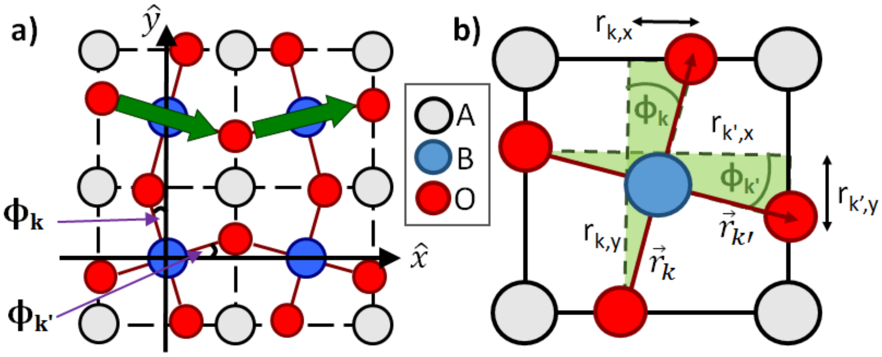

Figure 4.6: Calculation of the octahedral rotation angle of the antiferrodistortive modes in ABO_3 compounds. (a) Schematic of the AFD mode at R in the BZ (cf. Figure 3.5), identifying the angles Φ_k and $\Phi_{k'}$ of the octahedral cage relative to the system axes. (b) Diagram defining direction vectors $\mathbf{r}_k$ and $\mathbf{r}_{k'}$ and nomenclature in the j^{th} cell used to calculate the rotation angle via Eqn. 4.8.

The AFD calculations from a typical MD run are tested on a symmetrically (001)PbO terminated film constructed from 10×10 × 10 unit cells (4700 atoms), run at 300 K using a canonical ensemble with a Nosé-Hoover thermostat with relaxation constant 10 fs. The system was equilibrated for 20 ps until properties were converged, followed by a 60 ps production run using a 0.2 fs timestep. Full details regarding the thin film calculations

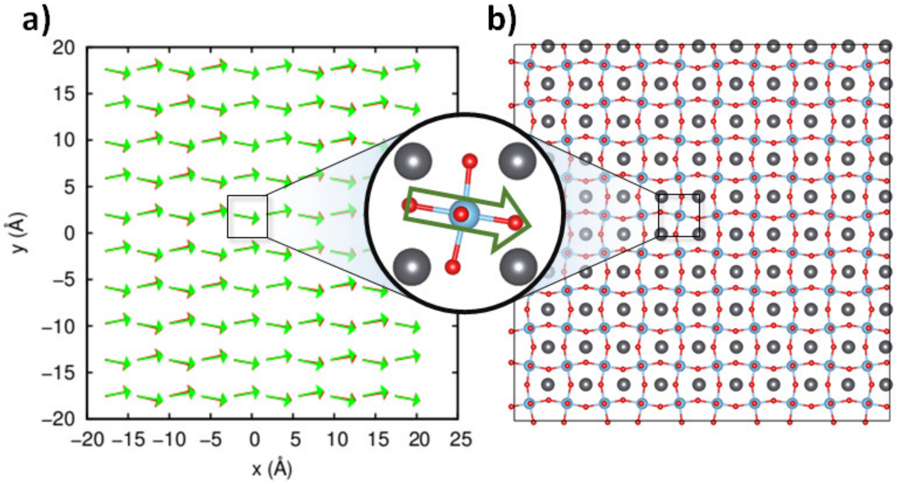

Figure 4.7: Antiferrodistortive surface relaxation of a $PbTiO_3$ film at 300 K. (a) Unit vectors depicting the octahedral cage rotation at each unit cell on the top (green) and bottom (red) surfaces. (b) Average atomic configuration of the top surface. Inset shows the vector calculated in comparison to the atomic structure of an arbitrary unit cell.

are available in Chapter 5. An AFD distortion, not given in the initial positions of the atoms, is shown to condense in the surface layer as found in the zero-temperature solutions. The AFD vectors of each unit cell on the top and bottom surfaces are averaged over the simulation and shown in Figure 4.7a. For comparison, the average coordinates of the surface atoms from the same simulation are displayed in Figure 4.7b, showing excellent agreement and validation of the AFD calculation.

4.3 Toroidal and Hypertoroidal Momenta

A multipole expansion of the current density $\mathbf{j} = \nabla \times \mathbf{p}$ ($\mathbf{p}$ is the dipole moment) with respect to the position vector $\mathbf{r}$ gives rise to a series of higher order terms [162]. The lowest order independent term is the toroidal moment:

$$T_\alpha = \frac{1}{10V}\int [(\mathbf{r}\cdot\mathbf{j}\ )r_\alpha - 2r^2 j_\alpha]d^3r \tag{4.9}$$

where V is the volume of the system and α labels the Cartesian components. Physically this term represents the average curl of the dipole moments [163]. This is more readily apparent applying integral theorems which can show equation 4.9 simplifies to:

$$\mathbf{T} = \frac{1}{V}\sum_i \mathbf{T}_i = \frac{1}{2V}\sum_i \mathbf{r}_i \times \mathbf{p}_{it} \tag{4.10}$$

where T_i is the local toroidal moment at unit cell i located at $\mathbf{r}_i$ and $\mathbf{p}_{it}$ is the transverse component of the dipole moment [164]. T_z can then be understood to probe the local toroidal ordering of the electric dipoles along the basis $\hat{\mathbf{e}}_\theta$ [163].

For systems with symmetrically twinned vortices the toroidal moment cancels. An example of such a system are the Landau-Lifshitz domains discussed in §2.5. To quantify the ordering of dipoles in these systems a hypertoroidal moment $\mathbf{h}$ was defined by Prosandeev and Bellaiche by defining $\mathbf{J} = \nabla \times \mathbf{T}$ [165]. In the same manner as the derivation of the toroidal moment, it can be shown that a multipole expansion of $\mathbf{J}$ gives:

$$h_\alpha = \frac{1}{10V}\int [(\mathbf{r}\cdot\mathbf{J}\ )r_\alpha - 2r^2 j_\alpha]d^3r \tag{4.11}$$

$$\Rightarrow \mathbf{h} = \frac{1}{2V}\sum_i \mathbf{r}_i \times \mathbf{T}_{it} \tag{4.12}$$

$$= \frac{1}{4V}\sum_i \mathbf{r}_i \times (\mathbf{r}_i \times \mathbf{p}_{it})_t \tag{4.13}$$

where $\mathbf{T}_{it}$ is the transverse component of the toroidal moment at unit cell i [164]. The hypertoroidal moment can be interpreted as the average curl of the toroidal moment (equation 4.9), quantifying the local ordering of toroidal moments along $\hat{\mathbf{e}}_\theta$ [163].

Practically, the transverse components of the dipole and toroidal momenta can be approximated from their fluctuation amplitudes $\mathbf{p}_{it} \approx \mathbf{p}_i - \langle \mathbf{p} \rangle$. However, this approximation makes the hypertoroidal moment varient to translation of the reference frame under 2D and 3D periodic conditions [164].

4.4 Dielectric Response

An equilibrium state is stationary such that the physical properties do not change with time. However, over small time intervals the value of an observable fluctuates due to the thermal motion of the constituent atoms. For particles suspended within a colloidal suspension these small fluctuations result in Brownian motion [166]. For a ferroelectric, this importantly results in fluctuations of the order parameters. The resistive force creating the thermal fluctuations can be related to external excitations by the fluctuation dissipation theorem [167].

In the limit of no applied field, this theorem enables conjugate properties to be determined via their correlation functions. This provides a convenient approach to calculate the susceptibility (dielectric response, χ) of a ferroelectric material, defined in equation 2.5, using the fluctuations of the local polarisation at constant field strength:

$$\chi_{\alpha\beta} = \frac{V}{\epsilon_0 k_B T}(\langle P_\alpha P_\beta \rangle - \langle P_\alpha \rangle \langle P_\beta \rangle) + \chi_{\infty,\alpha\beta} \tag{4.14}$$

where T is the temperature of the system with volume V, $\langle \cdots \rangle$ are thermal averages and Cartesian components are specified using the indices α and β. The high frequency susceptibility χ_∞ is typically much smaller than the statistical error of χ from an MD simulation which is on the order of 5-20% [168]. Using DFPT with the Wu-Cohen exchange-correlation functional [111] with ultrasoft pseudopotentials in CASTEP [112, 119], the optical susceptibility of the $PbTiO_3$ cubic phase is determined to be 8.24. This is negligible in comparison to 5% of the dielectric constant which is to the order of 10^4 [32]. The electric displacement field $\mathbf{D} = \epsilon_0 \boldsymbol{\mathcal{E}} + \mathbf{P}$ and equation 2.27 relate the susceptibility and the dielectric constant whose terms are often used interchangeably:

$$D_\alpha = \epsilon_0 \mathcal{E}_\alpha + P_\alpha = \epsilon_0(\delta_{\alpha\beta} + \chi_{\alpha\beta})\mathcal{E}_\beta = \epsilon_{\alpha\beta}\epsilon_0\mathcal{E}_\beta \tag{4.15}$$

$$\Rightarrow \quad \epsilon_{\alpha\beta} = \chi_{\alpha\beta} + \delta_{\alpha\beta} \tag{4.16}$$

Ferroelectrics are fundamentally anisotropic resulting in χ being defined as a tensor with 6 independent components. The symmetry of a particular phase can reduce this further. Tetragonal $PbTiO_3$ will have two independent and non-zero elements in the susceptibility tensor, χ_{zz} and $\chi_{xx} = \chi_{yy}$.

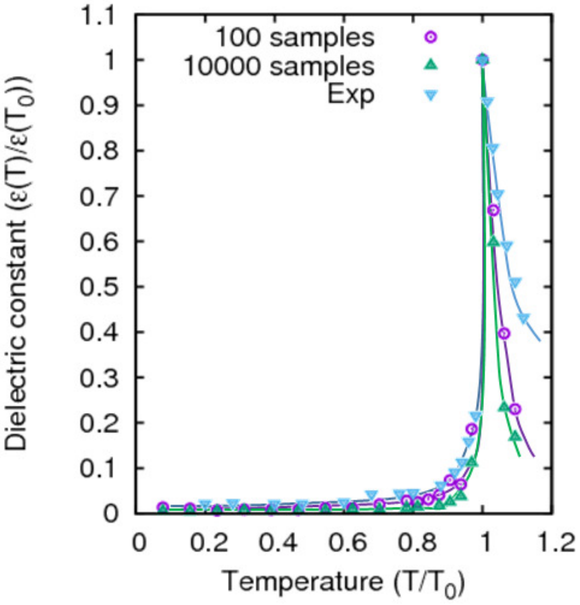

Figure 4.8: Dielectric constant of $PbTiO_3$ as calculated using fluctuation perturbation theorem of a MD simulation and observed from experiment (data from ref. [169]). Axes have been normalised against the transition temperature T_0 and peak dielectric constant $\epsilon(T_0)$ recorded in each method MD.

On approach to the phase transition temperature T_0, dipole moments become correlated resulting in the fluctuations becoming correlated over all distances and a divergence in the dielectric response χ. To test the implementation of the susceptibility using the fluctuation-dissipation theorem (eqn. 4.14), MD simulations were performed on bulk $PbTiO_3$ using DL_POLY [132] with the Gindele forcefield [23] for temperatures in the range 50 K $\leq T \leq$ 700 K. Steps of 50 K were used far from the transition temperature (T< 500 K) with 20 K steps used in the vicinity. To compensate for the statistical error in χ and the undervaluation of the transition temperature of the forcefield ($T_0^{FF} = 650\ K$), the dielectric constant and temperature are expressed in reduced units. The profile of the susceptibility with an increase in temperature is shown in Figure 4.8 with the susceptibility calculated using 100 and 10000 polarisation samples during the MD runs, and compared with experimental data from [169]. The dielectric response is observed to become asymptotic about the transition temperature in good qualitative agreement with experiment.

4.5 Piezoelectric Response Tensor

Differentials of the free energy (equation 2.1) gives rise to a number of Maxwell relations defining physical effects. Notably, the strain and polarisation are given as the derivatives of $\mathcal{G}$ with respect to the stress and electric field [25]:

$$\eta_{ij} = -\left(\frac{\partial \mathcal{G}}{\partial \sigma_{ij}}\right)_{T,E} \tag{4.17}$$

$$P_i = -\left(\frac{\partial \mathcal{G}}{\partial E_i}\right)_{T,\eta} \tag{4.18}$$

Second order derivatives also provide important properties, such as the piezoelectric effect d_{ijk}:

$$d_{ijk} = -\left(\frac{\partial^2 \mathcal{G}}{\partial E_k \partial \sigma_{ij}}\right)_T = \left(\frac{\partial \eta_{ij}}{\partial E_k}\right)_{T,\sigma} \tag{4.19}$$

$$= -\left(\frac{\partial^2 \mathcal{G}}{\partial \sigma_{ij} \partial E_k}\right)_T = \left(\frac{\partial P_k}{\partial \sigma_{ij}}\right)_{T,E} \tag{4.20}$$

Both the converse (4.19) and direct (4.20) piezoelectric effects with the fluctuation-dissipation theorem [167] can be applied to express the piezoelectric tensor as the cross-correlation of the polarisation and strain [170]:

$$d_{ij} = \frac{V}{k_B T}\langle \Delta P_i \Delta \eta_j \rangle \tag{4.21}$$

where $\Delta P_i = P_i - \langle P_i \rangle$ and $\Delta \eta_j = \eta_j - \langle \eta_j \rangle$ are the deviations of the polarisation and strain from the thermal average and i,j are indices representing vector elements. The rank of both the piezoelectric and strain tensors have been reduced by exploiting the symmetry of the strain by using Voigt notation.

The convergence of the d_{33} component is shown in Figure 4.9 for a MD simulation of bulk $PbTiO_3$. DL_POLY is used to evolve the system implementing an NσT ensemble at 50 K, maintained using the Nosé-Hoover thermostat and barostat with relaxation constants of 0.01 ps and 0.1 ps, respectively. The cross-correlation of the polarisation (eqn. 4.2) and strain (eqn. 4.7) are updated each timestep to record the convergence of the piezoelectric coefficient (eqn. 4.21). Whilst the full tensor is defined in a single MD run, a very long production run is required to gather sufficient statistics for an accurate result (> 1 *ns*). The converged value is determined to be 47±1 pC/N, where the error is defined as the standard deviation over the final 10^6 timesteps. This is in excellent quantitative agreement with the value calculated using GULP [131] which uses second derivatives of the internal energy returning 49 pC/N.

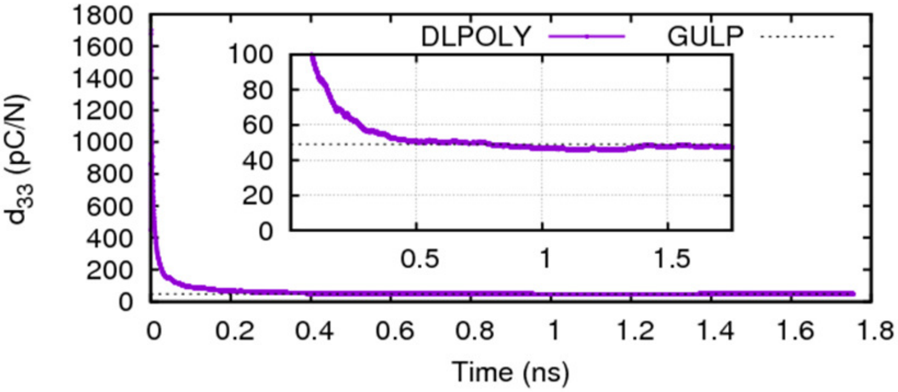

Figure 4.9: Convergence testing and comparison of the d_{33} piezoelectric coefficient of $PbTiO_3$ calculated using (a) the cross-correlation between the polarisation and strain during a MD simulation (dynamics performed using DL_POLY [132]) and (b) from energy derivatives as implemented in GULP [131].

4.6 Summary

In this chapter the key properties used to quantify ferroelectric and electromechanical behaviour during molecular dynamics simulations were introduced. The calculation of each property and the forcefield to be used in this thesis was validated by comparing results to MD simulations, DFT and experimental observations from the ferroelectric literature. The implementation and chosen forcefield were shown to be suitable and accurate to study both bulk and thin films.

5

$PbTiO_3$ Ultrathin Films

Exotic domain morphologies in ferroic materials are an exciting avenue for the development of novel nanoelectronics. In this chapter, large scale molecular dynamics is used to construct a strain-temperature phase diagram of the domain morphology of $PbTiO_3$ ultrathin films. By sampling a wide range of strain values over a temperature range up to the Curie temperature T_c, it is found that epitaxial strain induces the formation of a variety of closure- and in-plane domain morphologies. The local strain and ferroelectric-antiferrodistortive coupling at the film surface vary for the strain mediated transition sequence and this could offer a route for experimental observation of the morphologies. Remarkably, a new nanobubble domain morphology is identified that is stable in the high-temperature regime for compressively strained $PbTiO_3$. It is demonstrated that the formation mechanism of the nanobubble domains morphology is related to the wandering of flux closure domain walls, which is characterised using the hypertoroidal moment. These results provide insight into the local behaviour and dynamics of ferroelectric domains in ultrathin films to open up potential applications for bubble domains in new technologies and pathways to control and exploit novel phenomena in dimensionally constrained materials.

The results in this Chapter have been partly discussed in J.B.J.Chapman, A.V.Kimmel & D.M.Duffy, Physical Chemistry Chemical Physics **119**, 4243 (2017).

5.1 Introduction

Domain walls in thin films have shown promising functionalities, such as induced electric and magnetic properties, and the formation of unusual controllable phases that are not observed in the bulk samples [171–174]. Recent direct observation of so-called *wandering* domain walls in thin films [175], whereby the direction of the domain wall tangent significantly varies along the wall length, and the ability to control the direction of the domain wall suggests viable mechanisms for tuning intrinsic ferroelectric and piezoelectric properties [176, 177]. Figure 5.1a shows an example of domain wall wandering by continuous dipole rotation recently observed in PZT using aberration corrected transmission electron microscopy [175].

The orientation of the polarisation in ferroelectric films is influenced by a delicate balance between the epitaxial strain and screening of the depolarising field. The misfit strain from growth substrates has been shown to promote exotic polar orientations that are not observed in bulk samples [36, 37]. The pioneering theoretical investigation by Pertsev *et al* consisted of a thermodynamic phenomenological analysis assuming single domain structures under short-circuit[1] boundary conditions for (001)$PbTiO_3$ films [36, 37]. The eponymous Pertsev (misfit-strain vs temperature) diagram revealed large compressive strains stabilise the c-phase ($P_x = P_y = 0; P_z \neq 0$) whilst tensile strains reorientate the polarisation in-plane along $\langle 110 \rangle$ ($P_x = P_y \neq 0; P_z = 0$). This single phase behaviour was reproduced with DFT [178].

Compensation of the intrinsic depolarising field through screening has

---

[1] Depolarising field $\mathcal{E}_d$ partially screened

been shown to induce the formation of novel ordered domain structures [179]. A rich variety of new closure domain morphologies, such as Landau-Lifshitz stripe domains [152,180], vortex and triclinic domains [5], have been predicted in $PbTiO_3$, and $BaTiO_3$ thin films under open-circuit[2] boundary conditions using density functional theory, effective Hamiltonian and inter-atomic potential models [181, 182]. Tantalising experimental evidence for these closure domains in platlets and dots of $BaTiO_3$ has been presented in the form of 90° stripe super-domains bifurcated by 180° domain walls [78, 183, 184] and recent direct observation of vortices in $PbTiO_3/SrTiO_3$ superlattices [185] (Figure 5.1b). Similar investigations into PZT ultrathin films have revealed supplementary novel phases showing the strong interplay between strain, dipole, antiferrodistortive and alloying degrees of freedom, offering a diverse range of properties for strain engineered electronics [66, 180, 186].

The insight into the atomistic mechanisms of formation of dense domain morphologies is fundamentally and industrially important for the next generation of emergent technologies. Density functional theory (DFT) calculations have been extensively applied to various ferroelectric materials and these have provided fundamental insight into the origin of ferroelectricity, domain wall behaviour, grain boundaries and interfacial phenomena [187–190]. However, extrapolation of the theoretical results of domain morphologies to experimental length scales, for direct verification of any predicted effects, is inhibited by the scaling limits of the ab initio methods. Further, any modelling of domain wall dynamics at DFT level is computationally challenging since this requires large ensembles and long computation times. Semi-empirical forcefields, parametrised to reproduce material properties, provide robust tools for modelling long timescale dynamics of many thousands of atoms and dense sampling of strain values to narrow the gap between simulation and experiment.

---

[2] Depolarising field $\mathcal{E}_d$ uncompensated

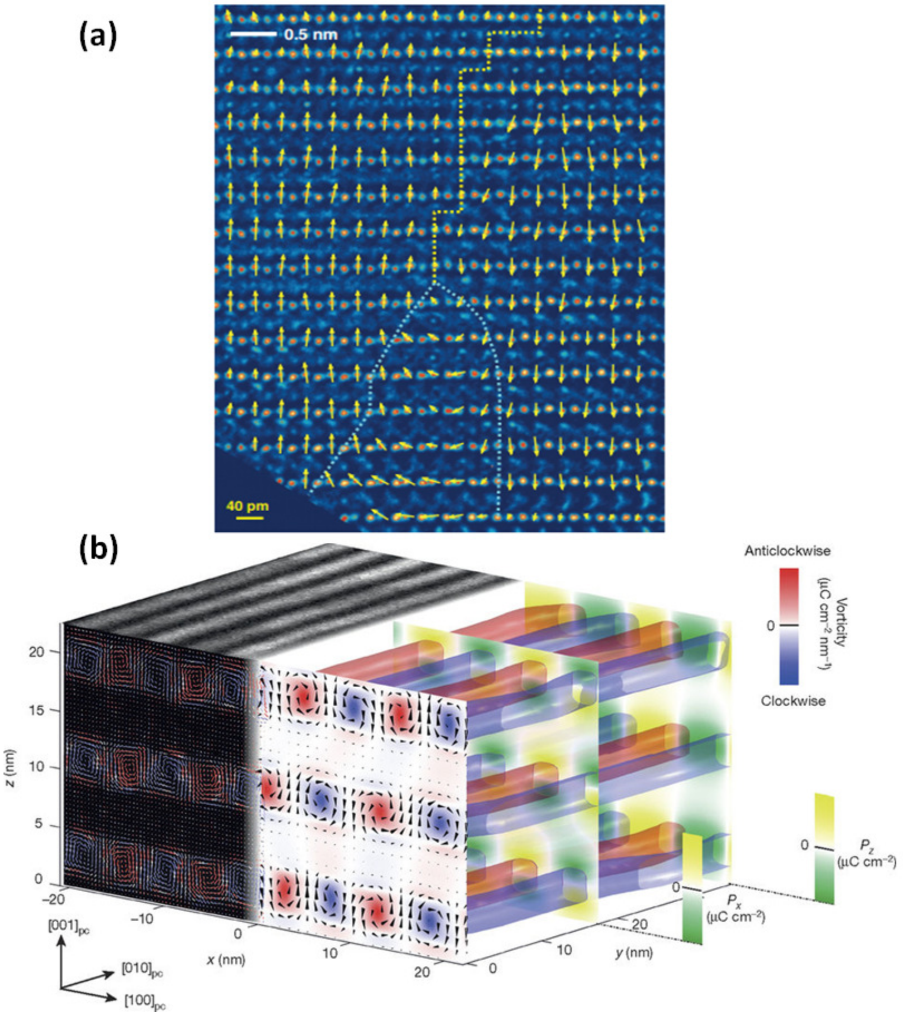

Figure 5.1: Experimental evidence of flux-closure domains in ferroelectrics. (a) Continuous dipole rotation in PZT observed using abberation correction transmission electron microscopy from Ref. [175]. (b) Vortex domains in a PbTiO$_3$/SrTiO$_3$ superlattice observed using high-resolution scanning transmission electron microscopy and modelled with a phase-field simulation from Ref. [185]. Figures (a) and (b) have been reproduced with permission from Nature Publishing Group and the American Association for the Advancement of Science, respectively.

In this Chapter, the domain morphologies formed in PbTiO$_3$ films are modelled using molecular dyanamics, calculating the misfit-strain – temperature (Pertsev diagram [36]) of symmetrically terminated PbTiO$_3$ films for a wide range of strain and temperature values (§5.3). In Section 5.4 the dielectric response of the $PbTiO_3$ films is investigated. Ferroelectric-antiferrodistortive coupling at the film surfaces and polarisation channels at domain wall confluences are identified in Section 5.5. Remarkably, a new nanobubble domain morphology is discovered that is stable in the high-temperature regime which is characterised in Section 5.6.

5.2 Simulation Methodology

Properties of strained (001)$PbTiO_3$ ultrathin films under open circuit conditions are studied using molecular dynamics as implemented in the DL_POLY code [132]. The adiabatic core-shell forcefield derived in Gindele *et al* is used which reproduces the structural parameters of the cubic and tetragonal phases, the Born effective charge tensors, the elastic properties and soft phonon modes of $PbTiO_3$ in excellent agreement with density functional theory (DFT) calculations [23]. Furthermore, the model correctly describes the enhanced antiferrodistortive c(2x2) surface relaxation of $PbTiO_3$ in agreement with ab initio calculations [156, 157] (see §4.2).

We use a large supercell of size $10 \times 10 \times 10$ (z=10 layer PbO only) to create a symmetrically terminated ferroelectric slab containing 4700 atoms (and larger in some cases, explicitly mentioned) with three dimensional periodic boundary conditions. A 100 Å vacuum gap in the growth direction $[001]_p$ was imposed on the system so the film is continuous and infinite along the pseudocubic $[100]_p$ and $[010]_p$ directions.The homogeneous biaxial misfit strain was defined as

$$\eta = \frac{a_s}{a_f} - 1 \tag{5.1}$$

where a_f is the cubic lattice parameter at the Curie temperature T_c. The properties of the system were calculated at different values of strain via variation of the effective substrate lattice parameters a_s in the range $3.8 <$

$a_s < 4.05$ (Å). The misfit strain was imposed by a Nosé-Hoover canonical (NVT) ensemble with a 10 fs relaxation constant. For each misfit strain the system was heated over a temperature range of 25< T <1000 (K) in 25 K increments; equilibrated at each temperature for 20 ps using a 0.2 fs timestep, with statistics gathered over a subsequent 60 ps production run. To confirm the consistency of our results we repeated several calculations using random selections of misfit strains within a set of larger systems ($10 \leq N_{x,y} \leq 26$). We note a small variation (within 10%) of the temperature and strain values of phase changes with larger systems and attribute this to the competitive energy balance between an increase of the domain volume against the domain wall area.

The initial slab configuration was prepared to include two anti-aligned *out-of-plane* ideal Kittel domains with imposed ferroelectric displacements within each domain. To satisfy periodic boundary conditions the film contained two domain walls centred on the PbO(100) planes whose surface normal was parallel to the pseudocubic $[100]_p$ direction.

5.3 Misfit-strain –vs– Temperature

Figure 5.2a presents the results of the observed domain morphologies over the full temperature and strain range considered. Our results are in excellent agreement with observations from other theoretical methods [176, 191] so we adopt the nomenclature of Jiang *et al* whereby a,b,c label principle axes along which the polarisation is finite. A superscript d indicates the out-of-plane polarisation is in the form of periodic domains. The definition of each phase in relation to behaviour of the local and macroscopic polarisation is summarised in Table 5.1 and characterised from the polarisation profile which is shown in Figure 5.2b for $\eta = -2.25\%$. We note our misfit strain phases are broadened consistently by a factor of 2 with respect to the those observed by the effective Hamiltonian approach [176]. This

Domain	Total Polarisation	Local Polarisation
$\mathbf{c^d}$	$P_x = P_y = P_z = 0$	$P_z^j \neq 0$
$\mathbf{bc^d}$	$P_x = P_z = 0, P_y \neq 0$	$P_z^j \neq 0$
$\mathbf{abc^d}$	$P_x \neq P_y \neq 0, P_z = 0$	$P_z^j \neq 0$
$\mathbf{aac^d}$	$P_x = P_y \neq 0, P_z = 0$	$P_z^j \neq 0$
aa	$P_x = P_y \neq 0, P_z = 0$	$P_z^j = 0$
p	$P_x = P_y = P_z = 0$	$P_z^j = 0$
(†)	$P_x = P_y = P_z = 0$	$P_z^j \neq 0,$ $P(x,y,z) \neq P(x,y',z)$

Table 5.1: Morphological definitions based on microscopic polarisations of each local unit cell P_k^j and the overall macroscopic polarisation $P_k = \sum_j P_k^j/N$. $P_z^j \neq 0$ is the criterion that the local out-of-plane polarisation can be non-zero, but due to the depolarising field $P_z = 0$ for all cases necessary from the open-circuit boundary conditions. The nomenclature of Jiang *et al* [176] is adopted whereby a,b,c label principle axes along which the polarisation is finite. A superscript d indicates the out-of-plane polarisation is in the form of periodic domains. The local polarisation criteria are not applied to the surface and 1st subsurface layers due to surface relaxations. (†) wandering domain walls which converge to produce $\mathbf{c^b}$ domains.

can partially be attributed to strong strain-polarisation coupling ($\propto P^2$) as this forcefield underestimates bulk polarisation by 40% [23].

We observe three distinct ferroelectric domain morphologies: **aa**, $\mathbf{c^d}$ and $\mathbf{abc^d}$ (shown in Figures 5.3, 5.4 & 5.6, of which we henceforth loosely refer to as phases). Between these distinct phases we find two strain induced transitional ferroelectric phases $\mathbf{bc^d}$ and $\mathbf{aac^d}$. A paraelectric phase **p** exists for all phases above the Curie temperature $T_c(\eta)$. The high symmetry paraelectric phase **p** is indicative of short range forces becoming increasingly favourable at high temperature and exists across all values of misfit strain. The paraelectric transition temperature is dependent on misfit strain but the minimum value occurs for freestanding films ($\eta = 0$). Remarkably, in addition to the three distinct phases, we have identified a fourth previously unreported misfit-strain domain phase at high temperatures which we refer to as nanobubble domains $\mathbf{c^b}$.

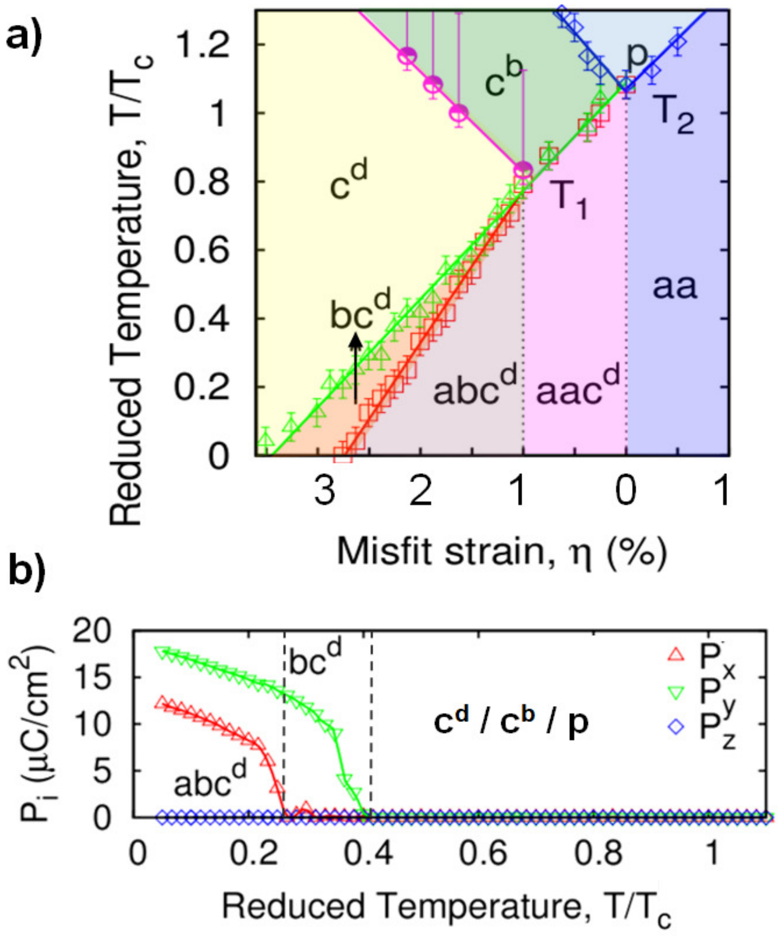

Figure 5.2: Domain morphology dependence on misfit strain and temperature. (a) Pertsev diagram for 3.8 nm thick (001)$PbTiO_3$ calculated using the core-shell model. (b) Macroscopic polarisation dependence on temperature for η =-2.25%.

5.3.1 aa Domains

Under tensile strain ($\eta > 0$) below the paraelectric transition temperature, with corresponding substrate lattice parameters $a_s > a_0$, the polarisation is oriented parallel to the substrate interface [178, 192]. Domains form with ordered regions polarised along the a and b principle axes separated via 90° domain walls (Figure 5.3). As the magnitude of the polarisation in each domain is equivalent, the domains are classified as **aa** and are similar to those presented by Kouser *et al* using a model Hamiltonian [191].

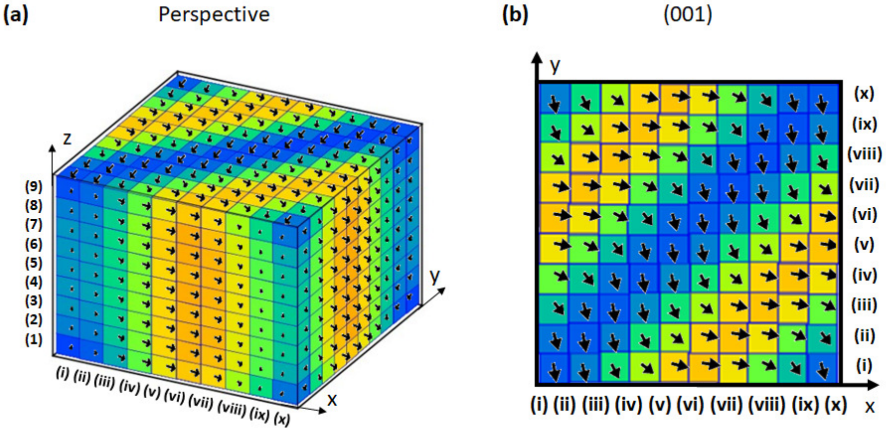

Figure 5.3: Representative **aa** domain pattern forming in $PbTiO_3$ thin films under tensile strain. Shown using a perspective view (a) and the top (001) surface (b), for $\eta = 0.5$ % at 300 K. Each cube represents a unit cell with the colour identifying the relative magnitude of P_x averaged over the 60 ps simulation. Local dipoles of the cross-sectioned surfaces are overlayed.

5.3.2 c^d domains

Under compressive strain ($\eta < 0$) we observe the formation of closure domains that consist of periodic 180° out-of-plane stripe domains $\mathbf{c^d}$ (Figure 5.4). This is consistent with experimental XRD results for $PbTiO_3$ films of similar thickness [69, 193] and $PbTiO_3/SrTiO_3$ superlattices [185, 194, 195]. Morphologically, these are *Landau-Lifshitz* domains having 90° closure domain *caps* at the surface as previously observed in theoretical studies of PbTiO$_3$ films using interatomic potentials [152, 196].

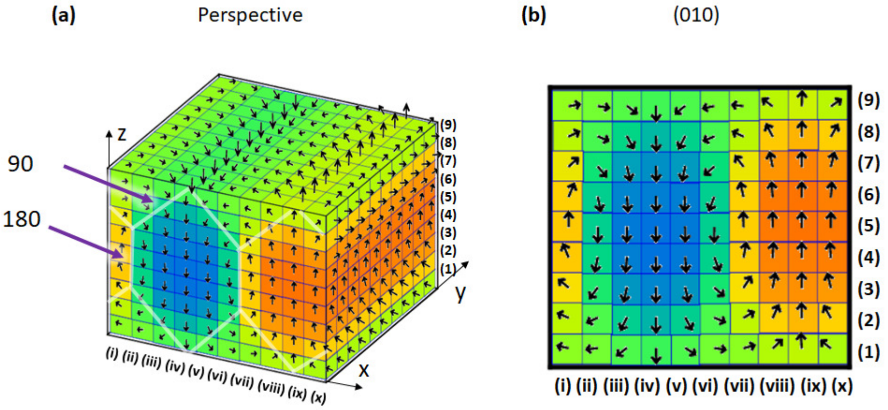

Figure 5.4: $\mathbf{c^d}$ domains. 300 K domain pattern of a 3.9 nm thick PbTiO$_3$ thin film simulated using a $10\times10\times10$ supercell under a compressive strain of $\eta = -2.25$ %. (a) perspective view of the supercell with white lines included to guide the eye to the domain walls and their confluences. (b) x-z cross-section. The colour of each unit cell represents the magnitude of the P_z component of the polarisation averaged over the calculation.

A film thickness dependence has previously been identified by Belletti *et al* for the $\mathbf{c^d}$ phase showing the 180° domain walls (see Figure 5.4a) to vanish into a vertex as the film thickness is decreased [152]. Our simulations reproduce this dependence which further validates our model (see Figure 5.5(i)). By comparing the configurational energy per unit cell when varying the supercell dimensions (N_x, N_y) and film thickness (N_z), we further demonstrate our model satisfies the Kittel scaling law (§2.5), obeying a linear dependence between the optimal domain width and the square root of the thickness (Figure 5.5). For films using $a_s = 3.905$ Å at 25 K the law is satisfied for $N_z \geq 5$ (001)PbO layers (2 nm) which returns a periodicity of 4.0 nm (domain width of 2.0 nm) in agreement with experimental observations [69].

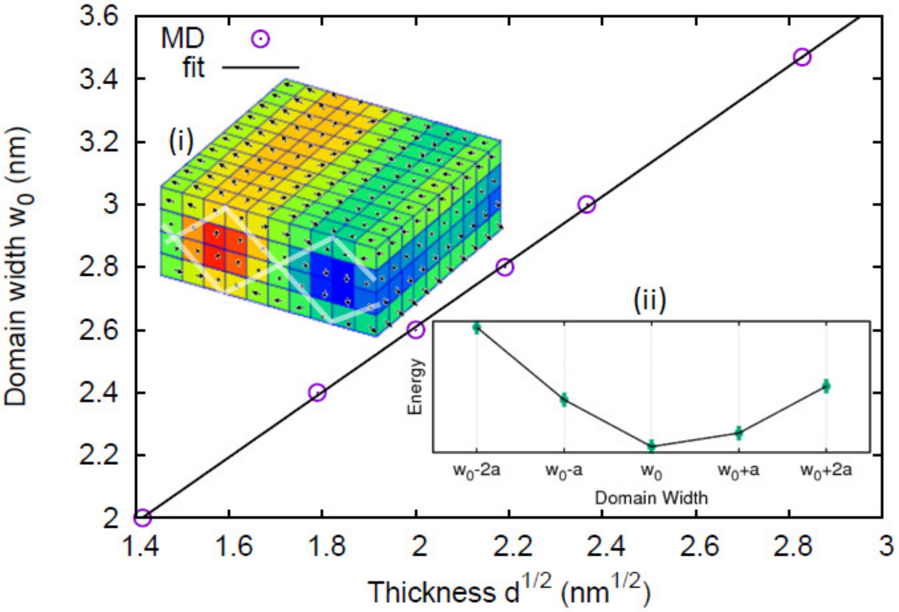

Figure 5.5: Observation of Kittel's scaling law, showing the optimal domain width w_0 is linearly proportional to the square root of the PbTiO$_3$ films thickness $d^{1/2}$. Subfigure (i) antichiral vortex domain pattern in 2 nm thick films. (ii) Energy profile for changes to the domain width, in increments of a unit cell a, for a fixed film thickness.

5.3.3 $\mathbf{abc^d}$ and Transitional Domain Morphologies ($\mathbf{bc^d}$ and $\mathbf{aac^d}$)

Under sequentially decreased compressive strains, components of polarisation can condense, first parallel to the domain walls and then parallel to the domain periodicity (Figure 5.2) forming $\mathbf{bc^d}$, $\mathbf{abc^d}$ and finally $\mathbf{aac^d}$ domains through second order transitions. For each of these domains, out-of-plane stripe domains persist with the additional components superimposed. The x-z profile of the $\mathbf{bc^d}$ is identical to that of the $\mathbf{c^d}$ (Figure 5.4).

For compressive strains between 1< η <3.75 (%) the P_x component also condenses forming $\mathbf{abc^d}$ domains (Figure 5.6). The symmetry breaking between the P_x and P_y critical temperatures (Figure 5.2b) occurs due to the requirement for dipoles to reorientate to form the closure domains parallel to the direction of domain periodicity [176, 191]. Our simulations show that the 180° domain walls of the adjacent $\mathbf{bc}^d$ phase collapse into to a vertex creating infinitely long cylindrical *chiral tubes* [186] as the polarisation parallel to the domain periodicity (P_x) stabilises further reducing the symmetry. This is consistent with observations in theoretical studies on PZT films [186]. Further to previous investigations, we observe that these chiral tubes propagate towards the film surface as the epitaxial compression is reduced.

Our model shows a critical misfit strain of 1% upon which the chiral tubes reach the surfaces of the film and *dissipate*, equalizing the macroscopic in-plane polarisation components whilst maintaining distinct out-of-plane stripe domains, $\mathbf{aac^d}$ domains. The $\mathbf{aac^d}$ domains have a similar cross-section to the $\mathbf{abc^d}$ domains in Figure 5.6 with the quantitative exception $P_x = P_y$ and the loss of the chiral centres such that there is no remnant of the 90° domain caps (which still exist for the $\mathbf{abc^d}$ domains observable in Figure 5.6 above the chiral centre pointer). For compressive strains in the range $0 < \eta < 1$ (%) the magnitude of P_z in the $\mathbf{aac^d}$ domains

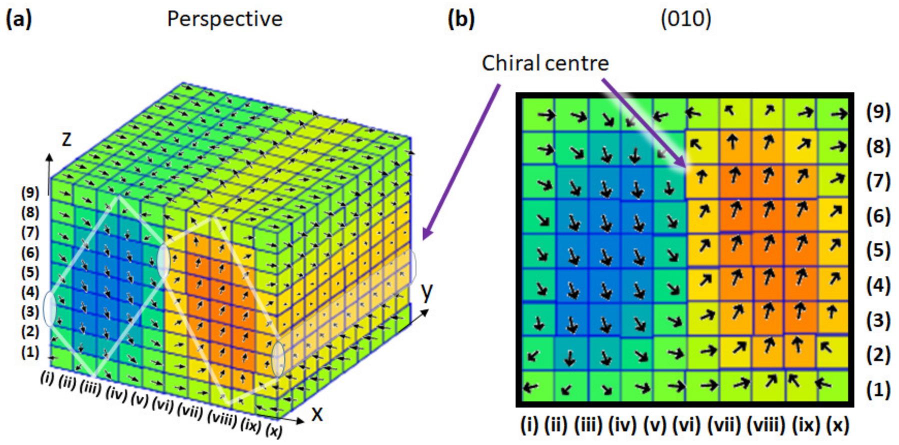

Figure 5.6: $\mathbf{abc^d}$ domains in $PbTiO_3$ films under a compressive strain of $\eta = -2.25$ % at 25 K. (a) Perspective view with the chiral centre and domain structure emphasised. (b) x-z cross-section. Each unit cell is represented by a cube whose colour is proportional to the time averaged P_z component of the polarisation.

reduce continuously to a limiting vanishing point of freestanding films upon which the **aa** domain pattern is recovered. Second order transitions of the polarisation by means of continuous dipole rotation with the local structure transitioning through low symmetry triclinic phases, such as we observe, have been been identified in an effective Hamiltonian simulation on PZT subjected to variations in the depolarising field strength [179].

5.4 Dielectric Response

To reduce the error in our domain transition temperatures we evaluate the characteristic dielectric response of the films as it is known that susceptibility of ferroelectrics exhibits a divergent Curie-Weiss behaviour at the phase transition temperature. The susceptibility $\chi_{\alpha\beta}$ and dielectric $\epsilon_{\alpha\beta}$ tensors are calculated from fluctuations in the total polarisation using equation 4.14 [168, 197].

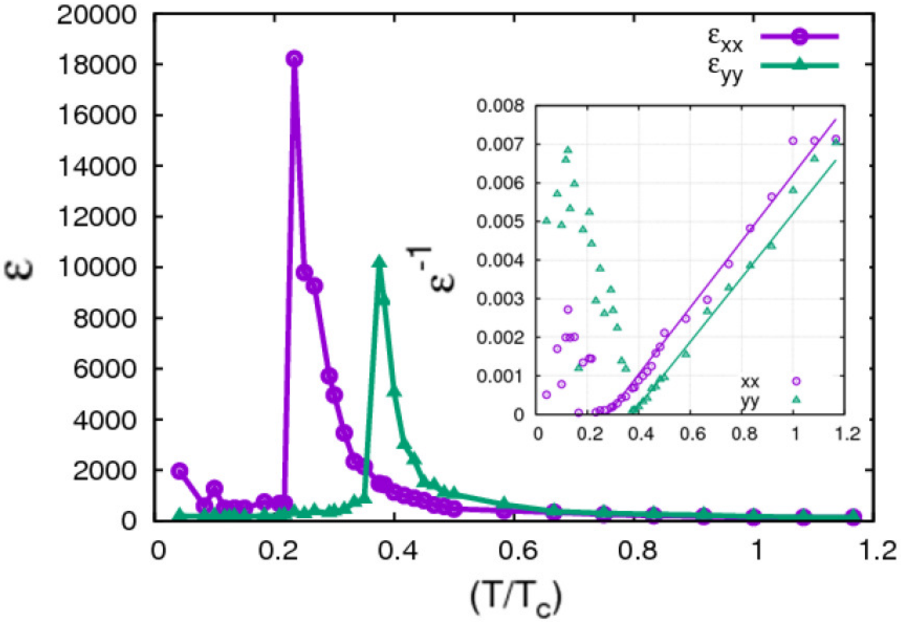

Figure 5.7: Temperature dependence of the static dielectric constant of a $PbTiO_3$ film for $\eta = -2.26\%$ identifying transition to different ferroelectric domains. A divergent response is observed for the $\mathbf{c^b} \rightarrow \mathbf{bc^d}$ transition (ϵ_{yy}) and $\mathbf{bc^d} \rightarrow \mathbf{abc^d}$ (ϵ_{xx}) transitions. Inset: Inverse dielectric constant with linear extrapolation from the high temperature response providing a more accurate estimation of the domain *phase* transition temperatures.

We find that both the $\mathbf{c^d} \rightarrow \mathbf{bc^d}$ and $\mathbf{bc^d} \rightarrow \mathbf{abc^d}$ transitions are accompanied by large dielectric response. Indeed, Figure 5.7 shows asymptotic behaviour for χ_{xx} and χ_{yy} corresponding to the condensation of P_x and P_y components, respectively.

The transition temperature between the domain phases are then determined from the linear high temperature dependence of the inverse dielectric constant ϵ^{-1} (Figure 5.7-inset). For $\eta = -2.26\%$ shown in Figure 5.7, the transition temperatures from the extrapolation are $0.27T_c$ and $0.36T_c$ for the $\mathbf{bc^d} \rightarrow \mathbf{abc^d}$ and $\mathbf{c^d} \rightarrow \mathbf{bc^d}$ transitions, respectively, with an uncertainty of $\pm 4.4\%$. Our studies are performed for the system under open circuit electrical boundary conditions which results in the presence of a strong depolarising field. The latter prevents the formation of an out-of-plane dielectric response ($\epsilon_{zz} = 0$). A corresponding increase in χ_{zz} would be expected for imperfect screening approaching the Curie temperature [191].

Historically, local dielectric properties have been overlooked in ferroelectric literature owing to the experimental challenges with characterisation. However, two recent reports have shown exciting prospects utilising local dielectric phenomena. In a MD study [198], it was observed that static 180° domain walls can increase the total dielectric response of $BaTiO_3$ by almost a factor of two. This is contrary to the long standing doctrine that susceptibility arises from intrinsic contributions from changes in the polarisation of the bulk of the domain [199, 200], and secondary extrinsic contributions from domain wall motion induced by applied stimuli such as an electric field or mechanical stress [201–203]. Further, a joint experiment and MD study on $PbTiO_3/SrTiO_3$ superlattices has observed conditions upon which the capacitance becomes negative [204]. The controversial concept of negative capacitance has been proposed to overcome the power consumption limits of field effect transistors [205]. Consequently, it is important to report the local dielectric behaviour of the $PbTiO_3$ film with its different domain morphologies.

An advantage of the MD model used in this investigation is the local dielectric permittivity tensor for each unit cell j can be calculated using an analogous fluctuation formula which has been numerically validated for homogeneous and inhomogeneous structures with different dimensionlities [206, 207]:

$$\chi^j_{\alpha\beta} = \frac{\langle v^j \rangle}{\epsilon_0 k_B T}(\langle P^j_\alpha P^j_\beta \rangle - \langle P^j_\alpha \rangle \langle P^j_\beta \rangle) \approx \epsilon^j_{\alpha\beta} \tag{5.2}$$

where k_B, T and ϵ_0 are the Boltzmann constant, simulation temperature and permittivity of free-space, respectively and $\langle v^j \rangle$ is the time-averaged volume of the unit cell. α and β correspond components of the basis vector having labels of x, y or z which define the tensor element. P^j is the local polarisation of unit cell j and $\langle \cdots \rangle$ defines a time average over the simulation.

As for the bulk permittivity, the high-frequency (optical) susceptibility χ_∞ is negligible in relation to the static component.

Each component of the local susceptibility (row) is shown in Figure 5.8 at four different temperatures (column) having domain pattern $\mathbf{abc^d}$ at $0.05T_c$, $\mathbf{bc^d}$ at $0.3T_c$ and $\mathbf{c^d}$ at both $0.38T_c$ and $0.5T_c$. An x-z cross-section of the film is shown in each instance with with the averaged local polarisation vectors superimposed. The value of the susceptibility is averaged through $[010]_p$.

It was shown in ref. [204], that the negative capacitance arose despite the local non-shear susceptibilities always remaining positive. Our results similarly show that for each domain pattern, the diagonal components of the susceptibility remain positive at all temperatures and each unit cell. The controversial negative capacitance was identified to occur due to regions where the local susceptibility was far more responsive than the overall system [204]. For the superlattices, this occurred only in the PbTiO$_3$ layers and predominantly near the PbTiO$_3$-SrTiO$_3$ interface. In the PbTiO$_3$ films presented in this thesis, we observe that for each domain morphology, enhanced susceptibilities occur at domain walls and their confluences such as the chiral centre. The shear components are an order of magnitude smaller than the diagonal so are unlikely sources of negative capacitance but have been included for completeness. For the diagonal components, at each temperature the susceptibility of the domain is small in comparison to along the domain walls. This identifies the static domain walls have a significant, and even dominating, contribution to the overall dielectric property of the film supporting the recent claims in ref. [198].

The largest enhancements in ϵ_{xx} and ϵ_{yy} unsurprisingly occur at temperatures near the $\mathbf{abc^d} \rightarrow \mathbf{bc^d}$ and $\mathbf{bc^d} \rightarrow \mathbf{c^d}$ transitions, respectively. This coincides with the divergences in the total susceptibilities upon the transitions (Figure 5.7). In both cases, the enhancement occurs at the 180° domain wall separating the out-of-plane domains having a susceptibility

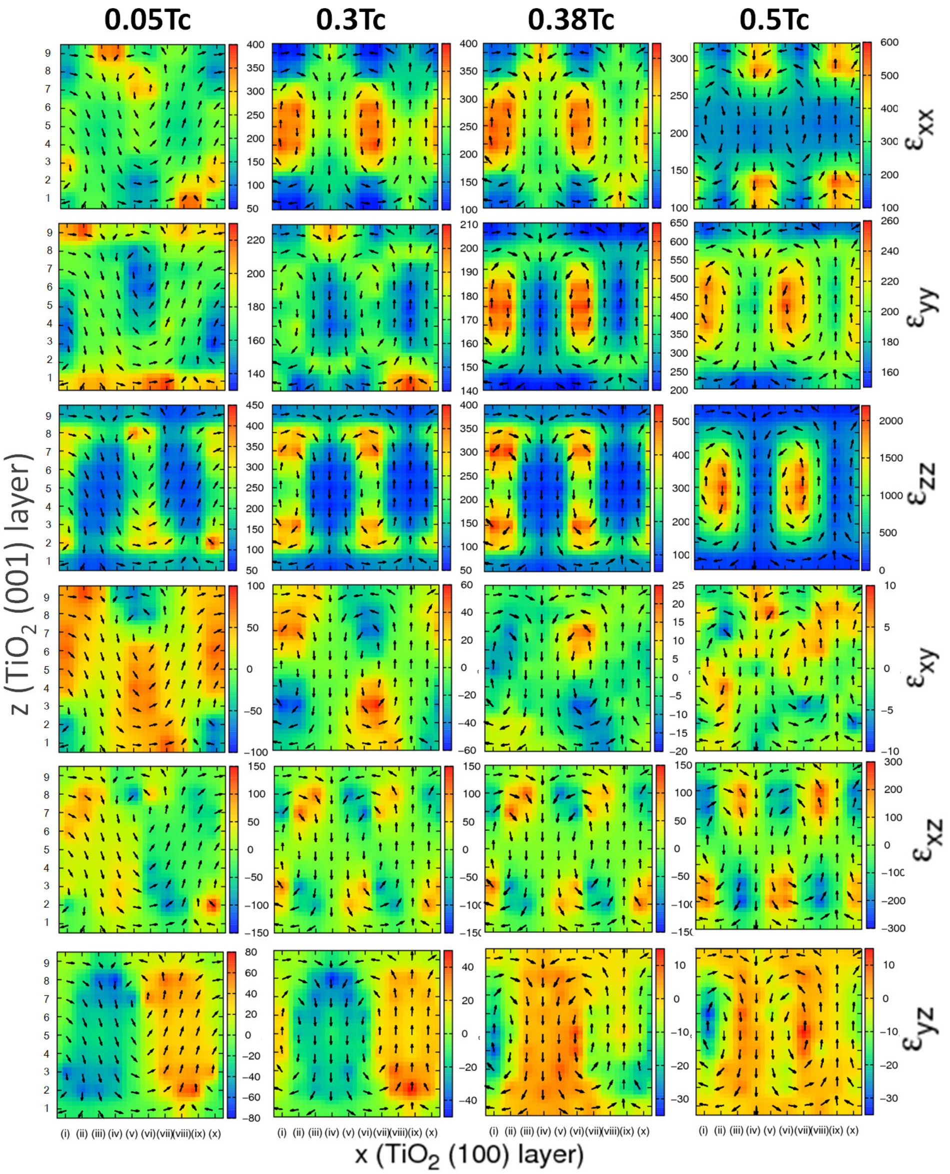

Figure 5.8: Local dielectric response in compressively strained $PbTiO_3$ thin films. The coloured contour map of each row identified the magnitude of the susceptibility for each component of the dielectric tensor (rows) at different temperatures (columns). The polarisation of each unit cell of the x-z cross-section are shown as unit vectors.

typically 2-4 times greater than the bulk of the domain. This identifies polarisation frustration at the domain wall and the likely nucleation site of the domain transitions.

In the $\mathbf{bc^d}$ and $\mathbf{abc^d}$ domain morphologies, ϵ_{zz} is largest for unit cells supporting a predominantly in-plane polarisation. As the temperature is increased, the enhancement moves from the 180°-90° domain wall confluence into the 180° domain wall. The susceptibility at the domain wall then increases substantially with temperature. This is a direct consequence of the overall domain pattern persisting but dipole magnitudes reducing, resulting in weakened long-range correlation and larger fluctuation amplitudes.

The identification of significant enhancements of different components of the susceptibility within the PbTiO$_3$ identifies new possibilities for the search for negative capacitance. Further to ref. [204] observing enhanced susceptibility in PbTiO$_3$ near the SrTiO$_3$ interface in superlattices causing negative capacitance, we identify that regions with rapid changes in dipole direction such as domain walls and their confluences have significantly enhanced susceptibilities relative to the rest of the film. This realisation opens possibilities of tuning the value of the capacitance by controlling the dipole frustration by shaping domain walls and, in doing so, changing the local susceptibility and therefore capacitance. Further, the polarisation frustration creating the enhanced dielectric properties could provide insight into Landauer's paradox [83], whereby calculations of single domain switching estimate an implausibly large nucleation barrier on the order of $10^8 k_B T$, far greater than values measured in experiment. These results show that local dipoles on surface layers of the PbTiO$_3$ that are parallel to the surface normal also have an associated anomalously large susceptibility, typically in ϵ_{xx} and ϵ_{yy}. Therefore, when screening is incomplete, these dipoles have substantial fluctuation amplitudes which will reduce the depolarisation energy, and therefore nucleation barrier due to equation 2.34, at these sites.

5.5 Novel Properties of bc$^\mathbf{d}$ and abc$^\mathbf{d}$ Domains

Theoretical studies have previously shown PbTiO$_3$ films to have different critical temperatures of the in-plane components of macroscopic polarisation [176, 191]. This results in the **abc$^\mathbf{d}$** → **bc$^\mathbf{d}$** → **c$^\mathbf{d}$** transition sequence under the compressive strain regime, but knowledge of the behaviour of the local polarisation within each domain remains limited. To address the lack of knowledge about the polar behaviour with domain morphology we have analysed the in-plane components of polarisation within each of the closure domain morphologies ($\eta < 0$) at $\eta = -2.15\%$.

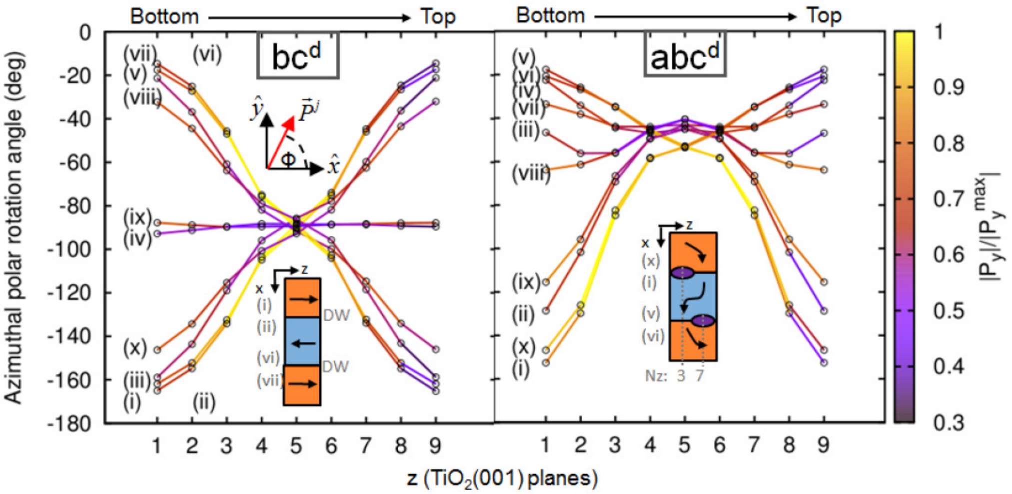

Figure 5.9: In-plane polarisation angle ($\phi = \tan^{-1}(P_y/P_x)$) and relative intensity of local polarisation chains in different PbTiO$_3$ domain morphologies confirming the domain wall in **bc**^{d} and chiral centre in **abc**^{d} domains are vortex centres in films. Bracketed Roman numerals index the unit cell column relative to the domain walls as defined in Figures 5.4 & 5.6 for each morphology. TiO$_2$ stack layers 1 and 9 are the rows of unit cells on the bottom and top surfaces, respectively. $[010]_p$ polarisation maximised through 180° domain walls and the chiral centres.

In the **bc$^\mathbf{d}$** domain phase, our simulations reveal the in-plane dipole rotations are not homogeneous throughout the film. The P_y component (perpendicular to both the domain wall and surface normals), has a maximum value within unit cells constituting the domain walls (cell stacks (i), (ii), (vi) and (vii) in Figure 5.9a) and reduces sharply for cells further from the domain wall, re-orientating along the *c*-axis at the centre of the film away from surface effects. The polar rotations at the surface layers act to change the anisotropy, forcing the domain walls to be more characteristic of magnetic Bloch-Néel walls than the distinctly Ising form in bulk [208]. Evidence for the existence of mixed Ising and Bloch-Néel character domain walls in ferroelectrics has recently been proposed in $PbTiO_3$ and $LiNbO_3$ from *ab initio* calculations [209]. Such dipolar rotations can cause band bending of the conduction states across the domain wall and may be a contributory cause for recent experimental observations of conductive domain walls [210].

We further identify the P_y component of local polarisation in the $\mathbf{abc^d}$ domains have a maximum magnitude about the chiral centres producing concentric tubes of increasing in-plane ferroelectricity (Figure 5.9b). The $\mathbf{c^d}$ domains exhibit no macroscopic or local polarisation parallel to $[010]_p$, only supporting rotations tangent to the $(010)_p$ plane which are required to close flux at surface layers.

The coupling between antiferrodistortive (AFD) rotations and the local dipole moments are rarely investigated, yet such interactions have been shown to influence Curie temperatures and phases that can produce improper ferroelectrics [180,211]. It has recently been proposed that control of AFD chiralities could be used in novel technologies such as four-state memory making the identity of methods to control AFD behaviour at atomic scales paramount [212]. Here, we demonstrate the effects of ferroelectric-antiferrodistortive coupling between the c(2x2) AFD surface reconstruction and the ferroelectric (FE) closure domain patterns at the surface of the $PbTiO_3$ film [156,157]. This is characterised by the rotation of the equatorial oxygen atoms about the titanium, with simultaneous out-of-plane distortions which vary along the direction of the domain wall normals $[001]_p$. The TiO_6 octahedral rotations are averaged over the full trajectory and through $[010]_p$, and are presented in Figure 5.10a for the $\mathbf{c^d}$, $\mathbf{bc^d}$ and $\mathbf{abc^d}$ domain configurations along both the surfaces.

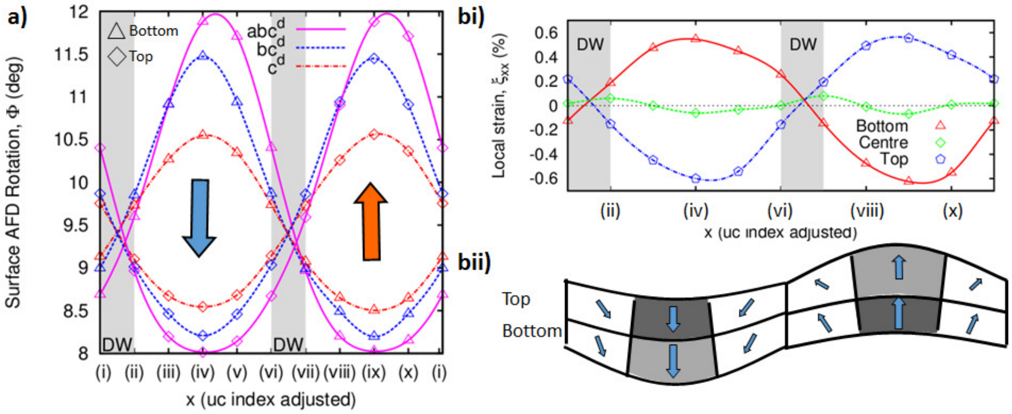

Figure 5.10: FE-AFD coupling on the surface of a 3.8 nm thick $PbTiO_3$ ultrathin film with different ferroelectric closure domain configurations. (a) Rotation angle (Φ) on the top (diamond) and bottom (triangle) surfaces for each closure domain configuration. The arrows represent the out-of-plane domain orientation. (bi) Local strain along the top surface (pentagon), bottom surface (triangle) and centre (diamond) of the film with the $\mathbf{c^d}$ domain morphology. (bii) Cartoon illustrating the local strain dependence on polarisation orientation at the top and bottom surface.

For the $\mathbf{c^d}$ domains a sinusoidal dependence is noted with a maximum rotation at the centre of the domain when the polarisation is pointing out-of-plane and minimised when the polarisation points into the plane (Figure 5.10a). Due to the symmetry of the domain pattern, the profiles of the rotation angle Φ for the top and bottom surface are identical, albeit inverted for any given point along $[100]_p$. The same relation has previously been noted for films with a $\mathbf{c^d}$ domain configuration modelled using a shell model which sampled three points along $[100]_p$ [152]. The angle variations for the other domain phases have not previously been reported, nor has direct explanation for the mechanism changing the rotation angle.

For both $\mathbf{bc^d}$ and $\mathbf{abc^d}$ the maxima and minima occur at the centre of the domains for the polarisation pointing out and in, respectively, although there is a slight shift in the absolute position along $[100]_p$ in the case of the $\mathbf{abc^d}$ domain due to change from 180° domain walls to chiral centres moving from the film centre and canting the domains (Figure 5.6). However, due to the change of symmetry of the domain patterns, at a given point along $[100]_p$ the top and bottom of the film no longer share inversion symmetry, breaking this relationship in the Φ profile. Further, the magnitude of the rotation increases upon transition into the successive domain phases ($\mathbf{c^d}$(red) $\rightarrow$ $\mathbf{bc^d}$ (blue) $\rightarrow$ $\mathbf{abc^d}$ (purple)).

A DFT study into the AFD modes of bulk $PbTiO_3$ has previously shown a direct strain dependence on the rotation angle, showing for strains larger than a critical value, the angle increases with tensile strain [213]. We show the local strain profile of a chain of unit cells along $[100]_p$ at the top, bottom and centre of the film in Figure 5.10b for the $\mathbf{c^d}$ phase. Comparison of the strain-profile to Figure 5.10a(red) shows a clear relationship between local strain and Φ, as is observed in bulk. Increases in local tensile strain enhance the rotation angle, whereas compressive strains suppress the rotation. A cartoon depicting the top and bottom surfaces is shown in Figure 5.10b(ii) demonstrating the strain-polarisation coupling acting as the mechanism promoting the variation in rotation angle. The transition from $\mathbf{c^d} \rightarrow \mathbf{bc^d} \rightarrow \mathbf{abc^d}$ occurs with positive increases in strain (at a fixed temperature, Figure 5.2a) revealing the cause for the increase in rotation angle with the domain phase sequence.

5.5.1 Phase Transition Mechanism from $\mathbf{c}^d$ to $\mathbf{bc}^d$

From the local unit cells calculated using the procedure in Chapter 4, the ideal coordinates of each atom can be calculated without a reference structure provided *a priori*. A useful metric for characterisation in comparison to bulk is the ferroelectric displacement of the titanium atoms. Since there is no practical reference structure from which the coordinates can be compared to, the ferroelectric displacement for a given Ti atom $\delta^{\mathbf{j}}_{\mathbf{Ti}}$ is approximated intrinsically as the displacement from the centrosymmetric coordinate defined by the midsection when tracing the lattice vectors $\mathbf{A^j}$ between Pb atoms. This is calculated as:

$$\boldsymbol{\delta}^j_{Ti} = \mathbf{r}^j_{Ti} - \left(\mathbf{r}^j_{Pb} + \frac{1}{2}\mathbf{A}^j\right) \tag{5.3}$$

where $\mathbf{r}^j_{Pb}$ is the position vector of the Pb atom in unit cell j closest to the coordinate origin and $\mathbf{r}^j_{Ti}$ is the position vector of the Ti atom.

In Figure 5.11a, the ferroelectric out-of-plane displacement of the titanium cores are given for each closure domain morphology, calculated within each local unit cell at the centre of the film ($N_z = 5$) and averaged through $[010]_p$. Only marginal changes[3] can be observed between the different domain phases which display the same behaviour as bulk 180° in tetragonal phase ferroelectrics (see Supplementary Figure E.2 for the ferroelectric displacements of 180° domains in bulk calculated using DFT). Necessarily, the transition from the $\mathbf{c^d}$ domains must arise from either in-plane ferroelectric displacements of the titanium cores or distortions to the corner linked network of oxygen octahedra. The octahedral rotation of the centre plane of unit cells has been calculated and averaged through $[010]_p$ (Fig. 5.11b). Transition from the $\mathbf{c^d}$ domain patterning to $\mathbf{bc^d}$ is found to correlate to the introduction of continuous cage rotations across the domains such that the maximal rotation occurs as a discontinuity at the domain walls (depicted in Fig. 5.11b-inset). This prominent cage rotation at the domain wall explains the introduction of a polar component along $[010]_p$ and the enhanced in-plane polarisation at the domain walls shown in Figure 5.10a.

---

[3] The method of calculation of the centrosymmetric coordinate provides an approximation based solely on the trigonal cell defined by the A-cation cores. As such, these small differences ($< 15\%$) are within the margin of error of the calculation.

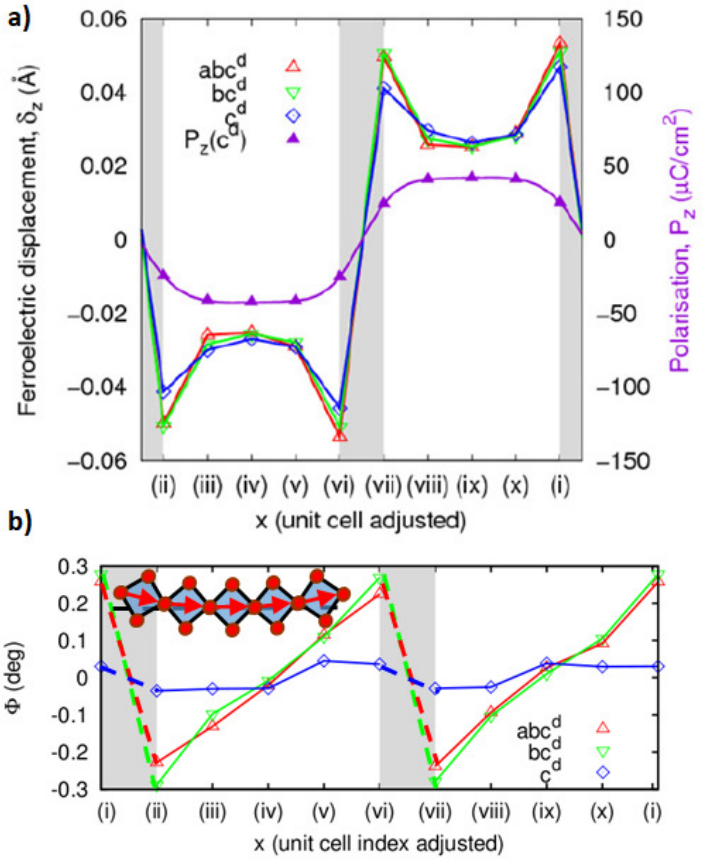

Figure 5.11: Properties at the centre of a 3.87 nm thick $PbTiO_3$ UTF, for each of the predicted ferroelectric closure domain morphologies. (a) Out-of-plane ferroelectric displacement of the $\mathbf{c^d}$, $\mathbf{bc^d}$ and $\mathbf{abc^d}$ domain patternings and polarisation profile of the $\mathbf{c^d}$. (b) In-plane octahedral cage rotations of the $\mathbf{c^d}$, $\mathbf{bc^d}$ and $\mathbf{abc^d}$ domains. Rotations are introduced upon the $\mathbf{c^d} \rightarrow \mathbf{bc^d}$ transition contributing to an enhanced P_y at the domain wall.

5.6 New High Temperature Nanobubble Domain Morphology

In addition to the previously predicted phases, our model finds an entirely new phase at temperatures above the $\mathbf{c^d}$ phase but below T_c. Our simulations show that in the compressive strain regime, in the vicinity of the effective Curie temperature, the homogeneity of the stripe $\mathbf{c^d}$ domains along the easy axis, the in-plane $[010]_p$ direction, breaks down. This is due to diffuse nucleation and growth of the reverse domain on the domain walls (Figure 5.12a), shown previously as a growth mechanism in bulk prototypical systems under an activation field using a Landau-Ginzburg-Devonshire model [90]. This first presents by the distortion of the 180° domain wall alignment with $(100)_p$ planes (Figure 5.12a-d), so-called '*wandering*' [175, 176]. Here we observed that, with further temperature increases leading to polarisation reduction, the degree of the anisotropy increases resulting in the domain wall pattern changing from linear stripe domains into *nanobubble domains* (Figure 5.12e). To confirm the prediction of this domain pattern, films of the same thickness were modelled using a larger simulation cell. Constructing the film using $26 \times 26 \times 10$ unit cells, the $\mathbf{c^b}$ domains were shown to persist, forming through the same mechanism and therefore not a consequence of the chosen supercell size (Figure 5.12 f-g).

The tendency for domain walls to wander emerges from the T_1 multiphase point in the Pertsev diagram increasing linearly with compression (Figure 5.2a). Once established, the nanobubble domains are shown to persist until $T_c(\eta)$. Similar arrays of nanoscale bubble domains have been predicted in PZT on the transition path between Landau-Lifshitz domains to a monodomain under an applied electric field at 10 K [179]. To our knowledge, these domains have not previously been identified in pure $PbTiO_3$ or for the condition of open circuit boundaries. The faceting instabilities of the nanobubble domains (Figure 5.12e-f) are analogous to those that occur

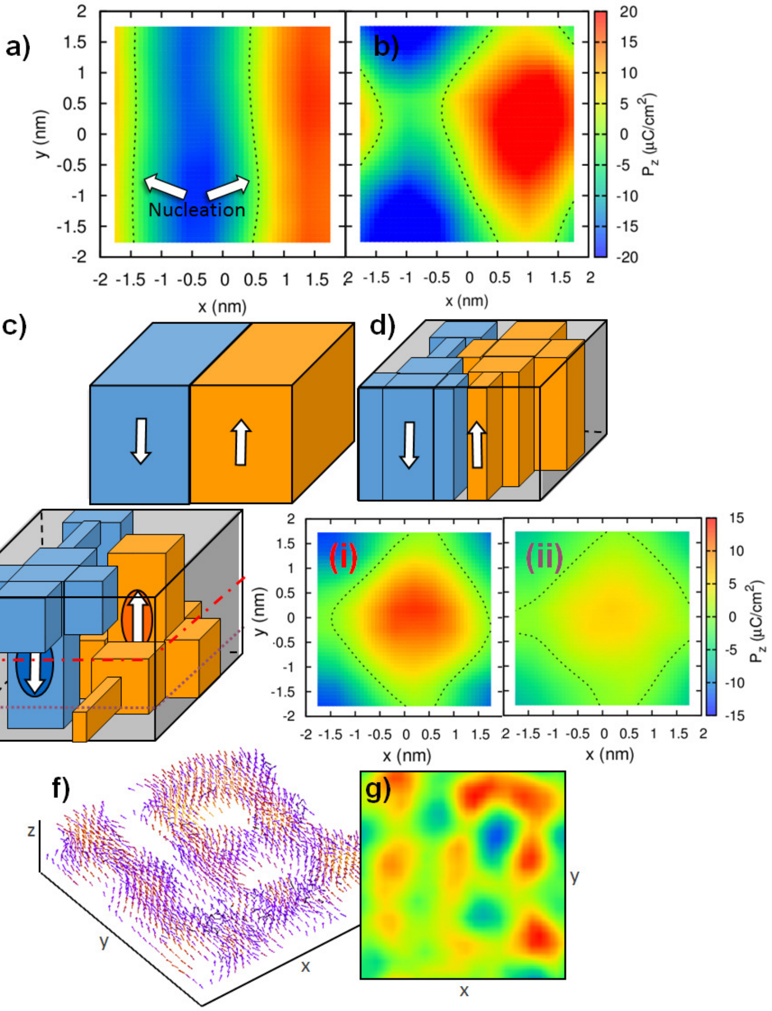

Figure 5.12: New ferroelectric domain morphology - nanobubble domains $\mathbf{c^b}$. Out-of-plane polarisation profile at the centre (N_z=5) of the $PbTiO_3$ film for (a) 180° domain wall along easy axis (b) wandering 180° domain wall. (c,d) Cartoons depicting the 180° domain wall structures near film centre. (e) Cartoon of the predicted $\mathbf{c^b}$ domain. Out-of-plane polarisation profiles from unit cells on the N_z=5 (i) and N_z=2 (ii) (001) planes of a $10 \times 10 \times 10$ simulation cell. Dotted lines define the interpolated $P_z = 0$ isoline. (f) Large scale simulation showing the local dipoles of $\mathbf{c^b}$ domains in compressively strained $PbTiO_3$ calculated using a $26 \times 26 \times 10$ cell containing 31772 atoms - for clarity only local dipoles with $P_z^j > 0$ are plotted leaving voids where $P_z^j < 0$. (g) Out-of-plane polarisation contour map of the centre (001) plane of (f) - red $P_z > 0$, blue $P_z < 0$.

from surface tension instabilities in thin magnetic films [214].

These high temperature bubble domains have since been experimentally verified by M. Gregg and A. Shilling in $25\mu m$ thick $BaTiO_3$ single crystals using piezoforce microscopy [215]. When successively cooled and heated across the Curie temperature, initially observed stripe domains ($\mathbf{c^d}$ domains reported in §5.3.2) were found to evolve into finely spaced bubble patterns of 180° domains polarised out of the surface plane strikingly similar to Figure 5.12g. Whilst the PFM was performed on a bulk crystal it is important to note that the domain pattern recorded on the surface via the PFM is not representative of that within the crystal. Instead, at the surface of the crystal the domains undergo a rearrangement within a *skin-layer*, limited in depth and indeed comparable to the thickness of the modelled thin film in this thesis. The existence of skin-layers in ferroelectrics were discovered by Kanzig [216] who determined a discrepancy in symmetry between the bulk and surface layer approximately 100 Å thick which acts akin to a thin film under compression. Gregg and Shilling used transmission polarised optical microscopy to show the bubble domain pattern persists in the skin-layer whereas ferroelastic domains exist in the bulk. Whilst the experiment observed these new bubble domains in $BaTiO_3$ and in this thesis they are predicted in $PbTiO_3$, it should be recognised that in both cases they are observed just below the Curie temperature T_c, in thin films and under compressive strain. This suggests these newly identified bubble domains are a general feature expected from tetragonal phase perovskite ferroelectrics (with a divalent A cation and tetravalent transition metal B cation).

The presence of nanobubble domains is generally difficult to detect as there is no change to the total polarisation (Figure 5.2b), nor is there an accompanied dielectric response (Figure 5.7). To address this difficulty a new order parameter, the hypertoroidal moment $\vec{h}$ (equation 4.13), was proposed in ref. [164]. Unlike the toroidal moment $\vec{T}$, which is physically interpreted as the average curl of the polarisation field, the hypertoroidal moment describes the average curl of the toroidal field. Therefore, it does not vanish for symmetries of twinned vortices such as the Landau-Lifshitz ($\mathbf{c^d}$) closure domains and yet it is sensitive to microscopic changes in polar ordering. Since $\vec{h}$ is multivalued for dimensionally constrained systems, dependent upon the choice of origin used to mimic the periodic supercell, we sample the surface of $\vec{h}$ for a set of supercells centred on coordinates corresponding to an xy scan of the central $(001)_p$ plane of the film. A similar procedure was first used to investigate the surface of the hypertoroidal moment for $PbTiO_3$ thin films with Landau-Lifshitz domains, switching due to strain gradients [152], where a sinusoidal dependence in h_z for the $\mathbf{c^d}$ domain configuration was shown as is found here (Figure 5.13a). Similarly, the turning points along $[100]_p$ correspond to the centres of the domains ($h_z(centre) = \pm|h_{z,max}|$) and the domain walls ($h_z(DW) = 0$) and therefore they have the same period as the underlying domain configuration.

For PZT films under an short circuit boundary conditions, the transition from closure domains to monodomains via nanobubble domains has been shown to correspond to an accompanying divergence in the hypertoroidal moment susceptibility [164] but the hypertoroidal moment surface for the domain morphology has not previously been characterised. Here, for the first time, we show the hypertoroidal moment surface for nanobubble ($\mathbf{c^b}$) domains (Figure 5.13b). The bubble domain cores correspond to the maxima (for the positively poled nanobubble) and minima (for the negatively poled nanobubble) in the surface of h_z. The origins of the hypertoroidal supercell corresponding to a vanishing moment agree with the $P_z = 0$ isoline in Figure 5.12e(i). As such we conclude the contours of the surfaces (a & b) show the hypertoroidal moment capable of characterising the polarisation distribution (Figure 5.12), supporting its proposed use as a suitable order parameter when the total polarisation remains unchanged.

Due to the domain transitions, wall wandering and multivalued prop-

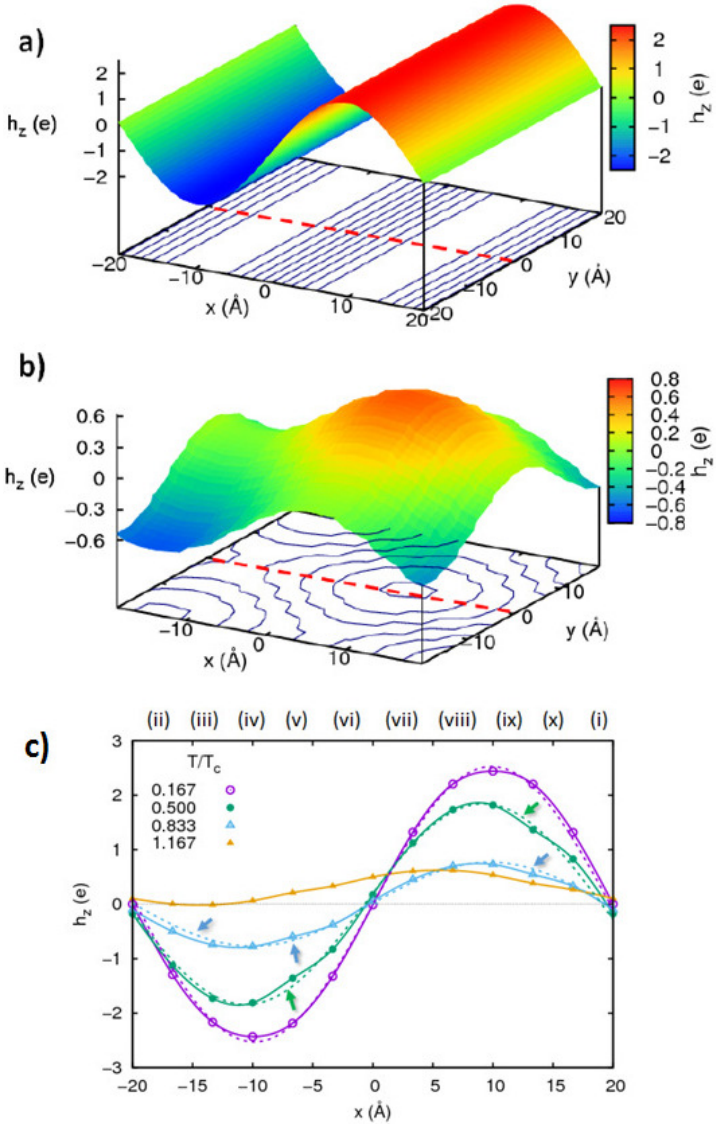

Figure 5.13: Surface of the out-of-plane component of the hypertoroidal moment (h_z) evaluated the central (001) plane of the PbTiO$_3$ ultrathin film for (a) $\mathbf{c^d}$ domain configuration (b) $\mathbf{c^b}$ domain configuration. (c) Cross section of the out-of-plane component of the hypertoroidal moment surface evaluated for domain configurations as a function of temperature. Data points correspond to supercell origins which centre on titanium coordinates in the simulation cell. The dotted lines are sinusoids of the form $h(x) = A \sin(2\pi x/L_x + \phi)$ fit by method of least squares to the h_z-surface cross-sections of the closure-domains. Arrows show kinks in the surface.

erty of $\vec{h}$, a common origin for the supercell used to mimic the periodic system cannot be defined. Therefore, to gain further insight into the temperature dependence, cross sections at $y_h = 0$ (see dashed line in Figure 5.13) are taken of the hypertoroidal moments surface at regular temperature intervals in Figure 5.13. The sinusoidal dependence of $\mathbf{c^d}$ is clearly evident at $0.167T_c$ but deformations to the sine wave are evident above $0.5T_c$, which is lower than the temperature at which deformations in the domain walls can start to be observed in the polarisation map (Figure 5.12a, $0.8T_c$). To guide the eye to these subtle deformations, a sinusoid (dotted) has been fitted to the h_z surface cross-sections. We assert that the kinks are evidence of small variations in the polarisation from the 180° walls into the domains, which lead to the wandering domain wall phenomenon.

5.7 Conclusions

In this Chapter, the domain morphologies which condensate under varying homogeneous strains and temperatures within ultrathin films of $PbTiO_3$ have been calculated using molecular dynamics with shell model interatomic potentials. We investigated the local behaviour of polarisation with the domains and identified a previously unreported high temperature nanobubble domain pattern. We have found that, in the vicinity of the Curie temperature, the 180° domain walls wander from the easy axis, leading to the formation of this new domain morphology. We characterised the nanobubble domains using the hypertoroidal moment surface (h_z) for the first time and showed that it can be used to identify minute changes in the polarisation profile which signalled the domain wall wandering. Ferroelectric-antiferrodistortive coupling was observed at the film surface. The rotation angle of the octahedral cages was determined to be dependent upon the local strain, increasing with tensile strain and consequently enhanced along the strain mediated transition sequence

$\Phi_{max}(\mathbf{c^d}) < \Phi_{max}(\mathbf{bc^d}) < \Phi_{max}(\mathbf{abc^d})$. Such surface properties provide a alternative means for experimental verification of the underlying domain structures.

In summary, the results from the forcefield calculations give unprecedented details about the response of the local polarization in ultrathin ferroelectric films to variations in strain and temperature, leading to the identification of a novel high temperature nanobubble domain pattern. Our studies provide guidance for the application of strain engineering to ultradense domain pattern construction.

6

$PbTiO_3/SrTiO_3$ Superlattices

In this Chapter, a model is developed to study the emergent technology of the piezoelectronic transistor (PET). Such devices have been proposed as an alternative to conventional metal-oxide-semiconductor (CMOS) transistors [98, 217], expected to operate at significantly higher speeds and lower power consumptions. A PET is constructed of a piezoelectric and a piezoresistor separated and sandwiched by electrodes. The piezoelectric expands when a voltage is supplied compressing the piezoresistor which becomes conductive from insulating [218]. In order to develop these devices, precise characterisation of the piezoelectric deformations are required at the nano-scale. Current experimental studies by our collaborators have investigated tetragonal $Pb(Zr_{0.2}Ti_{0.8})O_3$ (PZT) thin films epitaxially grown on a $SrTiO_3$ substrate, deposited with platinum electrodes and Focus Ion Beam milled into [001]-cross-sectioned films [218]. In their work, the PZT films are shown to exhibit a-c domains forming three different domain configurations, dependent on the inclination of the 90° domains, creating different rotation gradients or deformations. In this Chapter, the core-shell model is extended to be able to reproduce the set up of this screened epitaxial film, which provides direct atomic resolution of the deformations experimentally observed.

6.1 Derivation of Compatible Forcefield for use as a Dielectric Substrate

To model the experimental conditions, an additional perovskite forcefield is required to act as a dielectric substrate. Nb doped $SrTiO_3$ is commonly used for $Pb(Zr,Ti)O_3$ epitaxial films due to a good match of the lattice parameters of $SrTiO_3$ and excess charge carriers from Nb doping [218]. $SrTiO_3$ belongs to a class of ferroelectrics known as incipient or quantum paraelectrics [219] which also includes $CaTiO_3$ and $KTaO_3$. These materials are found to exhibit a high dielectric permittivity but the ferroelectric instability is suppressed by quantum fluctuations [220]. In Cochran's model [45], this is shown by the softening of the TO modes but they do not become stable. $SrTiO_3$ has a paraelectric cubic ($Pm3m$) phase and an AFD tetragonal phase condensing below 110 K [221] that occurs due to a soft mode at the R-point in the BZ [222]. Existence of a ferroelectric phase below 37 K is currently contested in recent literature [223, 224]. Further contention exists pertaining to the presence of soft modes, being real or imaginary, at different coordinates in the BZ. DFT using LDA predicts the TO modes at Γ to be real whereas both PBE and hybrid HSE06 expect these modes to be imaginary [225]. DFPT calculations using LDA with a planewave basis later revealed the ferroelectric Γ instabilities soften with increased volume whereas the AFD instability at R hardens [222].

We optimise the cubic structure of $SrTiO_3$ using the CASTEP package [112] with WC xc-functional [111], implementing a 2200 eV cut-off energy[1] to the planewave basis and sample the BZ using an $8 \times 8 \times 8$ MP grid. Forces and stresses are minimised below a tolerance of 1 meV/Å and 1 kPa, respectively. The properties of the cubic phase are given in Table 6.1. The phonon dispersion curve has been calculated for the cubic phase using

---

[1] The large cutoff energy is due to the use of a norm-conserving pseudopotential which are notoriously 'hard' for both O and Ti.

Gonze's variational method of DFPT with the WC xc-functional, norm-conserving pseudopotentials and using a $4 \times 4 \times 4$ special q-point mesh shifted by (0.25,0.25,0.25) to include the Γ-point shown in Figure 6.1.

The calculated lattice parameters of both phases are in good agreement with experiment when extrapolated to 0 K and significantly more accurate than DFT implementing the LDA (which overbinds resulting in an underestimation) and PBE xc-functionals (which overestimates). The Pulay pressure is minimised for these lattice parameters confirming the optimisation has converged to a minimum in the potential energy surface. The elastic constants are in good agreement with experiment with the greatest error for C_{11} which overestimates by 10.2%. We note the elastic constants were measured experimentally at room temperature whereas our calculations are at 0 K so we expect some discrepancy for any xc functional with LDA, GGA and hybrid functionals in the literature reporting similar errors [226]. These calculations show improvement over other xc functionals but prove less accurate than hybrid functionals which better incorporate the necessary exchange and correlation for accuracy in ferroelectric perovskites [103, 114].

Using the optimised lattice parameters, the TO modes at Γ are observed to be real, as predicted with DFPT-LDA in ref. [222]. Further calculations were performed fixing the lattice parameters to those calculated using LDA and PBE functionals (Figs. 6.1b (i) and (ii) respectively). The underestimated lattice parameters (and therefore volume) of LDA is shown to slightly soften the AFD modes at R (Fig. 6.1b(i)) whereas an increase to the volume softens the TO mode at Γ and hardens the modes at R (Fig. 6.1b(ii)). Therefore, we confirm the discrepancies in the predicted soft modes is attributed to changes in the volume [222, 223], which is most accurately predicted in these calculations. As the properties calculated by these first principles calculations are in excellent agreement with experiment and make an improvement over other functionals, it is accurate and suitable to fit the parameters of the forcefield.

Property	WC (Present)	DFT xc functional LDA [226]	PBE [226]	B3LYP [226]	Experiment [227]
a_0 (Å)	3.894	3.86	3.94	3.94	3.89
B (GPa)	187.62	215	195	187	179
c_{11} (GPa)	353.58	421.0	319.3	328.3	317.2
c_{12} (GPa)	104.64	122.1	97.5	105.7	102.5
c_{44} (GPa)	114.55	133.2	113.0	124.6	123.5

Table 6.1: Lattice parameters (a), bulk modulus (B) and elastic constants (C_{ij}) for cubic phase $SrTiO_3$ calculated from DFT with different xc-functionals and as observed in experiment.

Difficulties can arise fitting '*compatible*' forcefields with multiple compounds with recurring species. In this case, both Ti and O occur in both materials but the local chemical environments are sufficiently different despite being perovskites. Pb has a higher degree of covalency with oxygen than Sr as shown quantitatively in their respective Born effective charges (Supplementary Table E.4). Similarly, the Born effective charge of the titanium changes so classically it would expect to require different charges whether it has neighbouring Sr or Pb cations. One approach is to independently fit the forcefields and *mix* the parameters of each forcefield across the interface. The biggest disadvantage of this method is the failure to account for diffusion and the difficulty of transferability of the forcefield for complex interfaces. Arguably the best approach would involve fitting both compounds concurrently. In this thesis the $Pb(Zr,Ti)O_3$ forcefield from ref. [23] is used so the substrate forcefield requires fitting independently. To overcome problems with compatibility at the interface the short range Ti-O and O-O are chosen to remain unchanged. To increase the degrees of freedom the '*chemical*' parameters (charges and spring constants) are fitted which is validated from the Born effective charge analysis. The choice of which intrinsic Ti properties to use is then determined by the

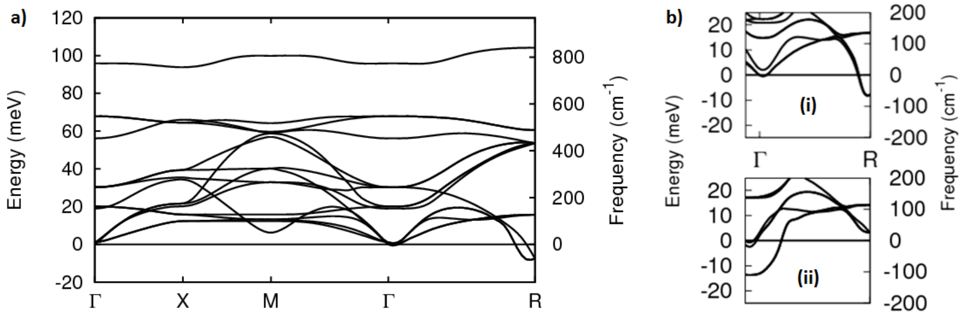

c)

a (Å)	3.86 ↓	3.89	3.94 ↑
ω(Γ) (cm⁻¹)	0.0	0.0	-109.6 ↓
ω(R) (cm⁻¹)	-62.9 ↓	-61.1	25.8 ↑

Figure 6.1: Phonon dispersion curve of the cubic phase of $SrTiO_3$ calculated using DFPT with the WC xc-functional at the equilibrium lattice parameter 3.89Å (a) and lattice parameters predicted by LDA 3.86 Å (bi) and PBE 3.94 Å (bii) when moving between high symmetry points $\Gamma(0,0,0)\rightarrow X(0,0,{}^1/_2)\rightarrow M(0,{}^1/_2,{}^1/_2)\rightarrow \Gamma \rightarrow R({}^1/_2,{}^1/_2,{}^1/_2)$. The table provides the soft mode frequency at Γ and R calculated at each volume.

nearest A-cation neighbour species. Nonetheless, getting the classical potentials to reproduce the first principles energy surface is extremely difficult particularly as the degrees of freedom of the fitting parameters is reduced. Consequently, a simplification is made. As most industrial applications and research efforts operate at temperatures far exceeding 110 K, the forcefield is fit only to the cubic paraelectric phase of $SrTiO_3$.

The phonon analysis identified that at the experimental volume the TO modes at Γ should be real. This was included as a fitting constraint which is further advantageous by helping to prevent the ferroelectric tetragonal phase from the $PbTiO_3$ phase sequence (inherent in the fixed Ti-O and O-O parameters) occurring for $SrTiO_3$. This constraint was found to be insufficient to prevent the condensation of spurious ferroelectric phases. The fixed Ti-O and O-O Buckingham potentials still favoured apical asymmetry that was necessary for the tetragonal phases in the PZT solid solutions of the parent forcefield [23]. To stabilise the short range forces and centrosymmetry at low temperatures an additional Buckingham interatomic potential between Sr-Ti was required. This was further beneficial by adding three degrees of freedom enabling better reproduction of the PES and calculated properties. Exact reproduction of all properties is too computationally expensive as every parameter set defines a distorted lattice structure and therefore not possible due to the simplicity of the interatomic potentials employed [17]. The Sr chemical parameters and Sr-O Buckingham potentials were initially set using the Pb terms from the Gindele forcefield [23]. The Sr-Ti parameters were set using the Ba-Ti parameters from a reduced phase $BaTiO_3$ forcefield derived in Ref. [228]. The fitting was performed using the algorithms and procedures outlined in Section 3.3.4. The final parameters of the forcefield given in Table 6.2.

Atom	Core charge (e)	Shell charge (e)	k_2 (eVÅ^{-2})	k_4 (eVÅ^{-4})
Sr	4.053462	-3.112560	12452.533	17052.705
Ti	8.412724	-5.194464	36926.634	22166.460
O	2.188907	-3.575294	457.77670	11245.576
Buckingham	**A (eV)**	**ρ (Å)**	**C (eVÅ^6)**	
Sr-O	3437.7024	0.316394	82.642973	
Sr-Ti	5505.2062	0.276585	992.68610	

Table 6.2: Optimised forcefield parameters for the reduced phase $SrTiO_3$ shell model. The cut-off radius is 6 Å with a Voter taper radius of 8 Å for all Buckingham potentials. The Ti-O and O-O Buckingham potentials are intentionally unchanged from ref. [23] so are not included.

The calculated properties and the relative errors reproduced by the derived forcefield are given in Table 6.3 as calculated using GULP [131]. The coordinates are not shown as they are exactly reproduced for all species even when symmetry constraints are removed. Whilst the lattice parameter reproduced by the forcefield is underestimated by 0.3% it remains more accurate than is calculated by first principles using the LDA. The bulk modulus and elastic constants are excellently reproduced within the given error tolerance. The greatest error in properties produced by the fitted forcefield is for the c_{44} elastic constant. This error is ultimately due to a fundamental limitation of all pair-potentials which, due to a phenomenon known as the *Cauchy violation*, results in the unphysical equivalence of c_{12} and c_{44} [229].

Property	DFT (present)	FF	Rel Error
a_0 (Å)	3.894	3.883	-0.295 %
B (GPa)	187.62	188.03	0.221 %
c_{11} (GPa)	353.58	353.54	-0.010 %
c_{12} (GPa)	104.64	105.27	0.610 %
c_{44} (GPa)	114.55	105.28	-8.092 %

Table 6.3: Lattice parameters (a), bulk modulus (B) and elastic constants (C_{ij}) for cubic phase $SrTiO_3$ from the derived shell model (FF) relative to the properties to which it was fit (DFT using the WC xc energy functional).

Molecular dynamics was performed on a 10 × 10 × 10 supercell with periodic boundary conditions in the $N\sigma T$ ensemble using the DL_POLY package [132]. Each temperature was equilibrated for 5 ps with statistics collected over 15 ps. The forcefield is shown to correctly reproduce a cubic paraelectric phase across all temperatures (Figure 6.2) as required for this reduced phase forcefield. The lattice parameter of $SrTiO_3$ is experimentally measured to be 3.905 Å at room temperature [194] which is matched by our forcefield at 300 K.

As a reduced phase forcefield has been derived, additional caution must be taken to ensure the correct behaviour is reproduced when combined with the ferroelectric. Heterostructures including m ferroelectric layers separated by n paraelectric can be modelled from first principles providing quantitative comparison. It is necessary to check the model reproduces the structure at the limit accessible by these methods. In these layered '*superlattices*'[2] a discontinuity in the polarisation across the ferroelectric-paraelectric interface creates strong electric fields acting to simultaneously

---

[2] Denoted as (m|n) for m ferroelectric and n dielectric layers.

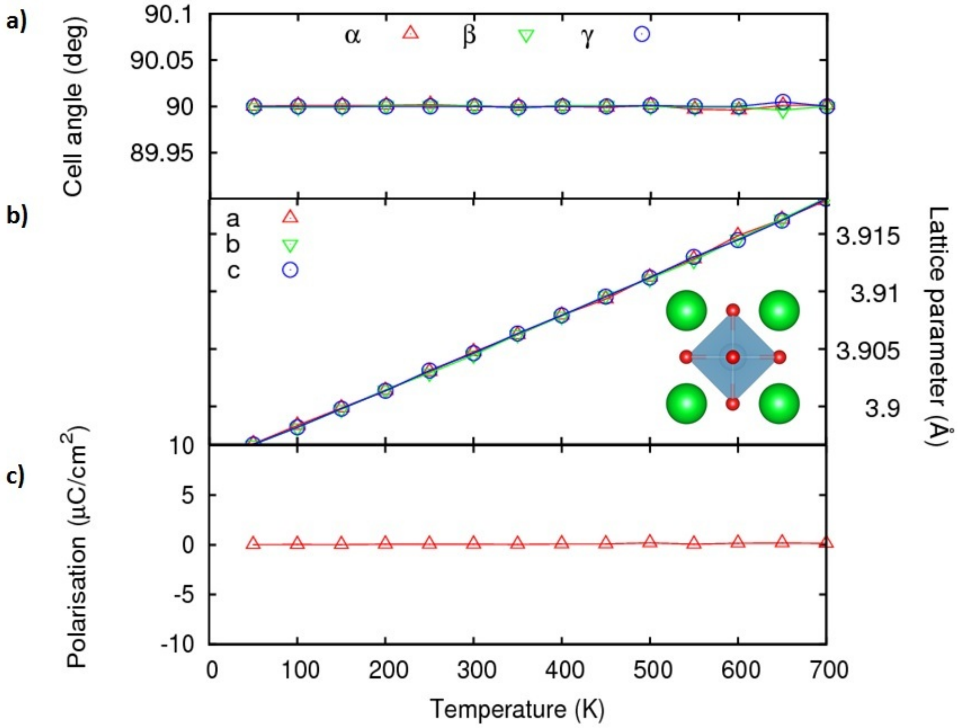

Figure 6.2: Dynamic properties of the derived reduced phase $SrTiO_3$ forcefield. The ensemble averaged cell angles (a) and lattice parameters (b) confirm the $SrTiO_3$ remains in the desired cubic phase across the tested temperature range. The inset shows the ensemble averaged configuration of the conventional unit cell of $SrTiO_3$ at 500 K. (c) The model experiences no spontaneous macroscopic polarisation as required.

suppress the polarisation in the ferroelectric whilst polarising the paraelectric. Due to the electrostatic energy cost of these built-in potentials the ground state can be significantly different from bulk [35]. The ground state of superlattices consisting of alternating single layers of $PbTiO_3$ and $SrTiO_3$ (1|1) have been shown to form from condensation of both ferroelectric and AFD distortions [35]. This is particularly important since in our forcefield we have omitted the AFD tetragonal phase. Fortunately, studies on thicker superlattices have shown the AFD influence to decrease when the thickness (m) of the ferroelectric is increased [35].

A combined experimental-*ab initio* investigation by Zubko *et al* provides quantitative profiles of the behaviour of the polarisation and tetragonality of (6|6) superlattices reproduced in Figure 6.3a [230]. In this thesis, a (6|6) superlattice is simulated by construction of a stack of 6 $PbTiO_3$ cells affixed to 6 $SrTiO_3$ cells along $[001]_p$, replicated 12 times along $[010]_p$ and $[100]_p$. No vacuum region is defined such that the superlattice repeats *ad infinitum*. The ferroelectric displacements in the initial condition of the $PbTiO_3$ are set to create two Kittel domains along $[100]_p$ as for the thin film calculations in Chapter 5. No ferroelectric displacements are set in the $SrTiO_3$ such that the atoms are in centrosymmetric positions. Molecular dynamics is performed at 10 K within the $N\sigma T$ ensemble using a 0.2 fs timestep to be closest to the conditions from Ref. [230]. The system was equilibrated for 20 ps with statistics gathered over a 60 ps production run. To compare with Figure 6.3a (from ref. [230]), the root mean square (rms) of the polarisation and lattice parameters is calculated for each (001) plane of unit cells (Fig. 6.3a)[3].

In the ferroelectric $PbTiO_3$ layers of our model, excellent agreement is noted with the first principles and experimental results in references [195, 230], showing both the polarisation and tetragonality to gradually decrease towards the paraelectric interface which has been confirmed experimentally by $t_{2g} - e_g$ splitting in electron energy loss spectroscopy [38, 230]. The initially defined ferroelectric Kittel domains are observed to relax into Landau-Lifshitz type closure domains predicted by DFT in these superlattices (Figures 6.3c) and for isolated $PbTiO_3$ films as was shown in Chapter 5. Incipient polarisation is induced within the $SrTiO_3$ which remains finite throughout the dielectric similarly predicted in [195, 230] (Figure 6.3c - shaded regions). The shell model artificially includes a slight plateau in

---

[3] In Ref. [230] the polarisation was defined using the Born effective charges (Eqn. 3.14) and displacements from the ideal coordinates. As such the polarisation map includes contributions from each sublattice layer. Such a definition is ill defined for the shell model so polarisation vectors can be included per unit cell only.

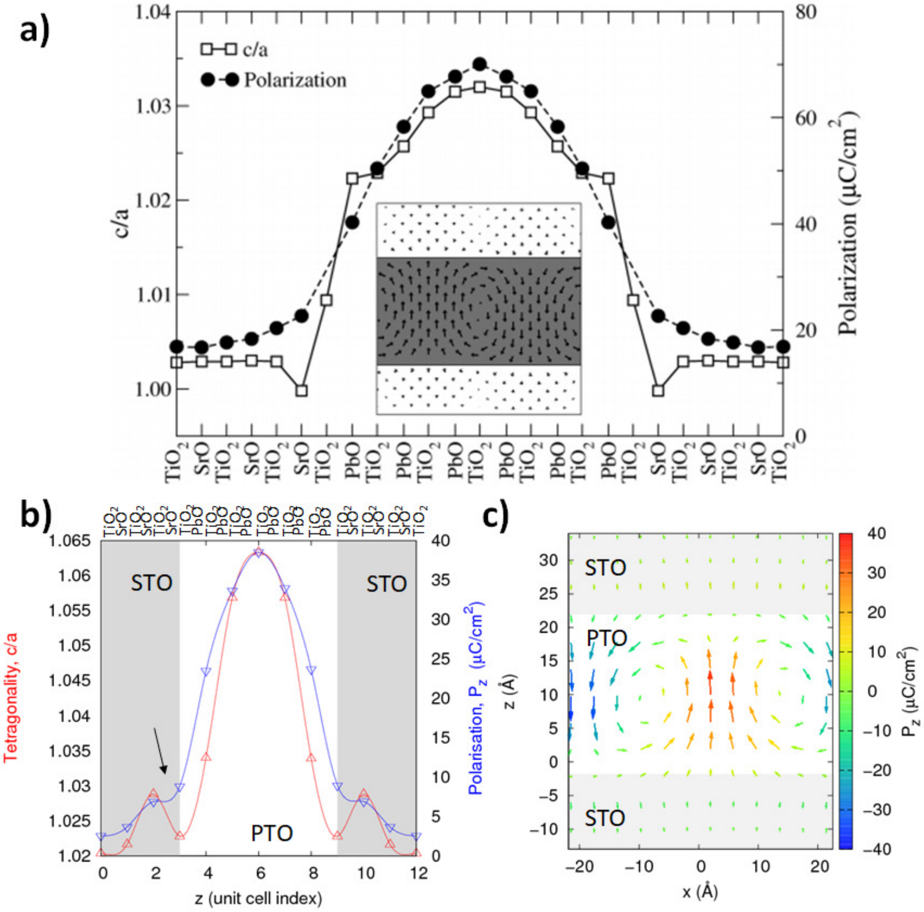

Figure 6.3: $PbTiO_3/SrTiO_3$ superlattices. (a) First principles calculation rms polarisation, tetragonality and polarisation vector map of a (6|6) superlattice ($12 \times 1 \times 12$ supercell) ($SrTiO_3$: white region). Reproduced (adapted) with permission from Ref. [230]. Copyright 2012 American Chemical Society. (b) RMS polarisation and averaged tetragonality for each (001) layer of unit cells in a (6|6) superlattice ($12 \times 12 \times 12$ supercell) calculated using the shell model. (c) Local polarisation vector map of the superlattice ($SrTiO_3$: grey region).

the polarisation with buckling in the tetragonality at the $PbTiO_3/SrTiO_3$ interface (Fig. 6.3b: arrow). However, as our model is concerned with the behaviour of the ferroelectric material, with the dielectric introduced to incorporate screening and strain, this discrepancy can be accepted as it occurs within the dielectric with the correct behaviour reproduced within the FE layers.

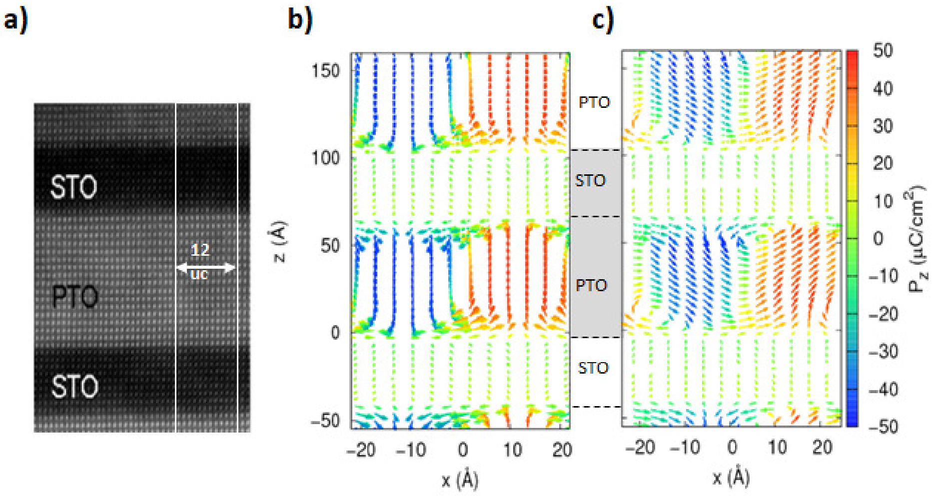

Figure 6.4: (a) HAADF STEM image of an (18|10) superlattice. Reproduced (adapted) with permission from Ref. [230]. Copyright 2012 American Chemical Society. Polarisation vector maps for a (18|9) superlattice calculated using the shell model revealing $\mathbf{c^d}$ domains when a_s = 3.8 Å (b) and $\mathbf{abc^d}$ domains when a_s = 3.9 Å (c). The layers belonging to the principle calculation cell are identified by the grey region between (b) & (c), with periodic images included to align with Figure (a) for clarity.

The shell model allows much larger systems to be modelled than by first principles. In the work by Zubko *et al*, the experiment was performed on (18|9) superlattices outside the current computational limits of conventional DFT (TEM of the experimental superlattice as shown in Figure 6.4a). Here, an (18|9) superlattice is simulated using an $N\sigma AT$ ensemble at 10 K for in-plane lattice parameters of 3.8 Å and 3.9 Å, with their polarisation vector maps shown in Figures 6.4 b and c, respectively. The domain phases in the $PbTiO_3$ layers follow the same strain mediated progression as for the unscreened thin films modelled in Chapter 5. Indeed, the TEM study shown in Figure 5.1b from [185] shows some signs of canting, an indicator that matches $\mathbf{abc^d}$ domains in Figure 6.4c.

Previous investigations have reported weak electrostatic coupling of the ferroelectric layers for $PbTiO_3/SrTiO_3$ superlattices with $n \geq 4$ [38]. Consequently, the ferroelectric layers in this limit have similar electrostatic boundary conditions to the isolated film *in vacuo* studied in the previous Chapter. We can therefore conclude the domain morphologies predicted for thin films also exist for epitaxial $PbTiO_3$ superlattices with insulating dielectric layers. Such a realisation greatly simplifies industrial manufacture of strain engineered devices such as the PET, which could implement the ferroelectric domain phases from Figure 5.2.

6.2 Electroded $PbZr_{0.2}Ti_{0.8}O_3$ on $SrTiO_3$

To model a PZT capacitor, an artificial electrode is required to modify the effective screening charge and the resulting depolarising field. In this model, an electrode is modelled using 6 layers of FCC Pt, characterised by a Finnis-Sinclair potential [231]. The electrode was attached to the surface of the perovskite film via a tethering potential determined using DFT by the following methodology. Slab calculations were constructed with 6 layers of *P4mm* ordered $PbZr_{0.5}Ti_{0.5}O_3$ with FCC phase Pt affixed to both (001) PbO terminated surfaces, in a c(2x2) cell (Figure 6.5). Geometry optimisation using the LFBG algorithm was performed using CASTEP [112], implementing the PBSol exchange-correlation functional. An 8×8×8 MP k-point grid was used with a cutoff energy of 450 eV for a *hard* pseudopotential of oxygen, and 200 eV otherwise, converged within energy and force tolerances of 1 meV and 5 meV/Å, respectively.

From the converged structure, the Pt atom above the Pb and O atoms

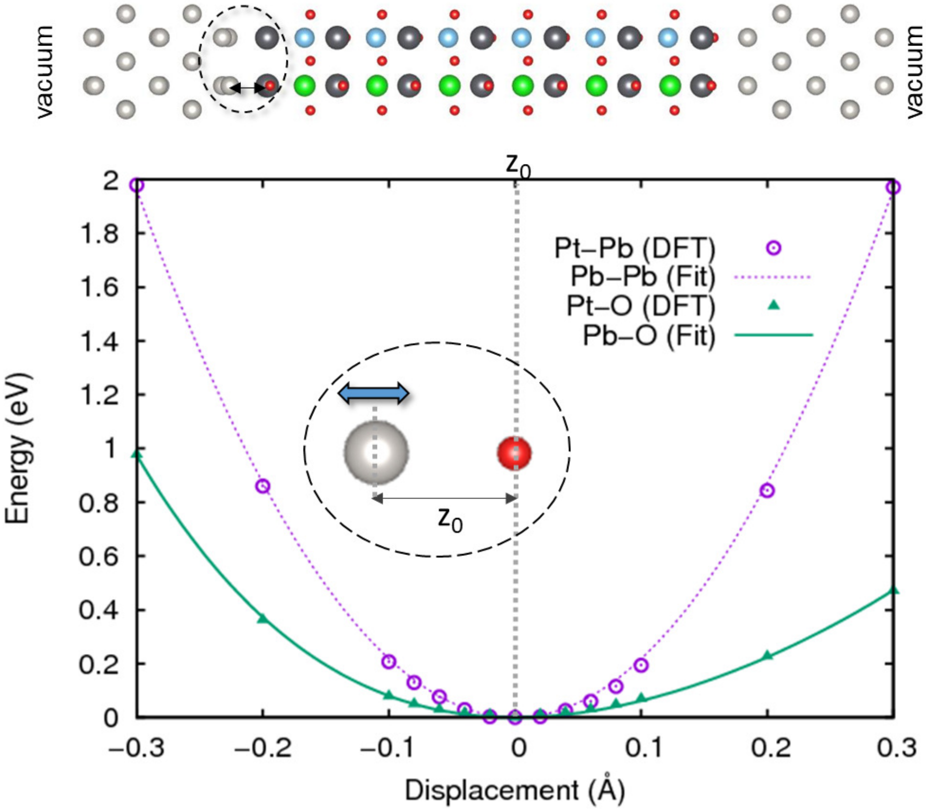

Figure 6.5: Fitting a tethering potential for FCC Pt attached to (001)PbO terminated *P4mm* ordered $\mathrm{PbZr_{0.5}Ti_{0.5}O_3}$. (a) Relaxed atomic structure of the Pt-PZT-Pt slab (positions of Pt atoms on the bottom surface of slab were fixed). (b) Quartic potential (Eqn. 6.1) fitted to the energy surface from DFT calculations generated by displacing the interfacial Pt atoms (highlighted in (a)) from their equilibrium positions parallel to the surface normal.

were displaced independently along [001]. Single point energy calculations, electronically minimised, were performed for each displacement to produce a DFT energy surface for the Pt displacement. This procedure was repeated for the Pt above the O atom. A quartic tethering potential of the form:

$$U_{\text{tether}}(r) = \frac{k}{2}(r_i - r_i^{\text{t=0}})^2 + \frac{k'}{3}(r_i - r_i^{\text{t=0}})^3 + \frac{k''}{4}(r_i - r_i^{\text{t=0}})^4 \tag{6.1}$$

was fit by method of least squares to each energy surface, given in Table 6.4 and shown in Figure 6.5. Test cases were performed at 20 K for a slab configuration constructed using a 40 × 40 × 20 simulation cell of $PbZr_{0.5}Ti_{0.5}O_3$ with 6 layers of FCC Pt attached to both surfaces and a 100 Å vacuum region with periodic boundary conditions. To provide a mirror charge, the Pt atoms above the ferroelectrically active Pb atoms are given a charges from 0.0e to -1.0e (charges of opposite sign were used for the top and bottom electrodes). 80 ps simulations were run using a time step of 0.2 fs. All simulations were stable with the electrodes maintaining the FCC phase and remaining tethered to the PZT film. A charge of 0.5e is found to recover bulk polarisation of the ferroelectric layers. Null charge of the Pt atoms results in closure domains as observed in Chapter 5.

	k'' (eVÅ^{-2})	k' (eVÅ^{-3})	k (eVÅ^{-4})
$U_{\text{Pt-Pb}}$	0.0	0.0	29.81 ± 0.12
$U_{\text{Pt-O}}$	14.02 ± 0.37	-9.29 ± 0.16	7.01 ± 0.18

Table 6.4: Potential parameters of Pt-Pb and Pt-O quartic tethering potentials with associated asymptotic standard errors between the fit and DFT reference data.

It is important to note the limitations of the model. In an ideal metallic electrode, abbundant mobile charge carriers will move to mirror the charge and moments in the ferroelectric preventing the build up of the screening charge and resultant depolarising field through the film which cause the closure domain morphologies. In a realistic electrode or surface, the ability to mirror depends on the number density of the carriers such that any incomplete screening causes partial suppression of the ferroelectric behaviour. This is naively achieved in this model by setting the Pt charge *a priori*. However, this charge will not change during the simulation in response to changes in local and macroscopic polarisation of the ferroelectric. Future work aims to incorporate the metrics defined in §4 into the DL_POLY code such that the polarisation can be calculated on-the-fly enabling the Pt charges to be updated at each timestep. Nonetheless, using the current implementation we provide a proof in principle solution of a realistic capacitor which we compare with experimental HR-TEM observations from M. Hytch [218, 232].

In the experiment, 100 nm thick $\mathrm{PbZr_{0.2}Ti_{0.8}O_3}$ thick was grown by epitaxy onto a [001] $\mathrm{SrTiO_3}$ (STO) substrate and capped with a Pt electrode. At room temperature, STO is cubic with lattice parameter $a = 3.905$ Å, $\mathrm{PbZr_{0.2}Ti_{0.8}O_3}$ is tetragonal with $a = 3.904$ Åand $c = 4.14$ Å. Due to the small lattice mismatch and mirror charges available from the electrode, it is expected that the PZT should favour an out-of-plane **c**-domain configuration. Indeed, in their experiment **c**-domains constituted roughly 80% of the volume fraction. The remaining 20% were **a**-domains (9 nm wide) separating the c-domains by a domain wall inclined at 45° to the substrate interface along the $(\bar{1}10)$ planes (Figure 6.6a-c). Typically, the **a**-domains in the so-called $\mathbf{a}-\mathbf{c}$-domain configuration form such that the base of one **a**-domain corresponds to the tip of the previous (see white arrow in Figure 6.6a), although they could also align tip-to-tip or base to base forming a 'caret' or 'vee' formation.

Using the model developed in this Chapter the experimental setup is constructed using a $40 \times 20 \times 20$ $\mathrm{PbZr_{0.2}Ti_{0.8}O_3}$ slab on a $40 \times 20 \times 8$ $\mathrm{SrTiO_3}$ substrate. The bottom 4 STO layers are fixed in their ideal positions using the experimental lattice parameter $a = 3.905$ Å which agrees with the forcefield at 300 K (Figure 6.2b). The *free* surface of the PZT is terminated with a (001)PbO layer. 6 layers of FCC Pt are attached to the *free*-surface of the PZT and the frozen surface of the substrate. Due to the presence of **a**-domains in the experiment, we assume the electrodes do not completely screen the surface charge. As such, we set the Pt charge in the model to -0.45e on the electrode capping the *free* PZT surface. The Pt on the bottom electrode are set to +0.45e and frozen with their initial coordinates. An $\mathbf{a}-\mathbf{c}$-domain is introduced into the initial configuration with the domain

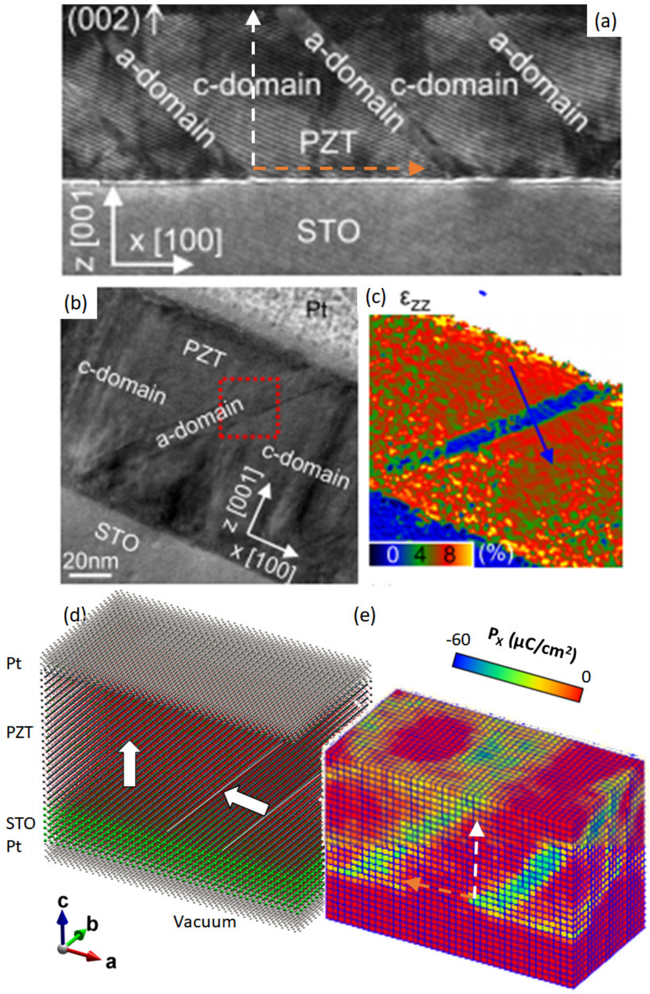

Figure 6.6: Formation of a-c domains in epitaxial $PbZr_{0.2}Ti_{0.8}O_3$ thin films grown on $SrTiO_3$. (a) HRTEM image of the cross-section of a Pt-PZT-STO film in a region containing three a-domains separating out-of-plane c-domains. (b) Close up HRTEM image of an the a-c domain (c) ϵ_{zz} strain deformation map produced by geometrical phase analysis. (d) Setup configuration for a molecular dynamics simulation for a Pt-PZT-STO-Pt film containing an a-c domain pattern. (e) Averaged domain structure following molecular dynamics at 300 K. Each cube represents a unit cell whose colour is the P_x component of polarisation. The simulation excellently reproduces the domain structure observed in experiment. Experimental results (a-c) reproduced with permission from Ref. [232]. Copyright 2018 Institute of Physics.

wall along ($\bar{1}10$) with the volume fractions in a 1:5 ratio (Figure 6.6d).

Molecular dynamics was performed at 300 K (which is $0.5T_c^{FF}$ and representative of the system at room temperature for the model). The simulation was evolved within the Nosé-Hoover canonical (NVT) ensemble with a 10 fs relaxation constant and a 100 Å vacuum region along [001] with 3D periodic boundary conditions. This fixes the in-plane strain but allows the out-of-plane stresses to minimise [27]. The system was raised to 300 K in 100 K intervals over a period of 60 ps, followed by a 60 ps equilibration period at the target temperature of 300 K. Statistics were gathered over a 80 ps production run. A 0.2 fs time step was used throughout.

Early during the equilibration, the initially constructed a-domain is observed to reform as two equally wide a-domains, each half the width of the initial, such that the volume fraction of the a- and c-domains is maintained in an approximate 1:5 ratio as was identified in the physical sample using HRTEM. Remarkably, these domains form such that their base coincides along [100] with the tip of the other, as was also observed in the experiment (highlighted by the white arrow in Fig. 6.6a). This new configuration remains stable throughout the remainder of the equilibration period and the subsequent production run. In Figure 6.6e, the averaged P_x component of the polarisation is plotted for the perovskite cells showing excellent agreement of domain structures between the simulation and experiment (cells polarised along [$\bar{1}00$] constitute the **a**-domains (blue) whereas **c**-domains are polarised along [001] such that $P_x \approx 0$ (red)).

6.3 Conclusion

To conclude, a cubic phase $SrTiO_3$ shell-model forcefield has been derived to be compatible with the PZT forcefield from ref. [23]. Density functional theory was used to provide an accurate energy landscape to which the parameters of the interatomic potentials were fit using a combination of the Shimada weight adjustment method and a basin hopping routine. The static and dynamic properties of the forcefield are shown to excellently reproduce the important properties of $SrTiO_3$ derived from DFT, remaining cubic and paraelectric across industrially applicable temperature ranges as required. (6|6) $PbTiO_3/SrTiO_3$ superlattices were modelled using the two forcefields finding good agreement in the polarisation and tetragonality in the $PbTiO_3$ layers as compared with first principles calculations and experiment from ref. [194]. The quantitative differences are understood to arise intrinsically due to the existing $PbTiO_3$ forcefield as the polarisation is underestimated in bulk by 40%. Similarly, the super-tetragonality is due to the WC xc-functional used in the fitting of the PZT forcefield. With these errors understood, the reproduction of the experimental results profiles is excellent. The behaviour of the polarisation within the $SrTiO_3$ is also well reproduced, with the exception of the plateau due to sublattice buckling at the interface. These discrepancies do not significantly alter the desired properties within the ferroelectric film so were deemed acceptable errors but highlights where improvements could be made in future work. Using (18|9) superlattices, we identified the dielectric ($SrTiO_3$) layers were sufficient to screen the dipole interactions between the ferroelectric slabs, such that the strain mediated domain morphologies present in isolated $PbTiO_3$ ultrathin films occur. This realisation provides experimentally achievable conditions to employ tuned domain phases in the development of $PbTiO_3$ piezoelectronic transistors and novel ferroelectric devices. Using an existing many-body interatomic potential for FCC Pt, a tethering potential is fit to the energy surface of DFT calculations of Pt electrodes on *P4mm* ordered $PbZr_{0.5}Ti_{0.5}O_3$. This chapter concludes with a final test case combining the PZT forcefield with the new $SrTiO_3$ parametrisation and Pt tethering potential, to model a Pt/$PbZr_{0.2}Ti_{0.8}O_3$/$SrTiO_3$ capacitor in comparison with experimental HRTEM results [218,232]. The model was found to excellently reproduce the **ac** domain structure observed in the physical sample. The model developed in this Chapter has been shown to be capable of simulating a real ferroelectric capacitor which in future work could be used to understand many critical phenomena including flexoelectric contributions near the domains and electrode / substrate interfaces and polarisation switching in a realistic (non-ideal) system.

7

Switching Dynamics of $PbZr_{1-x}Ti_xO_3$

In this Chapter molecular dynamics calculations, supplemented with electrical measurements from collaborators, are used to provide insight into the microscopic switching properties of near-morphotropic PZT. The simulations and experiments exhibit qualitatively similar hysteretic behaviour of the polarisation at different temperatures, showing widening of the Polarisation - Electric field hysteresis loops, and the decrease of the coercive field towards high temperatures. Remarkably, polarisation switching at low temperatures is shown to occur via a polarisation rotation and growth mechanism that is fundamentally different from the high temperature switching, where nucleation is rate limiting. Analysis of B-cation contributions show that nucleation and switching are facilitated by Zr centred unit cells and, by extension, Ti centred unit cells in Zr-rich environments. Ti-rich clusters in morphotropic PZT, at low temperature, are observed to have suppressed ferroelectric displacements which may incorrectly be perceived as ferroelectrically inactive '*dead-layers*'. These results provide a fundamental description of the microscopic behaviour during switching necessary to control and improve ultrafast switching in ferroelectric capacitors, and identify limitations in conventional transmission electron microscopy experiments when reporting dead-regions.

The results in this Chapter have been partly discussed in J.B.J.Chapman, O.T.Gindele, C.Vecchini, P.Thompson, M.Stewart, M.G.Cain, D.M.Duffy & A.V.Kimmel, Journal of the American Ceramics Society, **101**, 874 (2018) [233].

7.1 Introduction

Functional ferroelectric ceramics are utilized as critical components in many modern technologies which operate over a wide range of conditions. One of the most widely used ceramic materials is lead zirconate titanate $Pb(Zr_{1-x}Ti_x)O_3$ (PZT) [55], which is a disordered solid solution of $PbTiO_3$ and $PbZrO_3$ perovskite (ABX_3) compounds [23, 55, 60, 234–237] used for non-volatile memories, transducers, actuators, inkjet printheads, drug delivery implants and micropumps [8, 12]. The permutational freedom resulting from the random distribution of Ti and Zr over the B-sites unlocks rotational degrees of freedom of the BO_6 octahedra which provides a rich temperature-composition phase diagram (see §2.4 and Figure 2.6). Of particular importance is the morphotropic region around $0.47<x<0.52$, which exhibits exceptionally high electromechanical response vital for aeronautical, military and space applications [238–240]. It is essential to provide insight into the performance and polarisation switching dynamics of this material due to the wide range of operating conditions of PZT based devices. Although there have been a number of studies performed at room temperature and above, the low temperature ($T < 200$ K) properties of PZT are not well characterized.

In this thesis, the temperature effect on electromechanical properties of PZT are studied to provide insight into the switching mechanisms at different temperatures. In order to investigate the effect of temperature on the important properties of PZT, a series of classical molecular dynamics (MD) simulations, supplemented with electrical measurements of P-E loops in ceramic PZT (x=0.47) samples from collaborators, are performed. Large scale MD simulations are used to calculate hysteresis (P-E) loops for the PZT compound over a wide range of temperatures, which provides information about both the local polarisation in each unit cell and the macroscopic polarisation. Although P-E loops in PZT for different temperatures have been measured experimentally before [241], the temperature dependence of the coercive field (E_C) and its implications have not been discussed, and are presented in Section 7.3. The microscopic switching mechanisms are identified and compared in Section 7.4. The effect of the B-cation disorder and local environment is then analysed in Section 7.5.

7.2 Simulation and Experimental Procedure

7.2.1 Simulation Details

The adiabatic core-shell model forcefield, that accurately reproduces the full composition-temperature phase diagram for PZT, is used for these simulations [23]. A relatively large simulation cell of $PbZr_{0.5}Ti_{0.5}O_3$ was used ($20 \times 20 \times 20$ unit cells) corresponding to 4×10^4 atoms. The two species of B-cations (Ti and Zr) were randomly distributed over the B-sites to obtain the stoichiometry of $PbZr_{0.5}Ti_{0.5}O_3$. The DL_POLY 4 [132] code is used to perform the MD evolution, implementing an $N\sigma T$ (constant stress) ensemble and a Nosé-Hoover thermostat (0.01 ps) and barostat (0.1 ps). A time step of 0.2 fs was selected. Properties are calculated according to the procedures presented in Chapter 4.

Quasistatic P-E loop calculations were performed by ramping the electric field along [001] in 1 MV/m steps in a range from -30 MV/m to +30 MV/m. The system was equilibrated for 4 ps at each value of the electric field and the polarisation was calculated during a subsequent production run of 6 ps.

7.2.2 Experimental Details

For comparison with the theoretical predictions of the P-E loop behaviour, electrical measurements of ceramic PZT samples (x=0.47) were performed by collorators lead by C. Vecchini. The measurements were performed on the XMaS beam-line (BM28) at the European Synchrotron Radiation Facility (ESRF), where they used a method to measure P-E loops on the beam-line which has been previously described in [242], which is labelled ‘setup 1’. ‘Setup 2’ was created to produce a low temperature data point at 77 K and was performed at the National Physical Laboratory using a liquid nitrogen bath. P-E loops were measured in setup 1 on commercial ceramic plates of soft PZT by Morgan Electroceramics (PC5H). Earlier reports found the material’s composition to be x=0.47 with a rhombohedral symmetry at room temperature [243]. This places the composition at the MPB, at which a more recent neutron scattering study suggests [55] that an additional monoclinic phase coexists with the rhombohedral phase. A separate measurement point at 77 K was made in liquid nitrogen using a Fuji c91 (PZT composition similar to Morgan’s PC5H) sample that permitted higher electric fields to be applied. To measure the P-E loops, triangular electric field cycles of amplitude 1 kV/mm and a frequency of 0.1 Hz were applied to the device under test, while the polarisation was recorded simultaneously. For further details about the experimental setup see [233].

7.3 PZT P-E Hystersis

The P-E loop simulations for $PbZr_{0.5}Ti_{0.5}O_3$ (Fig. 7.1a) produce symmetric, well-saturated square-shaped loops characteristic of a hard ferroelec-

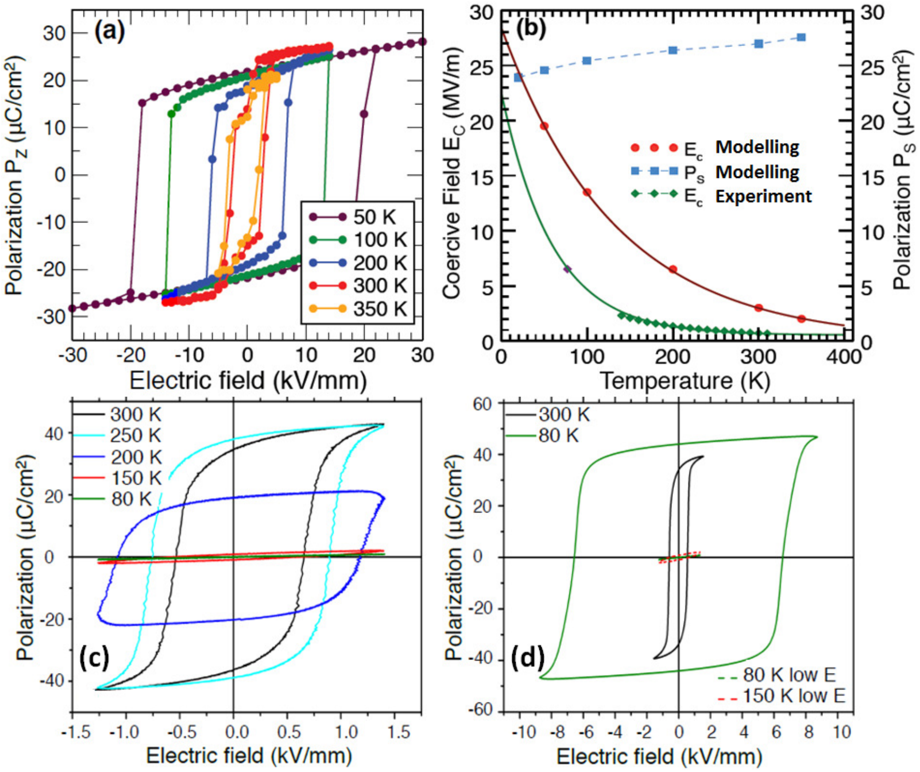

Figure 7.1: (a) Modelled temperature dependence of the z-component of polarisation (P_Z) with respect to the applied electric field E (P-E loops). With the temperature rise, the shape of P-E loops evolves from square-like (purple, green, blue) to complex shapes (red and yellow) due to increased polarisation fluctuation at high temperatures. (b) Temperature dependence of E_C (red) and P_S (blue), both inferred from the P-E loops in (a). E_C drops with temperature (maroon). Experimental data also plotted in green diamonds with one (77K) point in purple diamond (different sample, but same composition). (c) Measured P-E loops of PZT sample at different temperatures. With the temperature decrease the area of the loops reduce, demonstrating a dielectric-like response. (d) A comparison of 150 K and 80 K loops measured at high (9 kV/mm) and low (1.5 kV/mm) fields. The higher 9 kV/mm field restores the square shaped hysteresis loops.

tric system. As the temperature increases, the P-E loops becomes narrower and exhibits a more complex shape, signifying that the switching process occurs via a series of multiple events activated across a broader range of fields [244]. Above 300 K the shape of P-E loops becomes more complex because of increasing polarisation fluctuations in the system. At high temperatures a small amount of in-plane polarisation along x and y develops spontaneously, which reduces the z-component (P_z), whilst the total polarisation is unchanged. O. Gindele perfomed the P-E loops and obtained the value of E_C and P_S [24]. The temperature behaviour of P_S shows a monotonic increase, while E_C decreases with the temperature rise (Fig. 7.1b). Thus, at low temperatures (< 200 K) the values of E_C exceed the fields of several kV/mm usually applied in experiments and devices. The implication of this increase is that high fields are necessary for ferroelectric devices at low temperatures.

The experimental P-E curves (Fig. 7.1c) display the expected hysteretic behaviour with dielectric loss determined by the area enclosed within the P-E loop. Cooling the sample from room temperature to 250 K shows a slight increase of E_C. Further lowering of the temperature to 200 K is accompanied by a widening of the P-E loop that results in a lower P_S and an increase in E_C. This is in good qualitative agreement with the simulations and are typical for ferroelectric materials, as shown earlier for PZT [241], $BiFeO_3$ [245], $SrBi_2Ta_2O_9$ [246] and ferroelectric polymers [247]. Upon further cooling, it is observed that at temperatures below 160 K the P-E loops exhibit a very narrow hysteresis and low polarisation, similar to curves observed from lossy dielectrics. This is in agreement to observations made from measurements of PZT in a NASA report [241]. However, it is identified that the narrow loops and low coercive fields observed at low temperature in our data is a direct result of E_C becoming larger than the maximum applied voltage possible in setup 1, equating to 1.5 kV/mm for the PC5H samples. Upon using setup 2, applying high fields of 9 kV/mm on the thinner Fuji samples at 77 K, a distinctly ferroelectric square P-E loop is measured as shown in Figure 7.1d (labelled 80 K, solid), in contrast to the lossy curves of setup 1 below 160 K (Fig. 7.1c, reproduced in d as dashed curves, labelled 80 K low E and 150 K low E).

The electrical measurement of PZT ceramics and single domain modelling results demonstrate good qualitative agreement. This behaviour highlights the importance of temperature on measured material properties, where a small change of temperature strongly affects E_C and related quantities. However, quantitative differences are found between the modelled and experimental parameters. Indeed, the E_C in experiments is less than half that found in MD simulations. The lower value measured in the experiments is known to be due to the presence of domain walls, defects, grain boundaries and surface terminations in the ceramic samples relative to the simplified simulation model, as inhomogeneity in the local polarisation reduces the switching barrier. Indeed, for the parent compound $PbTiO_3$, the coercive field as calculated from the forcefield at 10 K is 130 kV/mm which matches other $PbTiO_3$ MD parametrizations [248] and is in excellent agreement with the intrinsic coercive field of 150 kV/mm calculated using density functional perturbation theory [249].

The coersive fields E_C observed in Fig. 7.1b are about an order of magnitude lower than the E_C value calculated from first-principles for switching through the polar ferroelectric mode in PZT by Beckman et al [250]. The lower E_C found in this model, which was fitted to a potential energy surface produced from DFT data which also has the large repolarisation barrier [23], suggests that the actual polarisation switching in PZT follows a lower energy path than the polar mode. Two intrinsic mechanisms that could lower the repolarisation barrier are polarisation rotation and domain wall motion after domain nucleation [90].

7.4 Switching Dynamics

To understand the origin of the low values of E_C and provide an insight into the switching mechanisms in the different temperature regimes, switching events at 100 K and 300 K are modelled using molecular dynamics. The system is initially pre-poled using an electric field orientated along [001] to induce a tetragonal phase with $P_z = 40$ μC/cm^2 and $P_x = P_y \approx 0$ μC/cm^2. A reverse field of magnitude 30 MV/m was applied along $[00\bar{1}]$ to facilitate picosecond switching at the start of the production run.

Phenomological models such as Landau theory, used to introduce concepts of ferroelectricity in Chapter 2, use order parameters to describe the free energy. It has recently been suggested by Geneste [251], that free energy should not be expressed solely in terms of the local order parameters but instead be expressed by a density of probability (DoP) of the order parameters. In MD simulations such as this, the DoP can be defined as the mean of the order parameters and characterised by its standard deviation σ [252]. In this Section the order parameter used is the polarisation, such that the mean of the DoP reproduces the averaged local polarisation. The evolution of the DoP during the switching simulations are shown in Figure 7.2 for each polar component at 100 K (a) and 300 K (b), where the y-axis represents the magnitude of the polarisation and the colour reflects the proportion of unit cells which have that given polarisation (in bins of 2 $\mu C/cm^2$) at each instant in the simulation.

Different switching times of 8 ps and 2 ps are registered for the 100 K and 300 K simulations, respectively, identified by $\langle P_z \rangle$ changing sign. This behaviour agrees well with experiments on PZT ceramics which identified decreased switching times with increasing temperature [253].

Remarkably, a stark contrast between the DoP for low and room temperature regimes is observed. At 300 K the average P_Z component changes the sign, whilst the average in-plane components of polarisation

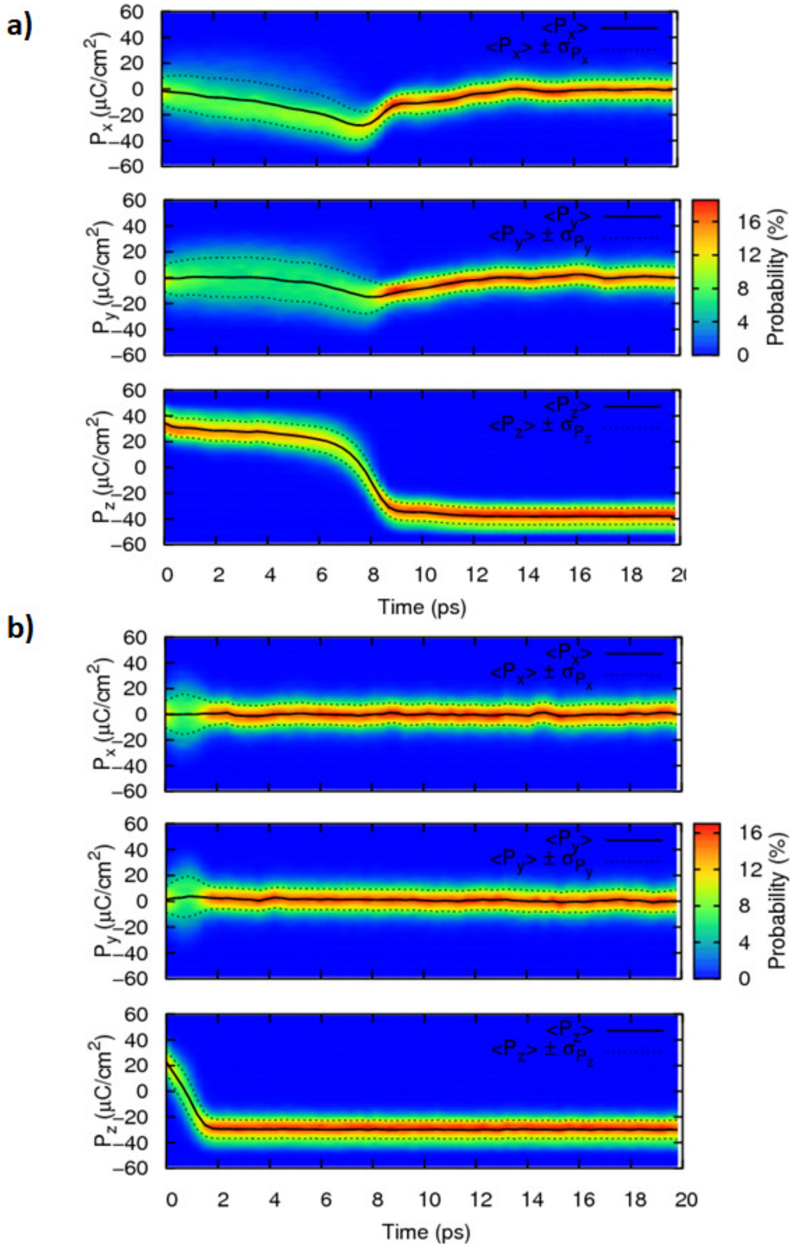

Figure 7.2: Behaviour of the local order parameter polarisation during switching at (a) 100 K and (b) 300 K. The solid black lines trace the mean of the i^{th} polarisation component $\langle P_i \rangle$. Dotted lines trace the standard deviation from the mean displacement $\langle P_i \rangle \pm \sigma_{P_i}$. Sign change of $\langle P_z \rangle$ indicates different switching times of 8 ps for 100 K and 2 ps for 300 K. At 100 K the reduction of P_z is accompanied by substantial deviations in the P_x and P_y components which corresponds to maintained polarisation rotation. In contrast, at 300 K the P_z component changes the sign, while the in-plane components of polarisation remains, on average, zero.

remains zero (Fig. 7.2b). This corresponds to the simulated sample switching through an intermediate quasi-paraelectric state. In contrast, at 100 K, the reduction in the average polarisation parallel to the switching field is accompanied by substantial build up in the P_x and P_y components showing polarisation rotation to within a standard deviation (Figure 7.2a). A polarisation rotation switching mechanism has been described in MD simulations of tetragonal $PbTiO_3$, in which the system switched via an intermediate orthorhombic phase [248], and further supports experimentally observed double current peaks in pre-poled PZT identifying non-180° switching [254]. We note that for the low temperature case the standard deviation in $P_{x,y}$ slightly increases during the switching event, which is indicative of bond softening [252] and the remnants of the competing rotational mechanism. At the higher temperature the system responded to the applied field by nucleation of small reversed domains that can switch rapidly (see §7.4.1). This prevents the build up of large polarisation components perpendicular to the driving field and reduces the time and energy required for polarisation reversal, resulting in the slanted hysteresis loops seen in Figure 7.1a.

7.4.1 Switching Mechanisms

The nucleation dominated switching at 300 K agrees well with experimental findings for thin PLZT films [255], where it was proposed that at room temperature PZT re-poles through multiple nucleation events, while at lower temperatures domain wall motion dominates the switching kinetics. Here we suggest that polarisation rotation initiates the low temperature switching. The difference between switching at low and room temperature are emphasised in Fig. 7.3, where a schematic sketch is presented together with snapshots of the simulated PZT system at 100 K and 300 K. The snapshots are plotted as 2D slices in the x-z plane in (b) and (c), demonstrating the distinctly different domain structures related to each switching

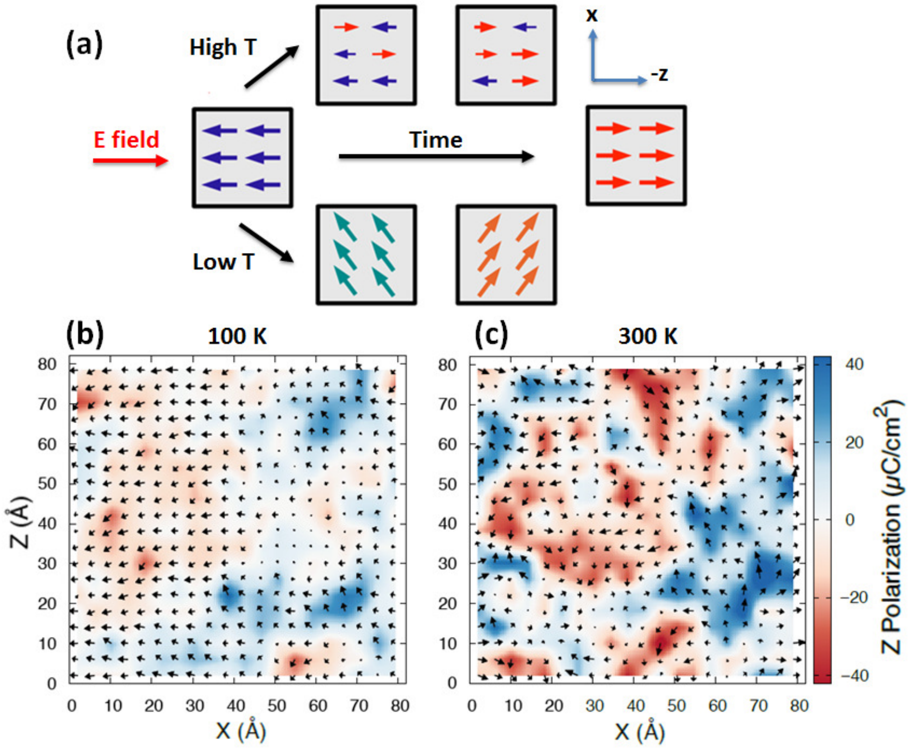

Figure 7.3: (a) Schematic representation of the different polarisation switching mechanisms: Polarisation rotation at lower temperatures (left) and nucleation of reversed domains at higher temperatures (right). The arrows correspond to the local dipole moments. (b) and (c) Snapshots of the local dipoles in PZT during MD simulated polarisation switching at 100 K and at 300 K. The snapshots were taken halfway through the polarisation reversal (total $P_Z = 0$) and each arrow corresponds to the local dipole moment of a conventional unit cell. The colour gradient represents the magnitude of P_Z. (b) The low temperature system (T=100 K) exhibits a homogeneous domain pattern during the switching process with well-defined in-plane contribution where P_Z is small and P_X is large. (c) At high temperature (T=300 K) PZT breaks up into multiple reversed domains, as seen by the many up (blue) and down (red) polarised parts.

process. The figures of the modelled system show the local dipole moments, for the system switching from P_Z to -P_Z at the state where $P_Z = 0$, halfway through the polarisation reversal (t(b)=7.9 ps, t(c)=0.85 ps). One can see that at 100 K (Fig. 7.3b) the system consists of large domains with significant in-plane polarisation and $P_Z \approx 0$. This agrees with Figure 7.2a, which showed a large contribution of the x-component of polarisation during the switching event. In contrast, the system at 300 K (Fig. 7.3c) exhibits a much denser domain pattern with small domains polarised along +z or -z and much less in-plane polarisation along x. Overall, the 100 K domain structure is more homogeneous than the 300 K domain structure.

The process leading to the large domains with large perpendicular polar components relative to the switching field at 100 K is shown in Figure 7.4). Each unit cell is represented by a cube whose colour indicates its local ferroelectric phase. This is defined by the average polarisation of the conventional unit cell over 50 fs increments ($\bar{\mathbf{P}}$). Following the approach taken in Ref. [252], if $|\bar{\mathbf{P}}| < 5\ \mu\text{C/cm}^2$ the unit cell is considered non-polar and cubic (C). If a component of $\bar{\mathbf{P}}$ exceeds $5/\sqrt{6}\ \mu\text{C/cm}^2$ then it is classed as ferroelectric. The phase is then identified by the number of components exceeding this limit (T=1,O=2,R=3). An x-z cross-section is taken at 1 ps (Fig. 7.4a) and 6 ps (Fig. 7.4b), with cartoons depicting both phase structures are shown in Figure 7.4(ii). Only switched unit cells ($P_z^j < 0$) are plotted such that the nucleation and growth process can be clearly seen.

When the switching field is applied to the system, in which preexisting domain walls are absent, octahedral shaped reverse domains are nucleated, approximately faceted by (101) surfaces (Fig. 7.4a). These are the 3-dimensional analogues to the bevelled diamond formations previously identified to be the shape which minimizes the nucleation barrier on 2-dimensional 180° domain walls during domain wall motion [90]. It is observed that nuclei exceeding some critical radius with this structure quickly grow on the facets that form charged domain walls with the [001] bulk,

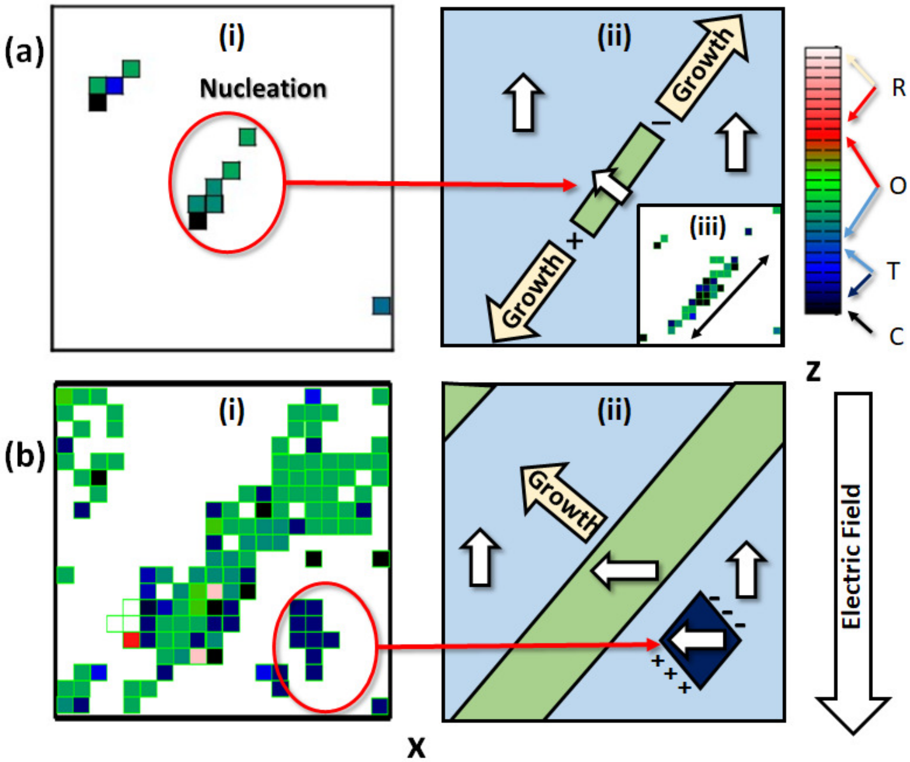

Figure 7.4: Low temperature switching mechanism of forward poled $PbZr_{0.5}Ti_{0.5}O_3$. Snapshots at (a) 1 ps and (b) 6 ps during the switching simulation at 100 K. (i) Negatively poled unit cells are plotted whose colour represents the local phase. (ii) Simplified cartoons of the snap-shots. Sub-figure (iii) shows the growth of the nucleated domain.

which tends to reduce the electrostatic energy penalty (Fig. 7.4a(iii)). This growth is followed by conventional domain wall motion (Fig. 7.4b). This nucleated domain accounts for the polarisation rotation observed in Figure 7.2a, as the local unit cells within the reverse domain adopt an orthorhombic structure with the polarisation rotating as the domain grows. In order to investigate finite size effects we repeated the 100 K simulation for a 60×20×60 simulation cell containing 3.4×10^5 atoms which showed comparable polarisation rotation during switching.

At both low and room temperatures the underlying domain structures

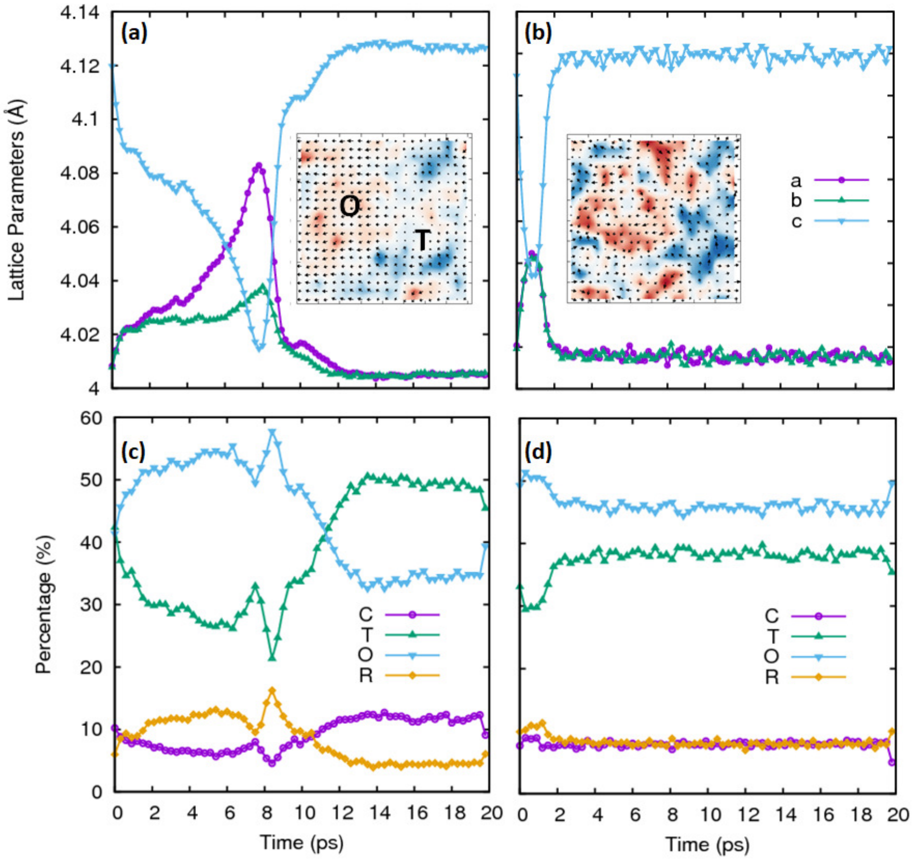

Figure 7.5: Average lattice parameters during the switching event at (a) 100 K and (b) 300 K. Proportion of the local unit cells having cubic, tetragonal, orthorhombic and rhombohedral phases during the simulation at (a) 100 K and (b) 300 K. Phases of the unit cells are defined by the average polarisation $\bar{P}$ of the cell over 50 fs increments. In an approach from [252], if $\bar{P} < 5\ \mu\mathrm{C/cm}^2$ the unit cell is considered non-polar and cubic (C). If a component of $\bar{P}$ exceeds $5/\sqrt{6}\ \mu\mathrm{C/cm}^2$ then it is classed as ferroelectric. The phase is then identified by the number of components exceeding this limit (T=1,O=2,R=3).

affect the macroscopic lattice parameters and reduce the tetragonality of the forward poled system during the switching event (Figure 7.5 a & b). The uncorrelated nature of the small nucleated domains at room temperature results in an intermediate macroscopic cubic structure, whereas at low temperature the lattice parameters reflect the growth of the rotating domain. In Figure 7.5 c and d, the system is decomposed into the proportion of local unit cells supporting C,T,O and R phases at each instant in time. At low temperatures, as the nucleated domain grows, the unit cells become orthorhombic as was shown by Figure 7.4 and by the density of probability of the polarisation (Figure 7.2a). Once the domain has grown and fully rotated the predominantly tetragonal local phase is restored. At room temperature there is again a spike in the percentage of locally orthorhombic cells (Fig. 7.5d) reflecting the bond softening and remnants of the low temperature switching mechanism. However, these small nucleated domains are uncorrelated, showing the different nature of the two switching types.

Note that, at zero field the forcefield supports the multiple phases of $PbZr_{0.5}Ti_{0.5}O_3$: monoclinic symmetry at 100 K, rhombohedral symmetry at 200 K and tetragonal symmetry at 300 K [23]. The monoclinic and rhombohedral phases could, therefore, be the origin of the the observed rotational mode, by facilitating the polarisation rotation. To rule out the correlation of the rotational switching mode with the low temperature symmetries, a strictly tetragonal PZT composition is modelled. Similar calculations are performed of polarisation switching events for tetragonal $PbZr_{0.2}Ti_{0.8}O_3$ at a field of 80 MV/m. Remarkably, it is observed that at low temperatures (100 K) the tetragonal $PbZr_{0.2}Ti_{0.8}O_3$ also exhibits rotational polarisation switching despite the temperature driven phase transition having only a tetragonal phase below the Curie temperature (see Appendix F, Figure F.1).

The observation of two different switching mechanisms at room and low temperatures is indicative of two competing mechanisms that we suggest have different field dependencies of the switching barrier. Vopsaroiu *et al* [256] analysed the temperature and field dependence of the switching time by considering a distribution of barriers. The barrier height falls linearly with applied field due to the linear increase in energy of the unfavorable polarisation state. In this model "clusters" of reversed polarisation are nucleated in a similar way to Ref. [257]. In the case of PZT, the intrinsic B-site cation disorder will naturally result a distribution of barriers for local clusters, of which those with particularly low barriers would correspond to the nucleation sites identified in Ref. [256]. The polarisation rotation switching mechanism would also be expected to have a barrier that decreases linearly with applied field, for the same reason, but the gradient of the decrease would be different. A steeper decrease for the rotation mechanism would ensure that rotation dominates at low temperatures, where the switching fields are higher due to the lower thermal energy. Thus the linear field dependence of the switching barriers could explain the cross-over between mechanisms at low temperature.

7.5 The Effect of Local Environment on the Microscopic Switching Events

In the previous Section two different switching mechanisms were identified at low and room temperature. In this Section, the behaviour of the low temperature switching mechanism is investigated in relation to the B-cation disorder. The DoP is used again, this time implementing the ferroelectric displacement δ (as defined in §5.5.1) as the order parameter. This is shown in Figure 7.6 for the 100 K (a) and 300 K (b) simulations. As would be expected, the closely related order parameters show the same behaviour and the same conclusions can be drawn as to the switching mechanisms. The comparison is highlighted in Figure 7.7 where the profile of the average local polarisation and average ferroelectric displacement of the x-components at

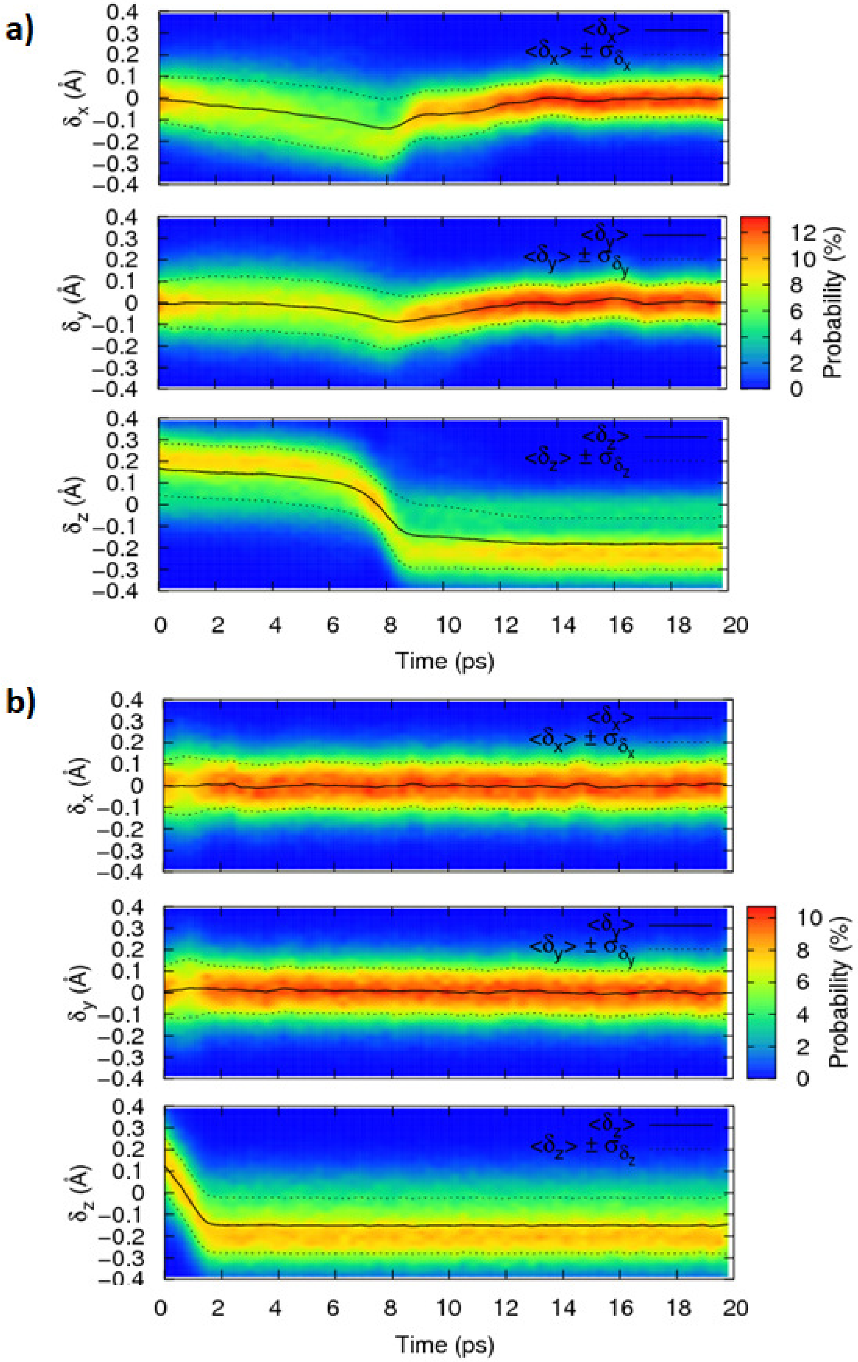

Figure 7.6: B-cation ferroelectric displacement density of probability during switching at (a) 100 K and (b) 300 K. The solid black lines trace the mean of the i^{th} ferroelectric displacement component $\langle\delta_i\rangle$. Dotted lines trace the standard deviation from the mean displacement $\langle\delta_i\rangle \pm \sigma_{\delta_i}$.

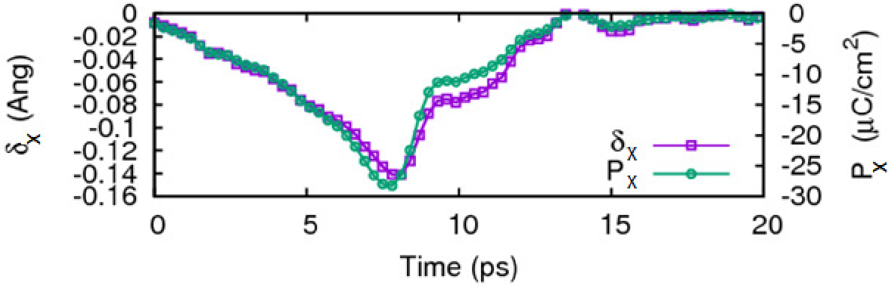

Figure 7.7: Comparison of the profiles of the average x-component ferroelectric displacement and polarisation.

100 K are overlayed. Nonetheless, there is not a perfect agreement showing that the octahedral oxygen cages (not considered in the approximation of δ) play a subtle role during switching. The behaviour of the cages is likely to be strongly dependent upon the local environment since the parent compounds of PZT, $PbTiO_3$ and $PbZrO_3$, have very different ferroelectric properties. In particular, $PbTiO_3$ adopts a high symmetry ferroelectric tetragonal phase whereas $PbZrO_3$ has a lower symmetry, antiferroelectric, orthorhombic phase that includes antiferrodistortive cage rotations [32].

In order to quantify the differences between the two B-cation species during low temperature switching, the DoP has been calculated considering the contributions from each species independently. This is shown in Figure 7.8 for Ti centred unit cells (a) and Zr centred unit cells (b).

Remarkably this analysis shows unexpected behaviour by a subset of Ti centred unit cells. Despite the probability of any unit cell having $P_z \approx 0$ being negligible either side of the switching event (Figure 7.2a), it is observed that only 53.2% of the Ti-centred unit cells have a ferroelectric displacement exceeding 0.1 Å resulting a distinctive double peak in the DoP (traced by the dashed line and highlighted by arrows). That is, almost half of the Ti atoms appear (on average) to be ferroelectrically inactive, yet the cell has a significant polarisation. This can only occur due to the offset of the octahedral cage. This result is particularly important in relation to high

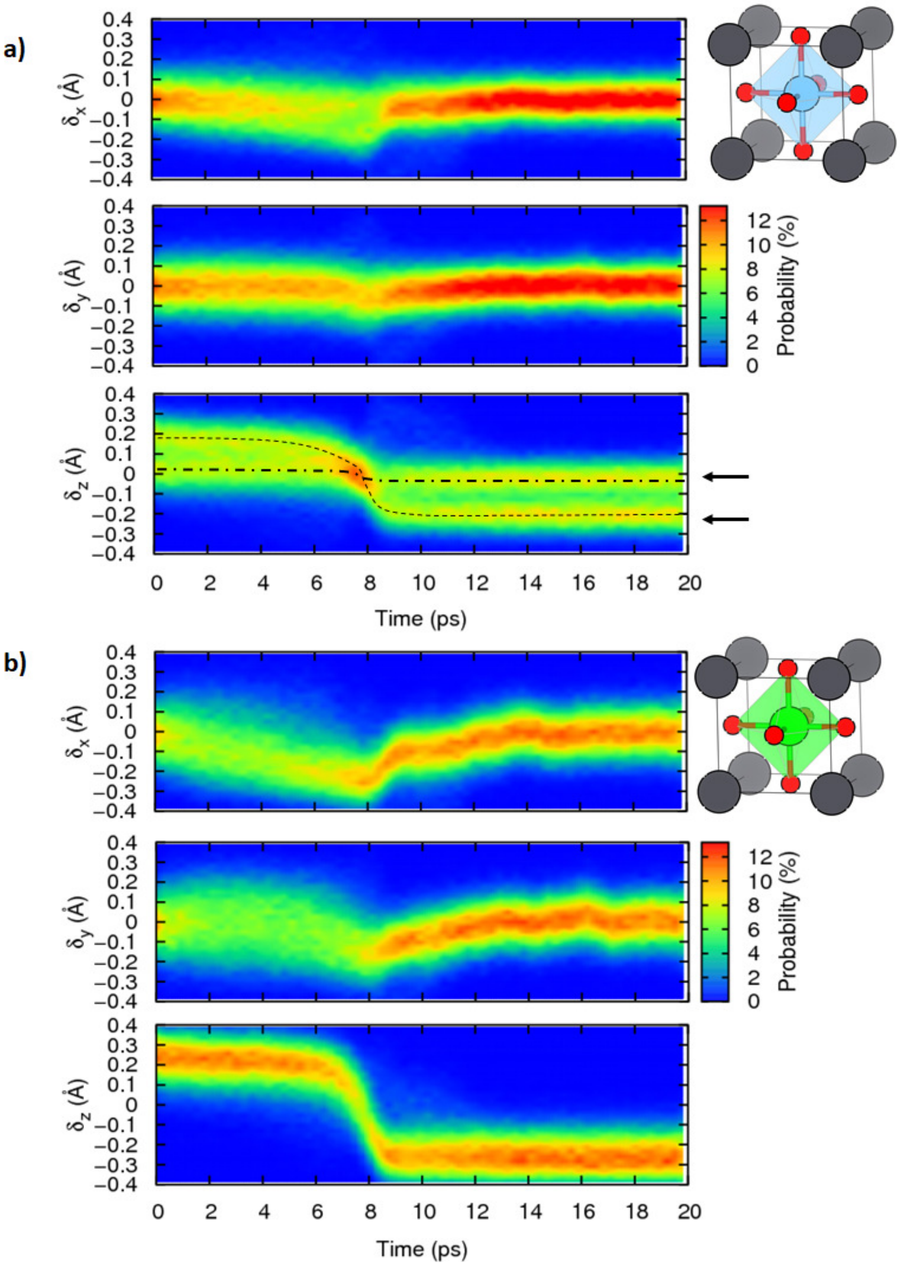

Figure 7.8: Behaviour of the B-cation displacements from the centre of the unit cell during the low temperature switching mechanism of PZT (100 K). (a) Contribution from Ti-centred and (b) Zr-centred unit cells. For δ_z^{Ti} an unexpected double peak is identified. Both peaks are traced by dotted black lines.

resolution transmission electron microscopy (HRTEM) reports in the ferroelectric literature. Typically in these experiments, the A and B cations of a perovskite can be directly viewed. This is due to the high nuclear charge of these cations, resulting in a high scattering power and a strong phase contrast [258]. Using these methods the cations can be resolved to a precision of a few picometers such that their ferroelectric displacements can be measured and the local polarisation approximated. However, until the invention of the abberation corrected TEM which produced Figure 5.1a in 2011, HRTEM measurements have been unable to detect oxygen atoms due to their weak scattering yield [258]. Difficulties in imaging oxygen are further found in other common scanning transmission electron microscopy approaches such as the high-angle annular dark-field technique [259]. Consequently, the results in Figure 7.8a show that the oxygen displacements can act as the ferroelectrically active atoms and inclusion of only the relative cation displacements in an analysis of ferroelectric behaviour can give rise to erroneous conclusions. In particular, one might conclude that in this switching simulation that there is a significant Ti-rich 'dead-layer' which remains unpolarised. However, from the polarisation DoP this is known not to be true.

The DoP of the Zr-centred unit cells (Figure 7.8b) shows that these cells are responsible for the polarisation rotation identified in §7.4. Unlike the DoP for Ti-centred cells which remains predominantly symmetric about $\delta_x = 0$ and $\delta_y = 0$, the x and y components of the ferroelectric displacements of Zr-centred cells are observed to significantly deviate from zero. This behaviour can be understood from differing properties of $PbTiO_3$ and $PbZrO_3$. $PbZrO_3$ has an orthorhombic groundstate resulting from a lowering in energy towards the M(0.5,0.5,0) and R(0.5,0.5,0.5) points in the simple cubic BZ on paths from Γ or X(0,5,0,0) [129]. Consequently, upon application of the electric field, Zr-centred unit cells attempt to switch via the eigendisplacements associated with these soft modes. This is evident from the spike in the adoption of orthorhombic and rhombohedral local phases observed in Figure 7.5c, corresponding to the modes at M and R, respectively. The 30% of unit cells remaining in a tetragonal phase can be attributed to the Ti-centred unit cells since the energetically favourable eigenvector of $PbTiO_3$ are from displacements condensing from the Γ-point soft-mode, which is the tetragonal phase structure.

In order to understand why some ferroelectric displacements of Ti are suppressed, the local environment is sampled in Figure 7.9a. For each instant in time during the simulation (x-axis), the unit cells contributing to each bin recording a range of ferroelectric displacements (y-axis) are probed to identify the number of Ti centred unit cells in the first coordination sphere of B-cations. The average Ti coordination (which can be any value between 0 and 6, inclusive) is identified by the z-axis (colour map). The trace of the peaks from the DoP is overlayed for comparison. Any bins that have no contributions are undefined and represented by white-space.

It is immediately clear from Figure 7.9a that the local environment surrounding a Ti-centred cell is significant. Those Ti-centred cells in Zr-rich environments correspond to large ferroelectric displacements, whereas the Ti-centred cells in Ti-rich regions have suppressed displacements. At the beginning of the production run (t=0 ps) and the end of the simulation (t=20 ps), 2D histograms (y-z slices of Figure 7.9a at the respective times) are plotted alongside the instantaneous histograms of the DoP at the same instants in time in Figure 7.9b. It is apparent that the double peak arises from the disparity between Ti-rich and Zr-rich environments, with the local minimum in the DoP relating to the equally rich environments (3 Ti and 3 Zr neighbouring cells).

From the ferroelectric displacement DoP it was discovered that the Zr-centred unit cells facilitated the polarisation rotation, but it remains unclear as to which local environment initialises the nucleation of the reverse domain seen in Figure 7.4. To address this, the volume fraction of unit cells

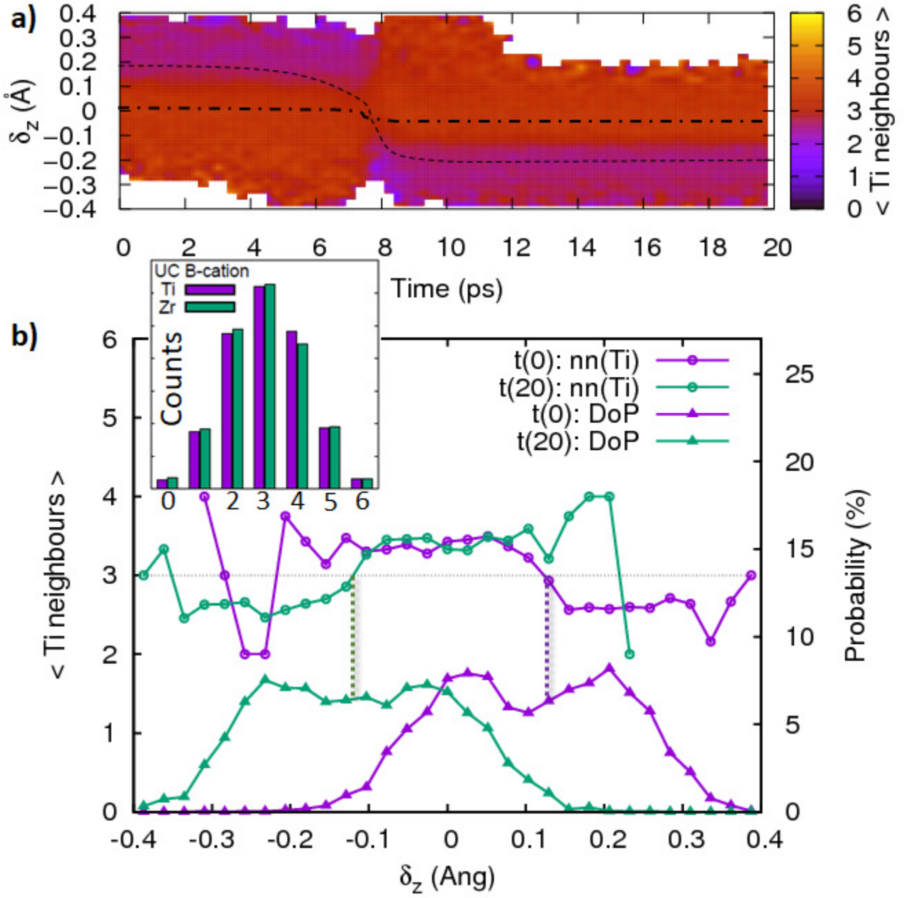

Figure 7.9: Effect of local environment within $PbZr_{0.5}Ti_{0.5}O_3$ on the switching dynamics. (a) Average Ti coordination of nearest neighbouring cells for the ferroelectric displacement distribution of Ti-centred unit cells. (b) Histograms of the average Ti coordination of the ferroelectric displacement distribution at 0 ps and 20 ps in comparison to the density of probability. Inset: Structural distribution of the number of nearest neighbouring Ti cells from Ti-centred (purple) and Zr-centred (green) unit cells.

polarised anti-parallel to the applied field is recorded during the switching event and presented in Figure 7.10 as a function of the Ti coordination surrounding Ti-centred cells (a) and Zr-centred cells (b).

For both Ti and Zr-centred cells there is a clear trend that cells with fewer Ti nearest neighbours begin to switch before those in a Ti-rich en-

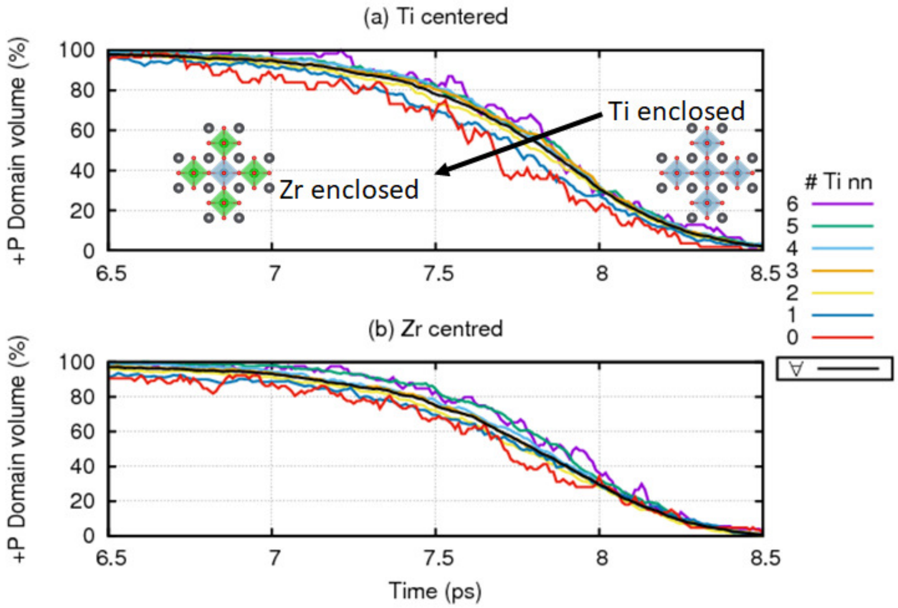

Figure 7.10: Volume fraction of un-switched (a) Ti-centred and (b) Zr-centred unit cells, decomposed into the contributions from cells with different Ti nearest neighbour coordination. The average from all contributions is shown by the black line. Inset figures show a 2D representation of Zr (green) and Ti (blue) rich coordination.

vironment. Indeed, when the reverse domains first start nucleating (Figure 7.4a) this occurs as a gradual rotation such that cells don't begin to have a negative P_z component until approximately 6 ps into the production run. At 6.5 ps, 10% of Zr-centred unit cells in very Zr-rich environments have switched but the majority of other unit cells remain positively polarised. From 6.5 ps to 8.5 ps, all other cells become negatively polarised such that they align in parallel to the applied field. The cells with 6 Ti nearest neighbours switch 0.25 ps after those with 6 Zr nearest neighbours such that there is an approximate 10% difference in switching speeds observed in this simulation between the two environmental limits. This highlights potential methods to improve the switching rate of PZT capacitors. Since Zr-rich regions facilitate switching, it would be advantageous to ensure that there are Zr rich clusters near electrode contact points.

7.6 Rhombohedral PZT

In the previous Sections it has been shown that two switching mechanisms exist for morphotropic PZT and that the rotational mechanism persists within Ti rich $\mathrm{PbZr_{0.2}Ti_{0.8}O_3}$. In this section, the switching dynamics of nominally rhombohedral phase $\mathrm{PbZr_{0.8}Ti_{0.2}O_3}$ is studied.

A $20 \times 20 \times 20$ supercell of $\mathrm{PbZr_{0.2}Ti_{0.8}O_3}$ is forward poled using an 30 MV/m electric field along [001] at 100 K. Unlike the morphotropic PZT, the rhombohedral PZR (r-PZT) breaks into domains when forward poled. Since the rhombohedral unit cell has 8 degenerate polarisation orientations (along $\langle 111 \rangle$), upon application of the [001] field those orientations whose z-components align parallel become favorable such that 4 of the 8 variants persist. This is referred to as a *4R* engineered domain configuration in the literature [260]. In this simulation, only two species of domain condense into the forward poled structure ($[\bar{1}11]$ and $[1\bar{1}1]$), separated by a 71° domain walls along [110] (Figure 7.11a). Such walls traversing at 45° from [001] are characteristic of [001] poled rhombohedral ferroelectrics and are also observed PMN-rich PMNPT [261]. The formation of two domains is likely an artificial finite size effect of the supercell creating a *2R* state opposed to *4R*. Whilst such a configuration usually appears from poling along [101], it is worth considering here as 2R states have been experimentally found to have large piezoelectric coefficient d_{33} and mechanical quality factor Q_{m33} due to the persistent 71° domains [260]. These are useful for high power applications requiring resonant frequency [262, 263].

The response to the application of the reverse field (30 MV/m along $[00\bar{1}]$) is significantly different from morphotropic and tetragonal phase PZT. In this case, reverse domains nucleate that rapidly propagate along the [001] direction to create a column faceted by $\langle 110 \rangle$ (see Figure F.2 in

Appendix F). Within a given domain, such as the $[1\bar{1}1]$, the nucleated reverse domain is that whose orientation is its mirror about the (001) plane, in this case $[1\bar{1}\bar{1}]$. The column-like reverse domains grow by reorientating the z-component of the polarisation of the adjacent cells within the original domain (Figure 7.11b). This reversal does not propagate across the pre-existing 71° domain wall such that it is conserved as has been observed experimentally for 2R engineered domains [260]. The same process is observed to occur in the switching of the $[\bar{1}11]$ domain.

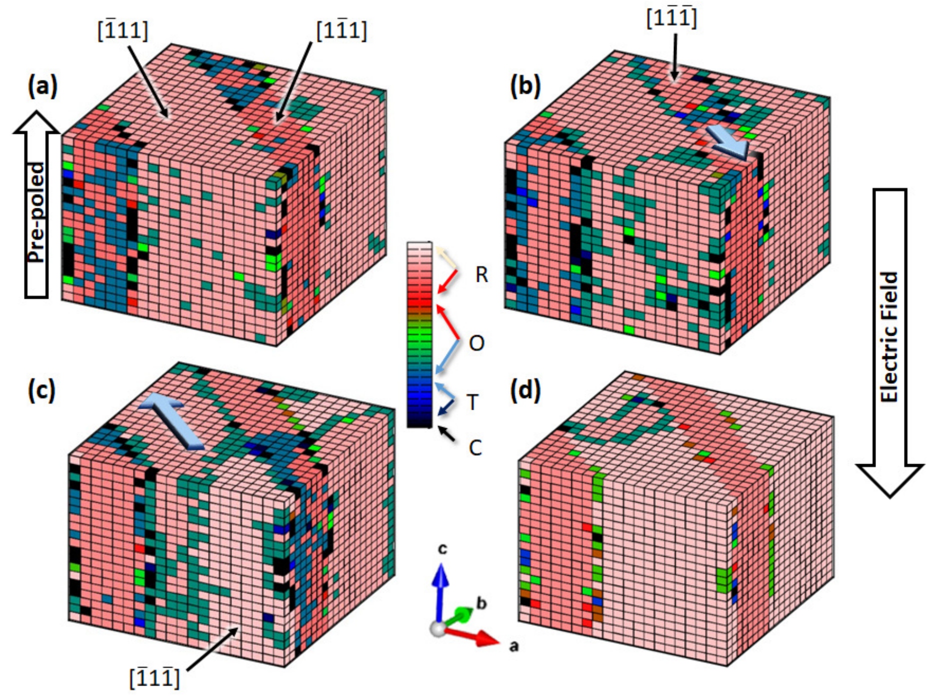

Figure 7.11: Switching of forward-poled rhombohedral *2R* $PbZr_{0.8}Ti_{0.2}O_3$ at 100 K. Domain configuration at (a) 1 ps (b) 2 ps (c) 5 ps and (d) 14 ps. Each unit cell is represented by a cube whose colour identifies the local phase, determined from the local polarisation (see Figure 7.5). The electric field nucleated a reverse domain which grows via domain wall motion preserving the existing domain walls. Arrows show growth direction in (b) and (c) of the $[1\bar{1}\bar{1}]$ and $[\bar{1}1\bar{1}]$ domains.

Another difference between morphotropic PZT and rhombohedral PZT is the switching and nucleation rate. From the density of probability of the ferroelectric displacement in Figure 7.12 we can identify that, unlike the switching of $PbZr_{0.5}Ti_{0.5}O_3$, the polarisation begins to switch as soon as the reverse field is applied at 0 ps. This is likely a consequence of Zr-centred unit cells facilitate switching as was discovered in §7.5. Nonetheless, the switching rate is considerably slower only approaching complete reversal after the full 20 ps production run.

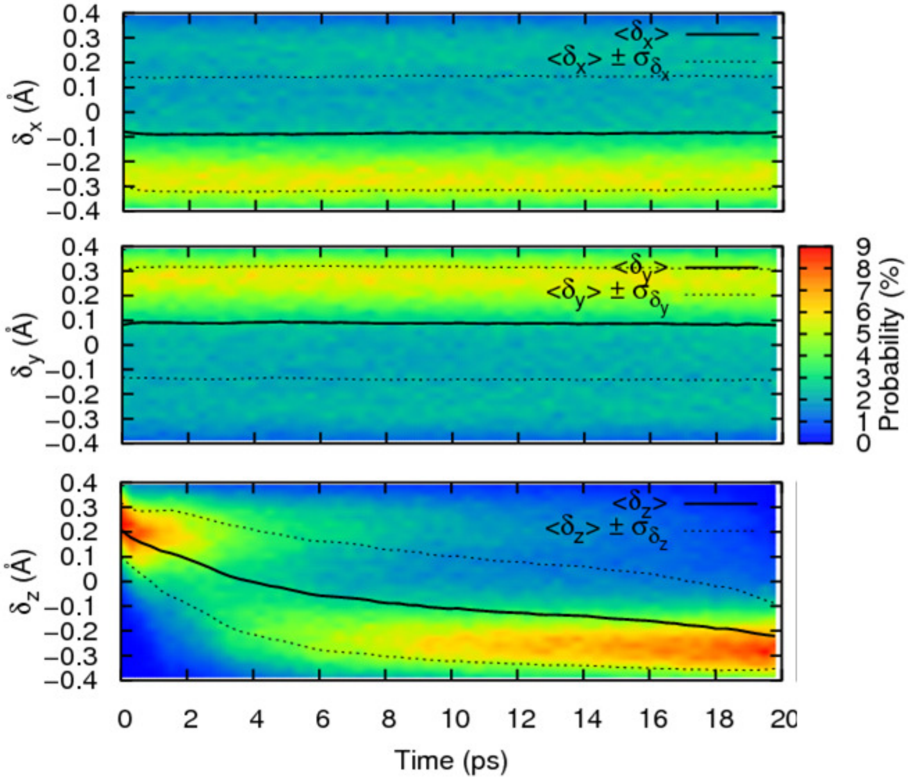

Figure 7.12: B-cation ferroelectric displacement density of probability during switching at 100 K. The solid black lines trace the mean of the i^{th} ferroelectric displacement component $\langle\delta_i\rangle$. Dotted lines trace the standard deviation from the mean displacement $\langle\delta_i\rangle \pm \sigma_{\delta_i}$.

In a future study it would be desirable to investigate $PbZr_{0.8}Ti_{0.2}O_3$ using a larger simulation cell to facilitate a 4R configuration over a range of temperatures. Nonetheless, this MD study has reported on the switching mechanism in 2R domains showing the persistence of 71° domains walls, which will inform the development of high quality factor piezoelectrics.

7.7 Conclusions

In this chapter, classical MD simulations of polarisation switching dynamics have been performed in near-morphotropic PZT and rhombohedral phase PZT, using a shell model force field. The hysteretic behaviour of the polarisation with applied electric field for different temperatures is reported. The shape of the P-E loops was found to be temperature dependent and to exhibit a narrowing towards high temperatures. Further, it was shown that E_C increases with decreasing temperature which was confirmed experimentally by electrical measurements. The nature of the switching mechanism, observed from the simulations at room temperature, were in good agreement with earlier experimental studies on PLZT thin films [255] where domain nucleation was found to be the dominating switching process. It has shown in this work, however, that at low temperatures the electric-field induced switching of electrical polarisation proceeds via the rotation of polarisation which has a reduced barrier compared to nucleation driven switching at larger fields. Switching was identified to be facilitated by Zr-centred unit cells, and by extension, Ti centred cells in Zr-rich environments. At low temperatures, Ti-rich environments were observed to have suppressed ferroelectric displacements but remained ferroelectrically active due to the octahedral cage distortion. Finally, a cursory look at switching in rhombohedral PZT identified the rapid formation of columnar reverse domains but a slower switching speed in comparison to morphotropic PZT. These findings provide useful insight into the operational temperature/voltage conditions of ferroelectric-based devices used in aeronautical and space applications.

8

Intrinsic Mechanisms of Ferroelectric Ageing

In this Chapter, a fundamental insight into the microscopic mechanisms of the ageing processes is provided. Using large scale molecular dynamics simulations of the prototypical ferroelectric material $PbTiO_3$, it is demonstrated that experimentally observed ageing phenomena can be reproduced from intrinsic interactions of defect-dipoles related to dopant-vacancy associates, even in the absence of extrinsic effects. Variation of the dopant concentration is shown to modify the material's hysteretic response, identifying a universal method to reduce loss and tune the electromechanical properties of inexpensive ceramics for efficient technologies.

The results presented in this Chapter have been partly discussed in J.B.J.Chapman, R.E.Cohen, A.V.Kimmel & D.M.Duffy, Physical Review Letters **119**, 177602 (2017).

8.1 Introduction

Technologies utilising ferroelectric components are ubiquitous in modern devices, being used from mobile phones, diesel engine drive injectors and sonar to print heads and non-volatile memory [8, 12, 264, 265]. Doping with transition metals has been shown experimentally to improve electromechanical properties of widely used ferroelectrics. For example, doping of $BaTiO_3$, $PbTiO_3$, $Pb(Zr_{1-x}Ti_x)O_3$ (PZT) and $(1\text{-x})Pb(Mg_{1/3}Nb_{2/3})O_3$-$xPbTiO_3$ (PMNPT) is used to improve the functional properties and efficiency of these simple and cheap oxides [266–274]. However, the fundamental origin of the electromechanical improvements is not understood and requires full characterisation to enable properties to be directly tuned for purpose and functional lifetimes to be accurately predicted.

Dopant interactions can be classified as intrinsic (bulk or volume) or extrinsic (boundary). Extrinsic coupling is associated with domain wall and grain boundary effects. Defects, including dopants and vacancies, migrate to domain walls and subsequently pin their propagation, resulting in fatigue of the material's switching properties [275]. Intrinsic effects occur independent of interaction with domain walls, as they arise due to the interaction between defect induced dipoles $\mathbf{p_d}$ and the spontaneous polarisation of the domain surrounding the defect site $\mathbf{P_s}$. Strong evidence from electron paramagnetic spin resonance (ESR) and density functional theory (DFT) calculations has shown dopants (or impurities), such as iron Fe^{3+} and copper Cu^{2+}, in PZT (or Mn^{2+} in $BaTiO_3$) substitute the B-cations as acceptors, which bind to charge compensating oxygen vacancies V_{O}^{2-} to form thermodynamically stable defect complexes [276, 277]. In Kröger-Vink notation, the divalent dopant-vacancy associates can be written as $(B''_{\mathrm{Ti}} + V_{\mathrm{O}}^{\bullet\bullet})^{\times}$, where B''_{Ti} is an unspecified divalent dopant substituting a Ti^{4+} site, $V_{\mathrm{O}}^{\bullet\bullet}$ is an oxygen vacancy with a +2e charge relative to the defect free site, $'$ identifies a negative charge unit (-e), $\bullet$ represents a positive

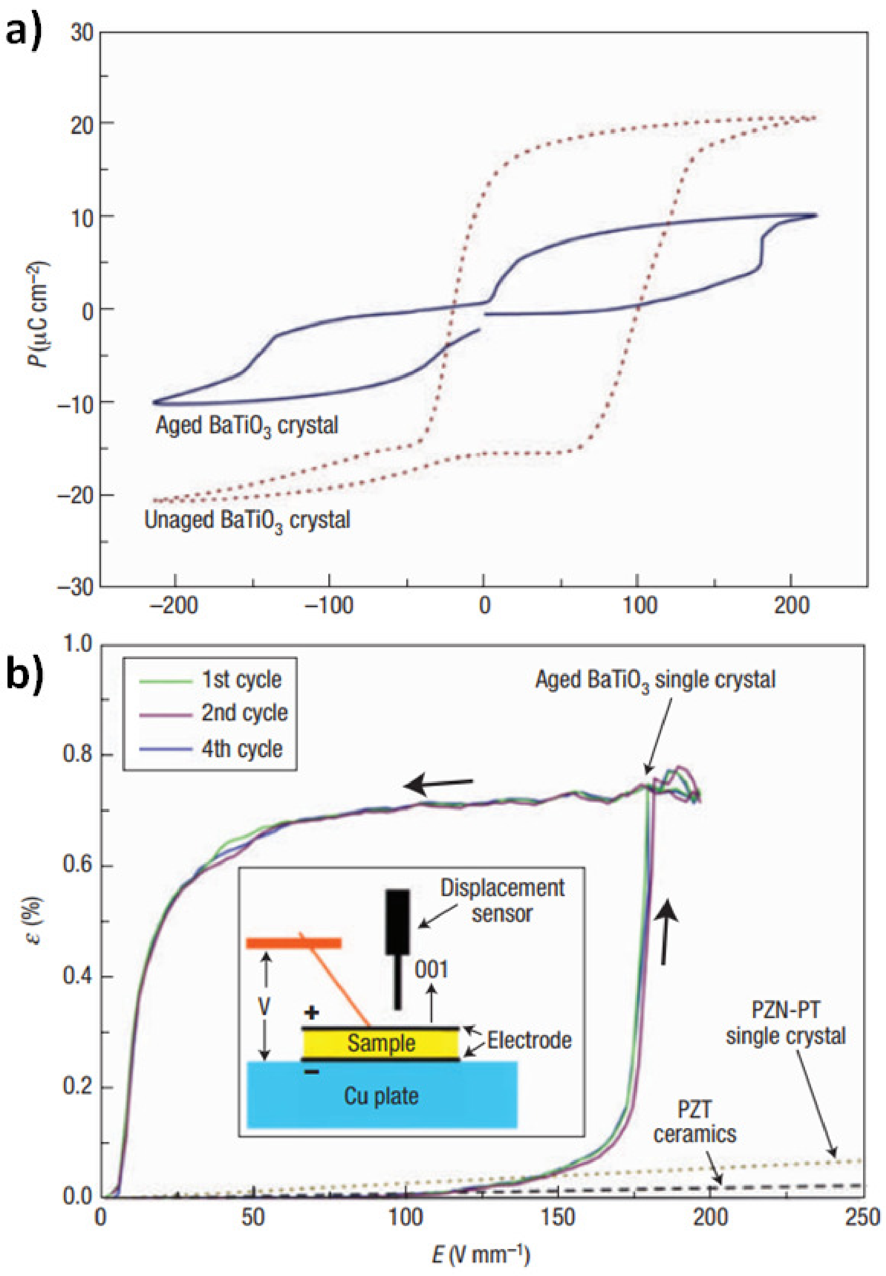

Figure 8.1: Ageing phenomena observed in BaTiO$_3$ single crystals. (a) Double P-E hysteresis loop of an aged sample (solid) compared with the bistable hysteresis (dashed) of the same unaged sample. (b) Large recoverable electric field induced strain along $[001]_p$, in comparison with PZT ceramics and PZN-PT single crystals. Reprinted with permission from Ref. [270]. Copyright (2004) Nature Publishing Group.

charge unit (+e) and × stands for charge neutrality. Density functional theory calculations have shown defect-dipoles $\mathbf{p_d}$ spontaneously form for $(Fe^{'}_{\mathrm{Ti}} + V^{\bullet\bullet}_{\mathrm{O}})^{\bullet}$ [278] and $(Cu^{''}_{\mathrm{Ti}} + V^{\bullet\bullet}_{\mathrm{O}})^{\times}$ [277] associates in $\mathrm{PbTiO_3}$ and $(Mn^{''}_{\mathrm{Ti}} + V^{\bullet\bullet}_{\mathrm{O}})^{\times}$ in $\mathrm{BaTiO_3}$ [271,279], and the energetically favourable orientation is along the polar axis [001]. Group-IIIB and group-VB acceptor substitutes on Ti sites in $\mathrm{PbTiO_3}$ have been shown to form immobile clusters of dopant-vacancy associates which have different structures when the associate is aligned parallel or perpendicular to the polar axis [280]. $(V^{''}_{\mathrm{Pb}} + V^{\bullet\bullet}_{\mathrm{O}})^{\times}$ divacancy complexes in $\mathrm{PbTiO_3}$ have been calculated to have a local dipole moment twice the bulk value [281].

Ageing is simply defined as the change in a material's properties over time. It has been proposed that in aged ferroelectrics, defect-dipoles produced from dopant-vacancy associates will slowly rotate to align in parallel with the domain symmetry to minimise its energy state [91, 270, 282]. The co-alignment and subsequent correlated behaviour of these aged defect-dipoles has been proposed to create a macroscopically measurable internal bias, which in turn has been conjectured to be responsible for experimentally observed ageing phenomena, including a 10 to 40-fold increase in piezoelectric coefficients, shifts in the hysteresis along the electric field axis and pinched/double hysteresis loops typically associated with antiferroelectrics (Figure 8.1) [264, 270–272].

In this Chapter, large scale classical molecular dynamics is used to model ageing arising from defect-dipoles of dopant-vacancy associates in tetragonal bulk lead titanate ($\mathrm{PbTiO_3}$). In Section 8.3 it is shown that all the experimentally observed large signal effects (P-E and S-E hysteresis) of aged prototype perovskite ferroelectrics; pinched and double hysteresis, shifted hysteresis and a large recoverable electromechanical response can be reproduced from intrinsic effects alone and we identify the microscopic mechanisms of each case. Temperature dependence is studied in Section 8.4 and dopant concentration is shown to modify the hysteretic response which identifies a universal method to reduce loss and tune the electromechanical properties of ferroelectric ceramics.

8.2 Simulation Methodology

Ideal and aliovalent-doped bulk $PbTiO_3$ is studied using classical molecular dynamics (MD) as implemented in the DL_POLY code [132]. The adiabatic core-shell interatomic potentials derived in Gindele *et al* [23], which reproduce the properties of bulk and thin films of $PbTiO_3$ in excellent agreement with DFT calculations [23, 283], are used. The prototype $PbTiO_3$ has been chosen as it has a single ferroelectric phase, which reduces competing effects and because it is a parent compound for two of the most widely used ferroelectric materials throughout industry (PZT and PMNPT).

In this study intrinsic effects are investigated, therefore, three - dimension periodic boundary conditions are implemented to mimic an infinite crystal, devoid of surfaces, interfaces and grain boundaries. A moderate supercell has been chosen, constructed from $12 \times 12 \times 12$ unit cells, approximately 125 nm^3, corresponding to 8640 atoms (for the ideal bulk). This system size is large enough for ensemble sampling but sufficiently small to prevent the formation of 90° domain walls. Coupling between strain and polarisation is enabled using the constant-stress Nosé-Hoover ($N\sigma T$) ensemble with thermostat and barostat relaxation times of 0.01 ps and 0.1 ps, respectively. A 0.2 fs timestep is used in all instances. Initial calculations were run at 100 K to prevent diffusion of the vacancies [284,285] and to allow the correct characterisation of each effect. The temperature dependence, for the range from 50 K to 400 K, were then investigated.

Polarisation - electric field (P-E) hysteresis is calculated using a quasistatic approach. Starting at 0 kV/mm, the electric field is cycled between the limits ±150 kV/mm in 16.7 kV/mm intervals. For each field strength the system is restarted using the coordinates, velocities and forces from the previous calculation and equilibrated for 4 ps to enable the system to equilibrate following the E-field impulse. This is followed by an 8 ps production run over which statistics are collected (total of 12 ps per iteration). This approach is advantageous over a continuous hysteresis which requires a shallow gradient for the electric field, large simulation sizes and very long run times to achieve similar accuracy.

A dopant-vacancy concentration $n_d = 100(N_{\mathrm{Ti}}^{\mathrm{ideal}} - N_{\mathrm{B}''})/N_{\mathrm{Ti}}^{\mathrm{ideal}}$ is introduced into the supercell initially containing $N_{\mathrm{Ti}}^{\mathrm{ideal}}$ Ti atoms, by randomly selecting a total of $N_{\mathrm{B}''}$ Ti atoms to be replaced with generic divalent dopants B''_{Ti}. Each dopant is coordinated by six nearest neighbouring oxygen-sites from which a charge compensating oxygen vacancy, $V_{\mathrm{O}}^{\bullet\bullet}$, can be introduced. This configuration mimics $(B''_{\mathrm{Ti}} + V_{\mathrm{O}}^{\bullet\bullet})^{\times}$ dopant-vacancy associates observed from ESR experiments. A schematic of the associate is shown in the inset of Figure 8.2a.

In experiments, it is observed that the properties of an aged sample can be removed by heating above the Curie temperature for a long period and then rapidly quenching. It has been hypothesised that during this 'un-ageing' process in the cubic phase of the prototype ferroelectric, each orientation of the defect-dipole is equally probable such that vacancies will thermally hop between the neighbouring oxygen site adjacent to the dopant and eventually $^1/_6$ defect-dipoles will populate each of the six possible directions [270]. These are then frozen when quenched into the ferroelectric phase. Ferroelectrics can then be intentionally aged again by applying a bias field for a significantly long period. It is believed this causes defect-dipoles to align. Even in the absence of an intentional ageing field, defect-dipoles in a sample left for a long period will align with the spontaneous polarisation of the domain [272].

When constructing the supercell for a particular simulation, the choice of which oxygen is removed neighbouring the dopant depends on the aged /

unaged condition:

1. Unaged condition:
   To simulate unaged tetragonal $PbTiO_3$, $N_{B''}/6$ defect-dipoles are assigned along each of the six possible orientations causing the total moment to cancel, Figure 8.2b.

2. Aged condition:
   To simulate an aged $PbTiO_3$ sample, each $V_O^{\bullet\bullet}$ is selected to situate on the oxygen-site along the ageing direction (defined below) relative to its associated dopant. For these simulations the ageing direction is arbitrarily chosen along $+\hat{x}$ (see Figure 8.2a). This initialises all defect dipoles $\mathbf{p_d}$ as parallel, polarised along $[\bar{1}00]$ as shown in Figure 8.2c.

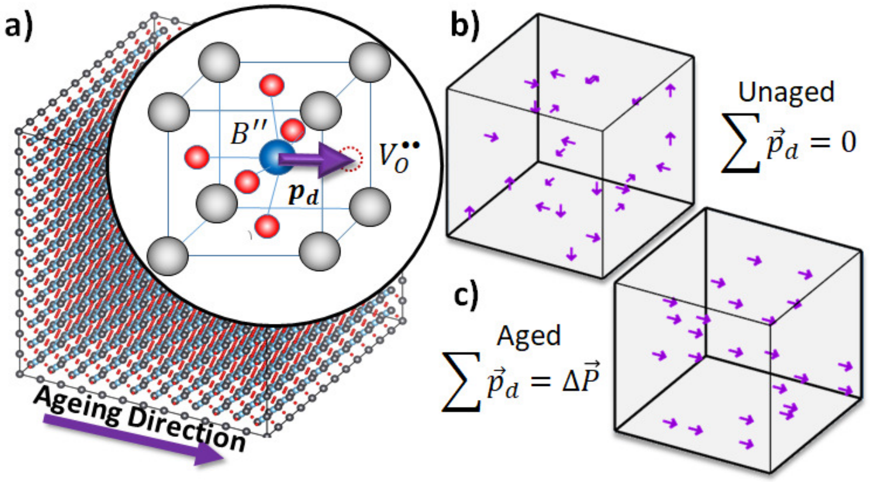

Figure 8.2: System configuration for MD simulations of ageing. (a) $PbTiO_3$ supercell including defect-dipoles from $(B''_{Ti} + V_O^{\bullet\bullet})^{\times}$ associates (inset). (b) Defect-dipoles in unaged $PbTiO_3$ are randomly orientated. (c) Aged $PbTiO_3$ is modelled by aligning all defect dipoles along the ageing direction [100].

The ageing direction is defined relative to the driving field for the hysteresis characterisation. If the defect dipoles are co-aligned with the driving field we label this as aged($\|$), whereas perpendicular alignments are labelled aged($\perp$). The strain is calculated as $\Delta\epsilon = (c_0 - c)/c$ where c_0 is the relaxed lattice constant (parallel to the drive field orientation) under no applied field.

To check the viability of the forcefield with the $(B''_{\mathrm{Ti}} + V^{\bullet\bullet}_{\mathrm{O}})^{\times}$ associates the phase transition is tested for unaged ($n_d = 1.38$ %) $\mathrm{PbTiO_3}$. Given ESR experiments have ascertained these associates exist [276] (often as an unintentional consequence of the fabrication processes as opposed to intentional doping), it is expected that the unaged $\mathrm{PbTiO_3}$ should behave very similar to the ideal prototype system since this agrees well with the experimentally observed transition. Indeed, a comparison between the unaged and pure systems show the temperature driven phase transition to be reproduced remarkably well (Figure G.1 in Appendix G). Further, as has been shown from DFT, preferential alignment of the dopant-vacancy associate in the forcefield calculation is along the polar axis, which is 0.46 eV lower in energy than an axial alignment. This is very comparable to the 0.45 eV and 0.86 eV DFT energy differences for $(Fe'''_{\mathrm{Ti}} + V^{\bullet\bullet}_{\mathrm{O}})^{\bullet}$ and $(Cu''_{\mathrm{Ti}} + V^{\bullet\bullet}_{\mathrm{O}})^{\times}$ associates, respectively [276]. For the forcefield this value was calculated from a $3 \times 3 \times 3$ fixed volume cell, containing a single $(B''_{\mathrm{Ti}} + V^{\bullet\bullet}_{\mathrm{O}})^{\times}$ associate and geometry optimised using GULP [131].

The polarisation, d_{33} and d_{13} piezoelectric coefficients were calculated for the bulk, aged and unaged $\mathrm{PbTiO_3}$ cases at 10 K, shown in Table 8.1. The polarisation is shown to still support the bulk value, signifying the forcefield remains well behaved. A 15 % increase in the intrinsic d_{33} coefficient is observed for both the aged and unaged cases. This brings the quantity into the experimentally observed range of 52-65 pC/N [286].

	P_s	d_{33}	d_{13}
Bulk	48.18	47.8±0.8	-14.0±0.8
Unaged	48.97	54.1±1.0	-15.1±1.0
Aged	49.05	55.8±1.1	-15.4±1.0

Table 8.1: Polarisation and piezoelectric coefficients of aged and unaged $PbTiO_3$ at 10 K with n_d=1.38% in comparison to bulk ($n_d = 0\%$).

8.3 Intrinsic Mechanisms of Ageing

Firstly we discuss results obtained at 100 K, to observe the ideal behaviour minimising the likelihood of thermal diffusion or hopping. In all instances, the response is highly non-linear, typical of ferroelectrics. For the ideal bulk case a symmetric, square loop indicative of a hard ferroelectric is observed. We note our bulk coercive field E_c^{int} corresponds to the material's intrinsic coercive field, which greatly exceeds those measured experimentally for Pb-based ferroelectrics [265]. This is because our model excludes grain boundaries, surfaces and domain walls, which would all act as nucleation sites and lower the energy barrier for reversal in physical samples [256]. Our result of 130 kV/mm (at 10 K) matches other MD models [248] and is in excellent agreement with the intrinsic coercive field of 150 kV/mm calculated using density functional perturbation theory [249].

8.3.1 Unaged $PbTiO_3$

In the unaged $PbTiO_3$ simulation, a symmetric, square P-E hysteresis loop is observed, which is similar to that calculated to the bulk, defect free sample (Figure 8.3a). The computed coercive field of the unaged $PbTiO_3$ is reduced relative to the ideal bulk value by approximately 35% ($0.65E_c^{\text{int}}$). The reduction of the coercive field from E_c^{int} occurs because the dopant-vacancy associates break local symmetry. This creates localised areas where the activation energy for nucleation of reverse domains is reduced [256,287], bringing it closer to typical experimental values which are on the order of kV/mm.

As well as the P-E hysteresis, strain-electric field (S-E) *butterfly* hysteresis loops are an important large-signal[1] indicator used for characterisation (shown for the bulk and unaged cases in Figure 8.3b). For the bulk case which starts in its positively polarised state, the application of a reverse electric field causes the system to compress due to the converse piezoelectric effect (eqn. 4.19). This happens until the coercive field is reached (O → A) and the polarisation reverses such that the strain becomes positively defined (A → B). As the polarisation and field are now aligned, the converse piezoelectric effect causes the system to elongate (B → C). During the upswing of the electric-field (C → O) from the minimum field to zero-field the strain decreases back to the bulk value. The continued upswing to the maximum field strength ($O \rightarrow D \rightarrow E \rightarrow F$) and subsequent down-swing to zero-field (F → O) mirrors that of the path $O \rightarrow A \rightarrow B \rightarrow C \rightarrow O$, creating a curve resembling a butterfly.

Introduction of the dopant-vacancy associates in an unaged state are observed to create a similar S-E butterfly hysteresis (Figure 8.3b) to the bulk. As for the P-E hysteresis, the reduction in the coercive field is apparent. In Table 8.1, it was observed that the d_{33} piezoelectric coefficient, calculated from a fluctuation-perturbation approach, increased with the introduction of dopant-vacancy associates regardless of whether they were in an aged or unaged state. Since the converse piezoelectric coefficient can be interpreted as the gradient of the S-E butterfly hysteresis from equation 4.19, this is consistent with the unaged S-E hysteresis in Figure 8.3b which is observed to have steeper gradients than the bulk.

---

[1] Polarisation and strain are referred to as large-signal parameters as they are only generated by the application of high activation voltages ($\approx kV/mm$) [264]. It is common for butterfly curves to be defined such that the zero-point is the minimum of the whole loop or at the value of zero-field, the latter is used here.

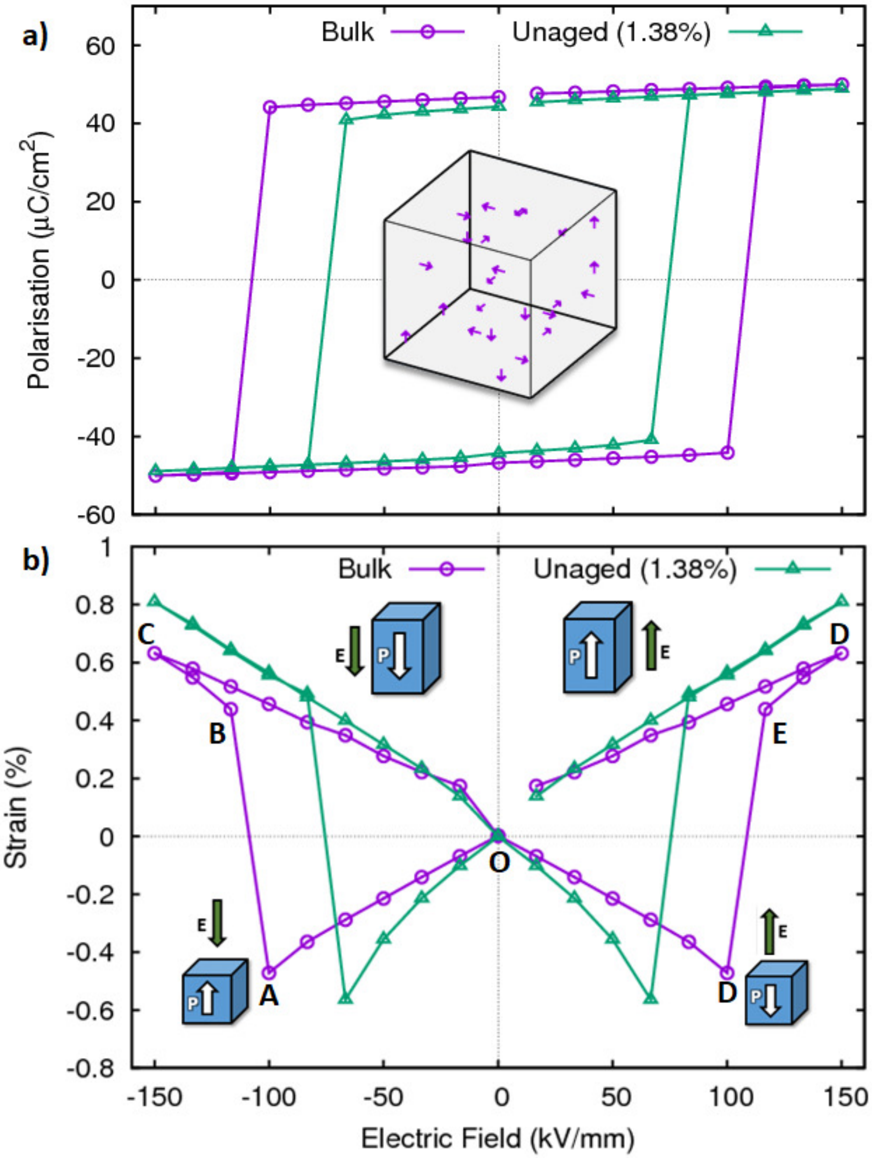

Figure 8.3: Polarisation (a) and strain (b) hysteresis of bulk and unaged ($n_d = 1.38\%$) $PbTiO_3$ at 100 K. Inset-a: Randomly aligned defect dipoles from $(B''_{Ti} + V_O^{\bullet\bullet})^\times$ associates within the simulation cell.

8.3.2 Parallel Poling of Aged $PbTiO_3$

When poling parallel to the ageing orientation the system exhibits a shifted hysteresis curve along the abscissa as shown in Figure 8.4a. Such an effect is often documented in the literature and is characterised as the internal bias field E_{bias}:

$$E_{\text{bias}} = \frac{1}{2}(E_c^+ + E_c^-) \tag{8.1}$$

As an example, a unipolar electric field applied to the doped material $Pb_{0.99}[Zr_{0.45}Ti_{0.47}\,(Ni_{0.33}Sb_{0.67})_{0.08}]O_3$ has been observed to create bias fields 3-10% of E_c for temperatures in the range 50-175°C [288]. This *unipolar fatigue* has been suggested by Balke *et al* [289] to be caused by separation and agglomeration of free-charges during the electric loading (such as the diffusion of oxygen vacancies), and these separated charges create an internal bias field off-setting the hysteresis. The charge agglomeration model has had success describing field and temperature dependence of experimentally observed bias fields in ceramic ferroelectrics. In the model, supported by a recent drift-diffusion model [290, 291], distributed vacancies move along the effective field lines (the superposition of the external field and the depolarising fields resulting from the microstructure of the ceramic grains) until equilibrium is reached when the bound charges are compensated. In the ageing model applied in this thesis, the dopant-vacancy associates can be considered the final bound charge-compensated states and a consistent solution with the agglomeration model on a single crystal of $PbTiO_3$ as $t \to \infty$.

Ageing parallel to the poling field is shown to induce an asymmetric S-E hysteresis (Figure 8.4b). Instances of highly asymmetric S-E loops have been experimentally reported in a range of ferroelectric materials [292]. In Ref. [293], the authors report a strain difference of 0.15% in Li doped $(Bi_{0.5}Na_{0.4}K_{0.1})_{0.98}Ce_{0.2}TiO_3$ ceramics which they propose is due to align-

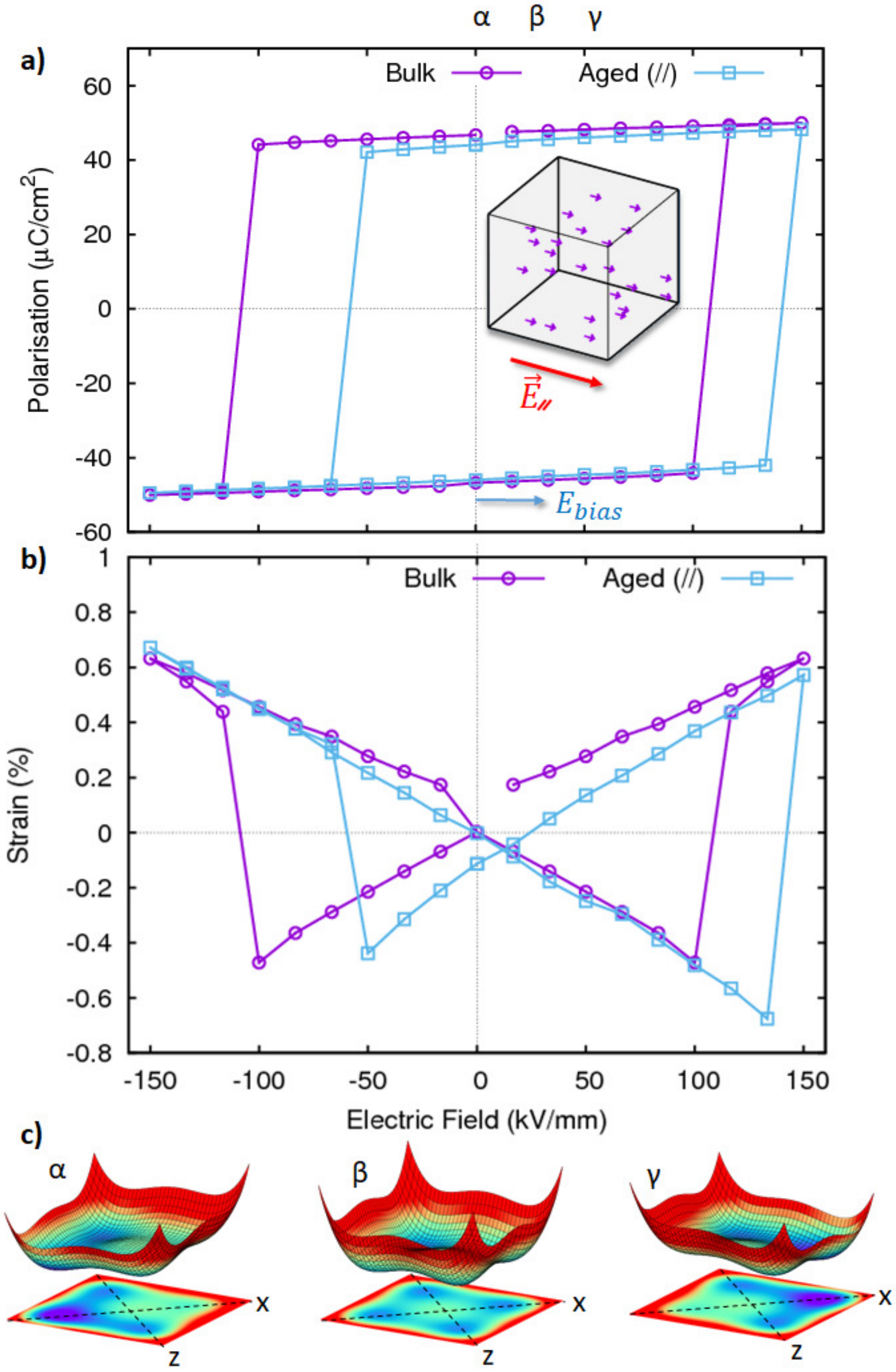

Figure 8.4: Polarisation (a) and strain (b) hysteresis of bulk and aged $(n_d = 1.38\%)$ $PbTiO_3$ at 100 K where the poling field is applied parallel to the ageing alignment. Inset: Parallel alignment of the defect dipoles from $(B''_{\mathrm{Ti}} + V_{\mathrm{O}}^{\bullet\bullet})^{\times}$ associates within the simulation cell and the poling field. (c) Cartoon potential energy surface at α, β and γ in (a). Shift along the abscissa and asymmetric butterfly hysteresis observed.

ment of $(\mathrm{Li}_{\mathrm{Ti}}^{\prime\prime\prime}\text{-}\mathrm{V}_{\mathrm{O}}^{\bullet\bullet})^{\prime}$ associates. The strain difference for a $(B_{\mathrm{Ti}}^{\prime\prime} + V_{\mathrm{O}}^{\bullet\bullet})^{\times}$ concentration of 1.38% in this model is determined to be 0.097%, remarkably similar to the dilutely doped experimental studies [293].

These effects can be understood as the modification of the $\mathcal{W}$-potential from the bias field generated by the dopant-vacancy associates which superimpose the poling field. A cartoon depicting the $\mathcal{G}(x, z)$ free energy surface is shown in Figure 8.4c for points α, β and γ labelled in Figure 8.4a. For the null-field (α), the bias applies a linear term to the potential such that it favours one polar orientation over the other. The symmetric potential (β) is only recovered when $E_{\text{bias}} + E_{//} = 0$. As such, using our prototypical system, we provide evidence that the asymmetry of both the P-E and S-E hysteresis are likely to arise from an excess orientation of defect dipoles along the poling direction and is a general feature of ageing that may be exploited for technological applications.

8.3.3 Perpendicular Poling of Aged PbTiO$_3$

Figure 8.5a shows the hysteresis of an aged single domain simulated sample, with a defect concentration of 1.38%, in response to a driving field perpendicular to the direction in which the material was aged. Interestingly, when the system is equilibrated with no applied field the spontaneous polarisation **P** reorientates parallel to the ageing direction. This shows the internal bias created from the defect-dipoles is sufficient to overcome the switching barrier [91]. This observation provides direct evidence supporting the work of Zhang *et al* [272] who observed that non-switching defect-dipoles from $(\mathrm{Mg}_{\mathrm{Ti}}^{\prime\prime}{-}\mathrm{V}_{\mathrm{O}}^{\bullet\bullet})^{\times}$ associates in BaTiO$_3$ create restoring forces that promote reversible domain switching[2]. Under the application of the perpendicular driving field there is an almost linear response until 67 kV/mm ($\approx E_c^{\text{int}}/2$), at which point the field strength is sufficient to switch the po-

---

[2] Referred to as the '*symmetry conforming principle*' by X. Ren [270].

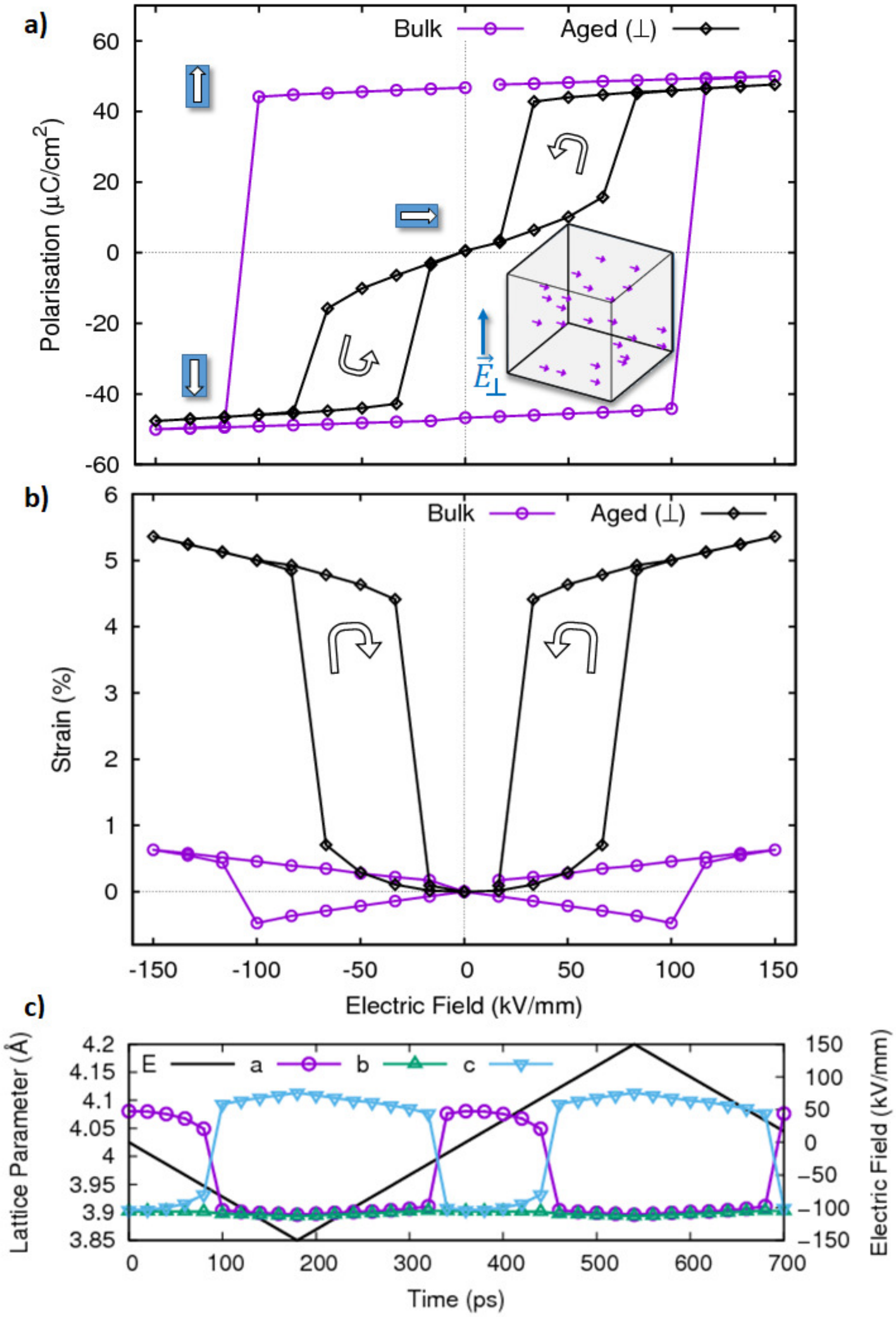

Figure 8.5: Polarisation (a) and strain (b) hysteresis of bulk and aged ($n_d = 1.38\%$) $PbTiO_3$ at 100 K where the poling field is applied perpendicular to the ageing alignment. Inset: Perpendicular alignment of the defect dipoles from $(B_{\text{Ti}}^{''} + V_{\text{O}}^{\bullet\bullet})^{\times}$ associates within the simulation cell and the poling field. (c) Average local lattice parameters a, b & c during hysteresis, showing reorientation of the polar axis for high field strengths of $E_{\perp}$. Double hysteresis and large non-linear recoverable strain observed.

larisation parallel to the driving field. As the electric field decreases to zero, the polarisation again reorientates along the ageing axis such that no remnant polarisation P_r remains in the poling direction. Thus in our work, the iconic double-hysteresis indicative of aged ferroelectrics is observed without the requirement of either domain walls or grain boundaries [264, 270].

It has been observed that ageing doped $BaTiO_3$ is capable of producing a large recoverable non-linear electric field induced strain of 0.75%; far greater than those measured in PZT or PMNPT (see Figure 8.1 [270, 271]). It is argued that a strong restoring force from aligned defect-dipoles induces polar axis rotation parallel to the defect-dipoles enabling reversible switching of 90° domains. This process could lead to the realisation of strain values of 6% in $PbTiO_3$. In Figure 8.5b, we show that ageing perpendicular to a poling field in $PbTiO_3$ leads to a large recoverable strain in excess of 4.5%. This large non-linear strain arises from the reorientation of the polar axis along the ageing direction due to the internal bias from the defect dipoles at subswitching fields (Figure 8.5c, $c \rightarrow a$, $\Delta\epsilon = (c_0 - a)/a$). On analyzing the switching behaviour, we find that, in this instance, the 90° switching occurs via near-homogeneous polarisation rotation over a small field range which is a switching mechanism predicted in bulk $PbTiO_3$ [248] and $BaTiO_3$ [91]. Our ageing results are in excellent agreement with a complementary bond valence model study of ageing in ideal $BaTiO_3$ which has used fixed dipoles introduced into the crystal structure [294]. Therefore, we show the volume effect of the dopant-vacancy associates to be a fundamental cause of this ageing phenomenon and identify a domain wall mechanism is not required for the full reproduction of experimental observations. We do note that this doesn't exclude extrinsic contributions to the ageing phenomena. Using a supercell containing $PbZr_{0.1}Ti_{0.9}O_3$ with $n_d = 1.07\%$, *ceteris paribus*, perpendicular poling is shown to create a double hysteresis loop for this Ti rich, tetragonal phase composition of PZT (Figure G.2 in Appendix G). The remarkably large recoverable strain achievable in aged $PbTiO_3$, and the solid solutions that contain it, give it an effective d_{33} to be an ideal piezoelectric component to make the piezoelectronic transistor a reality.

8.4 Effect of Temperature and Defect Concentration on (⊥) Aged $PbTiO_3$

The results of an investigation into the effect of temperature on the ageing phenomenon in $PbTiO_3$ are shown in Figure 8.6 for $n_d = 1.38\%$. As the temperature increases, a decrease in the effective coercive field and saturation polarisation are observed, corresponding to a narrowing of the double hysteresis as indicated by the trend arrows. This is analogous to the behaviour known for the square loop of the ideal prototype. Near room temperature under poling fields comparable to E_c, vacancy hopping becomes thermally activated causing limited events whereby a subset of defect dipoles reorientate. This was observed by tracking the displacement of each oxygen atom relative to its initial position. This reorientation can create asymmetric loops as seen at 400 K ($0.67T_c$), clearly demonstrating that at high temperatures/large fields the defect-dipoles can readily realign, elucidating the microscopic mechanism for aged → unaged transitions. No defect-dipoles were observed to switch below 300 K ($0.5\mathrm{T}_c$). At 300 K a single hopping event was observed (1/24 vacancies) and two (1/12 vacancies) at 400 K, over the full hysteresis. We note that due to the relatively short simulation times these hopping frequencies will be under-sampled for accurate statistics and would be an interesting subject for future investigation.

Defect concentrations close to and above 1.38% are shown to form closed double hysteresis loops as described in §8.3. As the concentration is increased the enclosed area of the hysteresis loops decrease due to the increased strength of the internal bias E_{bias}, which lowers the barrier for

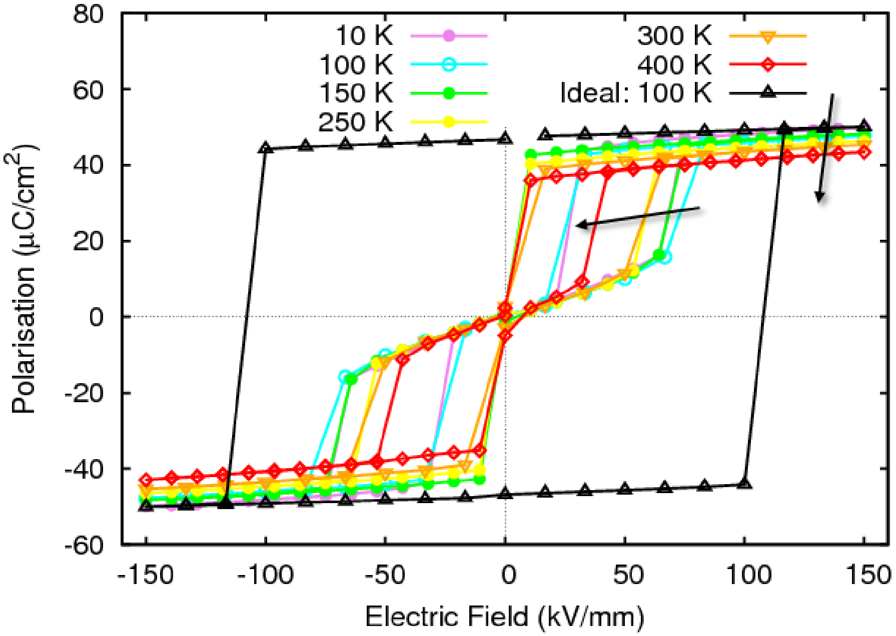

Figure 8.6: Temperature dependence of the P-E hysteresis for a dilute concentration (n_d=1.38%.) of aged dopant-vacancy associates in $PbTiO_3$.

the reorientation of the polar axis. For intermediate defect concentrations (0.78% in this model), pinched hysteresis loops are produced (Figure 8.7a). This form of P-E loop is the most common large signal observation noted in experimental studies of aged ferroelectrics [265,295,296]. The work dissipated (area enclosed by the P-E loop, Eqn. 2.33) decreases with the dopant level (Figure 8.7b). Increased defect concentrations start to pinch the square loop which, upon further increases, leads to a closed double hysteresis and gradual reduction of area. Thus, the dissipated energy losses, effective coercive fields and hysteretic behaviour of ferroelectric materials can be controlled by varying the applied fields and dopant levels. It should be noted that in this study we are limited by the constraint of zero total dipole moment in the unaged simulation cell, which restricts the number of dopants $N_{B''}$ to factors of six. Thus, the concentrations identifying pinching and double hysteresis are, in fact, upper bounds.

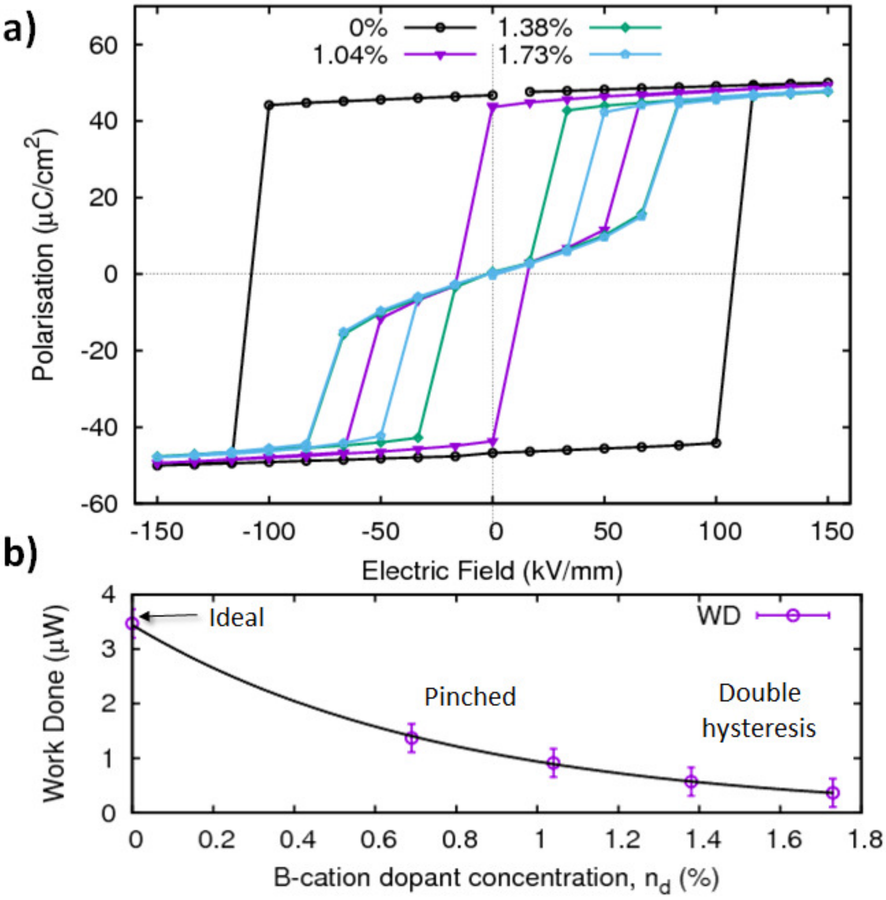

Figure 8.7: The effect of dopant concentration on the hysteresis of $PbTiO_3$. (a) Low concentrations retain the square loop of the pure ferroelectric. Pinching is observed at dopant concentrations greater than 0.78% which close to form double hysteresis loops with further increases in concentration ($\approx 1.38\%$). (b) Work done to create hysteresis over a period T. A solid line is plotted to guide the eye.

8.5 Conclusions

In conclusion, molecular dynamics has been used to model ageing in boundary-free single domain doped $PbTiO_3$. It has been shown that all the large-signal characteristics of ageing: pinched and double polarisation hysteresis, hysteresis shifts, asymmetric butterfly loops and large recoverable non-linear strains, can be reproduced from intrinsic effects of defect-dipoles from dopant-vacancy associates alone. The effects result from the net defect dipole orientation with respect to the poling field. Variation the dopant concentration was observed to modify the material's hysteretic response, suggesting a mechanism for tuning ferroelectric and electromechanical properties for enhanced device performance. This work identifies and clarifies the microscopic mechanisms involved the ageing phenomena and suggests practical methods to inexpensively improve functional performance of ferroelectric ceramic based technologies.

9

Conclusions

Perovskite ferroelectrics are hailed as a wonder material which offer a myriad of exciting advancements for technological miniaturisation and optimisation, requiring precise characterisation of size and time effects on the active ferroelectric components. In this work, we used large scale molecular dynamics with accurate shell-model forcefields to investigate three important questions in the ferroelectrics community vital to aid in the development of the next generation of technologies, including the piezoelectronic transistor. Some of the results presented directly concern the physical properties of the two of the most commonly used materials $\mathrm{Pb(Zr_{1-x}Ti_x)O_3}$ and its parent compound $\mathrm{PbTiO_3}$.

What are the ferroelectric and dielectric properties of $\mathrm{PbTiO_3}$ ultrathin films and PZT-STO heterostructures?

For many years, it had been believed the collective behaviour causing ferroelectricity would be destroyed by surface effects in films and structures thinner than a critical thickness of 100 Å. However, exciting observations have shown that not only can the phenomena persist, but can produce exotic domain structures such as vortices. This has garnered wide interest in perovskite ferroelectrics as replacement materials to overcome fundamental size limits suffered by silicon based electronics. To utilise these materials it is necessary to characterise the ferroelectric and piezoelectric properties of these materials in ultrathin dimensionally constrained topologies which remains in its infancy.

In Chapters 5 and 6 we developed models to investigate the ferroelectric and piezoelectric properties of lead titanate ultrathin films and screened lead zirconate titanate films on stronium titanate substrates. A systematic study of 3.8 nm thick $PbTiO_3$ films with temperature and homogenous misfit identified that ferroelectricity persists below a strain mediated Curie temperature, which is minimised under freestanding conditions, in agreement with experimental XRD studies [69]. Under compressive strains, closure domains are formed, typified by a Landau-Lifshitz domain structure commonly associated with ferromagnetic systems, which have significantly lower anisotropies than ferroelectric systems. Nonetheless, $\mathbf{c^d}$, $\mathbf{bc^d}$ and $\mathbf{abc^d}$ domain morphologies featuring out-of-plane periodic arrangements with 90° domain closure caps are found, which supports TEM measurements by Jia [175] who first directly observed continuous dipole rotations in these highly anisotropic materials. Under tensile strains the polarisation was observed to reorientate in-plane forming 90° **aa**-domains.

Several exciting properties were identified that can be manipulated through strain-engineering to tune the macroscopic properties of the material. First, dipole moments in unit cells approaching 180° domain walls in the $\mathbf{bc^d}$ and $\mathbf{abc^d}$ configurations were discovered not to display the expected Ising-like behaviour whereby the dipole magnitudes reduce and flip across the interface. Instead, a distinct Bloch-Néel behaviour was observed, consisting of in-plane rotations across the domain wall, supporting the identification from DFT calculations of $PbTiO_3$ and $LiNbO_3$ [209]. Second, the identification of coupling between ferroelectric and antiferrodistortive relaxations and the surface offers a direct property for experimental observation for the predicted $\mathbf{c^d} \rightarrow \mathbf{bc^d} \rightarrow \mathbf{abc^d}$ strain-mediated transition sequence under increasing compression. Third, we calculated the local dielectric response for the domain morphologies that exist under compressive strain, which identified significant enhancements of the susceptibility in regions of dipole frustration. This observation gives insight into Landauer's paradox and offers possible methods to maximise any possible negative capacitance which can arise when regions of local susceptibility are vastly more responsive than the overall system. A fully quantitative study of negative capacitance in this system would be a very exciting topic for further investigation.

Under compression just below the Curie temperature, we identified a previously unobserved 'nanobubble' domain morphology which bears striking resemblence to recent experimental observations of domains on the surface layers of single crystal tetragonal phase $BaTiO_3$ [215]. In our study, we discovered the domain walls of the out-of-plane stripe domains would wander from the easy axis and divide to form nanobubbles of alternating polarity. These domains are exciting as they offer the potential revival of bubble domain memory first trialled with magnetic bubble domains in the 1980's and they produce accessible regions on the materials surface whereby continuous dipole rotations can be studied and characterised further.

To study superlattices and heterostructures we developed the model further to incorporate a compatible $SrTiO_3$ substrate and Pt electrode layers. A $SrTiO_3$ forcefield was derived based upon the results from DFT calculations that reproduced structural properties across temperatures of interest. This potential was used in conjunction with the Gindele PZT potential [23] to model $PbTiO_3/SrTiO_3$ superlattices, giving excellent agreement with previous first-principles and experimental studies [194]. We further revealed that straining the superlattice system would induce the same strain-mediated domain morphologies identified for isolated $PbTiO_3$ films and therefore provides direct conditions for which these patternings could be created to develop $PbTiO_3$ piezoelectronic transducers.

Proof of principle calculations of a Pt-PZT-STO capacitor were performed which incorporated a many-body Pt potential tethered to the free-surfaces of the ferroelectric using a potential derived from DFT calculations of Pt-PZT-Pt films. A room temperature calculation using tetragonal phase $PbZr_{0.2}Ti_{0.8}O_3$ within the ferroelectric layer of the capacitor was shown to reproduce the **ac** domain structure observed with TEM from a sample shared by collaborators [218]. The developed model was shown to be capable of simulating a real ferroelectric capacitor which in future work could be used to understand many critical phenomena, including flexoelectric contributions near the domains and electrode / substrate interfaces, and polarisation switching in a realistic (non-ideal) system to directly relate to TEM measurements as has been performed in this work.

The results in these Chapters show that ultrathin ferroelectric materials can realise ultra-dense domain patterns, exhibit enhanced piezoelectric properties and produce unique effects at domain walls which can be exploited for technological gains.

How does the temperature and local composition initiate and affect switching dynamics in lead zirconate titanate?

As well as maximising the domain density it is necessary to maximise the domain wall motion. In comparison to magnetic systems, whose massless spins can be coerced into flipping at speeds approaching (and even exceeding) the effective speed of sound [12], domain wall velocities within ferroelectrics are fundamentally restricted by their real momentum. As such, it becomes necessary to understand the dynamics of domain switching within industrially significant materials to enable switching rates to be optimised. To address this question, we investigated how temperature and local composition in morphotropic PZT affects switching dynamics (Chapter 7).

Molecular dynamics simulations of P-E hysteresis were verified with supporting electrical measurements from collaborators for morphotropic $PbZr_{0.5}Ti_{0.5}O_3$. These results identified the temperature dependence of the shape of the hysteresis loops, which narrowed as it approached the paraelectric transition temperature. The coercive field was observed, both in experiment and simulation, to increase with decreasing temperature. Experimental evidence in the literature, as well as our electrical measurements, observed the hysteresis to suddenly narrow and polarisation drop below 160 K. On the other hand, the simulations predict the coercive field and polarisation to continue to increase down to absolute zero. Further electrical measurements using a different experimental setup determined the narrowing was an artefact arising from the coercive field exceeding the maximum applied voltage in the experimental setup, confirming the results of the simulations. These results have profoundly significant ramifications for ferroelectric applications in low temperature conditions, such as for aeronautic and space exploration industries, which will require significant voltage levels for successful operation.

The fundamental nature of the switching mechanism was observed to change with temperature. At room temperature, nucleation driven switching was observed, in agreement with experimental studies of PLZT thin films [255]. At low temperatures, the switching dynamics is governed by coherent polarisation rotation similar to a mechanism identified in $PbTiO_3$ [248]. The switching was identified to be facilitated by Zr-centred unit cells, and by extension, Ti centred cells in Zr-rich environments. At low temperatures, Ti-rich environments were observed to have suppressed ferroelectric displacements, but they remained ferroelectrically active due to the octahedral cage distortion. These results have important consequences for reports suggesting observation of ferroelectric ‘dead-regions’ from an analysis the ferroelectric displacements of B-cations since the, often difficult to observe, oxygen atoms can produce the dipole moment. Switching in rhombohedral PZT identified the rapid formation of columnar reverse domains but a slower switching rate in comparison to morphotropic PZT.

What causes perovskite ferroelectrics to 'age'?

It has been known for many years that ferroelectric materials age. That is, a repeated experiment on the same sample can yield significantly different results between the first measurement and a second measurement some period of time later. The ageing phenomena manifests through several large-signal characteristics including pinched and double P-E hysteresis, shifting of the hysteresis along the x-axis, asymmetric S-E butterfly curves and large non-linear strains. To resolve this question, specifically what causes the experimentally observed large-signal distortions, we investigated correlated behaviour of dipole moments formed from the association of divalent Ti substitutes with oxygen vacancies in $PbTiO_3$ (Chapter 8) recently calculated to be thermodynamically stable from DFT calculations [276,277].

From the simple assumption that defect-dipoles from the dopant-vacancy associates cause ageing, we were able to conclusively show through molecular dynamics simulations every large-signal effect could be described. Pinched and double hysteresis loops were observed to manifest due to an alignment of defect dipoles perpendicular to a poling field resulting in a bias field which would reorientate the polarisation along the defect-dipole alignment at low field strengths. This is further responsible for the observation of large recoverable non-linear strains, far exceeding those of typical high strain materials such as PMNPT. Intentional doping of PZT therefore provides a cheap, suitable material for high sensitivity actuators that could be used as the piezoelectric component in piezoelectronic transistors.

An alignment of defect dipoles parallel to a poling field results in a bias field which supports or acts against the applied field. This superposition causes the P-E hysteresis to shift relative to the abscissa. For the strain hysteresis this manifests as an asymmetry. Random alignment of the defect-dipoles, the unaged condition, recovered bulk hysteresis behaviour typical of experiments.

Significantly, variation the dopant concentration was observed to modify the material's hysteretic response, suggesting a mechanism for tuning ferroelectric and electromechanical properties for enhanced device performance. This work identifies and clarifies the microscopic mechanisms involved the ageing phenomena and suggests practical methods to inexpensively improve functional performance of ferroelectric ceramic based technologies.

Overall, through the use of atomistic scale modelling, the work in this thesis provides insights to directly improve the functional control of ferroelectric materials. Future collaborations and feedback between experiment and theoretical models will continue to improve our fundamental understanding, our ability to manipulate ferroelectric materials, to tune their properties and accelerate the development of this field to produce faster, cleaner and more affordable ferroelectric devices.

Appendices

Appendix A

Nomenclature

A.1 Symbols

a_0, a	(Equilibrium) Lattice parameter
a_f	Lattice parameter at T_c
a_s	Effective substrate lattice parameter
A	Generic observable
$\mathbf{A}^j, A_\alpha^j$	Local lattice vector of j^{th} unit cell (for axis α)
$\mathcal{A}$	Generic parameter
B_0	Bulk modulus
B_0'	Derivative of the bulk modulus with respect to pressure
c	Lattice parameter along the polarisation axis
$C_{\alpha\beta}$	elastic constants
d	Film thickness
$\mathbf{d}, d_\alpha$	Dipole moment
$d_{\alpha\beta}$	Piezoelectric coefficients (matrix form)
$d_{\alpha\beta\gamma}$	Piezoelectric tensor
$\mathbf{D}, D_\alpha$	Displacement field
D_{c-s}, D_{s-s}	Core-shell and shell-shell dynamic matrices
$D(r_{ij})$	Core-shell separation penalty function
e_i^{target}	Target error threshold
E	Eigenenergy of the Schrödinger equation

$\mathbf{E}, E_\alpha, \mathcal{E}_\alpha$	Electric field
$E_\perp$	Poling field applied parallel to a defined ageing orientation
$E_{//}$	Poling field applied parallel to a defined ageing orientation
E_{bias}	Internal bias field
E_c, E_c^+, E_c^-	Coercive field, on the upswing/downswing
E_c^{int}	Intrinsic coercive field
E_{cut}	Cut-off energy
$E_{\text{i+e}}$	Eigenenergy of Scrödinger equation with the Born-Oppenheimer approximation
E^{wall}	Effective domain wall energy
E_{xc}	Exchange-correlation energy
$\mathcal{E}_0$	Crossing field
$\mathcal{E}_d$	Depolarising field
f^{out}	Outputted observable calculated from fitted potential
f^{ref}	Reference observable
$\mathbf{f}_{ij}$	Force acting between particles i and j
$\mathbf{F}, F_\alpha$	Force acting on a particle
$F[n]$	Universal energy functional
$\mathcal{F}$	Weighted objective function
$\mathcal{F}_0$	Free energy density of prototype state
$\mathcal{F}_n$	n^{th} expansion coefficient of free energy
g_{ij}	Pair correlation function
$\mathbf{G}, G_\alpha$	Reciprocal lattice vector
$G_{\alpha\beta}$	Mass-metric tensor
$\mathcal{G}$	Gibbs free energy density
$\mathbf{h}, h_\alpha$	Hypertoroidal moment
$\hat{H}(\mathbf{r}, \mathbf{R})$	Time independent Hamiltonian of electronic and nuclear coordinates, respectively
$\hat{H}_{\text{i+e}}(\mathbf{r}; \mathbf{R})$	Born-Oppenheimer Hamiltonian
$\hat{H}_{KS}^\sigma$	Kohn-sham Hamiltonian for spin σ
$\mathbf{j}$	Current density
$\mathbf{k}, k_\alpha$	Wavevector
k_2, k_4	Spring constants
k, k', k''	Tethering potential parameters
L	Degrees of freedom for Nosé-Hoover thermostat
$\mathbf{L}, L_\alpha$	Lattice vector
$\mathcal{L}$	Lagrangian

M_i, m_i	Mass
$n(\mathbf{r})$	Electron density
n_d	Dopant concentration
N	Number of particles/electrons
N_{ref}	Number of reference observables
$N_{\mathrm{Ti}}^{\mathrm{ideal}}$	Number of Ti atoms in the ideal system
$N_{\mathrm{B}''}$	Number of dopant substitutions
$\mathbf{p}, p_\alpha$	Momentum
$\mathbf{p}_{it}$	Transverse component of the polarisation
$\mathbf{P}, P_\alpha$	Polarisation
$\mathbf{P}^j, P_\alpha^j$	Local polarisation of unit cell j
q_α	Generalised coordinate
q_i	Charge of particle i
Q	Effective mass for heat transfer from the Nosé-Hoover Lagrangian
$Q_{\alpha\beta\gamma\delta}$	Electrostriction coefficient
$\mathbf{r}, r_\alpha$	Position vector (coordinate). Also **R**
r_{ij}	Distance between particles i and j
r_{cut}	Cut-off radius
S	Entropy (Also action)
t	Time
t^j	Tetragonality of j^{th} unit cell
T	Temperature
T_c	Curie temperature
T_0	Curie-Weiss temperature
$\hat{T}_n$	Lattice translation operator of band index n
$\hat{T}_i(\mathbf{R})$	Nuclear kinetic energy operator
$\hat{T}_e(\mathbf{r})$	Electronic kinetic energy operator
$\hat{T}_{ie}(\mathbf{r}, \mathbf{R})$	Nuclear-electron interaction operator
$\hat{T}_{ee}(\mathbf{r}, \mathbf{r}')$	Electron-electron interaction operator
$\mathbf{T}, T_\alpha$	Toroidal moment
$\mathbf{T}_{it}$	Transverse component of the toroidal moment
u_i	Displacement
U	Internal energy density
U_b	Domain wall energy barrier
U_{c-s}	Core-shell potential
$\hat{U}_{ii}(\mathbf{R})$	nuclear-nuclear interaction operator

U_{ij}^{Buck}	Buckingham interatomic potential with parameters A_{ij}, ρ_{ij} and C_{ij}
$U_{ij}^{\text{Correction}}$	Long-range correction to interatomic potentials
U_{ij}^{Disp}	Van der Waals (dispersion) potential
$\mathbf{v}, v_\alpha$	Velocity
v_s^σ	Effective Kohn-Sham potential
V	Total volume
V_{ext}	External potential
V_{xc}	Exchange-correlation potential
w	Domain wall width
w_i	Weighting factor
W	Work done
X_i	Charge of core
Y_i	Charge of shell
$Z_{\alpha\beta}^*$	Born effective charge tensor
β	Thermodynamic beta $(1/k_BT)$
$\delta_i, \delta_{i,\alpha}$	Ferroelectric displacement
δe_i	Relative error between target and fitted observable
Δt	Time step
ϵ_0	Permittivity of free space $(8.854\times10^{-12}\text{Fm}^{-1})$
$\epsilon_{\alpha\beta}$	Dielectric tensor
ϵ_i^σ	Eigenenergy of the Kohn-Sham equation
ζ	Characterisation parameter of Gaussian
η	Homogeneous biaxial strain $(\eta_{11} = \eta_{22})$
$\eta_{\alpha\beta}$	Strain tensor
μ	Dynamic exponent
ν^j	Local volume
ξ, λ	Reaction coordinate
$\rho(\mathbf{r})$	Charge density
σ	Bounding charge density
$\sigma_{\alpha\beta}$	Stress tensor
τ	Goldschmidt tolerance factor
$\tau_{i\alpha}$	Displacement of atom i along direction α
$\phi(\mathbf{r})$	Eigenfunction of the Schrödinger equation applying the Born-Oppenheimer approximation
$\phi_{i\mathbf{k}}^\sigma(\mathbf{r})$	Eigenfunction of the Kohn-Sham equation
$\Phi(\mathbf{r}, \mathbf{R})$	Many-body eigenfunction of the Schrödinger equation with $\hat{H}(\mathbf{r}, \mathbf{R})$
Φ^j	Lateral rotation of octahedral cage
$\chi_{\alpha\beta}$	Dielectric susceptibility tensor

A.2 Glossary of Abbreviations

A	A-cation (Pb,Sr,Ba etc)
AFD	Antiferrodistortive
AFM	Atomic Force Microscopy
B	B-cation (Ti,Zr etc)
BFGS	Broyden-Fletcher-Goldfarb-Shanno (minimisation method)
BTO	Barium Titanate ($BaTiO_3$)
BZ	Brillouin Zone
DFPT	Density Functional Perturbation Theory
DFT	Density Functional Theory
DRAM	Dynamic Random Access Memory
DW	Domain Wall
EH	Effective Hamiltonian
FE	Ferroelectric
FeRAM	Ferroelectric Random Access Memory (Also FRAM)
GGA	Generalised Gradient Approximation
IP	Interatomic Potential
LDA	Local Density Approximation
LGD	Landau-Ginzburg-Devonshire (phenomenological method)
MD	Molecular Dynamics
MP	Monkhorst-Pack (unbiased k-point grid)
MRAM	Magnetic Random Access Memory
PBC	Periodic Boundary Conditions
PET	Piezoelectric Transistor
PFM	Piezo(response) Force Microscopy
PMNPT	Lead Magnesium Niobate - Lead Titanate ($(1\text{-}x)Pb(Mg_{1/3}Nb_{2/3})O_3\text{-}xPbTiO_3$)
PTO	Lead Titanate ($PbTiO_3$)
PZT	Lead Zirconate Titanate ($Pb(Zr_{1-x}Ti_x)O_3$)
STO	Strontium Titanate ($SrTiO_3$)
TEM	Transmission Electron Microscopy
TOM	Transmission Optical Microscopy
UTF	Ultrathin Film
XC	Exchange-Correlation (also xc)
XRD	X-Ray Diffraction

Appendix B

List of Publications

B.1 Journals

J. B. J.Chapman*, A. V. Kimmel & D. M. Duffy, “Novel High-Temperature Ferroelectric Domain Morphology in $PbTiO_3$ Ultrathin Films”, *Physical Chemistry Chemical Physics* **19**, 4243 (2017)

J. B. J. Chapman*, R. E. Cohen, A. V. Kimmel & D. M. Duffy, “Atomistic Modelling of Ageing in Ferroelectrics”, *Physical Review Letters* **119**, 177602 (2017)

J. B. J. Chapman*, O. T. Gindele, C. Vecchini, P. Thompson, M. Stewart, M. G. Cain, D. M. Duffy & A. V. Kimmel,“Low Temperature Ferroelectric Behaviour in Morphotropic $Pb(Zr_{1-x}Ti_x)O_3$”, *Journal of the American Ceramics Society* **101**, 874 (2018)

J. B. J. Chapman*, O. T. Gindele, A. V. Kimmel & D. M. Duffy “Polarisation Switching and Perceived Dead-regions of PZT”, *In preparation for submission to Physical Review B* (2018)

B.2 Conferences and Seminars

J.B.J.Chapman, O.T.Gindele, A.Kimmel & D.Duffy
Oral: *Switching Dynamics & Mechanisms in* $Pb(Zr,Ti)O_3$ *from Atomistic Modelling*
ISAF-IWATMD-PFM: *IEEE International Symposium on Applications in Ferroelectrics - International Workshop on Acoustic Transduction Materials and Devices - Piezoresponse Force Microscopy Workshop*
Atlanta, USA (2017)

J.B.J.Chapman, R.E.Cohen, A.Kimmel & D.Duffy
Poster: *Atomistic Modelling of Ageing in Ferroelectrics*
ISAF-IWATMD-PFM: *IEEE International Symposium on Applications in Ferroelectrics - International Workshop on Acoustic Transduction Materials and Devices - Piezoresponse Force Microscopy Workshop*
Atlanta, USA (2017)

J.B.J.Chapman, R.E.Cohen, A.Kimmel & D.Duffy
Oral: *Atomistic Modelling of Ageing in Ferroelectrics*
Thomas Young Centre (TYC) Postgraduate Conference
London, UK (2017)

J.B.J.Chapman, O.T.Gindele, A.Kimmel & D.Duffy
Invited Talk: *Switching Dynamics & Mechanisms in* $Pb(Zr,Ti)O_3$ *from Atomistic Modelling*
FERRO-2017: *Fundamental Physics of Ferroelectrics and Related Materials*
Williamsburg, USA (2017)

J.B.J.Chapman, R.E.Cohen, A.Kimmel & D.Duffy
Poster: *Atomistic Modelling of Ageing in Ferroelectrics*
FERRO-2017: *Fundamental Physics of Ferroelectrics and Related Materials*
Williamsburg, USA (2017)

J.B.J.Chapman, J.M.Gregg, A.Schilling, A.Kimmel & D.Duffy
Poster: *Novel Ferroelectric Nanobubble Domains in Strained Prototypical Perovskite Films*
TYC 10th Anniversary Symposium
London, United Kingdom (2016)

J.B.J.Chapman, J.M.Gregg, A.Schilling, A.Kimmel & D.Duffy
Invited Seminar: *Novel Ferroelectric Nanobubble Domains in Strained Prototypical Perovskite Films*
Geophysical Laboratory, Carnegie Institute of Washington
Washington DC, USA (2016)

J.B.J.Chapman, J.M.Gregg, A.Schilling, A.Kimmel & D.Duffy
Oral: *Novel Ferroelectric Nanobubble Domains in Strained Prototypical Perovskite Films*
FERRO-2016: *Fundamental Physics of Ferroelectrics and Related Materials*
Washington DC, USA (2016)

J.B.J.Chapman
Oral: *Nanoscale Domain Morphology and Dynamics in* $PbTiO_3$ *Strained Ultrathin Films*
Bi-annual Nanostrain Project Meeting
Grenoble, France (2015)

J.B.J.Chapman, A.Kimmel & D.Duffy
Oral: *Nanoscale Domain Morphology and Dynamics in* $PbTiO_3$ *Strained Ultrathin Films*
EMF-2015: *European Meeting on Ferroelectricity*
Porto, Portugal (2015)

J.B.J.Chapman, A.Kimmel, M.Cain & D.Duffy

Poster: *Domain Morphologies and Characteristics in Ferroelectric Ultrathin Films*
ISIF-ISAF-PFM: *International Symposium on Applications of Ferroelectrics - International Symposium on Integrated Functionalities - Piezoresponse Force Microscopy Workshop*
Singapore, Singapore (2015)

J.B.J.Chapman, A.Kimmel, M.Cain & D.Duffy
Poster: *Domain Morphologies and Characteristics in Strained Ferroelectric Ultrathin Films*
DIELECTRICS-2015: *IoP Dielectrics Workshop*
London, United Kingdom (2015)

J.B.J.Chapman, A.Kimmel & D.Duffy
Poster: *Modelling Domain Dynamics in Strained Ferroelectric Ultrathin Films*
PIEZO 2015: *Electroceramics for End-users VIII*
Maribor, Slovenia (2015)

Appendix C

Computer Codes Used Throughout this Thesis

C.1 Custom Codes

This Section outlines and briefly describes the codes developed to complete the work in this thesis. Note, this list is not exhaustive and does not include automation tools or utilities to extract or compare data from different software, or codes which have not been used to contribute to this thesis. Versions of the software source code can be made available on request.

C.1.1 PoPP.DPZ.py

Polarisation and other Perovskite Properties (PoPP.DPZ.py) is the principal code used to calculate properties from the molecular dynamics output files of DL_POLY 4 [132] (specifically OUTPUT and HISTORY). The main properties calculated are outlined in Chapter 4. The atoms constructing each perovskite unit cell are determined from Find_UC.DPZ.py.

C.1.2 Find_UC.DPZ.py

Find_UC.DPZ.py is a code used to define the conventional perovskite unit cells (Figure 4.1) of the atoms defined in a DL_POLY CONFIG file (assumes no inherent order in atom list). The user can define a list of atoms of expected B-cations (default: Ti, Zr, Sr, Mg, Nb). During operation, the code identifies all relevant B-cations in CONFIG then searches for 6 nearest neighbouring A-cation (user defined with defaults: Pb, Sr, Ba) cores and shells, and 8 nearest neighbouring X-anions (default: O) cores and shells, generating a binary file of neighbour indices that can be imported for use in properties codes. Exceptions and cut-off lengths are included to handle incomplete unit cells such as those on surfaces or including vacancies. This code can also define A-cation centred unit cells.

C.1.3 ABbX3_CellGen.DPZ.py

ABbX3_CellGen.DPZ.py is a code written to generate CONFIG and FIELD files for DL_POLY with perovskite structures. The code allows for solid solutions of two parent perovskites (eg PZT from PTO and PZO). Any composition can be chosen and B-cations are by randomly distributed satisfying the chosen stoichiometry. However, an option allows B-cation ordering to be defined and imported (see example p4mm_order_gen.py). As well as bulk, slabs can be generated and each surface can be chosen to be AO or BO_2 terminated. Another perovskite such as $SrTiO_3$ can be attached to either surface (with either termination) to construct substrates or superlattices. For these substrate layers, N layers can be frozen. Electrodes can be affixed to either the main or substrate layers. A range of other parameters can be adjusted to optimise the initial structure such as lattice parameters and ferroelectric displacements. Paraelectric, monodomain and out-of-plane stripe domains patterns can be chosen. To generate more complex initial domain structures ferroelectric displacements can be imported for each atom individually using external modules such as ac_domain_gen.py. A template CONTROL file can be exported.

ac_domain_gen.py

Creates a binary array that can be imported by ABbX3_CellGen.DPZ.py to construct ac domains such as used in Chapter 6. Periodicity and domain widths can be adjusted.

p4mm_order_gen.py

Creates a binary array that can be imported by ABbX3_CellGen.DPZ.py to determine an ordered B-cation arrangement. In this case a *P4mm* (stacked chequerboard) structure which is a stable chemical ordering of $PbZr_{0.5}Ti_{0.5}O_3$.

Defect_ABbX3_CellGen.DPZ.py

This is a modified (with limited functionality) version of the ABbX3_Cell Gen.DPZ.py code used to construct supercells containing $(B''_{\mathrm{Ti}} + V_{\mathrm{O}}^{\bullet\bullet})^{\times}$ using the procedure outlined in Chapter 8.

Defect_PMNPT_CellGen.DPZ.py

A similar code to Defect_ABbX3_CellGen.DPZ.py but creates CONFIG and FIELD files of $(1\text{-x})Pb(Mg_{1/3}Nb_{2/3})O_3\text{-x}PbTiO_3$ using a random site matrix (RSM) to generate the chemical ordering [151].

C.1.4 Plot_polarisation_3D_cubes.py

A script written to plot properties of each unit cell using coloured cubes representing the magnitude of the relevant properties (such as Figure 5.3). Can create Figures for a given timestep (.eps) or videos over a range of timesteps (.gif). Uses output files from the PoPP.DPZ.py code.

C.1.5 Local_disp.py

This code calculates the Density of Probability (of either ferroelectric displacements or polarisation) using the output files of the PoPP.DPZ.py code. Can calculate for the entire system and for contributions from specific B-cation centred unit cells (see Chapter 7).

C.1.6 Vol_frac.py

This code calculates the local structure of each perovskite unit cell as used in §7.4, using the output files of the PoPP.DPZ.py code. Can calculate for the entire system and for contributions from specific B-cation centred unit cells.

C.1.7 FF_fit_run.py

This code operates according to the flowchart in Figure 3.11 to fit interatomic potentials. Creates GULP [131] input files and reads output files to automate fitting through the variation of weights and parameters.

C.1.8 Find_UC.CAS.py

Generates unit cell lists from CASTEP [112] .cell or -out.cell files, using the same method as Find_UC.DPZ.py. Using the Born effective charges calculated from DFPT (Table E.4) the polarisation can be approximated according to equation 3.14. Note, this serves as an approximate method which can be used if Berry phase calculations cannot be performed.

C.2 Large External Codes

This Section details the open-source and propitiatory software packages used to carry out the work presented in this thesis.

C.2.1 CASTEP

CASTEP [112] is a code to calculate material properties from first principles. For its density functional theory capabilities it uses a plane wave basis set and pseudopotentials which can be generated ‘on-the-fly’ to suit requirements of the Hamiltonian. It can also perform density functional perturbation theory calculations [119] and *ab initio* molecular dynamics. The code can be used to calculate energetics, atomistic structure, phonon-dispersion, infra-red and Ramen spectroscopies as well as core-level spectra and electronic response and dielectric properties. Throughout this thesis versions 8.0 and 16.1 were used.

C.2.2 DL_POLY

DL_POLY (which throughout this thesis refers to DL_POLY_4) [132] is a general purpose classical molecular dynamics code, developed from the version DL_POLY_CLASSIC. It is highly parallelised using equi-spatial domain decomposition and capable of simulating up to a billion particles. DL_POLY can handle many common analytic forcefield forms but can also accept tabulated potentials such that any classical pair-potential can be implemented and used with a range of boundary conditions, ensembles and constraints. Work in this thesis has been performed using a modified version of DL_POLY 4.0.7. Modifications to the source-code of this version are detailed in Appendix D.

C.2.3 GULP

The general utility lattice program GULP [131] is a package to perform classical molecular and lattice dynamics calculations for 0-D to 3-D structures and can be used for forcefield fitting. Work in this thesis has been performed using versions 3.4 and 4.0.

C.2.4 VESTA

VESTA [161] is a visualisation package to display structural models from a variety of input formats, and overlay with volumetric data such as electron densities and crystal morphologies. Work in this thesis has used Windows and Linux versions 3.4.2 and earlier.

Appendix D

DLPOLY Modifications

D.1 read field module

The PMN-PT forcefield was parametrised for a Rydberg pair potentials.

$$U_{ab}(r_{ij}) = (A + Br_{ij}) \exp\left(- \frac{r_{ij}}{\rho} \right) \tag{D.1}$$

This form of short range potential is not hard-coded into the DLPOLY source code. We note any pair potential may be supplied to DLPOLY in tabular form. However, to simplify parameter changes and generalise usage, the analytic form has been implemented. To conform with the DLPOLY standard a keyword *rydb* is chosen to be read by the FIELD file having a potential key of *keypot*= 12. The following modifications were made to the module read_field.f90.

At line 1180:

```
! JC 09.03.16
! Added keyword option for Rydberg potential when
! reading FIELD
Else If (keyword == 'rydb') Then
  keybnd(nbonds)=11
Else If (keyword == '-ryd') Then
  keybnd(nbonds)=-11
Else
```

```
      ! End of changes
```

At line 1246:

```
! JC 09.03.16
! Convert A and C in rydberg to dlp internal units.
! A=prmbond(1,:) already converted above
   If (Abs(keybnd(nbonds)) == 11) Then
     prmbnd(3,nbonds)=prmbnd(3,nbonds)*engunit
   End if
! End of changes
```

At line 3036:

```
! JC 09.03.16
! Adding rydberg option
  Else If (keyword == 'rydb') Then
    keypot=12
! End of changes
```

At line 3080:

```
! JC 09.03.16
! Convert A and C of rydberg. A done above
  Else If (keypot == 12) Then
    parpot(3) = parpot(3)*engunit
! End of changes
```

At line 3164:

```
! JC 09.03.16
! Rydberg
  Else If (keypot == 12) Then
    gamdpd(keyvdw)=Abs(parpot(4))
! End of changes
```

D.2 vdw direct fs generate module

The force shifted constant array must first be calculated before direct creation of the potential array. The force-shift is included in module vdw_direct_fs_generate.f90 at line 192.

```
!==========================================================!
!                      JC 09.03.16                         !
!                 V=(a+cr)exp(-r/rho)                      !
! Rydberg corrections:                                     !
! Here,                afs  = -r*dU/dr                     !
!                bfs = -U-afs = -U-rdU/dr                  !
! Then                  afs = -dU/dr                       !
! adjusted after used to calculate integral limits)        !
!==========================================================!
     Else If (keypot == 12) Then

        a  =prmvdw(1,ivdw)
        rho=prmvdw(2,ivdw)
        c  =prmvdw(3,ivdw)

        If (Abs(rho) <= zero_plus) Then
           If (Abs(a) <= zero_plus) Then
              rho=1.0_wp
           Else
              Call error(467)
           End If
        End If

        b=rvdw/rho
        t1=Exp(-b)
        t2=a+c*rvdw

        afs(ivdw) = t1*(t2*b-c*rvdw)
        bfs(ivdw) =-(t1*t2) - afs(ivdw)
        afs(ivdw) = afs(ivdw)/rvdw
!==========================================================!
!                    End of change                         !
!==========================================================!
```

D.2.1 vdw forces module

$$G(r_{ij}) = -r_{ij}\frac{\partial}{\partial r_{ij}}U(r_{ij}) \tag{D.2}$$

$$f_j = -\frac{1}{r_{ij}}\left(\frac{\partial}{\partial r_{ij}}\right)r_{ij} \tag{D.3}$$

vdw_forces.f90 added line 362

```
!=====================================================!
!                    JC 09.03.16                      !
!                 Rydberg potential                   !
!                                                     !
!              V(r) = (a+c*r)exp(-r/rho)              !
!          g(r) = -(1/r)dV(r)/dr NB F=g(r)*r          !
!=====================================================!
   Else If (ityp == 11) Then

      a  =prmvdw(1,k)
      rho=prmvdw(2,k)
      c  =prmvdw(3,k)

      ! Set exponent to 1 if a=0 and rho=0
      If (Abs(rho) <= zero_plus) Then
         If (Abs(a) <= zero_plus) Then
            rho=1.0_wp
         Else
            Call error(467)
         End If
      End If

      b=rrr/rho
      t1=Exp(-b)
      t2=(a+c*rrr)

      If (jatm <= natms .or. idi < ltg(jatm)) &
      ! Potential energy U
```

```
      eng   = t1*t2
      ! Force=-grad(U)=gamma*r
      gamma = t1*((a/(rrr*rho))+(c/rho)-(c/rrr))

      ! vdw_direct_fs_generate.f90 has been updated.
      ! That module defines afs and bfs
      If (ls_vdw) Then ! force-shifting
         If (jatm <= natms .or. idi < ltg(jatm)) &
         eng   = eng + afs(k)*rrr + bfs(k)
         gamma = gamma - afs(k)/rrr
      End If
!=====================================================!
!                    End of changes                   !
!=====================================================!
```

D.3 vdw generate module

In order to be generalised, DLPOLY creates an interpolation array for both the pair potential U_{ab} and force gradient G_{ab} over the range $0 \leq r_{ij} \leq r_{vdw}$. The following routine was added at line 167 in the module vdw_generate.f90.

```
!=====================================================!
!                    JC 09.03.16                      !
!      Rydberg generate force and gradient arrays     !
!              V(r) = (a+cr)exp(-r/rho)               !
!=====================================================!
 Else If (keypot == 12) Then
   a  =prmvdw(1,ivdw)
   rho=prmvdw(2,ivdw)
   c  =prmvdw(3,ivdw)

   If (Abs(rho) <= zero_plus) Then
      If (Abs(a) <= zero_plus) Then
         rho=1.0_wp
      Else
         Call error(467)
```

```
   End If
End If

! Sigma-epsilon initialisation
If (.not.ls_vdw) Then
   sigeps(1,ivdw)=-1.0_wp
   sigeps(2,ivdw)= 0.0_wp
End If

Do i=1,mxgvdw
   r=Real(i,wp)*dlrpot

   b=r/rho
   t1=Exp(-b)
   t2=a+c*r

   ! U(r) = (a+cr)exp(-r/rho)
   vvdw(i,ivdw)=t1*t2
   ! G(r) = -rdU/dr
   gvdw(i,ivdw)=t1*(b*t2 - c*r)

   ! Sigma-epsilon search (unchanged from Buck and
   ! Born-Higgins-Meyer definitions)
   ! Assumes some safety against numeric black holes!!!
   If ((.not.ls_vdw) .and. i > 20) Then
      ! Find sigma
      If (Sign(1.0_wp,sigeps(1,ivdw)) < 0.0_wp) Then
        If (Nint(Sign(1.0_wp,vvdw(i-1,ivdw))) ==     &
          Nint(Sign(1.0_wp,vvdw(i,ivdw))))           &
          sigeps(1,ivdw)=(Real(i,wp)-0.5_wp)*dlrpot
      ! Find epsilon
      Else
        If ((vvdw(i-2,ivdw) >= vvdw(i-1,ivdw) .and.  &
             vvdw(i-1,ivdw) <= vvdw(i   ,ivdw)) .and. &
            (vvdw(i-2,ivdw) /= vvdw(i-1,ivdw) .or.    &
             vvdw(i-2,ivdw) /= vvdw(i   ,ivdw) .or.    &
```

```
                vvdw(i-1,ivdw) /= vvdw(i   ,ivdw)) )      &
                sigeps(2,ivdw)=-vvdw(i-1,ivdw)
         End If
      End If
   End Do
   vvdw(0,ivdw)=Huge(vvdw(1,ivdw))
   gvdw(0,ivdw)=Huge(gvdw(1,ivdw))
!=====================================================!
!                    End of change                    !
!=====================================================!
```

D.4 vdw lrc module

Dl_poly uses a cutoff for the pair potentials that is spherically symmetric. Necessarily, a long range correction must be applied to the potential energy U_{ab} and virial W_{ab}:

$$U^{ab}_{corr} = 2\pi \frac{N_a N_b}{V} \int_{r_{vdw}}^{\infty} g_{ab}(r) U_{ab}(r) r^2 dr \tag{D.4}$$

$$W^{ab}_{corr} = -2\pi \frac{N_a N_b}{V} \int_{r_{vdw}}^{\infty} g_{ab} \frac{\partial}{\partial r}(r) U_{ab}(r) r^3 dr \tag{D.5}$$

N_a, N_b are the numbers of the respective atom types the pair potential U_{ab} is acting between, V is the volume and g_{ab} is the pair correlation function. For the rydberg potential, at long range ($r > r_{vdw}$) then $g_{ab} = 1$. As with the Buckingham potential, the exponential in the integrand decays more rapidly than the r^3 causing the repulsive terms to be negligible in the corrections. The following modification is made to line 145 in the module vdw_lrc.f90.

```
!=====================================================!
!                     JC 09.03.16                     !
!                  Rydberg potential.                 !
!          Corrections to virial and potential.       !
!                e_ab   = (a+cr)exp(-r/rho)           !
!  e_corr = ( 2 pi N_a N_b / V ) int [^inf _rvdw]* &  !
!                (g_ab(r) e_ab(r) r^2 dr)             !
!  p_corr = (-2 pi N_a N_b / V ) int [*inf _rvdw]* &  !
!              (g_ab(r) de_ab(r)/dr r^3 dr)           !
```

```
! Limits to inf tend to zero.                            !
! So effectively evaluating:                             !
! e_corr = -const* int(g_ab(r) de_ab/dr r^3 dr |_rvdw !
! where g_ab=1 (assuming pcf = 1 at r_cut)               !
! As with Buck and Higgins potentials the exponential !
! decay terms win over coefficients and assumed          !
! negligible at rvdw.                                    !
!=======================================================!

   Else If (keypot == 12) Then

      c=prmvdw(3,k)
      r=rvdw

      eadd = 0.0_wp
      padd = 0.0_wp

!=======================================================!
!                    End of change                       !
!=======================================================!
```

D.5 core shell forces module

To prevent core-shell separations a quadratic penalty function is applied to the Lagrangian:

$$U^{cs}_{penalty}(w_{cs}) = D(w_{cs} - w_0)^2 \tag{D.6}$$

line 30

```
  ! JC 10.03.16
  ! Variable assignments for spring penalty
  Real( Kind = wp ) :: rpen, dpen, omega1, gamma1
  ! End of change
```

line 137

```
!=======================================================!
!                      JC 10.03.16                       !
```

```
!          14.03.16 - Correction to gamma term           !
! Core-shell separation penalty function:                !
!                D(w-w0)^2 if w >= w0                    !
!                Calling w0 -> rpen = 0.2 \ internal     !
!                Calling D  -> dpen = 5   /   units      !
!========================================================!

    rpen = 0.2_wp ! Ang
    omega1 = 0.0_wp
    gamma1 = 0.0_wp
    If (rabsq.gt.(rpen**2_wp)) Then
        dpen   = 5.0_wp ! 10000eV
        ! Define penalty additives for spring potential
        ! and force
        omega1 = dpen*0.5_wp*prmshl(1,kk)*           &
                 ((rabsq**0.5_wp-rpen)**2_wp)
        gamma1 = dpen*prmshl(1,kk)*                  &
                 (rabsq**0.5_wp-rpen)/(rabsq**0.5_wp)
        ! Update terms with the penalty
        omega  = omega + omega1
        gamma  = gamma + gamma1
    End If
!========================================================!
!                      End of change                     !
!========================================================!
```

D.6 Testing Implementation of Rydberg IP

The modifications to the DL_POLY source code for the implementation of the Rydberg potential are tested with the PMNPT ((1-x)Pb($Mg_{1/3}Nb_{2/3}$)O_3-xPbTiO_3) forcefield from ref [151]. Configurations are generated using the Random Site Model which ensures the presence of chemical ordered regions (COR). Three different atomic layout's (with different local COR's) are calculated for each composition. Excellent agreement shows the implementation works correctly.

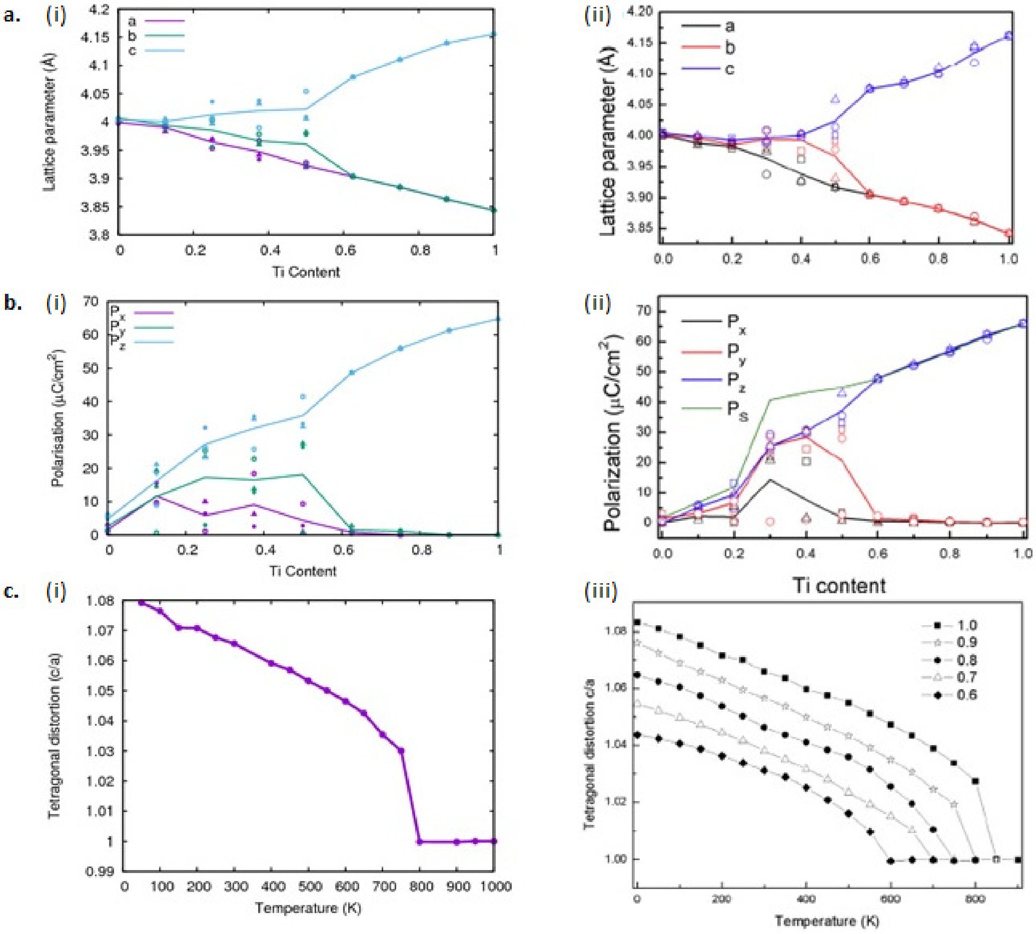

Figure D.1: Comparison of results generated using the (i) modified version of DL_POLY 4 and post-processing scripts (§4) with ref [151] which used DL_POLY Classic. (a) Lattice parameters, (b) magnitude and components of polarisation as a function of Ti composition for PMNPT. Three different atomic arrangements are calculated for each composition. (c) Comparison of the temperature dependence of the polarisation for pure $PbTiO_3$.

Appendix E

DFT: supplementary calculations of $BaTiO_3$

E.1 Properties of $BaTiO_3$ and other Ferroelectric Perovskites using DFT

Property	WC (Present)	DFT LDA [226]	Functional PBE [226]	B3LYP [226]	Exp. [130]	Experiment Exp.2 [297]	Exp.3 [298]
a (Å)	3.9771	3.96	4.03	4.04	4.00		
B (GPa)	181.46	196	175	176	162		134
C_{11} (GPa)	319.62	358.1	310.4	297.5	206	255	187
C_{12} (GPa)	112.38	115.2	107.2	115.7	140	82	107
C_{44} (GPa)	127.76	149.8	139.8	145.4	126	108	112

Table E.1: Comparison of the optimised lattice parameter (a), bulk modulus (B) and elastic constants (C_{ij}) of cubic ($Pm\bar{3}m$) $BaTiO_3$ as calculated from DFT or measured experimentally.

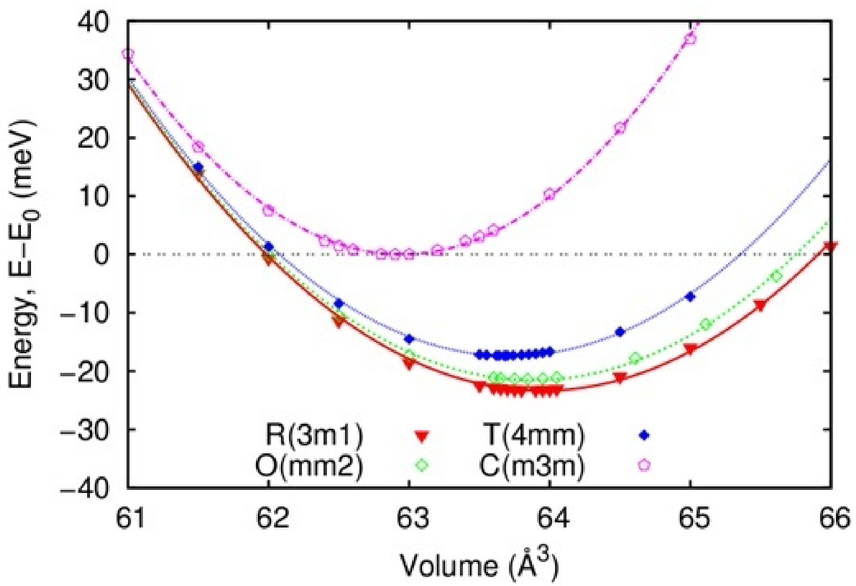

Figure E.1: Phases of $BaTiO_3$ calculated from first principles showing the correct phase sequence from the relative energies of the curve minima. Fitting of Eqn. 3.11 to the symmetry preserving deformations provided the bulk moduli of each phase. The energies have been shifted such that the macroscopic crystal energy of the equilibrium cubic phase defines the origin.

a (Å)	c (Å)	$\Delta_{T,Ti,z}$	$\Delta_{T,O1,z}$	$\Delta_{T,O1,z}$		Reference
3.9615	4.0570	0.0160	-0.0310	-0.0188		DFT-GGA-WC (Present)
3.994*	4.036*	0.0143	-0.0307	-0.0186		DFT-LDA [299]
3.991*	3.0352*	0.0165	-0.0272	-0.0156		DFT-GGA-PW91 [300]
4.0048	4.2087	0.0177	-0.0402	-0.0234		DFT-GGA [301]
3.9910	4.0352	0.0224	-0.0244	-0.0105		Exp. [302]
3.986	4.026	0.015	-0.023	-0.014		Exp. [303]

C_{11}	C_{12}	C_{13}	C_{33}	C_{44}	C_{55}	Reference
301	108	93	139	78.6	126	DFT-GGA-WC (Present)
300	109	90	149	124	128	DFT-LDA-PAW [304]
275	179	152	165	54.4	113	Exp. [305]
222	134	111	151	61.1	134	Exp. [306]

Table E.2: Lattice parameters, atomic displacements and elastic constants of tetragonal (*P4mm*) $BaTiO_3$. *(Lattice parameters fixed to experimental values).

a (Å)	α (°)	$\Delta_{R,Ti,z}$	$\Delta_{R,O1,x}$	$\Delta_{R,O1,z}$	Reference
3.9971	89.859	-0.0118	0.0116	0.0185	DFT-GGA-WC (Present)
4.001	89.87	-0.011	0.013	0.0192	DFT-LDA [299]
4.000	90.00	-0.012	0.01	0.0195	DFT-GGA [300]
4.073	89.74	-0.015	0.0141	0.0245	DFTGGA-PW91 [301]
4.003	89.84	-0.013	0.011	0.0191	Exp. [305]
4.004	89.87	-0.011	0.011	0.018	Exp. [307]

Table E.3: The lattice parameters and atomic displacements for rhombohedral (*R3m1*) $BaTiO_3$ as calculated by DFT or measured by experiment.

$BaTiO_3$	Z^*_{Ba}	Z^*_{Ti}	$Z^*_{O\parallel}$	$Z^*_{O\perp}$	Z^*_{Ti}/Z^{Formal}_{Ti}	Reference
	2.76	7.27	-5.74	-2.15	1.82	GGA-WC (Present)
	2.74	7.30	-5.78	-2.13	1.83	GGA-PBE (Present)
	2.77	7.25	-5.92	-2.15	1.81	LDA [308]
	2.64	7.37	-5.95	-2.16	1.85	LDA [38]

$PbTiO_3$	Z^*_{Pb}	Z^*_{Ti}	$Z^*_{O\parallel}$	$Z^*_{O\perp}$	Z^*_{Ti}/Z^{Formal}_{Ti}	Reference
	3.87	7.13	-5.85	-2.57	1.79	GGA-WC (Present)
	3.86	7.15	-5.85	-2.56	1.79	GGA-PBE (Present)
	3.90	7.06	-5.83	-2.56	1.77	LDA [51]
	3.87	7.03	-5.76	-2.57	1.76	LDA [38]

$SrTiO_3$	Z^*_{Sr}	Z^*_{Ti}	$Z^*_{O\parallel}$	$Z^*_{O\perp}$	Z^*_{Ti}/Z^{Formal}_{Ti}	Reference
	2.55	7.21	-5.71	-2.02	1.80	GGA-WC (Present)
	2.54	7.12	-5.66	-2.00	1.78	LDA [308]
	2.56	7.26	-5.73	-2.15	1.82	LDA [51]
	2.53	7.55	-5.92	-2.07	1.89	LDA [38]

Table E.4: Born effective charges of $BaTiO_3$, $PbTiO_3$ and $SrTiO_3$ in the cubic phase. Large anomalous contributions occur due to B-O hybridisations shown relative to the formal ionic charge.

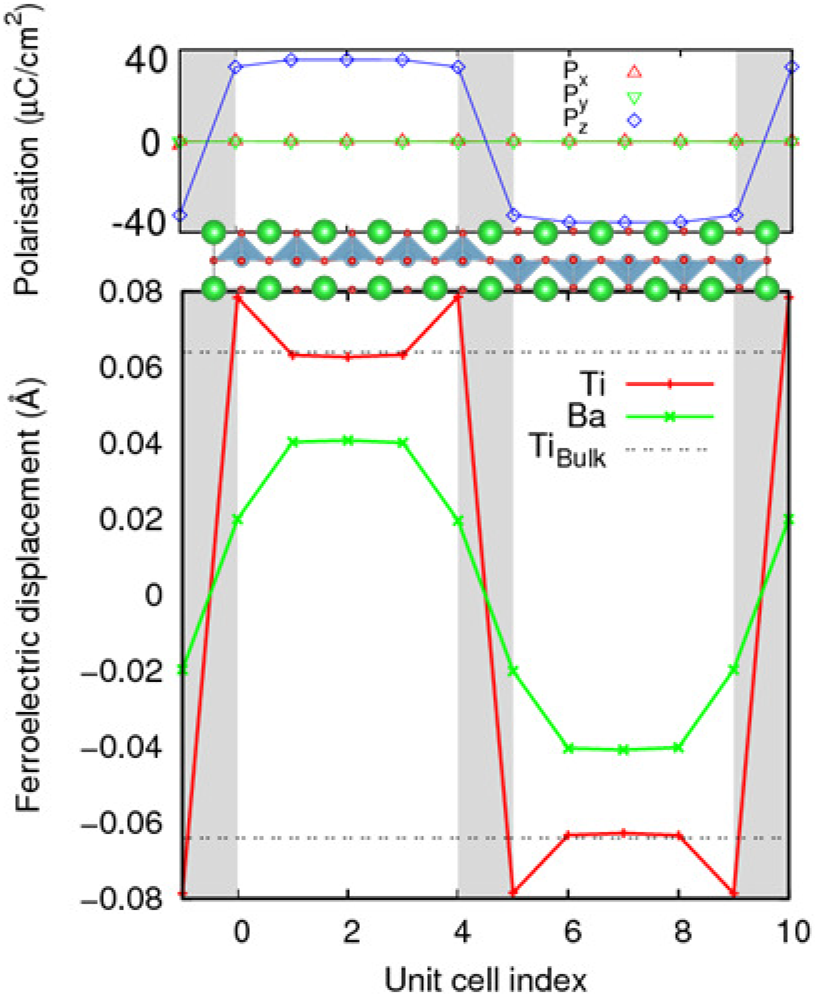

Figure E.2: Ferroelectric displacement and polarisation of 180° domain walls in $BaTiO_3$ calculated using DFT.

Appendix F

Switching Dynamics: Supplementary Figures

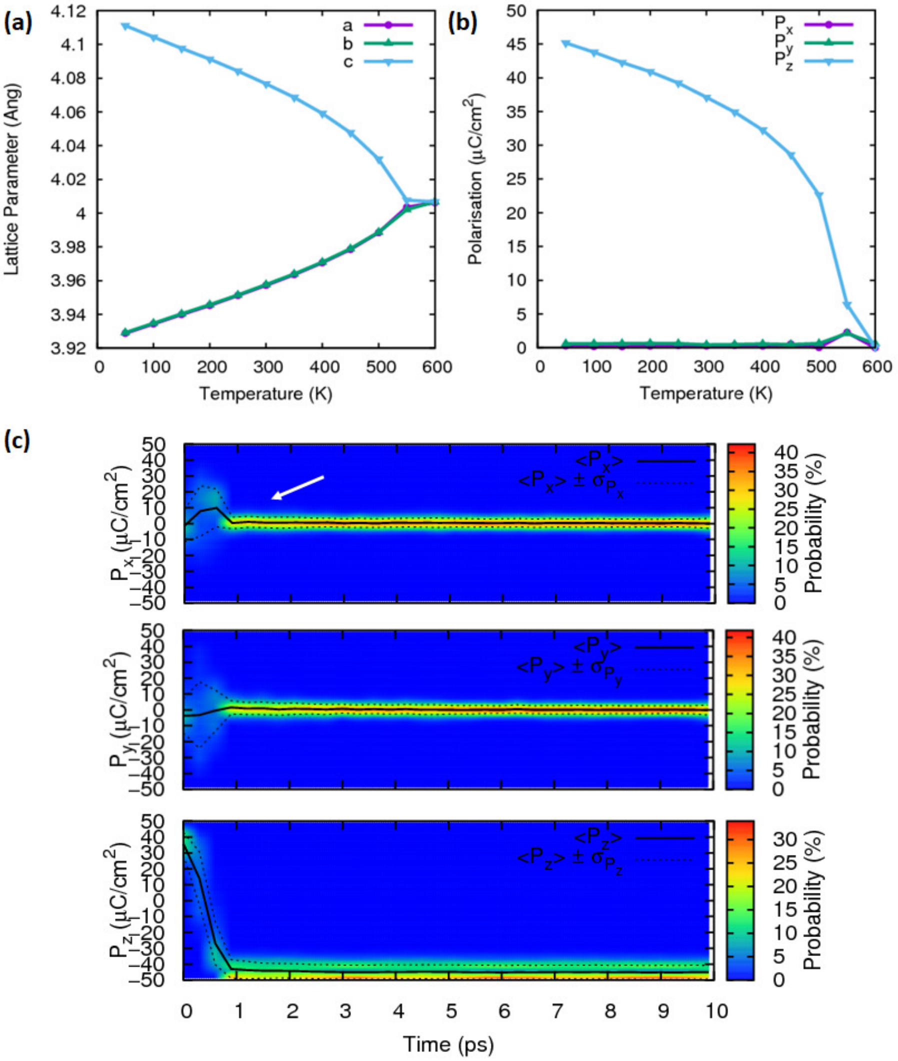

Figure F.1: Properties of $PbZr_{0.2}Ti_{0.8}O_3$ using the Gindele forcefield. (a) Temperature dependence of the average local lattice parameters and (b) polarisation. (c) Behaviour of the local order parameter polarisation during switching at 100 K. The solid black lines trace the mean of the i^{th} polarisation component $\langle P_i \rangle$. Dotted lines trace the standard deviation of the mean $\langle P_i \langle \pm \sigma_{P_i}$.

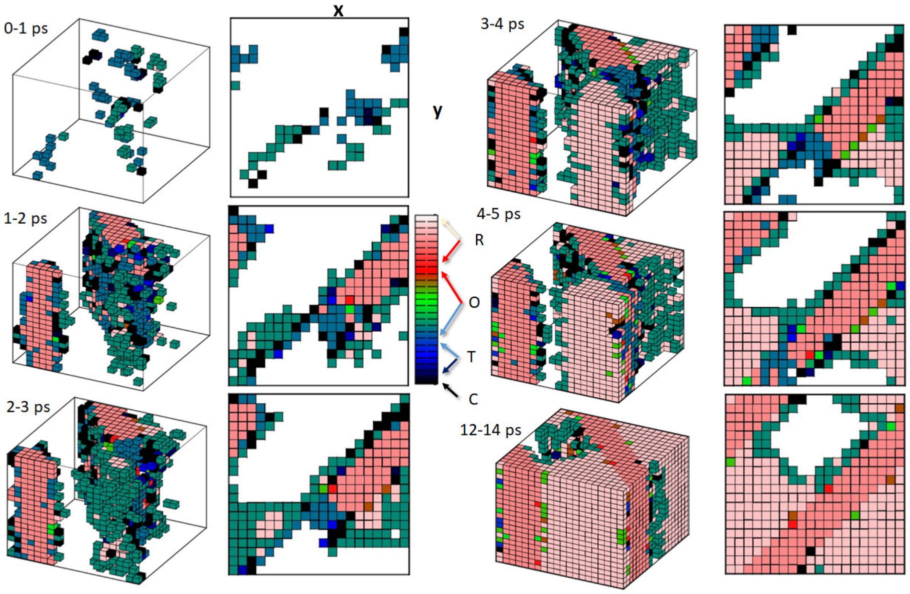

Figure F.2: Switching of forward-poled rhombohedral $PbZr_{0.8}Ti_{0.2}O_3$ at 100 K. Perspective and top view of negatively poled ($P_z < 0$) unit cells during switching. Each unit cell is represented by a cube (or square) whose colour identifies the local phase, determined from the local polarisation.

Appendix G

Mechanism of Ageing: Supplementary Figures

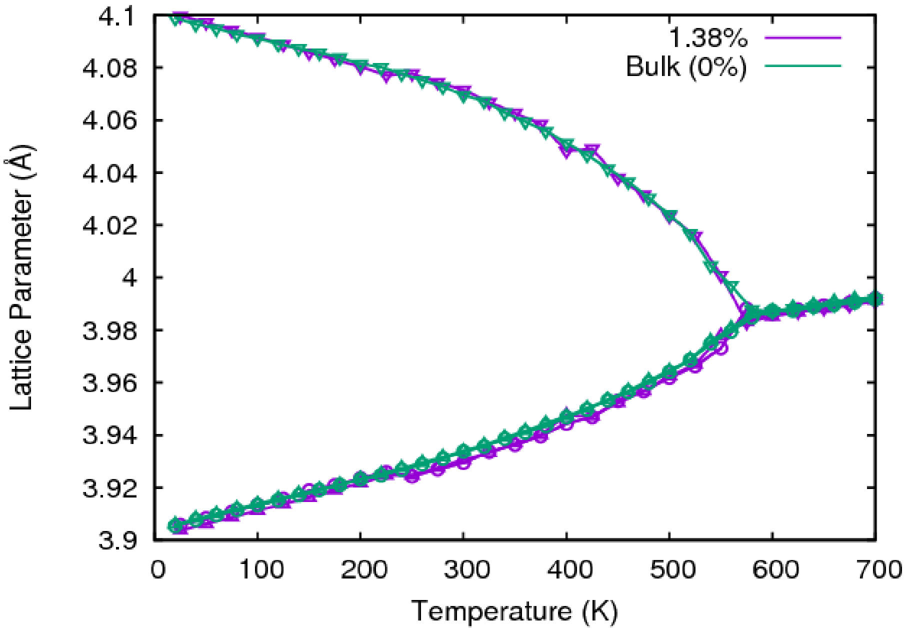

Figure G.1: Validation test of the Gindele PZT forcefield [23] when modified to include randomly distributed $(\mathrm{B}''_{\mathrm{Ti}}+\mathrm{V}^{\bullet\bullet}_{\mathrm{O}})^{\times}$ associates in an unaged dipole configuration. Temperature dependence of the local lattice parameters are correctly maintained.

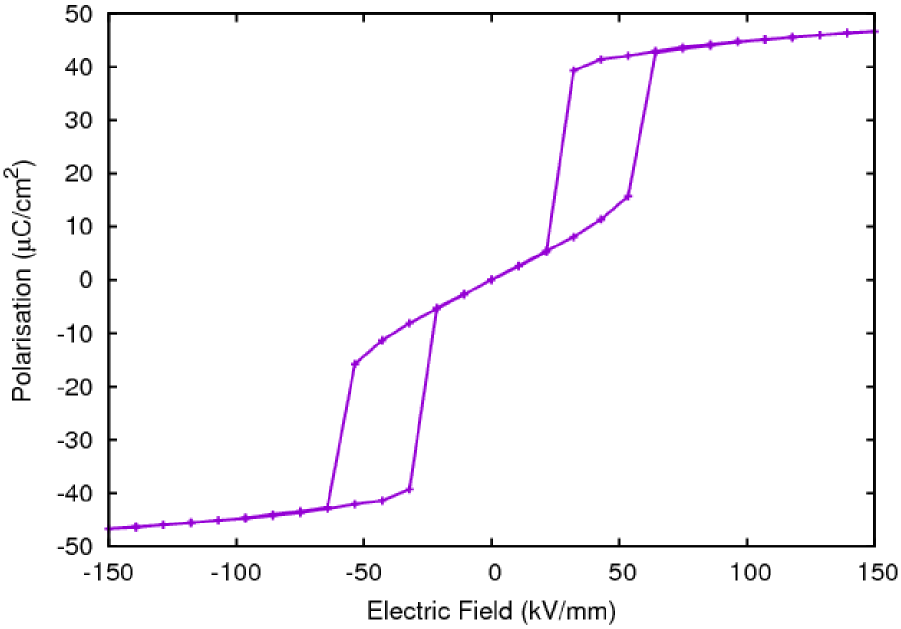

Figure G.2: Observation of double hysteresis in PZT. Polarisation hysteresis of aged tetragonal phase $PbZr_{0.1}Ti_{0.9}O_3$ at 100 K where a poling field is applied perpendicular to the ageing alignment.

Bibliography

[1] P. Cogez, *'International Technology Roadmap for Semiconductors-2012 Update Overview':*
http://www.itrs.net/reports.html *[Accessed 09/05/15].*

[2] V. Garcia and M. Bibes, *Inside story of ferroelectric memories*, Nature **483**, 7 (2012).

[3] M. Bibes, *Nanoferronics is a winning combination*, Nature Materials **11**, 354 (2012).

[4] A. M. Ionescu, *Nanoelectronics: Ferroelectric devices show potential*, Nature Nanotechnology **7**, 83 (2012).

[5] I. I. Naumov, L. Bellaiche, and H. X. Fu, *Unusual phase transitions in ferroelectric nanodisks and nanorods*, Nature **432**, 737 (2004).

[6] I. I. Naumov, L. M. Bellaiche, and H. Fu, *Multi-stable vortex states in ferroelectric nanostructure*, US Patent: **US 2006008** (2006).

[7] I. I. Naumov, L. M. Bellaiche, S. A. Prosandeev, I. V. Ponomareva, and I. A. Kornev, *Ferroelectric nanostructures having switchable multi-stable vortex states*, US Patent: **US 7593250** (2009).

[8] J. F. Scott and C. A. Paz de Araujo, *Ferroelectric memories.*, Science **246**, 1400 (1989).

[9] J. F. Scott, *Applications of modern ferroelectrics.*, Science **315**, 954 (2007).

[10] S. V. Kalinin et al., *Defect-mediated polarization switching in ferroelectrics and related materials: from mesoscopic mechanisms to atomistic control.*, Advanced Materials **22**, 314 (2010).

[11] J. A. Armstrong, N. Bloembergen, J. Ducuing, and P. S. Pershan, *Interactions between light waves in a nonlinear dielectric*, Physical Review **127**, 1918 (1962).

[12] G. Catalan, J. Seidel, R. Ramesh, and J. F. Scott, *Domain wall nanoelectronics*, Reviews of Modern Physics **84**, 119 (2012).

[13] W. Lee et al., *Individually addressable epitaxial ferroelectric nanocapacitor arrays with near Tb inch*$^{-2}$ *density*, Nature Nanotechnology **3**, 402 (2008).

[14] D. H. Do et al., *Structural visualization of polarization fatigue in epitaxial ferroelectric oxide devices*, Nature Materials **3**, 365 (2004).

[15] M. Dawber, K. M. Rabe, and J. F. Scott, *Physics of thin-film ferroelectric oxides*, Reviews of Modern Physics **77**, 1083 (2005).

[16] A. Sepliarsky et al., *Atomic-level simulation of ferroelectricity in oxide materials*, Current Opinion in Solid State and Materials Science **9**, 107 (2005).

[17] S. Tinte, M. G. Stachiotti, M. Sepliarsky, R. L. Migoni, and C. O. Rodriguez, *Atomistic modelling of BaTiO3 based on first-principles calculations*, Journal of Physics: Condensed Matter **11**, 9679 (1999).

[18] J. M. Vielma and G. Schneider, *Shell model of BaTiO3 derived from ab-initio total energy calculations*, Journal of Applied Chemistry **114**, 4827475 (2013).

[19] M. G. Stachiotti, *Ferroelectricity in BaTiO3 nanoscopic structures*, Applied Physics Letters **84**, 251 (2004).

[20] S. Tinte and M. G. Stachiotti, *Surface effects and ferroelectric phase transitions in BaTiO3 ultrathin films*, Physical Review B **64**, 235403 (2001).

[21] E. Heifets, E. A. Kotomin, and J. Maier, *Semi-empirical simulations of surface relaxation for perovskite titanates*, Surface Science **462**, 19 (2000).

[22] T. Shimada, K. Wakahara, Y. Umeno, and T. Kitamura, *Shell model potential for* $PbTiO_3$ *and its applicability to surfaces and domain walls*, Journal of Physics: Condensed Matter **20**, 324225 (2008).

[23] O. Gindele, A. V. Kimmel, M. G. Cain, and D. M. Duffy, *Shell Model force field for Lead Zirconate Titanate* $PbZr_{(1-x)}Ti_xO_3$, Journal of Physical Chemistry C **119**, 17784 (2015).

[24] O. T. Gindele, *Atomistic Simulations of Ferroelectric Lead Zirconate Titanate*, PhD thesis, University College London, 2016.

[25] D. Damjanovic, *Ferroelectric, dielectric and piezoelectric properties of ferroelectric thin films and ceramics*, Reports on Progress in Physics **61**, 1267 (1998).

[26] K. M. Rabe, M. Dawber, C. Lichtensteiger, C. H. Ahn, and J.-M. Triscone, *Modern Physics of Ferroelectrics: Essential Background*, pages 1–30, Springer Berlin Heidelberg, Berlin, Heidelberg, 2007.

[27] L. D. Landau, Physikalische Zeitschrift der Sowjetunion **11**, 26 (1937), in *Collected Papers of L. D. Landau*, edited by D. ter Haar, Pergamon Press, 1965.

[28] L. D. Landau, Physikalische Zeitschrift der Sowjetunion **11**, 545 (1937), in *Collected Papers of L. D. Landau*, edited by D. ter Haar, Pergamon Press, 1965.

[29] A. F. Devonshire, *Theory of barium titanate .1.*, Philosophical Magazine **40**, 1040 (1949).

[30] A. F. Devonshire, *Theory of barium titanate .2.*, Philosophical Magazine **42**, 1065 (1951).

[31] A. F. Devonshire, *Theory of ferroelectrics*, Advances in Physics **3**, 35 (1954).

[32] M. E. Lines and A. M. Glass, *Principles and Applications of Ferroelectrics and Related Materials*, International series of monographs on physics, OUP Oxford, 1977.

[33] V. Fridkin and S. Ducharme, *Ferroelectricity and Ferroelectric Phase Transition*, pages 1–9, Springer Berlin Heidelberg, Berlin, Heidelberg, 2014.

[34] R. E. Cohen, *Origin of Ferroelectricity in Perovskite Oxides*, Nature **358**, 136 (1992).

[35] C. Lichtensteiger et al., *Ferroelectricity in Ultrathin-Film Capacitors*, chapter 12, pages 230–265, Wiley-VCH Verlag GmbH & Co. KGaA, 2011.

[36] N. A. Pertsev, A. G. Zembilgotov, and A. K. Tagantsev, *Effect of mechanical boundary conditions on phase diagrams of epitaxial ferroelectric thin films*, Physical Review Letters **80**, 1988 (1998).

[37] N. A. Pertsev, A. K. Tagantsev, and N. Setter, *Phase transitions and strain-induced ferroelectricity in SrTiO3 epitaxial thin films*, Physical Review B **61**, R825 (2000).

[38] P. Aguado-Puente, *First-Principles Study of Screening Mechanisms of the Depolarising Field in Nanosized Capacitors*, PhD thesis, Universidad de Cantabria, 2011.

[39] J. Junquera and P. Ghosez, *First-Principles Study of Ferroelectric Oxide Epitaxial Thin Films and Superlattices: Role of the Mechanical and Electrical Boundary Conditions*, Journal of Computational and Theoretical Nanoscience **5**, 2071 (2008).

[40] J. R. Hook and H. E. Hall, *Solid State Physics*, Manchester Physics Series, John Wiley & Sons, 2nd edition, 2006.

[41] K. J. Choi et al., *Enhancement of ferroelectricity in strained BaTiO3 thin films*, Science **306**, 1005 (2004).

[42] E. Bousquet, N. Spaldin, and P. Ghosez, *Strain-induced ferroelectricity in simple rocksalt binary oxides*, Physical Review Letters **104**, 37601 (2010).

[43] J. H. Haeni et al., *Room-temperature ferroelectricity in strained SrTiO3*, Nature **430**, 758 (2004).

[44] J. A. Sanjurjo, E. López-Cruz, and G. Burns, *High-pressure Raman-study of zone-center phonons in PbTiO3*, Physical Review B **28**, 7260 (1983).

[45] W. Cochran, *Crystal stability and the theory of ferroelectricity*, Advances in Physics **9**, 387 (1960).

[46] V. V. Lemanov, A. V. Sotnikov, E. P. Smirnova, M. Weihnacht, and R. Kunze, *Perovskite CaTiO3 as an incipient ferroelectric*, Solid State Communications **110**, 611 (1999).

[47] T. Lee and L. A. Aksay, *Hierarchical structure-ferroelectricity relationships of barium titanate particles*, Crystal Growth and Design **1**, 401 (2001).

[48] G. Shirane, S. Hoshino, and K. Suzuki, *Crystal structures of lead titanate and of lead-barium titanate*, Journal of the Physical Society of Japan **5**, 453 (1950).

[49] B. S. Kwak et al., *Strain relaxation by domain formation in epitaxial ferroelectric thin films*, Physical Review Letters **68**, 3733 (1992).

[50] A. Bussmann-Holder, *The polarizability model for ferroelectricity in perovskite oxides*, Journal of Physics: Condensed Matter **24**, 273202 (2012).

[51] W. Zhong, R. D. Kingsmith, and D. Vanderbilt, *Giant LO-TO splitting in perovskite ferroelectric*, Physical Review Letters **72**, 3618 (1994).

[52] J. R. Tessman, A. H. Kahn, and W. Shockley, *Electronic polarizabilities of ions in crystals*, Physical Review **92**, 890 (1953).

[53] R. Migoni, H. Bilz, and D. Bauerle, *Origin of Raman-scattering and ferroelectricity in oxidic perovskites*, Phyical Review Letters **37**, 1155 (1976).

[54] J. D. Axe, *Apparent ionic charges and vibrational eigenmodes of BaTiO3 and other perovskites*, Physical Review **157**, 429 (1967).

[55] N. Zhang et al., *The missing boundary in the phase diagram of* $PbZr_{(1-x)}Ti_xO_3$., Nature Communications **5**, 5231 (2014).

[56] L. B. Kong, J. Ma, W. Zhu, and O. K. Tan, *Preparation and characterization of lead zirconate ceramics from high-energy ball milled powder*, Materials Letters **49**, 96 (2001).

[57] D. I. Woodward, J. Knudsen, and I. M. Reaney, *Review of crystal and domain structures in the PbZrxTi1-xO3 solid solution*, Physical Review B **72**, 104110 (2005).

[58] B. Noheda et al., *Polarization rotation via a monoclinic phase in the piezoelectric 92% $PbZn_{1/3}Nb_{2/3}O_3$-8% PbTiO3*, Physical Review Letters **74**, 2059 (2001).

[59] L. Bellaiche, A. García, and D. Vanderbilt, *Electric-field induced polarization paths in Pb(Zr1-xTix)O3 alloys*, Physical Review B **64**, 060103(R) (2001).

[60] A. Bogdanov, A. Mysovsky, C. J. Pickard, and A. V. Kimmel, *Modelling the structure of Zr-rich $Pb(Zr_{1-x}Ti_x)O_3$, x=0.4 by a multiphase approach*, Physical Chemistry Chemical Physics **18**, 28316 (2016).

[61] D. L. Corker, A. M. Glazer, R. W. Whatmore, A. Stallard, and F. Fauth, *A neutron diffraction investigation into the rhombohedral phases of the perovskite series $PbZr_{1-x}Ti_xO_3$*, Journal of Physics: Condensed Matter **10**, 6251 (1998).

[62] I. Grinberg, V. R. Cooper, and A. M. Rappe, *Oxide chemistry and local structure of PbZrxTi1-xO3 studied by density-functional theory supercell calculations*, Physical Review B **69**, 144118 (2004).

[63] R. Resta, *Theory of the electric polarization in crystals*, Ferroelectrics **136**, 51 (1992).

[64] R. Resta, *Macroscopic polarization in crystalline dielectrics - the geometric phase approach*, Reviews on Modern Physics **66**, 899 (1994).

[65] R. D. Kingsmith and D. Vanderbilt, *Theory of polarization in crystalline solids*, Physical Review B **47**, 1651 (1993).

[66] J. Liu, W. Chen, B. Wang, and Y. Zheng, *Theoretical Methods of Domain Structures in Ultrathin Ferroelectric Films: A Review*, Materials **7**, 6502 (2014).

[67] A. Pramanick, A. D. Prewitt, J. S. Forrester, and J. L. Jones, *Domains, domain walls and defects in perovskite ferroelectric oxides: a review of present understanding and recent contributions*, Critical Reviews in Solid State and Materials Sciences **37**, 243 (2012).

[68] J. Fousek and Safranko.M, *On equilibrium domain structure of BaTiO3*, Japanese Journal of Applied Physics **4**, 403 (1965).

[69] S. K. Streiffer et al., *Observation of nanoscale 180 degree stripe domains in ferroelectric PbTiO3 thin films*, Physical Review Letters **89**, 67601 (2002).

[70] J. Junquera and P. Ghosez, *Critical thickness for ferroelectricity in perovskite ultrathin films*, Nature **422**, 506 (2003).

[71] R. V. Wang et al., *Reversible chemical switching of a ferroelectric film*, Physical Review Letters **102**, 47601 (2009).

[72] D. C. Ma, Y. Zheng, B. Wang, and C. H. Woo, *Domain structures of ferroelectric thin film controlled by oxidizing atmosphere*, Applied Physics Letters **99**, 142908 (2011).

[73] D. D. Fong et al., *Stabilization of monodomain polarization in ultrathin PbTiO3 films*, Physical Review Letters **96**, 127601 (2006).

[74] C. Kittel, *Theory of the structure of ferromagnetic domains in films and small particles*, Physical Review **70**, 965 (1946).

[75] T. Mitsui and J. Furuichi, *Domain struture of Rochelle salt and* KH_2PO_4, Physical Review **90**, 193 (1953).

[76] M. G. Daraktchiev, G. Catalan, and J. M. Scott, *Landau theory of ferroelectric domain walls in magnetoelectrics*, Ferroelectrics **375**, 122 (2008).

[77] G. Catalan, A. Schilling, J. F. Scott, and J. M. Gregg, *Domains in three-dimensional ferroelectric nanostructures: theory and experiment*, Journal of Physics: Condensed Matter **19**, 132201 (2007).

[78] A. Schilling et al., *Domains in Ferroelectric Nanodots*, Nanoletters **9**, 3359 (2009).

[79] J. Valasek, *Piezoelectric and allied phenomena in Rochelle salt*, Physical Review **15**, 537 (1920).

[80] H. A. Haus and J. R. Melcher, *'Energy, Power Flow and Forces', Lecture Notes for Electromagnetic Fields and Energy 6.013, Massachusetts Institute of Technology. Available from:* http://web.mit.edu/6.013_book/www/book.html *[Accessed 6/10/16].*

[81] T. M. Correia et al., *A Lead-Free and High-Energy Density Ceramic for Energy Storage Applications*, Journal of the American Ceramic Society **96**, 2699 (2013).

[82] J. F. Scott, *Ferroelectrics go bananas*, Journal of Physics: Condensed Matter **20**, 21001 (2008).

[83] R. Landauer, *Electrostatic considerations in* $BaTiO_3$ *domain formation during polarization reversal*, Journal of Applied Physics **28**, 227 (1957).

[84] S. Liu, I. Grinberg, and A. M. Rappe, *Intrinsic ferroelectric switching from first principles*, Nature **534**, 360 (2016).

[85] L. B. Ioffe and V. M. Vinokur, *Dynamics of interfaces and dislocations in disordered media*, Journal of Physics C: Solid State Physics **20**, 6149 (1987).

[86] T. Tybell, P. Paruch, T. Giamarchi, and J. M. Triscone, *Domain wall creep in epitaxial ferroelectric* $Pb(Zr_{0.2}Ti_{0.8})O_3$ *thin films*, Physical Review Letters **89**, 97601 (2002).

[87] P. Paruch, T. Giamarchi, T. Tybell, and J.-M. Triscone, *Nanoscale studies of domain wall motion in epitaxial ferroelectric thin films*, Journal of Applied Physics **100**, 51608 (2006).

[88] R. C. Miller and A. Savage, *Velocity of sideways 180-degrees domain-wall motion in* $BaTiO_3$ *as a function of the applied electric field*, Physical Review **112**, 755 (1958).

[89] R. C. Miller and G. Weinreich, *Mechanism for the sidewise motion of 180-degrees domain walls in barium titanate*, Physical Review **117**, 1460 (1960).

[90] A.M.Rappe et al., *Nucleation and growth mechanism of ferroelectric domain-wall motion*, Nature **449**, 881 (2007).

[91] A. V. Kimmel, P. M. Weaver, M. G. Cain, and P. V. Sushko, *Defect-mediated lattice relaxation and domain stability in ferroelectric oxides*, Physical Review Letters **109**, 117601 (2012).

[92] L. X. He and D. Vanderbilt, *First-principles study of oxygen-vacancy pinning of domain walls in PbTiO3*, Physical Review B **68**, 134103 (2003).

[93] L. Hong, A. K. Soh, Q. G. Du, and J. Y. Li, *Interaction of O vacancies and domain structures in single crystal BaTiO3: Two-dimensional ferroelectric model*, Physical Review B **77**, 94104 (2008).

[94] E. Lafond, *et al, 'WSTS Semiconductor Market Forecast Spring 2017':* https://www.wsts.org *[Accessed 03/08/17].*

[95] C. S. Hwang, *FeRAM: Atomic Layer Deposition for Semiconductors*, Springer US, 1st edition, 2014.

[96] K. Uchino, *Ferroelectric Devices*, CRC Press Taylor and Francis Group, 2nd edition, 2009.

[97] J. S. Meena, S. M. Sze, U. Chand, and T.-Y. Tseng, *Overview of emerging nonvolatile memory technologies*, Nanoscale Research Letters **9**, 526 (2014).

[98] D. Newns, B. Elmegreen, X. H. Liu, and G. Martyna, *A low-voltage high-speed electronic switch based on piezoelectric transduction*, Journal of Applied Physics **111**, 084509 (2012).

[99] D. M. Newns, B. G. Elmegreen, X.-H. Liu, and G. J. Martyna, *The piezoelectronic transistor: A nanoactuator-based post-CMOS digital switch with high speed and low power*, MRS Bulletin **37**, 1071 (2012).

[100] R. M. Martin, *Electronic Structure: Basic Theory and Practical Methods*, Cambridge University Press, Cambridge, United Kingdom, 3rd edition, 2013.

[101] D. Sholl and J. A. Steckel, *Density Functional Theory: A Practical Introduction*, John Wiley & Sons, 2009.

[102] M. Born and J. R. Oppenheimer, *Quantum theory of molecules*, Annalen der Physik **84**, 475 (1927).

[103] P. Ghosez, *First-Principles Study of the Dielectric and Dynamical Properties of Barium Titanate*, PhD thesis, Universite Catholique de Louvain, 1997.

[104] P. Hohenberg and W. Kohn, *Inhomogeneous electron gas*, Physical Review **136**, B864 (1964).

[105] W. Kohn, Density functional theory: Fundamentals and applications, in *Highlights in Condensed Matter Theory*, edited by F. Bassani, F. Fumi, and M. P. Tosi, North Holland Physics Publishing, 1985.

[106] G. Vignale and M. Rasolt, *Current-density-functional and spin-density-functional theory for inhomogeneous electronic systems in strong magnetic-fields*, Physical Review B **37**, 10685 (1988).

[107] G. Vignale and W. Kohn, *Current-dependent exchange-correlation potential for dynamical linear response theory*, Physical Review Letters **77**, 2037 (1996).

[108] W. Kohn and L. J. Sham, *Self-consistent equations including exchange and correlation effects*, Physical Review **140**, A1133 (1965).

[109] N. W. Ashcroft and N. D. Mermin, *Solid State Physics*, HRW International Editions, 1988.

[110] H. J. Monkhorst and J. D. Pack, *Special points for Brillouin-zone integrations*, Physical Review B **13**, 5188 (1976).

[111] Z. G. Wu and R. E. Cohen, *More accurate generalized gradient approximation for solids*, Physical Review B **73**, 235116 (2006).

[112] S. J. Clark et al., *First principles methods using CASTEP*, Zeitschrift Fur Kristallographie **220**, 567 (2005).

[113] M. C. Payne, M. P. Teter, D. C. Allan, T. A. Arias, and J. D. Joannopoulos, *Iterative minimization techniques for ab initio total-energy calculations - molecular-dynamics and conjugate gradients*, Reviews of Modern Physics **64**, 1045 (1992).

[114] D. I. Bilc et al., *Hybrid exchange-correlation functional for accurate prediction of the electronic and structural properties of ferroelectric oxides*, Physical Review B **77**, 165107 (2008).

[115] G. P. Francis and M. C. Payne, *Finite basis set corrections to total energy pseudopotential calculations*, Journal of Physics-Condensed Matter **2**, 4395 (1990).

[116] S. Baroni, P. Gianozzi, and A. Tesla, *Green-function approach to linear response in solids*, Physical Review Letters **58**, 1861 (1987).

[117] P. Ghosez and J. Junquera, *Handbook of Theoretical and Computational Nanotechnology*, volume 7, American Scientific Publishers, 2006.

[118] X. Gonze and J.-P. Vigneron, *Density-functional approach to nonlinear-response coefficients of solids*, Physical Review B **39**, 13120 (1989).

[119] K. Refson, P. R. Tulip, and S. J. Clark, *Variational density-functional perturbation theory for dielectrics and lattice dynamics*, Physical Review B **73**, 155114 (2006).

[120] X. Gonze, P. Ghosez, and R. W. Godby, *Density-polarization functional theory of the response of a periodic insulating solid to an electric-field*, Physical Review Letters **79**, 4035 (1995).

[121] X. Gonze, P. Ghosez, and R. W. Godby, *Long-wavelength behavior of the exchange-correlation kernel in the Kohn-Sham theory of periodic systems*, Physical Review B **56**, 12811 (1997).

[122] A. Huller, *Displacement correlation and anomalous x-ray scattering in BaTiO3*, Solid State Communications **7**, 589 (1969).

[123] L. F. Mattheis, *Energy-bands for KNiF3, SrTiO3, KMoO3, and KTaO3*, Physical Review B **6**, 4718 (1972).

[124] A. J. Morris, R. J. Nicholls, C. J. Pickard, and J. R. Yates, *OptaDOS: A tool for obtaining density of states, core-level and optical spectra from electronic structure codes*, Computer Physics Communications **185**, 1477 (2014).

[125] J. R. Yates, X. Wang, D. Vanderbilt, and I. Souza, *Spectral and Fermi surface properties from Wannier interpolation*, Physical Review B **75**, 195121 (2007).

[126] W. A. Harrison, *Electronic Structure and the Properties of Solids*, W. H. Freeman and Co., San Francisco, 1980.

[127] P. Ghosez, X. Gonze, P. Lambin, and Michenaud, *Born effective charges of barium titanate: Band-by-band decomposition and sensitivity to structural features*, Physical Review B **51**, 6765 (1995).

[128] P. Ghosez, X. Gonze, and J. P. Michenaud, *Lattice dynamics and ferroelectric instability of barium titanate*, Ferroelectrics **194**, 39 (1997).

[129] P. Ghosez, E. Cockayne, U. V. Waghmare, and K. M. Rabe, *Lattice dynamics of BaTiO3, PbTiO3, and PbZrO3: A comparative first-principles study*, Physical Review B **60**, 836 (1999).

[130] H. K. Hellwege, *Ferroelectrics and Related Substances*, volume 3, Springer Verlag, Berlin, 1969.

[131] J. D. Gale and A. L. Rohl, *The General Utility Lattice Program (GULP)*, Molecular Simulation **29**, 291 (2003).

[132] I. T. Todorov, W. Smith, K. Trachenko, and M. T. Dove, *DLPOLY 3: new dimensions in molecular dynamics simulations via massive parallelism*, Journal of Materials Chemistry **16**, 1911 (2006).

[133] P. P. Ewald, *The calculation of optical and electrostatic grid potential*, Annalen der Physik **64**, 253 (1921).

[134] D. Frenkel and B. Smit, *Understanding Molecular Simulation*, Academic Press, San Diago, USA, 2nd edition, 2002.

[135] U. Essmann et al., *A smooth particle mesh Ewald method*, Journal of Chemical Physics **103**, 8577 (1995).

[136] D. E. Parry, *Electrostatic potential in surface region of an ionic-crystal*, Surface Science **49**, 433 (1975).

[137] D. E. Parry, *Correction*, Surface Science **54**, 195 (1976).

[138] B. G. Dick and A. W. Overhauser, *Theory of the dielectric constants of alkali halide crystals*, Physical Review **112**, 90 (1958).

[139] P. J. Mitchell and D. Fincham, *Shell-model simulations by adiabatic dynamics*, Journal of Physics: Condensed Matter **5**, 1031 (1993).

[140] S. R. Phillpot, S. B. Sinnott, and A. Asthagiri, *Atomic-level simulation of ferroelectricity in oxides: Current status and opportunities*, Annual Review of Materials Research **37**, 239 (2007).

[141] P. H. Hünenberger, *Thermostat algorithms for molecular dynamics simulations*, Advanced Polymer Science **173**, 105 (2005).

[142] S. Nosé, *A unified formulation of the constant temperature molecular-dynamics methods*, Journal of Chemical Physics **81**, 511 (1984).

[143] S. Nosé, *A molecular-dynamics method for simulations in the canonical ensemble*, Molecular Physics **52**, 255 (1984).

[144] W. G. Hoover, *Canonical dynamics: equilibrium phase-space distributions*, Physical Review A **31**, 1695 (1985).

[145] W. G. Hoover, *Constant-pressure equations of motion*, Physical Review A **34**, 2499 (1986).

[146] S. Melchionna, G. Ciccotti, and B. L. Holian, *Hoover NPT dynamics for systems varying in shape and size*, Molecular Physics **78**, 533 (1993).

[147] R. Dittmer et al., *Ergodicity reflected in macroscopic and microscopic field-dependent behavior of BNT-based relaxors*, Journal of Applied Physics **115**, 84111 (2014).

[148] K. Trachenko et al., *Modeling high-energy radiation damage in nuclear and fusion applications*, Nuclear Instruments and Methods in Physics Research B **277**, 6 (2012).

[149] A. Ruini, R. Resta, and S. Baroni, *Dynamical-charge neutrality at a crystal surface*, Physical Review B **57**, 5742 (1998).

[150] L. Fu, E. Yaschenko, L. Resca, and R. Resta, *Hartree-Fock studies of surface properties of BaTiO3*, Physical Review B **60**, 2697 (1999).

[151] M. Sepliarsky and R. E. Cohen, *First-principles based atomistic modelling of phase stability in PMN-xPT*, Journal of Physics: Condensed Matter **23**, 435902 (2011).

[152] G. D. Belletti, S. D. Dalosto, and S. Tinte, *Strain-gradient-induced switching of nanoscale domains in free-standing ultrathin films*, Physical Review B **89**, 174104 (2014).

[153] Y. Zhang, J. Sun, J. P. Perdew, and X. Wu, *Comparative first-principles study of prototypical ferroelectric materials by LDA, GGA, and SCAN meta-GGA*, Physical Review B **96**, 035143 (2017).

[154] Z. Wu and H. Krakauer, *First-principles calculations of piezoelectricity and polarization rotation in* $Pb(Zr_{0.5}Ti_{0.5})O_3$, Physical Review B **68**, 014112 (2003).

[155] M. Meyer, J. Padilla, and D. Vanderbilt, *Theory of PbTiO3, BaTiO3, and SrTiO3 surfaces*, Faraday Discussions **114**, 395 (1999).

[156] A. Munkholm et al., *Antiferrodistortive reconstruction of the PbTiO3(001) surface*, Physical Review Letters **88**, 16101 (2002).

[157] C. Bungaro and K. M. Rabe, *Coexistence of antiferrodistortive and ferroelectric distortions at the PbTiO3(001) surface*, Physical Review B **71**, 35420 (2005).

[158] Y. Umeno, T. Shimada, T. Kitamura, and C. Elsaesser, *Ab initio density functional theory study of strain effects on ferroelectricity at PbTiO3 surfaces*, Physical Review B **74**, 174111 (2006).

[159] M. Sepliarsky, M. G. Stachiotti, and R. L. Migoni, *Surface and substrate effects on the ferroelectric properties of PbTiO3 ultrathin films*, Ferroelectrics **335**, 3 (2006).

[160] M. Sepliarsky, M. G. Stachiotti, and R. L. Migoni, *Surface reconstruction and ferroelectricity in PbTiO3 thin films*, Physical Review B **72**, 14110 (2005).

[161] K. Momma and F. Izumi, *VESTA 3 for three-dimensional visualization of crystal, volumetric and morphology data*, Journal of Applied Crystallography **44**, 1272 (2011).

[162] N. A. Spaldin, *Fundamental size limits in ferroelectricity*, Science **304**, 1606 (2004).

[163] G. Thorner, J.-M. Kiat, C. Bogicevic, and I. Korner, *Axial hypertoroidal moment in a ferroelectric nanotorus: A way to switch local polarization*, Physical Review B **89**, 220103(R) (2014).

[164] S. Prosandeev and L. Bellaiche, *Hypertoroidal moment in complex dipolar structures*, Journal of Materials Science **44**, 5235 (2009).

[165] S. Prosandeev and L. Bellaiche, *Order parameter in complex dipolar structures: Microscopic modeling*, Physical Review B **77**, 060101(R) (2008).

[166] M. Doi, *Soft Matter Physics*, OUP Oxford, 2nd edition, 2015.

[167] H. B. Callen and T. A. Welton, *Irreversibility and generalized noise*, Physical Review **83**, 34 (1951).

[168] J. M. Caillol, D. Leveque, and J. J. Weis, *Theoretical calculation of ion solution properties*, Journal of Chemical Physics **85**, 6645 (1986).

[169] J. P. Remeika and A. M. Glass, *Growth and ferroelectric properties of high resistivity single crystals of lead titanate*, Materials Research Bulletin **5**, 37 (1970).

[170] A. Garcia and D. Vanderbilt, *Electromechanical behavior of BaTiO3 from first principles*, Applied Physics Letters **72**, 2981 (1998).

[171] S. Farokhipoor et al., *Artificial chemical and magnetic structure at the domain walls of an epitaxial oxide*, Nature **515**, 379 (2014).

[172] M. Daraktchiev, G. Catalan, and J. F. Scott, *Landau theory of domain wall magnetoelectricity*, Physical Review B **81**, 224118 (2010).

[173] J. Seidel et al., *Conduction at domain walls in oxide ferroelectrics*, Nature **8**, 229 (2009).

[174] D. Meier et al., *Anisotropic Conductance at improper ferroelectric domain walls*, Nature **11**, 284 (2012).

[175] C.-L. Jia, K. W. Urban, M. Alexe, D. Hesse, and I. Vrejoiu, *Direct Observation of Continuous Electric Dipole Rotation in Flux-Closure Domains in Ferroelectric Pb(Zr,Ti)O-3*, Science **331**, 1420 (2011).

[176] Z. Jiang et al., *Strain-induced control of domain wall morphology in ultrathin PbTiO3 films*, Physical Review B **89**, 214113 (2014).

[177] D. G. Schlom et al., *Strain tuning of ferroelectric thin films*, Annual Review of Materials Research **37**, 589 (2007).

[178] O. Dieguez, K. M. Rabe, and D. Vanderbilt, *First-principles study of epitaxial strain in perovskites*, Physical Review B **72**, 144101 (2005).

[179] I. Kornev, H. X. Fu, and L. Bellaiche, *Ultrathin films of ferroelectric solid solutions under a residual depolarizing field*, Physical Review Letters **93**, 196104 (2004).

[180] D. Sichuga, I. Ponomareva, and L. Bellaiche, *Phase diagrams of epitaxial Pb(Zr, Ti)O-3 ultrathin films from first principles*, Physical Review B **80**, 134116 (2009).

[181] T. Shimada, S. Tomoda, and T. Kitamura, *Ab initio study of ferroelectric closure domains in ultrathin PbTiO3 films*, Physical Review B **81**, 144116 (2010).

[182] A. R. Balakrishna and J. E. Huber, *Scale effects on the formation of polarization vortices in tetragonal ferroelectrics*, Applied Physics Letters **106**, 92906 (2015).

[183] R. G. P. McQuaid, L. J. McGilly, P. Sharma, A. Gruverman, and J. M. Gregg, *Mesoscale flux-closure domain formation in single-crystal BaTiO3.*, Nature Communications **2**, 404 (2011).

[184] L. J. McGilly and J. M. Gregg, *Polarisation closure in PbZr(0.42)Ti(0.58)O3 nanodots*, Nano Letters **11**, 4490 (2011).

[185] A. K. Yadav et al., *Observation of Polar Vortices in Oxide Superlattices*, Nature **530**, 198 (2016).

[186] D. Sichuga and L. Bellaiche, *Epitaxial Pb(Zr, Ti)O-3 Ultrathin Films under Open-Circuit Electrical Boundary Conditions*, Physical Review Letters **106**, 196102 (2011).

[187] D. Vanderbilt, *First-principles based modelling of ferroelectrics*, Current Opinion in Solid State and Materials Science **2**, 701 (1997).

[188] K. M. Rabe and P. Ghosez, *First-principles studies of ferroelectric oxides*, Topics in Applied Physics **105**, 117 (2007).

[189] P. Marton, T. Shimada, T. Kitamura, and C. Elsässer, *First-principles study of the interplay between grain boundaries and domain walls in ferroelectric PbTiO3*, Physical Review B **83**, 64110 (2011).

[190] X. Liu, Y. Wang, P. V. Lukashev, J. D. Burton, and E. Y. Tsymbal, *Interface dipole effect on thin film ferroelectric stability: First-principles and phenomenological modeling*, Physical Review B **85**, 125407 (2012).

[191] S. Kouser, T. Nishimatsu, and U. V. Waghmare, *Ferroelectric domains and diffuse transitions in ultrathin films of PbTiO3: Effects of strain and electrodes*, Physical Review B **88**, 64102 (2013).

[192] R. D. Kingsmith and D. Vanderbilt, *1st-principles investigation of ferroelectricity in perovskite compounds*, Physical Review B **49**, 5828 (1994).

[193] D. D. Fong et al., *Ferroelectricity in ultrathin perovskite films*, Science **304**, 1650 (2004).

[194] P. Zubko et al., *Ferroelectric Domains in PbTiO3/SrTiO3 Superlattices*, Ferroelectrics **433**, 127 (2012).

[195] P. Aguando-Puente and J. Junquera, *Structural and energetic properties of domains in PbTiO3/SrTiO3 superlattices from first principles*, Physical Review B **85**, 184105 (2012).

[196] M. G. Stachiotti and M. Sepliarsky, *Toroidal Ferroelectricity in PbTiO3 Nanoparticles*, Physical Review Letters **106**, 137601 (2011).

[197] I. Ponomareva, L. Bellaiche, T. Ostapchuk, J. Hlinka, and P. J, *Terahertz dielectric response of cubic BaTiO3*, Physical Review B **77**, 12102 (2008).

[198] S. Liu and R. E. Cohen, *Origin of stationary domain wall enhanced ferroelectric susceptibility*, Physical Review B **95**, 094102 (2017).

[199] Q. M. Zhang, H. Wang, N. Kim, and L. E. Cross, *Direct evaluation of domain-wall and intrinsic contributions to the dielectric and piezoelectric response and their temperature dependence on lead zirconate-titanate ceramics*, Journal of Applied Physics **75**, 454 (1994).

[200] D. a. Hall and P. J. Stevenson, *High field dielectric behaviour of ferroelectric ceramics*, Ferroelectrics **228**, 139 (1999).

[201] J. Karthik, J. C. Agar, a. R. Damodaran, and L. W. Martin, *Effect of 90° Domain Walls and Thermal Expansion Mismatch on the Pyroelectric Properties of Epitaxial* $PbZr_{0.2}Ti_{0.8}O_3$ *Thin Films*, Physical Review Letters **109**, 257602 (2012).

[202] F. Xu et al., *Domain wall motion and its contribution to the dielectric and piezoelectric properties of lead zirconate titanate films*, Journal of Applied Physics **89**, 1336 (2001).

[203] D. V. Taylor and D. Damjanovic, *Evidence of domain wall contribution to the dielectric permittivity in PZT thin films at sub-switching fields*, Journal of Applied Physics **82**, 1973 (1997).

[204] P. Zubko et al., *Negative capacitance in multidomain ferroelectric superlattices*, Nature **534**, 524 (2016).

[205] S. Salahuddin and S. Datta, *Use of negative capacitance to provide voltage amplification for low power nanoscale devices*, Nano Letters **8**, 405 (2008).

[206] I. Ponomareva, L. Bellaiche, and R. Resta, *Relation between dielectric responses and polarization fluctuations in ferroelectric nanostructures*, Physical Review B - Condensed Matter and Materials Physics **76**, 235403 (2007).

[207] I. Ponomareva, L. Bellaiche, and R. Resta, *Dielectric anomalies in ferroelectric nanostructures*, Physical Review Letters **99**, 227601 (2007).

[208] B. Meyer and D. Vanderbilt, *Ab initio study of ferroelectric domain walls in PbTiO3*, Physical Review B **65**, 104111 (2002).

[209] D. Lee et al., *Mixed Bloch-Neel-Ising Character of 180 degree ferroelectric domain walls*, Physical Review B **80**, 149904 (2009).

[210] S. Farokhipoor and B. Noheda, *Conduction through 71 domain walls in BiFeO3 thin films*, Physical Review Letters **107**, 127601 (2011).

[211] E. Bousquet et al., *Improper ferroelectricity in perovskite oxide artificial superlattices*, Nature **452**, 732 (2008).

[212] D. Sichuga, W. Ren, S. Prosandeev, and L. Bellaiche, *Chiral patterns of tilting of oxygen octahedra in zero-dimensional ferroelectrics and*

multiferroics: A first principles based study, Physical Review Letters **104**, 207602 (2010).

[213] J. L. Blok, D. H. A. Blank, G. Rijnders, K. M. Rabe, and D. Vanderbilt, *Interplay of epitaxial strain and rotations in PbTiO3/PbZrO3 superlattices from first principles*, Physical Review B **84**, 205413 (2011).

[214] A. A. Thiele, *Theory of static stability of cylindrical domains in uniaxial platelets*, Journal of Applied Physics **41**, 1139 (1970).

[215] J. M. Gregg and A. Schillling, *[Unpublished]*, Personal Correspondance (2015).

[216] W. Kanzig, *Space charge layer near the surface of a ferroelectric*, Physical Review **98**, 549 (1955).

[217] P. M. Solomon et al., *Pathway to the Piezoelectronic Transduction Logic Device*, Nano Letters **15**, 2391 (2015).

[218] M. Hytch et al., *Deformations and rotations in epitaxial Pb(Zr0.2,Ti0.8)O3 thin films grown on SrTiO3 investigated by transmission electron microscopy*, Personal Correspondance [In preparation for submission] (2016).

[219] R. A. Cowley, *Lattice dynamics + phase transitions of Strontium Titanate*, Physical Review **134**, A981 (1964).

[220] T. Schneider, H. Beck, and E. Stoll, *Quantum effects in an n-component vector model for structural phase-transitions*, Physical Review B **13**, 1123 (1976).

[221] H. Unoki and T. Sakudo, *Electron spin resonance of Fe3+ in SrTiO3 with special reference to 110 degrees K phase transition*, Journal of the Physical Society of Japan **23**, 546 (1967).

[222] N. Sai and D. Vanderbilt, *First-principles study of ferroelectric and antiferrodistortive instabilities in tetragonal SrTiO3*, Physical Review B **62**, 13942 (2000).

[223] R. A. Evarestov, E. Blokhin, D. Gryaznov, E. A. Kotomin, and J. Maier, *Phonon calculations in cubic and tetragonal phases of SrTiO3: A comparative LCAO and plane-wave study*, Physical Review B **83**, 134108 (2011).

[224] K. A. Muller, W. Berlinger, and E. Tosatti, *Indication for a novel phase in the quantum paraelectric regime of SrTiO3*, Zeitschrift Fur Physik B-Condensed Matter **84**, 277 (1991).

[225] R. Wahl, D. Vogtenhuber, and G. Kresse, *SrTiO(3) and BaTiO(3) revisited using the projector augmented wave method: Performance of hybrid and semilocal functionals*, Physical Review B **78**, 104116 (2008).

[226] S. Piskunov, E. Heifets, R. I. Eglitis, and G. Borstel, *Bulk properties and electronic structure of SrTiO3, BaTiO3 and PbTiO3 perovskites: An ab initio HF/DFT study*, Computational Materials Science **29**, 165 (2004).

[227] R. O. Bell and Rupprecht, *Elastic constants of Strontium Titanate*, Physical Review **90**, 129 (1963).

[228] J. B. J. Chapman, *Development of a Shell Model Forcefield for* $BaTiO_3$ *and its Application for Domain Walls and Surfaces*, MRes Dissertation, University College London (2014).

[229] M. W. Finnis and J. E. Sinclair, *A simple empirical N-body potential for transition metals*, Philosophical Magazine A: Physics of Condensed Matter, Structure, Defects and Mechanical Properties **50**, 45 (1984).

[230] P. Zubko et al., *Electrostatic Coupling and Local Structural Distortions at Interfaces in Ferroelectric/Paraelectric Superlattices*, Nano Letters **12**, 2846 (2012).

[231] A. P. Sutton and J. Chen, *Long-range Finnis-Sinclair potentials*, Philosphical Magazine Letters **61**, 139 (1990).

[232] T. Denneulin et al., Journal of Physics: Condensed Matter **30**, 215701 (2018).

[233] J. B. J. Chapman et al., *Low Temperature Ferroelectric Behaviour in Morphotropic* $Pb(Zr_{1-x}Ti_x)O_3$, Journal of the Americal Ceramics Society **101**, 874 (2018).

[234] B. Noheda et al., *A monoclinic ferroelectric phase in the PbZr(1-x)Ti(x)O3 solid solution*, Applied Physics Letters **74**, 2059 (1999).

[235] G. Shirane and K. Susuki, *Crystal structure of PZT*, Journal of the Physical Society of Japan **7**, 333 (1952).

[236] D. Phelan et al., *Single crystal study of competing rhombohedral and monoclinic order in lead zirconate titanate*, Physical Review Letters **105**, 1 (2010).

[237] J. Frantti et al., *Phase transitions of* $PbZr_xTi_{1-x}O_3$ *ceramics*, Physical Review B **66**, 64108 (2002).

[238] K. B. Lazarus, E. F. Crawley, J. D. Bohlmann, and F. Worth, *Static aeroelastic control using strain actuated adaptive structures*, Journal of Intelligent Material Systems and Structures **2**, 386 (1991).

[239] Y. H. Zhao and H. Y. Hu, *Active Control of Vertical Tail Buffeting by Piezoelectric Actuators*, Journal of Aircraft **46**, 1167 (2009).

[240] P. Jänker et al., *New Actuators for Aircraft , Space and Military Applications*, Actuator 2010, 12th International Conference on New Actuators , 346 (2008).

[241] M. W. Hooker, *Properties of PZT-Based Piezoelectric Ceramics Between -150 and 250 C*, Lockheed Martin Engineering Sciences Company , 1 (1998).

[242] J. Wooldridge et al., *Simultaneous measurement of X-ray diffraction and ferroelectric polarization data as a function of applied electric field and frequency*, Journal of Synchrotron Radiation **19**, 710 (2012).

[243] D. Wang, Y. Fotinich, and G. P. Carman, *Influence of temperature on the electromechanical and fatigue behavior of piezoelectric ceramics*, Journal of Applied Physics **83**, 5342 (1998).

[244] R. Xu et al., *Ferroelectric polarization reversal via successive ferroelastic transitions*, Nature materials **14**, 79 (2015).

[245] F. Yan, G. Z. Xing, and L. Li, *Low temperature dependent ferroelectric resistive switching in epitaxial BiFeO3 films*, Applied Physics Letters **104**, 13 (2014).

[246] A. Jiang et al., *Studies of Switching Kinetics in Ferroelectric Thin Films*, Japanese Journal of Applied Physics **42**, 6973 (2003).

[247] W. J. Hu et al., *Universal ferroelectric switching dynamics of vinylidene fluoride-trifluoroethylene copolymer films.*, Scientific Reports **4**, 47728 (2014).

[248] X. Zeng and R. E. Cohen, *Thermo-electromechanical response of a ferroelectric perovskite from molecular dynamics simulations*, Applied Physics Letters **99**, 142902 (2011).

[249] N. Sai, K. M. Rabe, and D. Vanderbilt, *Theory of structural response to macroscopic electric fields in ferroelectric systems*, Physical Review B **66**, 104108 (2002).

[250] S. P. Beckman, X. Wang, K. M. Rabe, and D. Vanderbilt, *Ideal barriers to polarization reversal and domain-wall motion in strained ferroelectric thin films*, Physical Review B **79**, 1 (2009).

[251] G. Geneste, *Correlations and local order parameter in the paraelectric phase of barium titanate*, Journal of Physics: Condensed Matter **23**, 125901 (2011).

[252] Y. Qi, S. Liu, I. Grinberg, and A. M. Rappe, *Atomistic description for temperature-driven phase transitions in* $BaTiO_3$, Physical Review B **94**, 134308 (2016).

[253] J. Y. Jo et al., *Domain switching kinetics in disordered ferroelectric thin films*, Physical Review Letters **99**, 1 (2007).

[254] T. M. Kamel and G. de With, *Double-peak switching current in soft ferroelectric lead zirconate titanate*, Journal of Applied Physics **102**, 44115 (2007).

[255] I. Stolichnov, A. Tagantsev, N. Setter, J. S. Cross, and M. Tsukada, *Crossover between nucleation-controlled kinetics and domain wall motion kinetics of polarization reversal in ferroelectric films*, Applied Physics Letters **83**, 3362 (2003).

[256] M. Vopsaroiu, J. Blackburn, M. G. Cain, and P. M. Weaver, *Thermally activated switching kinetics in second-order phase transition ferroelectrics*, Physical Review B **82**, 24109 (2010).

[257] A. Tagantsev, I. Stolichnov, N. Setter, J. Cross, and M. Tsukada, *Non-Kolmogorov-Avrami switching kinetics in ferroelectric thin films*, Physical Review B **66**, 214109 (2002).

[258] C. L. Jia, *Atomic-Resolution Imaging of Oxygen in Perovskite Ceramics*, Science **299**, 870 (2003).

[259] S. J. Pennycook, D. E. Jesson, P. D. Nellist, M. F. Chrisholm, and N. D. Browning, Handbook of Microscopy, in *Handbook of Microscopy*, edited by S. Amelinckx, pages 592–620, Wiley-VCH Verlag GmbH & Co. KGaA, Weinheim, Germany, 2 edition, 1997.

[260] S. Zhang et al., *Advantages and challenges of relaxor-PbTiO3 ferroelectric crystals for electroacoustic transducers - A review*, Progress in Materials Science **68**, 1 (2015).

[261] M. Ozgul, *Polarization switching and fatigue anisotropy in relaxor-lead titanate ferroelectric single crystals*, Phd, Pennsylvania State University, 2003.

[262] S. Zhang, N. P. Sherlock, R. J. Meyer, and T. R. Shrout, *Crystallographic dependence of loss in domain engineered relaxor-PT single crystals*, Applied Physics Letters **94**, 162906 (2009).

[263] S. Zhang et al., *Face shear piezoelectric properties of relaxor-$PbTiO_3$ single crystals*, Applied Physics Letters **98**, 182903 (2011).

[264] Y. A. Genenko, J. Glaum, M. J. Hoffman, and K. Albe, *Mechanisms of aging and fatigue in ferroelectrics*, Materials Science and Engineering B **192**, 52 (2015).

[265] J. Glaum, Y. A. Genenko, H. Kungl, L. A. Schmitt, and T. Granzow, *De-aging of Fe-doped lead-zirconate-titanate ceramics by electric field*

cycling: 180 degrees vs. non-180 degrees domain wall processes, Journal of Applied Physics **112**, 34103 (2012).

[266] H. Neumann and G. Arlt, *Effect of Mn substitutions on dielectric properties of high dielectric constant BaTiO3-based ceramic*, Ferroelectrics **76**, 303 (1987).

[267] G. Arlt and H. Neumann, *Internal bias in ferroelectric ceramics - origin and time-dependence*, Ferroelectrics **87**, 109 (1988).

[268] X. Ren and K. Otsuka, *Origin of rubber-like behaviour in metal alloys*, Nature **389**, 579 (1997).

[269] X. Ren and K. Otsuka, *Universal symmetry property of point defects in crystals*, Physical Review Letters **85**, 1016 (2000).

[270] X. Ren, *Large electric-field-induced strain in ferroelectric crystals by point-defect-mediated reversible domain switching*, Nature Materials **3**, 91 (2004).

[271] L. X. Zhang and X. Ren, *In situ observation of reversible domain switching in aged Mn-doped BaTiO3 single crystals*, Physical Review B **71**, 174108 (2005).

[272] L. Zhang, E. Erdem, X. Ren, and R.-A. Eichel, *Reorientation of (MnTi'*V_O^{**}*)(x) defect dipoles in acceptor-modified* $BaTiO_3$ *single crystals: An electron paramagnetic resonance study*, Applied Physics Letters **93**, 202901 (2008).

[273] S. Wu, L. Wang, L. Chen, and X. Wang, *Dipole orientation in Cr-modified BaTiO3 ceramics*, Journal of Materials Science: Materials in Electronics **19**, 505 (2008).

[274] P. Perez-Delfin et al., *Effect of Mn-acceptor dopant on dielectric and piezoelectric responses of lead lanthanum zirconate titanate piezoceramics*, Jounal of Applied Physics **110**, 34106 (2011).

[275] K. Carl and Härdtl, *Electrical aftereffects in Pb(Ti,Zr)O3 ceramics*, Ferroelectrics **17**, 473 (1978).

[276] P. Erhart, R. A. Eichel, P. Träskelin, and K. Albe, *Association of oxygen vacancies with impurity metal ions in lead titanate*, Physical Review B **76**, 174116 (2007).

[277] R. A. Eichel et al., *Defect-dipole formation in copper-doped PbTiO3 ferroelectrics*, Physical Review Letters **100**, 95504 (2008).

[278] H. Meštrić et al., *Iron-oxygen vacancy defect centers in PbTiO3: Newman superposition model analysis and density functional calculations*, Physical Review B **71**, 134109 (2005).

[279] J. F. Nossa, I. I. Naumov, and R. E. Cohen, *Effects of manganese addition on the electronic structure of BaTiO3*, Physical Review B **91**, 214105 (2015).

[280] Z. Zhang, P. Wu, L. Lu, and C. Shu, *Defect and electronic structures of acceptor substituted lead titanate*, Applied Physics Letters **92**, 112909 (2008).

[281] E. Cockayne and B. P. Burton, *Dipole moment of a Pb-O vacancy pair in PbTiO3*, Physical Review B **69**, 144116 (2004).

[282] P. V. Lambeck and G. H. Jonker, *The nature of domain stabilization in ferroelectric perovskites*, Journal of Physics and Chemistry of Solids **47**, 453 (1986).

[283] J. B. J. Chapman, A. V. Kimmel, and D. M. Duffy, *Novel high-temperature ferroelectric domain morphology in PbTiO3 ultrathin films*, Physical Chemistry Chemical Physics **19**, 4243 (2017).

[284] M. I. Morozov and D. Damjanovic, *Charge migration in Pb(Zr,Ti)O3 ceramics and its relation to ageing, hardening, and softening*, Journal of Applied Physics **107**, 34106 (2010).

[285] D. M. Smyth, *Ionic transport in ferroelectrics*, Ferroelectrics **151**, 115 (1994).

[286] Z. Kighelman, D. Damjanovic, M. Cantoni, and N. Setter, *Properties of ferroelectric PbTiO3 thin films*, Journal of Applied Physics **91**, 1495 (2002).

[287] R. Ahluwalia and W. Cao, *Influence of dipolar defects on switching behavior in ferroelectrics*, Physical Review B **63**, 11 (2000).

[288] J. Glaum, T. Granzow, L. A. Schmitt, H. J. Kleebe, and J. Rödel, *Temperature and driving field dependence of fatigue processes in PZT bulk ceramics*, Acta Materialia **59**, 6083 (2011).

[289] N. Balke, D. C. Lupascu, T. Granzow, and J. Rödel, *Fatigue of lead zirconate titanate ceramics. I: Unipolar and DC loading*, Journal of the American Ceramic Society **90**, 1081 (2007).

[290] Y. A. Genenko, *Space-charge mechanism of aging in ferroelectrics: An analytically solvable two-dimensional model*, Physical Review B - Condensed Matter and Materials Physics **78**, 214103 (2008).

[291] Y. A. Genenko et al., *Aging of poled ferroelectric ceramics due to relaxation of random depolarization fields by space-charge accumulation near grain boundaries*, Physical Review B **80**, 224109 (2009).

[292] Y. Q. Tan, J. L. Zhang, and C. L. Wang, *Aging behaviours of CuO modified BaTiO3 ceramics*, Advances in Applied Ceramics **113**, 223 (2014).

[293] J. Shi, H. Fan, X. Liu, and Q. Li, *Defect-dipole alignment and strain memory effect in poled Li doped (Bi0.5Na0.4K0.1)(0.98)Ce0.02TiO3 ceramics*, Journal of Materials Science: Materials in Electronics **26**, 9409 (2015).

[294] S. Liu and R. E. Cohen, *Multiscale simulations of defect dipole-enhanced electromechanical coupling at dilute defect concentrations*, Applied Physics Letters **111**, 82903 (2017).

[295] T. Rojac, S. Drnovsek, A. Bencan, B. Malic, and D. Damjanovic, *Role of charged defects on the electrical and electromechanical properties of rhombohedral Pb(Zr, Ti)O3 with oxygen octahedra tilts*, Physical Review B **93**, 14102 (2016).

[296] M. I. Morozov and D. Damjanovic, *Hardening-softening transition in Fe-doped Pb(Zr,Ti)O(3) ceramics and evolution of the third harmonic of the polarization response*, Journal of Applied Physics **104**, 34107 (2008).

[297] D. Berlincourt and H. Jaffe, *Elastic and piezoelectric coefficients of single-crystal barium titanate*, Physical Review **111**, 143 (1958).

[298] Z. Li, C. M. Grimsditch, S. K. Foster, and J. Chan, *Dielectric and elastic properties of ferroelectric materials at elevated temperature*, Journal of Physics and Chemistry of Solids **57**, 1433 (1996).

[299] P. Ghosez, X. Gonze, and J. P. Michenaud, *First-principles characterization of the four phases of barium titanate*, Ferroelectrics **220**, 1 (1999).

[300] M. Uludogan, T. Cagin, and W. A. Goddard III, *Ab initio studies on phase behavior of barium titanate*, Materials Research Society Symposium Proceedings **718**, 341 (2002).

[301] M. Uludogan and T. Cagin, *First principles approach to BaTiO3*, Turkish Journal of Physics **30**, 277 (2006).

[302] G. H. Kwei, A. C. Lawson, S. J. L. Billinge, and S. W. Cheong, *Structure of the ferroelectric phases of barium titanate*, Journal of Physical Chemistry **97**, 2368 (1993).

[303] G. Shirane, H. Danner, and P. Pepinsky, *Neutron diffraction study of orthorhombic BaTiO3*, Physical Review **105**, 856 (1957).

[304] J. J. Wang, F. Y. Meng, X. Q. Ma, M. X. Xu, and L. Q. Chen, *Lattice, elastic, polarization, and electrostrictive properties of BaTiO3 from first-principles*, Journal of Applied Physics **108**, 34107 (2010).

[305] A. Schaefer, H. Schmitt, and A. Dorr, *Elastic and piezoelectric coefficients of TSSG barium titanate single crystals*, Ferroelectrics **69**, 253 (1986).

[306] A. Khalal, D. Khatib, and B. Jannot, *Elastic and piezoelectric properties of BaTiO3 at room temperature*, Physica B **271**, 343 (1999).

[307] W. Schildkamp and K. Fisher, *Rhombohedral BaTiO3 - Study of the structure at 132-degrees-K and 196-degrees-K*, Zeitschrift Fur Kristallographie **105**, 217 (1981).

[308] P. Ghosez, J. P. Michenaud, and X. Gonze, *Dynamical atomic charges: The case of ABO(3) compounds*, Physical Review B **58**, 6224 (1998).